SILVER, MAGNESIUM AND ZINC SUBSTITUTED HYDROXYAPATITE FOR ORTHOPAEDIC APPLICATIONS

BY

MARYAM ASKARI LOUYEH

A thesis submitted to the University of Birmingham for the degree of

DOCTOR OF PHILOSOPHY

DEPARTMENT OF METALLURGY AND MATERIAL

MAY 2016

Abstract

Synthetic hydroxyapatite (HA) has been widely used for biomedical applications, in particular as a bone substitute and coating for implants, due to its similarity to the inorganic component of human bone. The aim of this study was to incorporate three divalent cations (silver, zinc and magnesium) into the hydroxyapatite structure via a wet chemical precipitation method to enhance its antibacterial properties, to avoid the need for the use of antibiotics. Material characterisation techniques such as XRD and Raman Spectroscopy confirmed that these ions were substituted within the crystal structure of HA, though did not follow the expected reaction stoichiometry and substitution ratios. HA material properties, such as crystal size, crystallinity and solubility were shown to change after ion substitution. Metal-substituted HA showed varying strengths of antibacterial properties against two bacterial strains of *E.coli* and *S. epidermidis*, which was attributed to different type of ions and substitution ratios and also different release profiles from the solid phase to the culture medium. The results from cell biological studies confirmed that the rate of osteoblast cell proliferation and cell differentiation were improved after cells being incubated with disks of substituted HA.

ACKNOWLEDGMENT **16**

1 INTRODUCTION **19**

1.1 Aims and objectives **22**

2 Literature Review **24**

2.1 Biomaterials **24**

2.2 Infections in prosthetics and implants **24**

2.2.1 Local Delivery for Treatment of Implant Infection 27

2.3 Calcium Phosphates **29**

2.3.1 Tricalcium phosphate (TCP) 32

2.3.2 Hydroxyapatite (HA) 32

2.4 Synthetic HA and Ion-Substitution **37**

2.4.1 HA synthesis with chemical precipitation 38

2.4.2 Ion substitution into HA 40

2.4.3 Methods of ion substitution in HA 41

2.4.4 Mechanism of antibacterial/antimicrobial activity of metal ions 42

2.5 Bone: A Solid Structure and Living Tissue **53**

2.5.1 The chemical Composition of the Human Bone Mineral 53

2.5.2 Hierarchical Structure 54

2.5.3 Bone Physiology 60

3 Materials and Methods **63**

3.1 Synthesis of ion substituted hydroxyapatite (wet precipitation technique) **64**

Reagents 64

Apatite synthesis reaction 66

Preparation of HA discs and sintering 68

3.1.1 X-Ray Diffraction 69
Phase Identification 72
Crystallinity 72
3.1.2 Crystal size (L_{002} reflection plane) 72
Lattice Parameters Determination 73
3.1.3 X-ray fluorescence 74
3.1.4 Fourier Transform Infrared Spectroscopy 75
3.1.5 Raman Spectrometry 76
3.1.6 Thermogravimetry (TG) 77
3.1.7 Inductively coupled plasma mass spectrometry 78
3.2 Cell culture 79
Maintenance of osteoblast cells 80
In Vitro cell Sub-Culture of 2T3 cells 80
Counting Viable Cells 81
3.2.1 Osteoblast cellular activity in response to (Ag, Mg, and Zn)/HA 84
Cell Proliferation 84
3.2.2 Alkaline Phosphatase Activity Assay 86
3.3 Antibacterial Measurements 87
3.3.1 Agar diffusion study - Zone of Inhibition (ZI) 87
3.3.2 Film adhering method (Quantitative) 88
3.3.3 Statistical Analysis 90
4 Results 92
4.1 X-ray Diffraction analysis 92
4.1.1 X-ray diffraction analysis of Non-Substituted Hydroxyapatite (NS-HA) 92
4.1.2 X-ray diffraction analysis of Silver-Substituted Hydroxyapatite (Ag-HA) 97

4.1.3 X-ray diffraction analysis of Magnesium-Substituted Hydroxyapatite (Mg-HA) 103
4.1.4 X-ray diffraction analysis of Zinc-Substituted Hydroxyapatite (Zn-HA) 109
4.2 Fourier transform infrared spectroscopy (FT-IR) 116
4.2.1 FT-IR for NS-HA 116
4.2.2 FT-IR for Ag-HA 119
4.2.3 FT-IR for Mg-HA 121
4.2.4 FT-IR for Zn-HA 123
4.3 Raman spectroscopy 125
4.3.1 Raman analysis for NS-HA 125
4.3.2 Raman analysis for Ag-HA 127
4.3.3 Raman analysis for Mg-HA 129
4.3.4 Raman analysis for Zn-HA 132
4.4 Thermal Stability Analysis 134
4.4.1 Thermogravimetric analysis of NS-HA 134
4.4.2 Thermogravimetric analysis of Ag-HA 135
4.4.3 Thermogravimetric analysis of Mg-HA 137
4.4.4 Thermogravimetric analysis of Zn-HA 139
4.5 ICP-MS Analysis 142
4.5.1 Release profile of substituted metal ions 144
4.6 X-ray Fluorescence Spectroscopy (XRF) 151
4.6.1 Characteristaion of Ag-HA by XRF 151
4.6.2 Characterisation of Mg-HA by XRF 153
4.6.3 Characterisation of Zn-HA by XRF 154
4.7 Cell Biology 154
4.7.1 Cell Proliferation results 155

4.7.2 Alkaline Phosphatase (ALP) Activity quantification 163
4.8 Antimicrobial efficacy tests 167
4.8.1 Agar diffusion study (Zone of Inhibition (ZI)) 167
4.8.2 Film Adhering Method (Quantitative analysis) 170
5 Discussion 176
5.1 X-ray Diffraction 176
5.1.1 X-ray diffraction analysis of Non-Substituted Hydroxyapatite (NS-HA) 176
5.1.2 X-ray diffraction analysis of Silver-Substituted Hydroxyapatite (Ag-HA) 181
5.1.3 X-ray diffraction analysis of Magnesium-Substituted Hydroxyapatite (Mg-HA) 184
5.1.4 X-ray diffraction analysis of Zinc-Substituted Hydroxyapatite (Zn-HA) 189
5.2 Fourier transform infrared spectroscopy (FT-IR) 192
5.3 Raman spectroscopy 197
5.4 Thermal Stability Analysis 201
5.5 Measuring the substituted ions in solid samples 205
5.5.1 Release profiles for Ion-substituted HA 212
5.6 Cell Biology 217
5.6.1 Cell Proliferation 218
5.6.2 Alkaline Phosphatase (ALP) activity quantification 225
5.6.3 Concluding statements 230
5.7 Microbiological assays 232
5.7.1 Measuring antibacterial activity 234
5.7.2 Concluding statement 242
6 Conclusion 244
6.1 The extent of ion substitution 244

6.2 Changes in crystal properties 245

6.3 Chemical structure 245

6.4 Solubility and release properties 246

6.5 Antimicrobial activity 246

6.6 Cell experiments 247

6.7 Recommendation for future work 247

7 References 249

LIST OF FIGURES

FIGURE 2. 1: A VIEW OF THE HA STRUCTURE ALONG THE C-AXIS. 35

FIGURE 2. 2: ANTIBACTERIAL MECHANISMS OF NANOPARTICLES AND THEIR IONS, ... 43

FIGURE 2. 3: HIERARCHICAL STRUCTURAL ORGANIZATION OF BONE 55

FIGURE 2. 4: THE 7 HIERARCHICAL LEVELS OF THE BONE 56

FIGURE 2. 5: LAMELLAR BONE 59

FIGURE 3. 1: SCHEMATIC DIAGRAM OF THE EXPERIMENTAL SETUP FOR HA PREPARATION 67

FIGURE 3. 2: DISCS OF HYDROXYAPATITE 68

FIGURE 3 3: INCIDENT AND DIFFRACTED X-RAYS ARE IN PHASE 70

FIGURE 3. 4: POWDER X-RAY DIFFRACTION MACHINE (BRUKER D8 DIFFRACTOMETER) 71

FIGURE 3.5: ADAPTED SCHEMATIC DIAGRAM OF RAMAN SPECTROSCOPY 77

FIGURE 4. 1: THE XRD DIFFRACTION PATTERNS OF SINTERED (1100 °C) AND NON-SINTERED HYDROXYAPATITE. 93

FIGURE 4. 2: THE XRD DIFFRACTION PATTERNS FOR SINTERED (1100 °C) SILVER SUBSTITUTED HYDROXYAPATITE WITH DIFFERENT AG CONCENTRATIONS. : 98

FIGURE 4. 3: THE XRD PATTERNS FOR NON-SINTERED SILVER SUBSTITUTED HYDROXYAPATITE WITH DIFFERENT AG CONCENTRATIONS 99

FIGURE 4. 4: CRYSTAL SIZE (TOP) AND DEGREE OF CRYSTALLINITY (BOTTOM) FOR SILVER SUBSTITUTED HYDROXYAPATITES WITH DIFFERENT CONCENTRATIONS. 101

FIGURE 4. 5: LATTICE PARAMETERS OF HA CRYSTAL (TOP) AND B-TCP CRYSTAL (BOTTOM) IN SILVER SUBSTITUTED HYDROXYAPATITES WITH DIFFERENT CONCENTRATIONS. 102

FIGURE 4. 6: THE XRD DIFFRACTION PATTERNS FOR SINTERED (1100 °C) MAGNESIUM SUBSTITUTED HYDROXYAPATITE WITH DIFFERENT MG CONCENTRATIONS 104

FIGURE 4. 7: XRD PATTERNS FOR NON-SINTERED MAGNESIUM SUBSTITUTED HYDROXYAPATITE WITH DIFFERENT MG CONCENTRATIONS 105

FIGURE 4. 8: CRYSTAL SIZE (TOP) AND DEGREE OF CRYSTALLINITY (BOTTOM) FOR MAGNESIUM SUBSTITUTED HYDROXYAPATITES WITH DIFFERENT CONCENTRATIONS. 107

FIGURE 4. 9: LATTICE PARAMETERS OF HA CRYSTAL (TOP) AND B-TCP CRYSTAL (BOTTOM) IN MAGNESIUM-SUBSTITUTED HYDROXYAPATITES WITH DIFFERENT CONCENTRATIONS. 108

FIGURE 4. 10: THE XRD DIFFRACTION PATTERNS FOR SINTERED (1100 °C) ZINC SUBSTITUTED HYDROXYAPATITE WITH DIFFERENT ZN CONCENTRATIONS 111

FIGURE 4. 11: XRD PATTERNS FOR NON-SINTERED ZINC SUBSTITUTED HYDROXYAPATITE WITH DIFFERENT ZN CONCENTRATIONS 112

FIGURE 4. 12: CRYSTAL SIZE (TOP) AND DEGREE OF CRYSTALLINITY (BOTTOM) FOR ZINC-SUBSTITUTED HYDROXYAPATITES WITH DIFFERENT CONCENTRATIONS. 114

FIGURE 4. 13: LATTICE PARAMETERS OF HA CRYSTAL (TOP) AND B-TCP CRYSTAL (BOTTOM) IN ZINC-SUBSTITUTED HYDROXYAPATITES WITH DIFFERENT CONCENTRATIONS. 115

FIGURE 4. 14: FT-IR SPECTRA OF SINTERED HYDROXYAPATITE 117

FIGURE 4. 15: FT-IR SPECTRA OF SILVER SUBSTITUTED HYDROXYAPATITE WITH DIFFERENT AG IONS CONCENTRATIONS. 120

FIGURE 4. 16: FT-IR SPECTRA OF MAGNESIUM SUBSTITUTED HYDROXYAPATITE WITH DIFFERENT MG ION CONCENTRATIONS 122

FIGURE 4. 17: FT-IR SPECTRA OF ZINC SUBSTITUTED HYDROXYAPATITE WITH DIFFERENT ZN CONCENTRATIONS. 124

FIGURE 4. 18: RAMAN SPECTRA OF SINTERED NS- HYDROXYAPATITE. 126

FIGURE 4. 19: RAMAN SPECTRA OF SILVER SUBSTITUTED HYDROXYAPATITE WITH DIFFERENT AG ION CONCENTRATIONS 128

FIGURE 4. 20: RAMAN SPECTRA FOR MAGNESIUM SUBSTITUTED HYDROXYAPATITE WITH DIFFERENT MG ION CONCENTRATIONS 131

FIGURE 4. 21: RAMAN SPECTRA OF ZINC SUBSTITUTED HYDROXYAPATITE WITH DIFFERENT ZN ION CONCENTRATIONS. 134

FIGURE 4. 22: TGA ANALYSIS OF SILVER SUBSTITUTED HYDROXYAPATITE WITH DIFFERENT AG ION CONCENTRATIONS. 136

FIGURE 4. 23 : TGA ANALYSIS FOR MAGNESIUM SUBSTITUTED HYDROXYAPATITE WITH DIFFERENT MG ION CONCENTRATIONS 138

FIGURE 4. 24: TGA ANALYSIS OF ZINC SUBSTITUTED HYDROXYAPATITE WITH DIFFERENT ZN IONS CONCENTRATIONS 141

FIGURE 4. 25: AG RELEASE PROFILE FROM AG-HA SAMPLE BASED ON TOTAL AG ION CONCENTRATION IN SOLUTION (TOP) AND PERCENTAGE OF AG IN THE POWDER WHICH IS RELEASED (BOTTOM) 146

FIGURE 4. 26: RELEASE PROFILE OF MAGNESIUM IN MAGNESIUM SUBSTITUTED HYDROXYAPATITE BASED ON TOTAL Mg^{2+} IONS CONCENTRATION IN PBS (TOP) AND PERCENTAGE OF RELEASED Mg^{2+} IONS. 149

FIGURE 4. 27: RELEASE PROFILE OF ZINC IN ZINC SUBSTITUTED HYDROXYAPATITE BASED ON TOTAL Zn^{2+} IONS CONCENTRATION IN PBS (TOP) AND PERCENTAGE OF RELEASED Zn^{2+} IONS FROM THE SAMPLES (BOTTOM). 151

FIGURE 4. 28: CELL GROWTH (MOUSE OSTEOBLAST CELL LINES (2T3)) VS. TIME (OVER 6 DAYS CULTURE) FROM THE ALAMARBLUE™ ASSAY (BLANK WELLS IS CONTROL) 156

FIGURE 4. 29: CELL GROWTH (MOUSE OSTEOBLAST CELL LINES (2T3)) VS. TIME (OVER 6 DAY CULTURE) FROM THE ALAMARBLUE™ ASSAY FOR AG-HA (NS-HA IS CONTROL). 158

FIGURE 4. 30: CELL GROWTH (MOUSE OSTEOBLAST CELL LINES (2T3)) VS. TIME (OVER 6 DAYS CULTURE) FROM THE ALAMARBLUE™ ASSAY FOR MG-HA (NS-HA IS CONTROL). 160

FIGURE 4. 31: CELL GROWTH (MOUSE OSTEOBLAST CELL LINES (2T3)) VS. TIME (OVER 6 DAY CULTURE) FROM THE ALAMARBLUE™ ASSAY 162

FIGURE 4. 32: ALP/ PROTEIN VALUES REPRESENTING OSTEOGENIC DIFFERENTIATION OF 2T3 CELLS AFTER SUBSEQUENT CULTURE AT DAY 7 FOR NS-HA AND AG-HA. 164

FIGURE 4. 33: ALP/ PROTEIN VALUES REPRESENTING OSTEOGENIC DIFFERENTIATION OF 2T3 CELLS AFTER SUBSEQUENT CULTURE AT DAY 7 FOR NS-HA AND MG-HA. 165

FIGURE 4. 34: ALP/ PROTEIN VALUES REPRESENTING OSTEOGENIC DIFFERENTIATION OF 2T3 CELLS AFTER SUBSEQUENT CULTURE AT DAY 7 FOR NS-HA AND ZN-HA. 166

FIGURE 4. 35: ZONE OF INHIBITION OF AG-HA SAMPLES AGAINST *S.EPIDERMIDIS* (TOP) AND *E.COLI* (BOTTOM). 168

FIGURE 4. 36: ZONE OF INHIBITION OF ZN-HA SAMPLES AGAINST *S.EPIDERMIDIS* (TOP) AND *E.COLI* (BOTTOM) 170

FIGURE 4. 37: CFU REDUCTION (%) OF AG-HA SAMPLES AGAINST *E.COLI* (TOP) AND *S.EPIDERMIDIS* (BOTTOM) 172

FIGURE 4. 38: CFU REDUCTION (%) OF ZN-HA SAMPLES AGAINST *E.COLI* (TOP) AND *S.EPIDERMIDIS* (BOTTOM) 174

FIGURE 5. 1: PROPOSED MECHANISMS FOR THE RELEASE OF METAL IONS FROM SOLID DISKS 214

LIST OF TABLES

TABLE 2. 1 EXISTING CALCIUM ORTHOPHOSPHATES AND THEIR MAJOR PROPERTIES 31

TABLE 2. 2 UNIT- CELL POSITIONS OF THE HA LATTICE WHERE; A=90°, B=90°, Ɣ=120° 34

TABLE 3. 1: WEIGHTS OF REACTANTS IN CHEMICAL PRECIPITATION METHOD TO MAKE AG SUBSTITUTED HA 65

TABLE 3. 2: WEIGHTS OF REACTANTS IN CHEMICAL PRECIPITATION METHOD TO MAKE MG SUBSTITUTED HA 66

TABLE 3. 3: WEIGHTS OF REACTANTS IN CHEMICAL PRECIPITATION METHOD TO MAKE ZN SUBSTITUTED HA 66

TABLE 4. 1: CHARACTERISTIC PEAKS OF SYNTHESISED HA (NON-SUBSTITUTED) AND COMPARISON WITH STOICHIOMETRIC HA USED AS A REFERENCE. 94

TABLE 4. 2: PRESENT PHASES, CRYSTALLINITY AND CRYSTAL SIZE FOR NS-HA. 95

TABLE 4. 3: LATTICE PARAMETERS OF HA AND B-TCP IN SINTERED (1100 °C) NS-HA. 96

TABLE 4. 4: PRESENT PHASES, CRYSTALLINITY AND CRYSTAL SIZE FOR SINTERED (1100 °C) AG-HA. 100

TABLE 4. 5: PRESENT PHASES, CRYSTALLINITY AND CRYSTAL SIZE FOR SINTERED (1100 °C) MG-HA 106

TABLE 4. 6: PRESENT PHASES, CRYSTALLINITY AND CRYSTAL SIZE FOR SINTERED (1100 °C) ZN-HA 113

TABLE 4. 7: ASSIGNMENTS OF MAIN BANDS OBSERVES IN THE INFRARED ABSORPTION SPECTRA OF HA. 119

TABLE 4. 8: CHARACTERISTIC RAMAN PEAKS OF HA OBSERVED IN THE RAMAN SPECTRA AND ASSIGNMENT. 127

TABLE 4. 9: RAMAN SHIFTS OBSERVED AND ASSIGNMENT FOR MG-HA 130

TABLE 4. 10: RAMAN SHIFTS OBSERVED AND ASSIGNMENT FOR ZN-HA 133

TABLE 4. 11 WEIGHT LOSS FOR NS-HA AND AG IONS SUBSTITUTED HA UP TO 1100 °C. 136

TABLE 4. 12: WEIGHT LOSS FOR NS-HA AND MG IONS SUBSTITUTED HA UP TO 1100 °C. 137

TABLE 4. 13: WEIGHT LOSS FOR NS-HA AND ZN IONS SUBSTITUTED HA UP TO 1100 °C. 139

TABLE 4. 14: AG IONS CONCENTRATION IN SILVER SUBSTITUTED HYDROXYAPATITE SAMPLES 143

TABLE 4. 15 MG IONS CONCENTRATION IN MAGNESIUM SUBSTITUTED HYDROXYAPATITE SAMPLES. 143

TABLE 4. 16 ZN IONS CONCENTRATION IN MAGNESIUM SUBSTITUTED HYDROXYAPATITE SAMPLES. 144

TABLE 4. 17: XRF MEASUREMENT FOR AG-HA SAMPLES. 152

TABLE 4. 18: XRF MEASUREMENT FOR MG-HA SAMPLES 153

TABLE 4. 19: XRF MEASUREMENT FOR ZN-HA SAMPLES..... 154

TABLE 4. 20: CONCENTRATION OF AG IONS DUE TO UNASSISTED RELEASE (PPM) OVER PERIOD OF 2, 4 AND 6 DAYS. 158

TABLE 4. 21: CONCENTRATION OF MG IONS DUE TO UNASSISTED RELEASE (PPM) OVER PERIOD OF 2, 4 AND 6 DAYS. 161

TABLE 4. 22: CONCENTRATION OF ZN IONS DUE TO UNASSISTED RELEASE (PPM) OVER PERIOD OF 2, 4 AND 6 DAYS. 162

List of Abbreviations

3D	Three-dimensional
(α/β-) TCP	(Alpha/Beta-) Tricalcium Phosphate
ACP	Amorphous Calcium Phosphate
Ag	Silver
Ag^{+}	Silver ion
Ag-HA	Silver substituted hydroxyapatite
ALP	Alkaline Phosphatase
ANOVA	Analysis of variance
BCP	Bisphasic Calcium Phosphate
BMP	Bone Morphogenic Protein
BSA	Bovine serum albumin
°C	Degree Celsius
Ca	Calcium
Ca^{2+}	Calcium ion
CaO	Calcium oxide
$CaCo_3$	Calcium Carbonate
$Ca(NO_3)_2$	Calcium Nitrate
Ca/P	Calcium/Phosphate ratio
CaP	Calcium phosphate
CDHA	Calcium-deficient Hydroxyapatite
CFU	Colony formation unite
CO_2	Carbon Dioxide
Cu^{2+}	Copper ion
CS	Compressive Strength
DI	De-ionised
$(NH_4)_2HPO_4$	Diammonium hydrogen phosphate
DMEM	Dulbecco's Modified Eagle Medium
DNA	Deoxyribonucleic Acid

DTS	Diametral Tensile Strength
ECM	Extracellular Matrix
E.coli	*Escherichia coli*
FBS	Foetal Bovine Serum
FT-IR	Fourier Transform Infrared Spectroscopy
FWHM	Full width at half maximum
h	Hour
HA	Hydroxyapatite
hMSCs	Human Adipose-derived Mesenchymal Stem Cells
I	Transmitted X-rays intensity
I_o	Incident of X-rays intensity
ICDD	International Centre for Diffraction Data
ICP-MS spectometry	Inductively coupled plasma mass
g	Gram
Mg	Magnesium
Mg^{+2}	Magnesium ion
Mg-HA	Magnesium substituted hydroxyapatite
MIC	Minimal Inhibitory Concentration
MPa	Mega Pascal = 1 N/mm^2
nm	Nanometer
NS-HA	Non-substituted hydroxyapatite
OC	Osteocalcin
ON	Osteonectin
OP	Osteopontin
KBr	Potassium bromide
PBS	Phosphate buffer solution
Sr^{2+}	Strontium ion
S. aureus	*Staphylococcus aureus*
SBF	Simulated body fluid
SD	Standard Deviation
S.epidermidis	*Staphylococcus epidermidis*
TGA	Thermogravimetric Analysis

Wt.	Weight
UV	Ultra violet
XRD	X-ray Diffraction
XRF	X-ray Florescence
Zn	Zinc
Zn^{2+}	Zinc ion
Zn-HA	Zinc substituted hydroxyapatite
ZI	Zone of inhibition

ACKNOWLEDGMENT

There are many people without whom this thesis would not have been possible. My positive side, who stood by me throughout these years, encouraged me to continue my experiments when I was pregnant and kept my company on weekends, holidays and evenings when I had to work late in the lab on my own; thank you for all your love, support and encouragement, I know with you by my side, I can achieve anything I aim for.

I would like to specially thank my supervisor, Prof. Afsie Sabokbar from the University of Oxford, for making me feel welcome when I first invited her to collaborate with Birmingham, giving me access to her department facilities and giving me the chance to experience and enjoy the state of collaborative work between different institutes. Her support and guidance as a supervisor was there throughout my project and beyond.

I would like to especially thank Prof. Liam Grover who gave me tremendous academic support and constant advise during the challenge to complete my PhD.

I also would like to express my deep gratitude for Dr. Rachel Sammons, who gave up her time, also allowing me to work in her lab and for providing me with a wealth of knowledge as I've worked with them on microbiology parts of this project.

I would like to thank other members of staff in Birmingham who facilitated my research including Dr. Artemis Stambolis, Dr. James Bowen, John Wedderburn, Dr. Stephen Baker and Frank Briddlestone for their advice, scientific support and for their help.

Sincere thanks goes to Dr. Ali Zarei, from University of Oxford, for his assistance with experimental set-up and analytical work and for helping cell biological part of my PhD to run as smoothly as possible.

My sincerest thanks go to my parents for their continued understanding, not only during my PhD, but also throughout my life so far. I wouldn't be where I am now without their years of hard work.

My immense gratitude goes to my husband, Ali, thank you so much for your love and for believing that I could achieve whatever goals I set for myself. Your kind words and valuable advice within the past year, it was a hard year and your support helped me overcome it easier. Also, Hannah, thank you for being patient with me while I was busy with writing my thesis, without you my life would be empty.

CHAPTER 1

INTRODUCTION

1 INTRODUCTION

In recent years, healthcare systems have witnessed an unprecedented demand in the number of orthopaedic surgeries, in particular ones which include the use of implants and prostheses. The ageing population and increasing number of sport injuries are regarded as the main contributors for the growth in such operations. Since patients are living longer following the fitting of prosthetics and expect to retain normal levels of activity, there is now a significant increase in the physical demands placed on prostheses. Although most implants will last up to 20 years, there is a subset of patients who will need a revision surgery within 5 years after the procedure for both hip and knee replacements (1, 2). Most common problems associated with patients who require revision surgeries include instability, aseptic loosening, infection, wear, osteolysis and a failure of the bone to grow into the prosthetic (1, 3).

Success of an orthopedic implants strongly relies on its interaction between its surface and the surrounding tissues after the implantation (4, 5). A perfect orthopaedic implants are currently unachievable due to inadequate osseointegration, which increases the risk of implant failure. Efforts to improve host cell-implant interaction have resulted in enhanced osseointegration (6). Implant infections are responsible for the failure of approximately 2% of orthopedic implants worldwide (7). Infection at the implant site is the result of bacterial adhesion to the implant surface and subsequent formation of biofilm. If bacterial adhesion happens before tissue regeneration, the host defense system often cannot prevent colonization for certain bacterial species that are capable of forming a protective biofilm layer(8). Since biofilm is extremely resistant to both immune system and antibiotics, it is critical to inhibit bacterial adhesion in order to prevent forthcoming infection. Skin is the most common source of the staphylococcus

species which is responsible for 60% of all prosthetic infections (9). To prevent infection during the surgery, applying prophylactic antibiotics has been shown to be most effective (9). If infection does occur, the most common therapy is a two-stage implant exchange plus 6 weeks of intravenous antibiotic administration resulting in long periods of hospitalization(10) both steps are costly and not feasible(11) (12).

Synthesized calcium phosphates (CaP), which are demonstrated biocompatibility for orthopaedic application and bioactive, have been widely used as orthopaedic implants. Hydroxyapatite (HA), which is a calcium phosphate, gained more attention due to its chemical and crystallographic similarities to the inorganic components of natural bone and other hard tissue in mammals(13). The three dimensional structure of HA shows great flexibility in accepting mixture of ions such as divalent ions (Mn^{2+}, Sr^{2+}, Cu^{2+}, Co^{2+}, Zn^{2+}, Mg^{2+}), monovalent ions (Na^{+}, K^{+}, Ag^{+}) and trivalent ions (Bi^{3+}, Ln^{3+}) in the calcium site. This ionic replacement can control the property and application of the HA in various subject such as catalysis (14), protein adsorption(15), ion exchangers(16) and biomaterials.

Studies have shown that synthesized HA, when compared to metallic or other ceramic biomaterials, can promote osteoblast (bone growth cells) and osteoclast (bone resorption cells) activity after implantation, and therefore improve osseointegration (direct structural and functional connection between living bone and the surface of HA implant). For this reason, synthesized HA has been widely used as implants materials in dentistry or orthopedics such as dental implants, periodontal treatment, alveolar ridge augmentation, maxillofacial surgery and otolaryngology(17). However, HA, due to its inherent characteristics of brittleness, poor tensile strength and low fracture, can only be used in none load bearing implants.

Since bacterial infection is major problem with orthopedic implant failures, over the years silver and zinc have been studied as an implant coating since they exhibit a broad range of antimicrobial activity and bacterial inactivation *in vitro* (18, 19) (20). Moreover, zinc can promote osteoblastic cell proliferation and differentiation and is thought to possess a selective inhibitory effect on osteoclastic bone resorption *in vivo* (21, 22). Several studies confirmed that HA with zinc or silver accelerated osteoblast activity compared to pure HA.

Magnesium is known to be an important trace element in bone and teeth and also during osteogenesis. Magnesium can promote osteoblast proliferation (23), and its depletion causes bone fragility and bone loss (24). As a result, many studies have investigated the preparation of calcium phosphate implant materials containing of Mg, which has been shown to improve their bioactivity.

Studying cytotoxicity is important factor to check biocompatibility before implantation. *In vitro* cytotoxicity is one of the recommended and appropriate tests for the biological assessment of the medical device (25). The antimicrobial properties of silver, zinc and biological effect of magnesium have a high dependence on the release of the ions from calcium phosphate (26, 27).

Based on previous studies, the replacement of calcium by silver, magnesium and zinc in HA is limited. This is related to the dissimilar size between candidate cations and Ca^{+2}, which leads to strong distortions of the HA crystal and alter their solubility and biodegradability in physiological fluids. These changes have a direct impact on the properties of substituted hydroxyapatite,(13, 28-30).

Introducing cations into hydroxyapatite structure has been studied for a long time in terms of reviewing the change in material characterization, interaction with microbiological culture and

cell biological behaviors. However, to date there has been no comprehensive studies of this and also measuring exact amount of substitution of cations (Ag, Zn, and Mg) in hydroxyapatite.

In this research, Ions (Ag, Mg, Zn) substituted hydroxyapatite and samples were analyzed considering three aspects:

1) Material characterization
2) Microbiological effect of HA against two most common infection causing bacteria (*E.coli* and *S.epidermidis*)
3) Proliferation and differentiation of osteoblast cells in contact to HA

1.1 Aims and objectives

The aim of this project was to study the effectiveness of silver, magnesium and zinc substituted hydroxyapatite as an improved formulation for orthopedic applications. It was critical to understand how the substituted ions will impact the chemical and crystal properties within the studied concentration range of the metal ions.

While it is known that the metal ions in hydroxyapatite powders will manifest some antibacterial properties, a key objective in this study was to establish the optimum concentration range for the selected metal ions by measuring their antibacterial response individually for each sample against selected bacterial species and compare with other chemical and physical properties.

In addition, this study will measure how the biological response and cell viability were affected versus selected cell lines *in vitro* and whether the metal ions have contributed to the osteoconductivity properties of the final powder.

CHAPTER 2

LITERATURE REVIEW

2 Literature Review

2.1 Biomaterials

Biomedical material science or the science of understanding and developing "Biomaterials" has been an exciting and rewarding research area of materials science. The most recent definition of biomaterials is: "*A biomaterial is a substance that has been engineered to take a form which, alone or as part of a complex system, is used to direct, by control of interactions with components of living systems, the course of any therapeutic or diagnostic procedure, in human or veterinary medicine"* (31). In particular, in recent years, because of an increased ageing population, there has been a growing number of bone-related diseases and fractures which demand treatments, some by incorporating implants with or without complimentary functionality (e.g. incorporated antibacterial activity for infection control, growth hormones etc). To guarantee that an implant can provide the desired function, its longevity and its overall success, suitable selection of biomaterial fit for the proposed application is essential..

Solid biomaterials can be classified as bimetals, biopolymers, bioceramics or biocomposites. The focus of this research is on the studying a new formulation of substituted hydroxyapatite with the enhanced antimicrobial activity. Hydroxyapatite is a calcium phosphate and a common bioceramic used mainly for its excellent osteo-conductive properties(32), , and its properties are reviewed in detail in section 2.3.

2.2 Infections in prosthetics and implants

Despite all the advances in the development of biomaterials, a significant number of implant procedures are affected by bacterial infection after implantation and revision surgeries as well as prolonged administration of antibiotics are required. Orthopaedic device-related infections

(ODRI) are responsible for the failure of 1-2% of orthopaedic implants worldwide (33). Implant joint infection is a relatively uncommon complication following hip and knee joint replacement and occurs approximately less than1 and 0.5%, respectively (34). These infections may require prolonged therapy and often removal of the affected prosthesis is necessary (35, 36).

Infection may also occur early or late, from direct intra-operative inoculation, wound infection or haematogenous seeding. The most common infections are due to coagulase-negative staphylococci (CoNS) which are part of the normal flora of human skin such as S. *epidermidis*, the most common CoNS pathogen that accounts for about 74% to 92% of all hospital-acquired CoNS infections and *S. haemolyticus*, the second most common CoNS, often a pathogen in endocarditis, septicemia, peritonitis, urinary tract infections, osteomyelitis, and wound infections. Other common pathogens include *S. aureus*,enterococci, streptococci, corynebacteria, enterobacteriaceae and anaerobes (37).

Infection occurs when bacteria are attached to the implant surface and biofilm, which is a resistant form of bacterial colony, starts to form. The biofilm develops through the following stages:

(i) surface adhesion followed by

(ii) multilayered cellular proliferation and

(iii) intercellular adhesion in an extracellular polysaccharide matrix.

Generally the body immune system cannot prohibit bacterial proliferation when a protective bacterial biofilm layer has been already formed (38). Hence, it is critical to prevent the initial colonisation and adhesion of bacteria in order to control infection.

Pathogenic microorganisms, particularly gram-positive *S. aureus* and *S. epidermidis*, have been found in approximately 90% of implants(7). Gram-negative *E.coli*, *Pseudomonas aeruginosa*, and the pathogens from the Proteus group (e.g., *P. mirabilis* and *P. vulgaris*) have also been found in implant-associated infections (7).

Implant infections are not only due to a poor surgical operation or host health factors (such as obesity or chronic diseases) but can also arise from the anatomical characteristics of the implant site and properties of the implanted device such as its size and shape (39).

Another major concern in recent years has been the increasing occurrence of infections from antibiotic-resistant bacteria. In a large surveillance in surgical site infections after orthopaedic interventions, 59% of the infections were due to the isolated methicillin-resistant *S. aureus* (MRSA) strains (40, 41). The reported incidences of MRSA infection at the surgical site increased from 32% to 64% between 1992 and 2003 (42). MRSA is associated with higher rates of patient morbidity and mortality than non-MRSA strains (43) and its control demands for new antibiotics or using alternative agents with minimum or no bacteria resistance (such as silver nanoparticles).

Minimizing and inhibiting post-surgery infections, in particular for orthopaedic applications, is becoming more critical as the aging population increases meaning more people will need such treatments in coming years (7).

The most common procedure to treat osteomyelitis (bone infection) is to remove the dead bone tissue from the infective site, irrigate the wound and administer systemically antibiotics for extended periods of time (44). The routine use of systemic antibiotic drugs for prophylaxis in post-operative complications is not appropriate for the alleviation of these ailments, due to poor

perfusion to the diseased ‘bone site’ as well as other antibiotic related symptoms such as allergic reactions, nephrotoxicity and ototoxicity (45).

Hence, the local delivery of drugs to bones or infected implant site is becoming more popular for the treatment of post-operative complications. This to a large extent can be achieved by preloading implants with antimicrobial agents, which can reduce the systemic body burden of drugs. For example, bone cements are often preloaded with antibiotics as a standard practice (46).

The delivery systems are certainly destined to play an important role in the fight against bacterial infections. In the treatment of orthopaedic infections, there are two main challenges faced by the surgeons when local delivery of antibiotics is followed as standard practice; avoiding antibiotic resistance and achieving antimicrobial activity without impairing peri-implant bone growth (i.e. osseointegration) (47).

2.2.1 Local Delivery for Treatment of Implant Infection

All drug delivery systems in this case antibiotic loaded implants should provide a local and controlled release profile at the site of implantation. Additionally, the release profile proven to be more effective is the one that allows burst release at the first hours after surgery (short time effect) followed by a sustainable therapeutic release over prolonged periods of time (long time effect) (48). Fast release provides high dose but short-term action. On the other hand, slow release may not reach the required antibiotic level. The release of antibiotics must occur before a protective biofilm layer forms protecting the bacterial colony. Bacteria protected by a biofilm can require 1000 times the antibiotic level necessary to combat bacteria in suspension.

Today, antibiotics can be loaded in two types of implants:

1) Polymers such as polyurethane (PU), silicon rubber, poly L-lactic acid (PLA), poly (glycolic acid) (PGA), polyhydroxyalkanoates (PHA) and polymethylmethacrylate (PMMA)(non-biodegradable), and

2) inorganic coatings such as hydroxyapatite from different sources (48).

Depending on the type of implant, the antibiotic release profile can be modulated in different forms. For instance in polymeric materials, the hydrophilic and hydrophobic chain ratios can be adjusted, or the right balance of biodegradability and biostability is set for.

In contrast, self-setting apatite is transformed into hydroxyapatite, which has high compatibility with the natural hard tissue, sets within half an hour in-situ and is easy to use in a clinical setting (49). More importantly, there is no limitation in the use of thermos-sensitive antibiotics due to the non-exothermic setting reaction. On the other hand, certain care is also needed to investigate the antibiotic activity at different pH. However, brittleness and poor strength of HAP has limited its use as an implant in loaded situations. Hence, HAP coated metal implant with sufficient mechanical strength has been proposed as an alternative (50). Although the load wearing capacity of HAP is low, in a recent report (51), gentamycin impregnated HAP cement was very effective to treat bone infection (e.g. osteomyelitis) in rats. It was showed that doxycycline is a broad-spectrum antibiotic with activity against a wide range of gram positive and gram-negative organisms (51).

The following sections review the properties and applications of calcium phosphate ceramics, and in particular hydroxyapatite as well as metal ions as antibacterial agents.

2.3 Calcium Phosphates

Calcium phosphates (CaP) are a group of minerals containing calcium ions (Ca^{2+}) together with orthophosphates (PO_4^{3-}), metaphosphates ($P_2O_7^{4-}$) and occasionally hydrogen or hydroxide ions (52) . Based on their composition, the vast majority of synthetic calcium phosphates are classified as 1. HA ($Ca_{10}(PO_4)_6(OH)_2$); 2. α- and β-tricalcium phosphates (TCP) $Ca_3(PO_4)_2$; 3. biphasic calcium phosphates (BCPs) which is a mixture of either α- or β-TCP with HA, and 4. amorphous calcium phosphates (53, 54) .

CaP play a significant role in human bodies and other mammals as they represent the inorganic part of healthy bones and teeth as well as pathological calcified tissues (55). Hence, they are biocompatible and are not considered foreign materials when implanted. They are also safe, non-toxic and exhibit bioactive behaviour. (54).

The first attempt to use calcium phosphates for clinical applications was as an artificial material to repair surgically bone defects in rabbits in 1920, but their use and introduction for orthopaedic applications in humans was not until the early 1970s (54). While trying to replace the dominant metallic materials, the main attention was to find how ceramic based materials could be improved in terms of bone integration, functionality, mechanical and chemical characteristics. Table 2.1 shows a list of known calcium orthophosphates and their major properties such as chemical formula, solubility and pH stability range. The ones which are stable around pH=7.0.

In human body, ceramic materials are found in two forms, bioinert or bioactive. Bioinert materials does not stimulate body reaction in the surrounding environment and tissue after implantation while a bioactive material can lead to certain biological responses and reaction at

its surface and will promote the formation of links between the tissue and implant material.

Table 2. 1 Existing calcium orthophosphates and their major properties (54)

Ca/P molar ratio	Compound	Formula	pH stability range in aqueous solutions at 25°C	Solubility at 25 °C (g/l)
0.5	Monocalcium phosphate monohydrate	$Ca_2(H_2PO_4).H_2O$	0.0-2.0	~18
0.5	Monocalcium phosphate anhydrous	$Ca_2(H_2PO_4)$	Stable at temperatures above 100 °C	~17
1.0	Dicalcium phosphate dihydrate, mineral brushite	$CaHPO_4.2H_2O$	2.5-6.0	~0.088
1.0	Dicalcium phosphate anhydrous, mineral monetite	$CaHP\ O_4$	Stable at temperatures above 100 °C	~0.048
1.33	Octacalcium phosphate (OCP)	$Ca_8(HPO_4)_2(PO_4).5H_2O$	5.5-7.0	~0.0081
1.5	α-Tricalcium phosphate (α-TCP)	α-$Ca_3(PO_4)_2$	These compounds cannot be precipitated from aqueous solutions	~0.0025
1.5	β- Tricalcium phosphate (β-TCP)	β-$Ca_3(PO_4)_2$	These compounds cannot be precipitated from aqueous solutions	~0.0005
1.5-1.67	Calcium-deficient hydroxyapatite (CDHA)	$Ca_{10-x}(HPO_4)_x.(PO_4)_{6-x}(OH)_{2-}$	6.5-9.5	~0.0094
1.67	Hydroxyapatite	$Ca_{10}(PO_4)_6\ (OH)_2$		~0.0003

Calcium phosphates are formed through a process called sintering (1100-1300ºC) during which amorphous or crystalline structures are formed. The sintering conditions and stoichiometry of the reaction can dictate the type, structure and composition of the final CaP. For example, at Ca/P ratios of 1.5 from TCP while stoichiometric HA is obtained at Ca/P ratio of 1.67(56). By changing this ratio between these two ranges, the final obtained CaP can be a biphasic mixture of TCP and HA phases.

Solubility of the formed CaP can also determine the type of application that it can be used for and depends whether a resorbable phase or and non-soluble phase is required(56).

2.3.1 Tricalcium phosphate (TCP)

Compared to HA, tri-calcium phosphate (TCP) with the formula of $Ca_3(PO_4)_2$, has lower Ca/P ratio, less stability and higher solubility. This phase is thermodynamically stable at very high temperatures (1000-1500º C) only.

Both α- and β-TCP have identical chemical composition but have different crystallographic structure, which gives them slightly different properties. α-TCP is a less stable phase and has higher solubility and degradation rates compared to β-TCP (57).

2.3.2 Hydroxyapatite (HA)

HA is a mineral from the apatite family with a general formula of $M_5(ZO_4)_3X$, where M is a rare-earth metal, such as Ca^{2+}, Cd^{2+}, Sr^{2+}, Ba^{2+}, Pb^{2+}, Zn^{2+}, or Mg^{2+}, ZO_4 could be PO_4, CO_3 or SO_4 and X is OH–, F–, Cl–, or CO_3^{2-} (58).

HA has a chemical formula of $Ca_5(PO_4)_3OH$ and is a naturally occurring CaP with the most

similar chemical composition to the mineral content of the bone(59, 60) . When compared to both α - and β -TCP, HA is a more stable and less soluble phase under physiological conditions and suitable for orthopaedic applications. In case of stoichiometric HA, the Ca/P ratio is 10:6 (or 1.67) which is the pure stable phase of HA. When Ca/P ratio is in the range of 1.5-1.67, Calcium Deficient Hydroxyapatite (CDHA) will be formed.

Due to its outstanding biological properties such as no inflammatory response, no toxicity and absence of fibrous or immunological reactions, HA is one of the most promising biomaterials for implant coating applications(61). HA exhibits a high degree of biocompatibility, mainly due to its identical chemical composition when compared with natural bone (62).

HA has been widely used in orthopaedic and dental applications as well as in drug delivery vehicles(63, 64).

The low solubility of HA makes it more suitable for long-term clinical and surgical applications, while its hard and brittle structure and faster setting time (in case of HA cements) makes it difficult to reshape and handle during operation(65) .

Chemistry of HA

Studies to investigate the exact composition of HA through chemical analysis were conducted as early as first half of 18^{th} century but it was until a century later that the current concept of the presence of various CaP crystal phases was introduced (66). Understanding the exact chemical structure and composition of HA has made it possible to optimize the synthesis process during which improved functionality or tailored properties can be restored to the final product.

Two main crystal forms are identified for HA: monoclinic and hexagonal with the hexagonal form being more stable than the monoclinic one against the introduction of foreign ions (i.e. ions other than Ca^{2+}, PO_4^{3-} and OH^- native to the HA structure) which makes it more practical for biomaterial applications(67, 68).

In the hexagonal form, the ten calcium (Ca) atoms contained in the unit cell (as listed in Table 2.2) are distributed between two different crystallographic Ca^{2+} sites, which are referred to as Ca(I) and Ca(II) as illustrated in Figure 2.1.

Table 2. 2 Unit- cell positions of the HA lattice where; α=90°, β=90°, ϒ=120° (69)

Atom	x/a	y/b	z/c
Ca(I)	1/3	2/3	0.0010
Ca(II)	0.2464	0.9938	1/4
P	0.3999	0.3698	1/4
O(I)	0.3272	0.4837	1/4
O(II)	0.5899	0.4666	1/4
O(III)	0.3457	0.2595	0.0736
OH	0.0000	0.0000	0.1930

There are strong bonds between the four Ca atoms at the Ca(I) positions and six oxygen atoms with an additional weaker bonding influence from a further three oxygen atoms. Consequently, the Ca(I) ions will be tightly confined in columns along the c-axis and shape a hexagonal arrangement along c-axis. The HA crystal structure may be changed if there is any disruption

to the metal-oxygen interactions at the Ca(I) sites and therefore Ca(I) sites can only tolerate the substitution of ions which are smaller than Ca (or possibly slightly larger than Ca at low concentrations). The six Ca(II) atoms are staggered over consecutive planes cutting the c-axis and are surrounded by seven oxygen atoms, which belong to phosphate groups and hydroxyl groups. The Ca(II) site under this arrangement can be subjected to local displacements by substitution with larger cations, while the overall crystal structure is not affected (68).

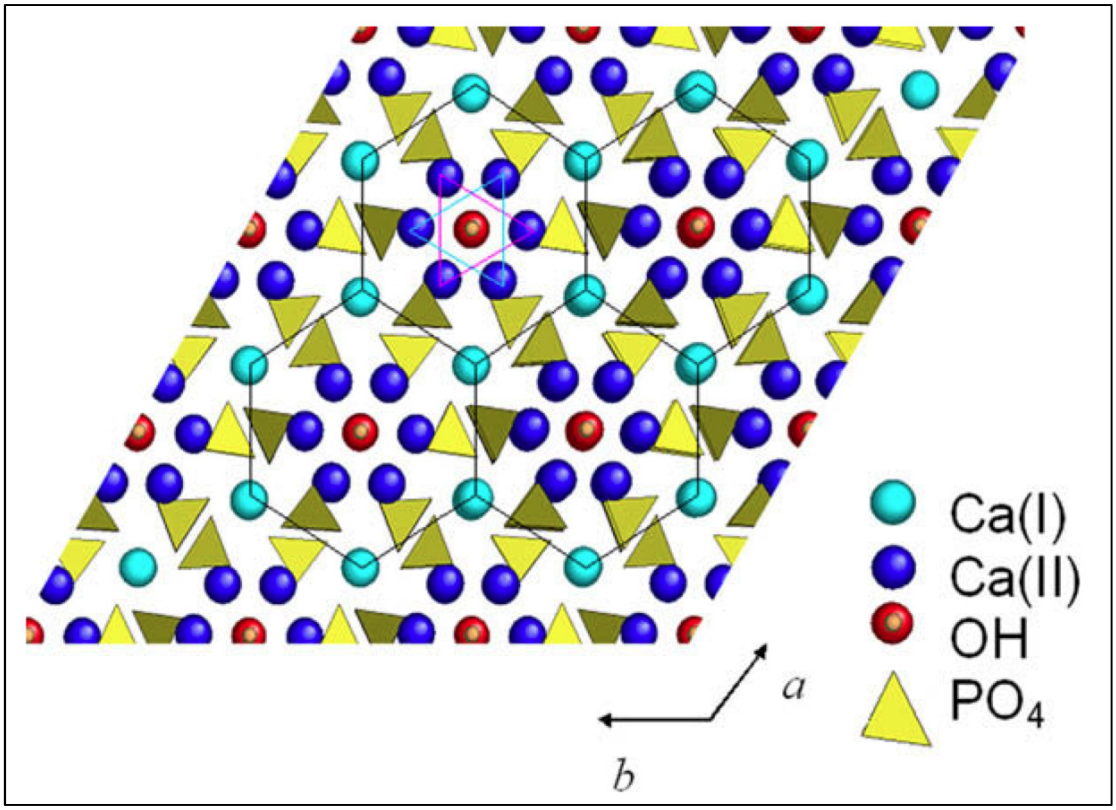

Figure 2. 1: A view of the HA structure along the C-axis. Black line connect Ca(I) columns in hexagonal networks. Cyan and magenta triangles connect staggered Ca(II) atoms lying in the same plane, but at different height with respect to the C-axis. (68)

HA as a coating for orthopaedic implants

HA is widely used solely or in combination with other implants to enhance the integration of medical implants and prosthetic components, in order to provide firm bonds to the host bone by ingrowth of new bone-like structure(70) .

Most CaP ceramics (except stable stoichiometric HA) are classified as resorbable biomaterials as they can experience degrees of solubilisation at certain physiological conditions. The body can readily use and assimilate the dissolution products of CaP biomaterials. HA-coated implants have been widely used and shown to be effective by enhancing the durability stability of the implants, as a result of better osteoconductivity and integration of the implant with bone tissue (71) .

When HA comes in contact with physiological fluids, a series of chemical reactions take place leading to the formation of new bones, in what is also called an osteoconductive process(61). The bioactive HA triggers a series of reformation processes at the surface of the material during which HA interaction with bone and the subsequent reactions, which lead to ion precipitation and generation of natural and biologically equivalent bone. As one of the noticeable effect of HA, it is able to improve bone formation between the gaps around the implant and also being capable of converting motion-induced fibrous membrane into a bony anchorage(72).

At the bone-HA implant surface, the interaction with the bone tissue will form bonds other than fibrous tissue layer type, which is critical to guarantee the fixation and stabilisation of implants. This interface and the underlying interactions are very similar to the type of interface which is observed when natural tissue repairs itself as it is dynamic, time-dependent and a function of chemical reactivity of the ceramic(61).

This is a clinical advantage for HA as its bioactivity can be modified by adjusting its synthesis

process, chemical composition, degree of crystallinity and its surface morphology(61). For example, smaller HA crystal sizes have been shown to be more soluble at the cost of reduced mechanical properties(73). HA, and generally all ceramics, are poor in terms of their mechanical properties and use for high load bearing applications while many of its crystallographic properties are similar to those of natural bone tissue (61). Hence, most clinical applications of HA are primarily as fillers, cements and coatings for orthopaedic implants.

HA and other functional bioactive coatings can be successfully deposited on the surface of prosthetic implants using thermal spray process (74). While the actual spraying parameters can impact the success of deposition, Kweh et al. (62) showed that the quality of HA coatings is also a function of the synthesized powder characteristics. These attributes are mainly the particle size, particle-size distribution and particle morphology, as they determine the flow characteristics and the subsequent melting behaviour of the HA particles in the plasma jet. In the same study, it was determined that spherical geometry and narrow size distribution can lead to better heat transfer and consistent melting profile which enhances the deposition of the coating powder and reduced porosity in the surface (62).

2.4 Synthetic HA and Ion-Substitution

The two main methods to synthesise HA are chemical synthesis (wet and dry) and biosynthesis, which is sourced from bacterial sources (75).

Dry chemical methods include solid-state reaction and mechanical alloying method.

In solid-state reaction, stoichiometric amounts of phosphate and carbonate salts are mixed and reacted following solid-state reaction principles, followed by calcification to obtain the crystal form chemical method(76).

Mechanical alloying is a repetitive cold welding, fracturing and re-welding of blended powders in a ball mill and is used for alloying elements which are difficult to combine by conventional melting methods. For mechanical alloying technique, reactants are mixed in water long milling times (up to 60h) have been employed in a dry environment without the need for heat treatment(76).

HA can also be produced by different wet chemical techniques such as precipitation, sol-gel, hydrothermal and hydrolysis reactions. This section reviews the wet chemical precipitation route, as it is simple, well understood, requires low processing temperature and can be readily adjusted to achieve novel formulations.

2.4.1 HA synthesis with chemical precipitation

Chemical precipitation is the most common method for the preparation of HA. Main precursors or reactants for the reactions have been a combination of a phosphate donor (such as orthophosphoric acid or diammonium hydrogen phosphate), and a calcium salt (calcium nitrate, calcium hydroxide, calcium hydrogen phosphate hydrate). Critical factors which determine the purity and quality of the HA product in wet precipitation techniques are the stoichiometry of the reaction and the quality of the raw materials used for the reaction (77).

The main underlying reaction during wet precipitation technique was proposed by Yogi and Aoki as is shown below(78) :

$$10Ca(OH)_2 + 6H_3PO_4 \longrightarrow Ca_{10}(PO_4)_6(OH)_2 + 18H_2O \qquad \text{Eq 2.1}$$

One of the main advantages of wet precipitation techniques is that the risk of contamination of the final product by the by-products is low because the main by-product is primarily water. As explained earlier, low processing costs and possible milder reaction conditions (temperature=90 °C and pH ≈10) make this technique more attractive. However, a slight change in the reaction conditions (e.g. reaction addition rate, temperature, pH) can have a major effect on the resulting products, which can be a disadvantage when compared to a more stable dry processing (62, 69, 79).

HA synthesis through wet precipitation method can be carried out in high and low temperature conditions. During the high temperature method, mixed calcium and phosphate reactants with accurate stoichiometry need to be heated at around 1000 ºC but it is difficult to control the crystal size and in particular the reaction produces HA nanocrystals (58). In contrast, low temperature alternative technique can take place at temperatures of lower than 100 ºC, while ageing of precipitates from super saturated solution of calcium and phosphate salts takes place. It is more convenient to control the size of the final crystals through low temperature technique, however, the final product mostly consists of other intermediate calcium phosphate phases unless the synthesis conditions and ageing time are carefully controlled(58).

Uskovovic et al. (58) have outlined the detailed pathway of HA synthesis by precipitation from supersaturated solutions of calcium and phosphate salts. These steps can be briefly summarised in the following steps:

(i) Nucleation of CaP clusters

(ii) Formation of amorphous clusters,

(iii) Formation of chain-like structures and their growth, and

(iv) Phase transformation through secondary precipitation.

As HA structure starts to form, free OH ions are incorporated into the HA crystals and pH of the solution decreases. Generally, an alkaline solution with high pH of 9.00-10.00 (e.g. ammonium hydroxide) is added drop wise in order to provide enough free OH^- ions for HA formation. Meanwhile, keeping the pH at alkaline levels ensures the balance of phosphate species to tip towards PO^{-3}_4 and minimises the possibility of protonated HPO^{2-}_4, $H_2PO^{-1}_4$ and H_3PO_4 species to form which would make precipitation of HA less favourable(58).

As the uptake of ions from the solution by the bulk solution decreases, the rate of pH drop also decreases. As the pH of the solution starts to stabilize, one may suggest that the solid phase is stable and the reaction is finished while the ions within the solid phase are still restructuring to form a more stable crystal structure.

2.4.2 Ion substitution into HA

The chemical composition and final structure of HA can be tailored by adjusting the chemical formulations and precursors of HA precipitation reaction. The possibility of incorporating foreign ions in the chemical structure of hydroxyapatite may explain why bones also function as a highly effective ion storage area.

HA in bone tissue is in the form of a calcium-deficient HA (CDHA), and incorporates a range of different ionic substitutions into its structure. Examples of these ions are K^+ (0.03-0.07

wt.%), Mg^{2+} (0.2-1.2 wt.%), Sr^{2+} (0.03-0.05 wt.%), Cl^{-} (0.1-0.4 wt.%) and F^{-} (0.01-0.07 wt.%) with further contributions from Zn, Fe, Cr, Co, Mn and Si ions in the ppm range (58, 68). The range of available ions, either incorporated into the crystal lattice or adsorbed on to the surface, represents the complex nature of the medium within which the hard tissue was mineralizing. It also denotes the flexibility of the apatite structure. The presence of these ions have been shown to act as a buffer in the bloodstream(80) or to influence the activity of osteoblast and osteoclast cells proliferation(81, 82).

In recent years, many biologically active ions have been incorporated into ceramic implant formulations to enhance the regeneration of tissue around the implant, promote osseointegration, degree of structural order (i.e. crystallinity) and dissolution rate (83) (8, 81) . This section will consider the use of three ions, Ag, Zn and Mg substitution, as they are the ones who were studied in this project and are also the most prominent ones in the literature. The mechanisms of their incorporation into HA is reviewed and the resulting changes to the bulk material and *in vitro* and *in vivo* responses are provided.

2.4.3 Methods of ion substitution in HA

Ions, and in particular Ag, can be incorporated in the HA structure with either of the following methods:

(i) Wet precipitation method, where all precursors are solubilized in water and precipitate at the same time (84)

(ii) Ion exchange between the previously prepared pure HA and a metal salt solution by submerging HA in the salt solution(85),

(iii) Sol-gel method(86), by which a colloidal solution is formed from monomers and will act as the precursor for an integrated network of ions and ceramic crystals

(iv) Ultrasonic spray pyrolysis (87), which is an aerosol synthetic method with deposition of metals on nanoparticles

(v) The microwave method (88)

Regardless of the technique used, the resulting material may be then subjected to heat treatment by sintering or drying which can affect the final structure or the crystal size(89).

2.4.4 Mechanism of antibacterial/antimicrobial activity of metal ions

Figure 2.2 illustrates a possible mechanism of antibacterial activity of ions, where the exact method of interactions is not fully determined. There are three mechanisms, which are thought to explain how ions can prohibit the growth of microorganisms (90-93):

(i) Penetration of ions through the cell membrane and change the regulation of ATP production and DNA replication,

(ii) Ion attachment to the cell membranes with electrostatic forces, which disrupts the integrity of the cell and also affects the free transportation of protons and other molecules in and out of cell, and

(iii) Induction of an oxygen stress by formation of free radicals (also called reactive oxygen species: ROS) which interfere in the normal function and can irreversibly damage bacteria (e.g. their membranes, DNA and mitochondria), resulting in bacterial death(94).

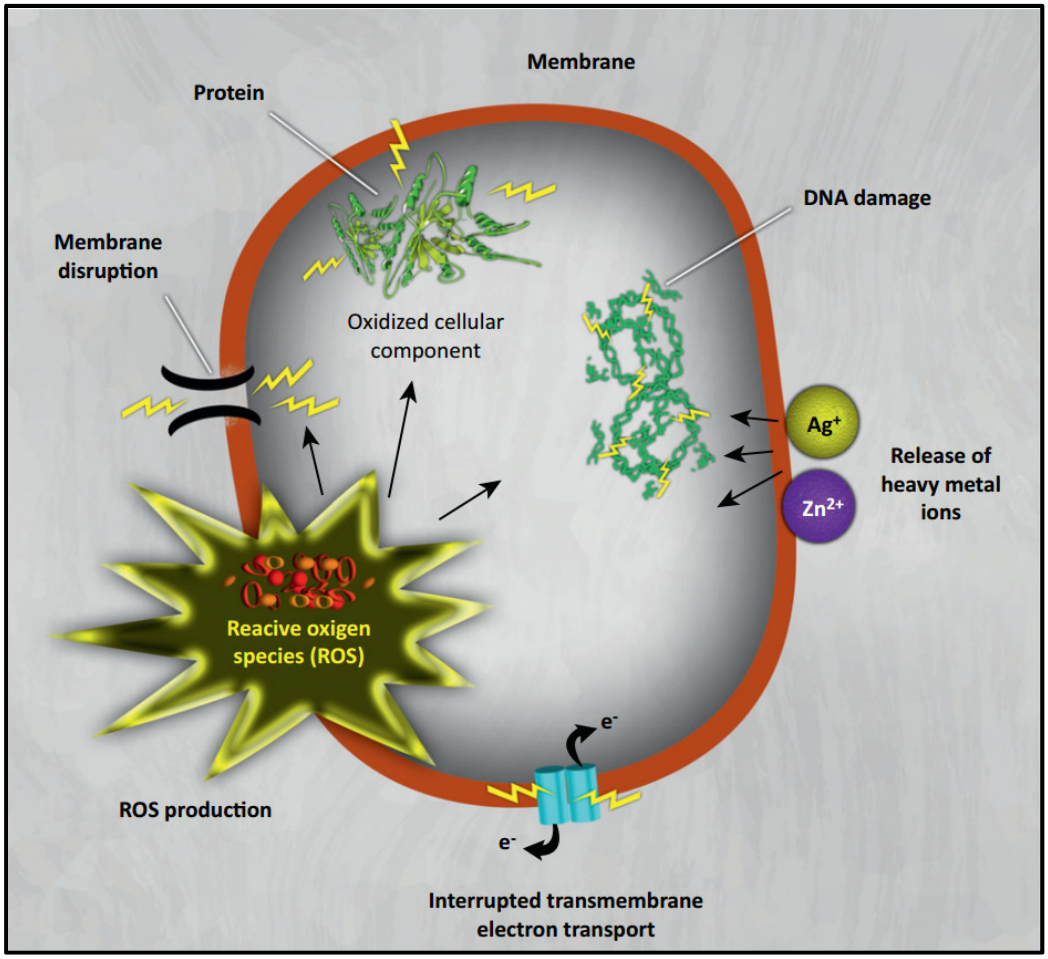

Figure 2. 2: Antibacterial mechanisms of nanoparticles and their ions, adopted from(94)

Further studies have also reviewed other possible interactions of metal ions with bacterial cells to explain their antibacterial activity. Kandile et al. (95) proposed that heavy metals can react with proteins via thiol (SH) groups leading to inactivation of proteins, but as explained earlier, the general concept is that silver nanoparticles follow mainly the mechanisms discussed above.

Ag substituted HA (Ag-HA)

The inhibitory and antimicrobial properties of silver against gram-positive and gram-negative bacteria, viruses, and fungi have long been known(96-98) Silver is effective at even very low concentrations (35 ppb) without having any negative cytotoxic effect on mammalian cells (99, 100). Another advantage of silver, and other metal ions in general, is that microorganisms have a relatively poor ability to develop immunity to silver. Silver as an infection control agent has been used in catheters and coatings of implants and dental materials (92, 101). Due to its large spectrum of antimicrobial activity and high efficiency, silver-doped HA has been one of the most studied ion substituted HA materials(102, 103).

Silver can interact with cells and show its antimicrobial activity through two mechanisms: (i) Direct interaction of silver ions on the surface of HA with the cell wall of microorganisms. (ii) Release of silver ions to the medium from the internal structure of HA surrounding the microorganism and then exerting its antibacterial activity(84).

Although silver has an established antimicrobial effect, it is toxic if its concentration in coatings is very high. It is necessary to establish the threshold of silver percentage in HA in order to optimize the antibacterial effects while avoiding cytotoxicity. However, there is discrepancy for optimum concentration due to the different substitution methods and biological test methodologies.

In a study of *in vitro* bacterial adhesion to Ag-HA prepared by Sol-gel process, a significantly reduced number of *Staphylococcus epidermidis* (*S.epidermidis*) and *Staphylococcus aureus* (*S.aureus*) on both 1 wt.% and 1.5 wt.% Ag-HA surfaces were observed and compared to the

surface of HA without Ag (19). In addition, significantly reduced adhesion of viable *S. aureus* was observed on 1 wt.% Ag-HA coating surface when compared to 1.5 wt.% Ag-HA surface after 3 hours of bacteria culture(19).

As far as cytotoxicity is concerned, no significant change in cell proliferation (by measuring double stranded DNA amount) was observed for 1 and 1.5 wt.% Ag-HA and HA without Ag (19). No difference of Alkaline phosphatase (ALP) specific activity between HA and 1 wt.% Ag-HA were observed over time, while a significantly less ALP specific activity was observed on 1.5 wt.% Ag-HA surface after 12 and 15 day culture (19). It was concluded that 1 wt.% Ag-HA has similar biological activity as HA, with respect to bone cell proliferation and differentiation, and Ag-HA can minimize the initial bacterial adhesion on its surface (19).

Ag-HA coating processed by co-sputtering has also been studied for its anti-bacterial and biological properties(19). *In vitro* bacterial adhesion study indicated a significantly reduced number of *S.epidermidis* and *S. aureus* on 2.05 ± 0.55 wt.% Ag-HA coating surface when compared to blank Ti and HA surface after 3 hours of bacteria culture (104). No significant cytotoxicity was reported for these coatings after incubation with human embryonic palatal mesenchymal cells for 24 hours (104).

Feng and co-workers used an ion exchange technique to prepare Ag-HA coatings and measured the antibacterial effect. HA coating was prepared by ion-beam-assisted deposition (IBAD) and was immersed in a 20 ppm $AgNO_3$ solution to carry out ion exchange reaction between Ag^+ and Ca^+ in HA (85). In this study, the treated samples showed antimicrobial activity versus *Escherichia coli*(*E.coli*)*, Pseudomonas aeruginosa*, *S. aureus,* and *S. epidermidis* compared to untreated samples. The minimum inhibitory concentration of $AgNO_3$ was determined to be

1.302 μg/ml (ppm). The amount of silver ions released in simulated body fluid (SBF) solution was shown to be the function of time, indicating an initial fast release of ions while reached a constant levels after 24 h (85) .

In another study by Feng and co-workers, they used the same material to evaluate the cytotoxicity of Ag coatings using murine macrophage, cell lines (RAW264.7) and human osteosarcoma osteoblast-like cells, (MG63)(105) . The results indicated that the number of macrophages in the coating treated with up to 20 ppm $AgNO_3$ solution did not change significantly when compared to Ag free coating, indicating Ag-HA coating with limited silver ions could effectively inhibit the bacterial growth without significant cytotoxicity (105).

Karlov and co-workers used silver concentration of up to 15 wt.% of Ag ions in coatings, which showed both antibacterial and cytotoxicity activity, while concentration of 5 wt.% had no inhibitory effect on bacterial growth. The optimum concentration of 7 wt.% was suggested as exhibiting a balanced ratio of antibacterial effect and minimum cytotoxicity(106). Oh et al. (87) also showed that a HA coating with 15 mol.% of Ag exhibited mild cytoxicity but this was also affected the shape of particles and the choice of synthesis route.

The release profile of silver ion is very critical for its biological activity as a sustained concentration of ions available in the environment depends upon it. Shirkhanzadeh et al. (107) studied the release of Ag ions from Ag-micro porous HA coating into SBF solution. It was reported, that 50% of Ag was released within the first 24 hours. The silver ions release was gradually decreased until the end of the experiment at day 7. Chen et al. (108) also prepared

Ag-doped HA powders of up to 5 %wt. and observed similar release profile while the maximum concentration of Ag in the medium was only 2.27 ppm after 14 days.

Ag-HA has also been used for bone cement applications, in addition to implant coatings. It has been shown, that HA cements with 1% metallico silver nanoparticles in the range of of 5- 50 nm in diameter, can have effective antibacterial activity against *S.epidermidis*, methicillin-resistant *S.epidermidis* (MRSE), and methicillin-resistant *S.aureus* (MRSA), where no significant cytotoxicity on fibroblasts and osteoblasts was observed with the use of the above ion concentrations(109).The microbiological effect of silver when incorporated in amorphous calcium phosphate has also been reviewed and antibacterial activity was observed at concentrations of 3 to 6 wt. % of Ag against *E. Coli, S.aureus, P. aeroginosa, C. diphteroides* and *C. albicans* (110).

Mg substituted HA (Mg-HA)

Magnesium (Mg) plays a key role in bone growth and metabolism by modulating osteoblast and osteoclast activity in biological apatite. Its level increases as calcification progresses and decreases as calcifications takes places (68).

Mg is one of the essential metals in biological apatite with concentrations of 0.44, 1.23, and 0.72 wt.% in enamel, dentin and bone, respectively (111). Although research on the role of Mg on bone health is still on going, most studies report a positive effect on all stages of skeletal metabolism and bone health, particularly in the process of osteoporosis(112),(28). Belluci et al. (113) demonstrated that Mg deficiency has a negative effect on bone metabolism and new bone

tissue formation around implant sites.

Mg-HA have been used in numerous orthopaedic and dental prosthetic examples (114). Zhao et al.**(115)** reported that Mg substituted HA surfaces promoted osteogenic differentiation of pre-osteoblasts and might improve implant osseointegration during the early stages of implantation**.** Bonfield and Gibson prepared bone mimetic HA ceramics with the co-incorporation of Mg^{2+} and CO_3^{2-} in a content of up to 0.5 and 1 wt.%, respectively by using a precipitation method. They expected, that the resulted materials would exhibit better bioactivity over pure HA, which was applied in the commercial application, such as bone implant fabrication(116). Mg concentration of up to 25.4 wt.% was used in odontostomatologic applications (117).

Mg has a smaller ionic radius (0.065nm) to calcium (0.099nm) which could allow it to substitutes either of Ca I and II positions (see section 2.3.1 HA chemistry); there is a preference for the Ca (II) position which is possibly due to the greater flexibility of the ions geometry at the this position(68). Solid state Nuclear Magnetic Resonance (NMR) studies have also confirmed that Mg ion can be substituted for Ca (II) position by up to 10% molar ratio of Mg (118).

Mg can also inhibit the nucleation and growth of HA crystals resulting in the reduction of HA crystallinity(119), while stabilizes the more acidic calcium phosphate intermediate phases during synthesis(120) .

Chiranjeevirao et al.(121) reported that Mg-HA solid solutions in the whole range of compositions were prepared by using calcium nitrate, magnesium nitrate, and ammonium dehydrate phosphate in an aqueous medium at pH=9.0. Similar work was carried out by Patel et al.(122) who prepared similar Mg-HA solid solutions using same reactants, but was

synthesized at more alkaline pH values, which was above 11. However, other researchers could not reproduce the results presented in that study (13, 123). Bigi et al.(13) showed that Mg exhibited similar effect as Zn ions inhibiting the crystallization of HA. It was reported that the unique crystalline apatite phase was only achieved with Mg concentrations in the range of 0 to 30 atom % (13). At Mg concentrations of 35 to 50 atom %, the structure became fully amorphous and other phases such as $Mg_3(PO_4)_2 \cdot 8H_2O$, and $NH_4MgPO_4 \cdot H_2O$ started to form. The same research group also reported, that the crystal size, degree of crystallinity, and the (Ca+Mg)/P ratio was decreased with increasing Mg concentration(13).

The opposite effects of Mg substitution for Ca on the crystal size and degree of crystallinity of apatite was reported by Yasukawa et al. (124) who prepared Mg-HA solid solutions with a Mg/(Mg + Ca) molar ratio ranging from 0 to 0.5 by a wet precipitation method, using $Mg(NO_3)_2 \cdot 6H_2O$, $Ca(OH)_2$, and H_3PO_4 as reagent. The crystal size of the apatite phase was increased and a more porous structure was formed with increasing Mg/(Mg + Ca) ratio from 0 to 0. 31 (124). When the ratio reached 0.38, an amorphous structure was formed. Fadeev et al. (33) followed a similar wet precipitation method using $Ca(NO_3)_2$, $Mg(NO_3)_2$, and $(NH_4)_2HPO_4$ (33) and reported that Mg had a destabilizing effect on the apatite structure.

Other studies showed that a maximum Mg concentration of 5.7%wt was substituted in the apatite crystal lattice for calcium with excess of Mg to be in the form of an additional amorphous phase (68) or adsorbed on the HA surface (119).

The effects of free magnesium ions on early bone formation have been exploited through the production of Mg-HA as bone defect fillers. Mg ions helped to increase osteoconductivity in a rabbit femoral defect filled with Mg-HA granules (125). While there are no specific studies

which isolate the role of Mg ions in adjusting material dissolution properties, there is evidence that Mg ions association with calcium phosphates may influence the surface structure in a way that implies increased solubility (126).

Zn substituted HA (Zn-HA)

Zinc (Zn) is the most abundant trace metal in bone mineral (ranging from 0.0126 to 0.0217 wt.%) and plays a key role in various body functions such as regulating nucleic acid metabolism, maintenance of membrane structure, hormonal activity and is an enzyme cofactor in more than 300 enzymes involved in bone metabolismjonna (68, 83, 89, 127). Zn also stimulates bone formation and mineralisation by inhibiting osteoclast differentiation and enhancing osteoblast activity (128), while it has been also shown that it can stimulate bone resorption at higher concentrations (129).

Ion substitution via wet precipitation has been a common technique for the preparation of Zn-substituted HA (Zn-HA) with varying ratios of Zn substitutions (126, 130-132). Zinc is well known for its inhibitory effect on HA crystal growth, but it has been shown that it can be quantitatively substituted in the HA lattice at concentrations of up to 20 atom. %. (133) .The smaller ionic radius of Zn (0.075nm compared to 0.099nm Ca) can result in a reduction in the lattice parameters of the apatite crystal (131). Tripathy et al. (134) reported that they could produce Zn-HA with a chemical formula of $Zn_{10}(PO_4)_6(OH)_2$ using a co-precipitation method in aqueous media. However, other studies suggested that because of the inhibitory effect of Zn on the crystallization of HA, the synthesis of Zn-HA over the entire compositional range was impossible (127, 132, 135).

Bigi et al. (127) performed a synthetic reaction using different concentrations of Zn in solution

(ranging from 0 to 100 atom%); however, the unique crystalline phase was only obtained with Zn concentrations of only up to approximately 25 atom%. With increasing Zn concentration above 25 atom% the XRD analysis showed the presence of an amorphous structure and the evaluation was hindered because of the peak broadening effect (127).

Li et al. (135) reported the synthesis of 20 mol% of Zn-HA by using $Ca(NO_3)_2$, $(NH_4)_3HPO_4$, and $Zn(NO_3)_2$ via a hydrothermal method and showed that the degree of crystallinity and crystal size of Zn-HA samples decreased with increasing Zn concentrations while the numbers of the Zn-HA crystals formed were increased (135).

In another study by Miyaji et al. (132) the limits of Zn substitution in the apatite structure was estimated to be 15 mol%.They used alternative reagents ($Ca(CH_3COO)_2 \cdot H_2O$, $Zn(CH_3COO)_2 \cdot 2H_2O$, and $(NH_4)_2HPO_4$) to avoid the incorporation of NO_3^{-2} or Cl^- into the apatite structure. The maximum concentration of 15% mol was reported which was a slightly lower value compared with the one reported by Li et al, who suggested that the small difference on the substituting limit value was attributed to the consequence of using a different synthesis method (135). These authors indicated that the Zn-HA samples were more difficult to prepare by using a precipitation method rather than using a hydrothermal method (135).

Chemical analysis confirmed that both Ca/P and (Ca+Zn)/P ratios decreased as Zn content increased resulting in a change in the stoichiometry of HA, loss of crystallinity and formation of irregular shapes of Zn apatite structures (133). Within the substituting limits, Miyaji et al. (132) found that the crystal size and degree of crystallinity was decreased with increasing Zn substitution. This was in good agreement with results reported Li et al. (135) . Furthermore, Miyaji et al. (132) suggested, that the order of the produced phases with increasing Zn

substitution was Zn substituted apatite, amorphous phase, and amorphous phase + parascholzite ($CaZn_2(PO_4)_2 \cdot 2H_2O$). Zn inhibits the crystal growth of apatite by being adsorbed onto the active growth sites which is why the (Ca+Zn)/P ratio and stoichiometry cannot be maintained (68, 119, 132).

Whether there is an actual substitution within the HA lattice, however, is not fully clear. There is much debate over the mechanism of Zn incorporation into HA. Some theoretical studies reported that ion substitution is not energetically favoured and that Zn occupation at Ca vacancies (particularly at the Ca (II) site) is probable with significant local structural distortion. Contrarily, Tang et al. (136) reported that Zn ions may favour the substitution at Ca (II) position, but also highlighted that Zn ions could be entrapped and act as a defect site given the fast crystallisation kinetics of precipitation.

Measuring ion adsorption values have shown high amounts of Zn ions being associated with HA particles, which is higher than what is expected to be normally substituted. Wang et al. (137) reported that Zn ions have a high affinity to adsorb on HA crystals at concentrations above 1wt%. They presented a Langmuir type adsorption isotherm for Zn and Mg ions on the active growth sites on the HA crystals. Two possible explanations are the formation of zinc-phosphate complexes at the surface and the ability of the surface bound Zn species to undergo hydrolysis and potentially block multiple active growth sites (119).

The mechanism of the antibacterial activity of HA with zinc ions is again not yet fully understood. It is proposed that Zn ions form strong bonds with thiolic, imidazole, amine, and carboxylic groups of proteins, causing structural changes and also affects the membrane permeability and transport resulting in cell death (138, 139) . It is also shown that Zn ions can

damage the enzymatic activity and DNA and RNA of bacteria with similar results (140).

In addition to its role as an antimicrobial agent, Zn-HA ceramics are used to regulate other biological functions. Kawamura et al. (141) used composite ceramics of Zn-TCP/HA as implants in the femor of New Zealand White rabbits for 4 weeks and reported increasing rates of bone formation at concentrations of 0.316 wt.%.

Grandjean-Laquerriere et al. (142) reported, that the addition of Zn-HA decreased the inflammatory reaction following the implantation of HA based prosthesis by increasing the production of cytokines. Li et al. (135) suggested that Zn substituted HA could consist of a new generation of biomaterials for bone tissue engineering.

2.5 Bone: A Solid Structure and Living Tissue

2.5.1 The chemical Composition of the Human Bone Mineral

Natural bone consists of organic and inorganic chemicals. The majority of the organic structure is formed of Collagen (90-95%) and calcium and phosphate form the most part of inorganic chemicals (143).

The inorganic phase of bone is primarily made of apatite crystal structure of which resembles and the mineral phase consists of a continuous cellular backbone.

HA is the main mineral available in bone, dentin and teeth (143). Bone is made of 25 wt.% water, 43 wt.% mineral, 29 wt.% collagen and 3 wt.% of non-collagenous organic molecules (144). The inorganic part of bone is also made of calcium, phosphate and hydroxyl ions in the ratio of the chemical formula, $Ca_{10}(PO_4)6(OH)_2$. It is important to note that natural bone apatite

is slightly different from the stoichiometric HA in terms of stoichiometry, crystal dimensions and a relative crystallinity of 33-37% with the degree of crystallinity of the stoichiomettric HA is assumed to be 100% (68, 133, 145).

The organic part of the bone is made of type I collagen which is a fibrillar protein composed of three protein chains, bound together in a triple helix by secondary hydrogen bonds..

2.5.2 Hierarchical Structure

The natural human bone is a complex network of living cells within a hard and dense connective structures with different arrangements and scales. Bone is a living tissue and with its microstructure is continuously evolving. The main role of the bone is to form the main supportive structure of the body as the skeleton, protect the organs, generate healing cells and carry out the homeostasis mineral ions (146).

Knowing the physical, chemical, and mechanical characteristics of human bone is vital in making of similar structures for medical applications.

To understand the bone architecture, it is critical to consider the involved scales and understand the structural relationship between them. The following section provides a detailed overview of bone structure and discusses how it can define the final structure of bone.

Figure 2.3 shows different classes of entities in bone in terms of their scale. These levels can be indicated as the continuum level (macro-structure), tissue level (meso-structure), cellular level and molecular level (microstructure)(147).

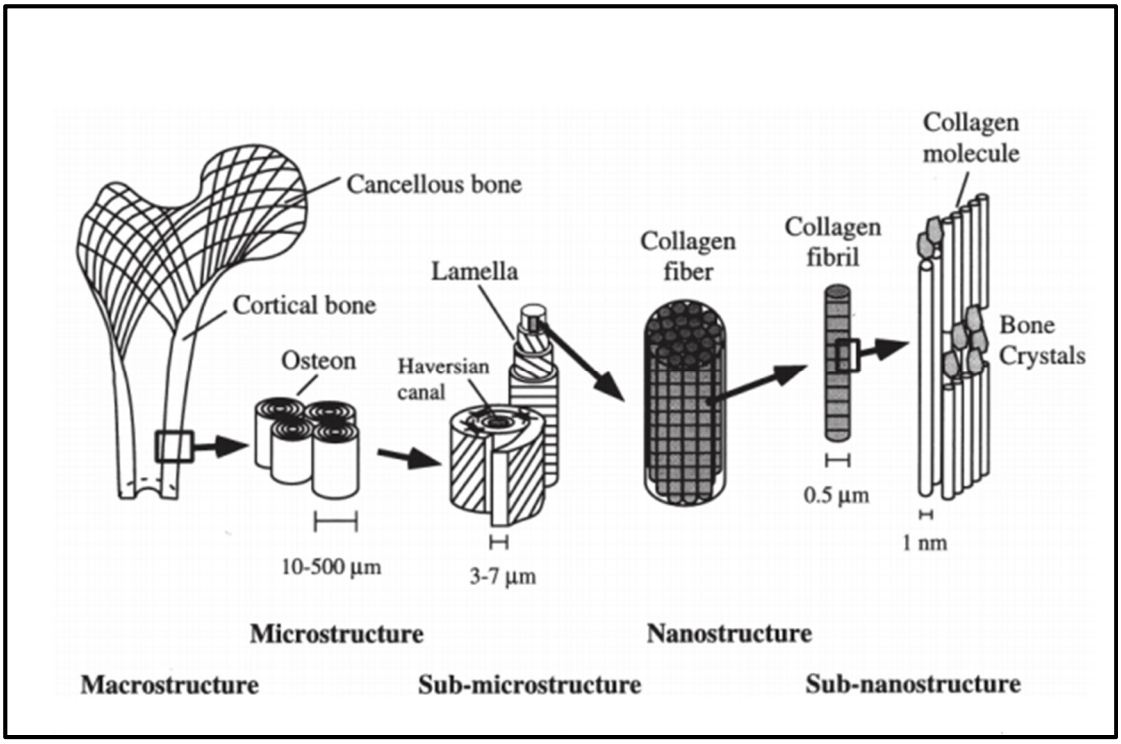

Figure 2. 3: Hierarchical structural organization of bone (a) cortical and trabecular bone (a) Cortical and trabecular bone; (b) Osteons with Haversian systems; (c) Lamellae; (d) collagen fiber assemblies of collagen fibrils; (e) bone mineral crystals, collagen molecules, and non-collagenous proteins(148)

A more detailed structure of bone can be seen as a well-defined hierarchically organized matrix, consisting of further entities at different scales which also define the structural-function in bone (149) The most detailed structural classification of bone was provided by Weiner and Wagner, who concluded that there are seven structural levels of hierarchy in the adult human bone (150) as illustrated in Figure 2.4.

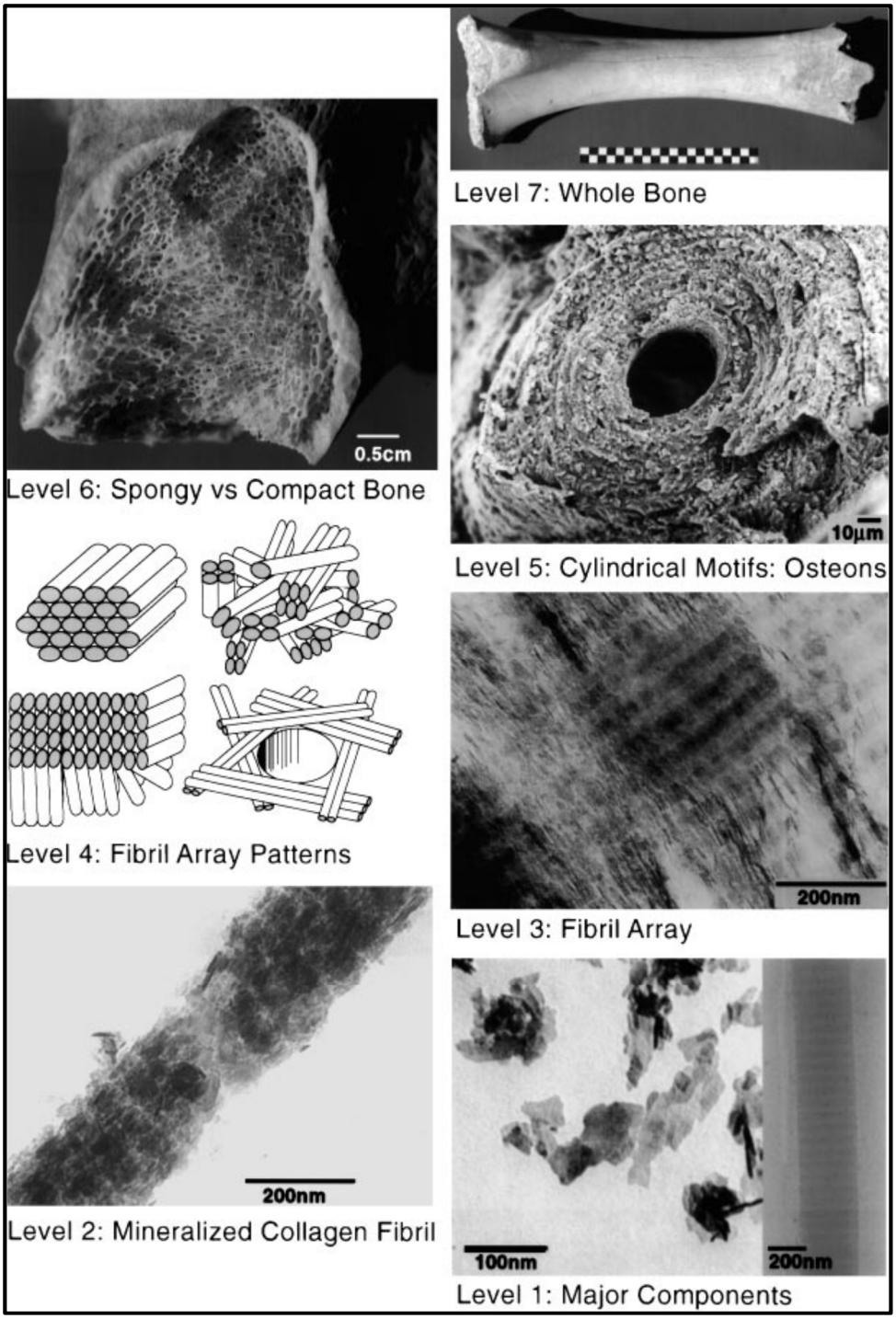

Figure 2. 4: The 7 hierarchical levels of the bone (150).

Macrostructure

The macrostructure or continuum level of the bone defines its overall shape i.e. the shape and

form of mature and grown bone (e.g. femur) and can measure between 3-750 mm.

Mature bones are made of either cortical (compact) bone on the outer surface of most bones and cancellous (spongy or trabecular) bone found near the ends of long bones and at the centre of flat bones (e.g. ribs) (148). These two types of bones are very similar in terms of compositions but each has different degree of porosity and ratio of organic to inorganic compounds.

Cortical bone is denser than trabecular bone, is formed from cylindrical lamellae and has a porosity of between 5 and 10%. Cancellous or trabecular bone are more porous (can have a porosity of up to 95%) and is made of trabecular struts with non-mineralized spaces filled within cancellous bone contain bone marrow (151). Cortical bone is denser than forms the outer shell around the trabecular bone in joints and in vertebrae and can account for about 80% if the total skeletal mass, while trabecular bone can form around 70% of the skeletal volume (144).

Microstructure and Sub-microstructure

At this scale (5 to 500 μm), the main components are osteons, Harvesian canals and lamellae. Osteons are large hollow fibers of lamellae and as Figure 2.5 shows, that are made of Harvesian canals (or secondary osteons) and contains blood cells (149). Harvesian canals are 100-200 μm in diameter and are surrounded by cement lines, which bind them to the bone matrix.

The sub-microstructure of bone consists of lamellae, which are fibrils consisting of calcium phosphate and collagen cells and are 3-7 μm thick.

Two main types of bone microstructure can be found at this level:

a) Woven bone, which is usually a transient tissue type and is composed of poorly organized mineralized collagen fibril bundles without a set pattern and can be used as a scaffold for further bone structure development or fracture healing (149)

b) Lamellar bone (Figure 2.5), which is a highly organized bone tissue and is composed of a series of lamellae (each lamella is in the range of 3 to 7 μm as discussed above). The lamellae are bands or bundles of mineral crystals and collagen fibers. The spaces between these arrays are filled with disordered materials (152).

As bone grows, the woven bone is replaced by lamellar bone or become highly mineralized having improved pattern and organization (144) .

Nanostructure and Sub-nanostructure

Collagen fibres are the most dominant structure at this scale (100 nm-1 μm) and with apatite can make up to 95% of the dry weight of bone. Collagen is the most abundant protein in the body and it accounts for 70-90% of non-mineralised component of bone (153). Type-1 collagen is the most abundant protein in mature bone. Collagen is responsible for the flexibility and tensile strength of bone.

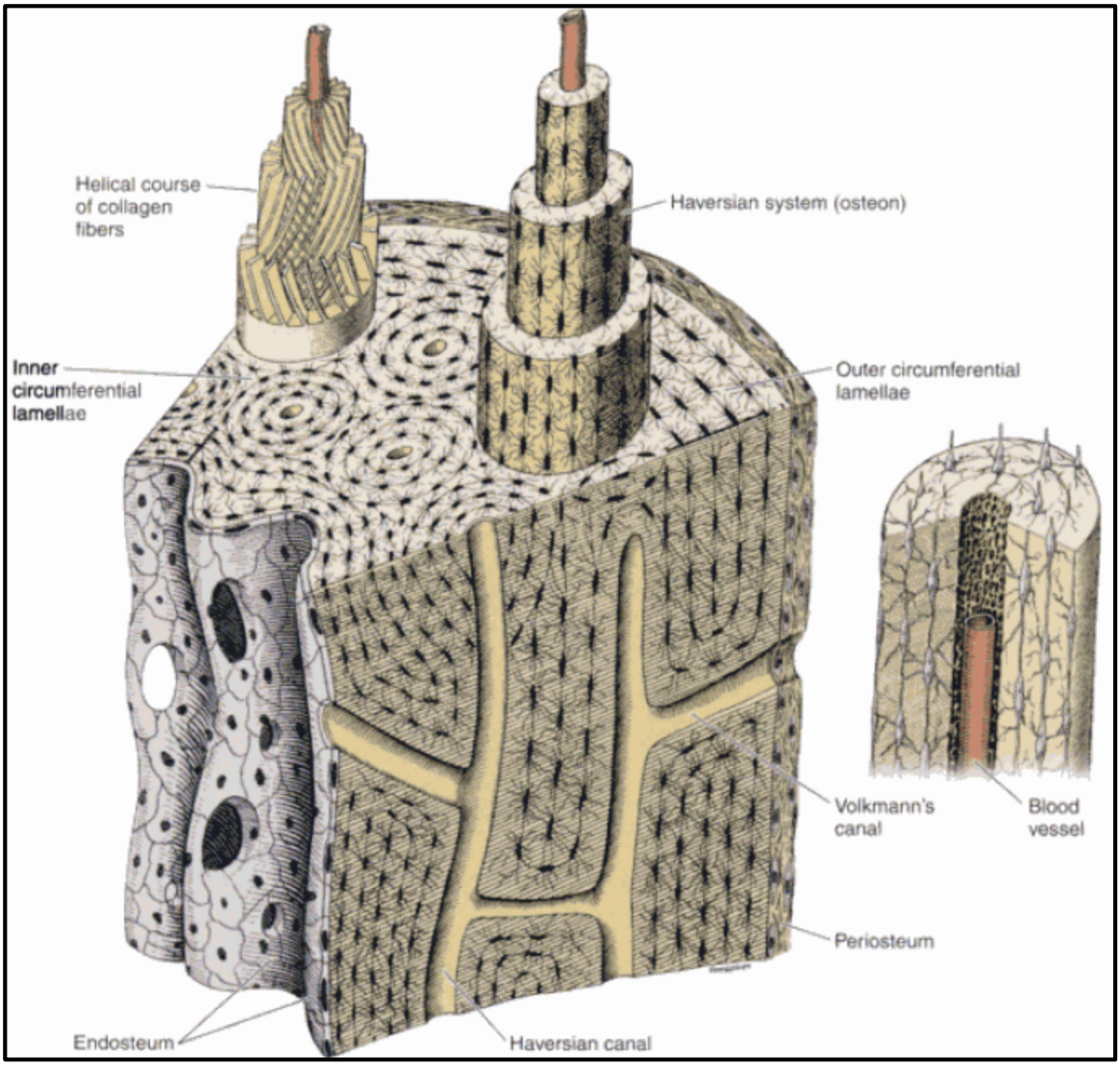

Figure 2. 5: Lamellar bone (154).

Other than collagen proteins are non-collagenous (NCP) and proteoglycans such as osteocalcin, alkaline phosphatase osteopontin and bone sialoproteins that are responsible for regulating bone mineralisation and bone formation (149).

At the smallest scale, bone minerals are present at molecular levels which are mainly comprised of apatite crystals. The mineral phase is in the form of thin plate like structure which are between 1.5-4 nm thick (155).

2.5.3 Bone Physiology

The bone cellular structure is composed of three functionally distinct cell types; osteocytes, osteoblasts, and osteoclasts. The overall function of these cells is to determines how the bone is remodelled.

Osteoclasts

Osteoclasts are giant multi-nucleated cells, typically 20 to 100 μm in size that are responsible for resorbing old bone by secreting acids and enzymes (156). Osteoclasts are active during bone remodeling and are generally more related to macrophages rather than osteocytes or osteoblasts (156).

Osteocytes

Osteocytes are small inactive cells, that form about 90% of all cells in human skeleton. These cells are derived from osteoblasts and regulate the extracellular concentration of calcium and phosphate ions through the release of calcitonin and parathyroid hormones. Osteocytes interact with osteoblasts and other osteocytes via canals within the bone matrix called canaliculi (157).

Osteoblasts

Osteoblasts (bone-forming cells) are small mononuclear cuboidal cells, which are derived from bone marrow mesenchymal stem cells and play a key role in bone matrix synthesis(157). Osteoblasts release alkaline phosphatase during their activity that catalyses the hydrolysis of pyrophosphates and polyphosphate ions releasing inorganic phosphates (158, 159). Calcium salts precipitate from the body fluids and bond with osteoids resulting in the formation of new bone tissue.

CHAPTER *3*

MATERIALS AND METHODS

3 Materials and Methods

This chapter outlines the detailed experimental procedures employed for:

- The preparation of cation-substituted hydroxyapatite (Ag, Zn, and Mg/ HAp)
- The analytical techniques that were used to characterise and study the chemical and physical properties of substituted apatites.
- In order to understand and model the biological activity and cellular response to the ion substituted HA samples and their impact on cell viability, cell proliferation and cell differentiation, animal cell lines were developed and analysed with all the synthesised samples. The results from these assays enabled us to establish the behaviour of hydroxyapatite and the addition of selected ions and predict their *in vivo* responses.
- To investigate the bactericidal effect, two types of tests (spread plate method and agar diffusion test) were developed using two pathogens associated with implant infection and failure.

The following techniques were used for the chemical and structural analysis:

1) X-ray diffraction (XRD) was employed to ascertain phase purity, degree of crystallinity, crystal size and lattice parameters of apatite and substituted apatites.

2) Fourier transform infrared spectroscopy (FT-IR,) Raman Spectroscopy and X-ray fluorescence (XRF) techniques were used to identify the chemical composition of the materials.

3) Thermogravimetric analysis (TGA) was employed to understand the thermal decomposition profile of the prepared samples and explain the behaviour of ceramics at sintering temperatures and subsequent chemical conversion (decomposition).

4) Inductively-Coupled Plasma-Mass Spectrometry (ICP-MS) was used to measure the concentration of soluble ions in the liquid phase.

3.1 Synthesis of ion substituted hydroxyapatite (wet precipitation technique)

Reagents

The reagents used for substituted HA synthesis were Diammonium hydrogen phosphate $(NH_4)_2HPO_4$ and Calcium Nitrate Tetrahydrate $Ca(NO_3)_2.4H_2O$ plus either of Silver nitrate $Ag(NO_3)_2$ for Ag-HA, Zinc nitrate $ZnNO_3$ for Zn/HA and Magnesium nitrate $Mg(NO_3)_2.H_2O$ for Mg/HA). These chemicals were introduced to the reaction in form of two separate solutions (A and B). Solution A was prepared by dissolving a calculated amount of $Ca(NO_3)_2 \cdot 4H_2O$ (for Ca-HA) and $Ag(NO_3)_2$ (for Ca-Ag-HA) in 200 ml deionised water (deionised water was used for all the experiments to minimise any side reaction of other interfering ions with the reactants). The amount of reactants was calculated by adjusting the concentration of $Ca(NO_3)_2 \cdot 4H_2O$ in order to keep the (Ca + x)/P ratio (x= substituted cation) constant at 1.8. The $(Ca^{+2} + x)/P$ ratio of 1.8 for this study used by the method developed by Bigi et al (83). The amount (weight) of the added cation (x) to the total cation ($x / Ca^{+2} + x$) was variable and was set to obtain a 1, 5, and 10 wt.%. Tables 3.1, 3.2, and 2.3 show the weights of each reagents for a 200 ml solution A.

Solution B was prepared by dissolving $(NH_4)_2HPO_4$ in 200 ml of deionised water and was identical for all of the samples.

Pure HA was prepared and used in all the experiments as the control sample.

All chemicals and reagents were supplied by Sigma-Aldrich and had the following grades:

- $AgNO_3$: (BioXtra, ≥ 99%)
- $MgNO_3$: (BioXtra, ≥ 98%)
- $ZnNO_3$: (crystallized, ≥ 99%)
- $Ca(NO_3)_2 \cdot 4H_2O$: (≥ 99.0%)
- $(NH_4)_2.HPO_4$: (ACS reagent ≥98%)
- NH_4OH: (ACS reagent, 28.0-30% NH_3 basis)

Deionised water was generated in a lab based deionisation water PURELAB Chorus 2 generation system.

Table 3. 1: Weights of reactants in chemical precipitation method to make Ag substituted HA (based on 200 ml of 1M solution of Ca+Ag ions) (unit)

Ag (%)	$Ca(NO_3)_2 \cdot 4H_2O$	$Ag(NO_3)_2$	$(NH4)_2HPO_4$
0	47.20	0	14.66
1	46.73	0.34	14.66
5	44.84	1.70	14.66
10	42.48	3.40	14.66

Table 3. 2: Weights of reactants in chemical precipitation method to make Mg substituted HA (based on 200 ml of 1M solution of Ca+Mg ions)

Mg (%)	$Ca(NO_3)_2 \cdot 4H_2O$	$Mg(NO_3)_2$	$(NH4)_2HPO_4$
0	47.20	0	14.66
1	46.73	0.512	14.66
5	44.84	2.56	14.66
10	42.48	5.12	14.66

Table 3. 3: Weights of reactants in chemical precipitation method to make Zn substituted HA (based on 200 ml of 1M solution of Ca+Zn ions)

Zn (%)	$Ca(NO_3)_2 \cdot 4H_2O$	$Zn(NO_3)_2$	$(NH4)_2HPO_4$
0	47.20	0	14.66
1	46.73	0.59	14.66
5	44.84	2.97	14.66
10	42.48	5.95	14.66

Apatite synthesis reaction

HA samples were prepared by using an adopted chemical precipitation method developed by Bigi et al. (83). 400 ml of solution A was transferred into a three-neck flask (Figure 4.1) and was heated and maintained at 90°C. 400 ml of solution B was heated in a separate container and was carefully poured into solution A from the top of the condenser. The pH values of the solution A and B were maintained at 11 by gradual addition of NH_4OH solution with a 5 ml pipette. The mixed Solution A and Solution B was kept agitated and heated to 90°C using a hot plate/magnetic stirrer for 5 hours. The temperature of the mixture was measured with a thermometer fixed on the neck of the flask. Heating was stopped at the end of the reaction and the suspension was allowed to cool. In order to obtain the precipitate, the solution was

centrifuged for 13 minutes at 10000 rpm at room temperature with a Beckman Coulter model J6-MI Centrifuge. The supernatant was collected and its pH checked. The HA precipitate was re-suspended with deionised water up to 5 times until the pH of the supernatant reached 7.0. Finally, the washed precipitate was dried overnight in an oven at 37°C. For any subsequent material characterisation, the dried HA precipitate was grounded into a uniform fine powder using a pestle and mortar.

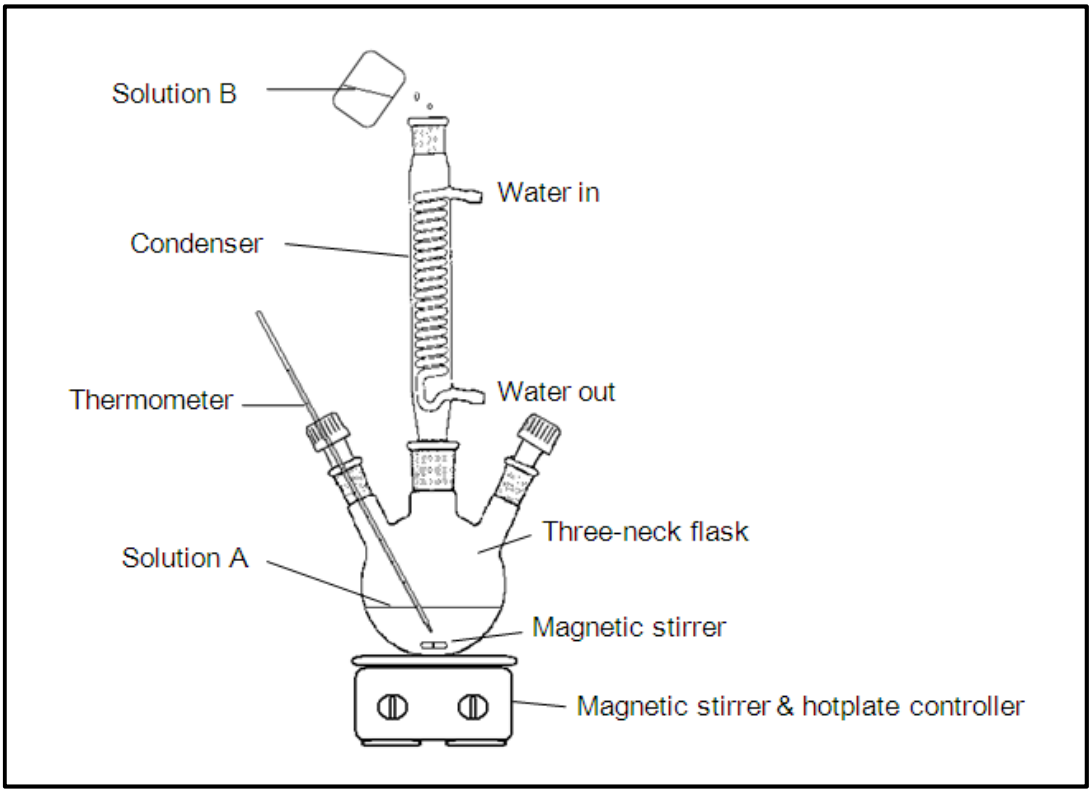

Figure 3. 1: Schematic diagram of the experimental setup for HA preparation taken with permission from Jiangling et al. (76)

Preparation of HA discs and sintering

For the microbiological and cell biological assays, HA samples were prepared in discs. For doing so 0.5 g of the sample powder was pressed at 155 Nm^{-2} force using a mechanically operated press machine (Instron 5582) and metallic dyes specially designed for making dense discs of 13mm diameter and 2mm thickness (Specac Ltd., Kent, UK).

All the discs were sintered in a furnace at 1100°C. The temperature of the furnace was set to increase at a rate of 5°C/min up to the set plateau temperature (1100°C) and it was remained at this temperature for 2 hours after which it was reduced to 26°C at the rate of 10°C/min (Figure 3.2). The calcination time was limited to 2 hours to prevent further decomposition of HA to TCP. These sintered powders (not disc) were used for all subsequent material characterisation assays.

Figure 3. 2: Discs of Hydroxyapatite

To obtain a smooth surface for biological assays, sample disks were polished with a fine sand paper and washed in an ultrasonic bath in water before being sterilised. The sintered discs were placed in sealed autoclave tubes and heat sterilised at 120°C for 20 minutes.

3.1.1 X-Ray Diffraction

X-ray diffraction (XRD) is a versatile, non-destructive instrument that is used for determination of atomic arrangement within a material, giving the crystalline phases from the atomic spacing and symmetry (160). In this technique, X-rays of a known wavelength are passed through a sample to fully investigate its crystalline structure. The wave nature of the X-rays means that the lattice of the crystal gives a unique diffraction, which results in pattern of peaks of 'reflections' at varying angles and with different intensities. The diffracted beams from atoms in successive planes cancel unless they are in phase, and the condition for this is given by the Bragg's law (161-163):

$$\lambda = 2.d.\sin\theta \qquad Eq.\ 3.1$$

where; λ is the wavelength of the X-rays, d is the distance between different plane of atoms in the crystal lattice and θ is the angle of diffraction.

Figure 3.3 shows the X-ray detector moves around the sample and measures the intensity of these peaks and the position of these peaks (diffraction angle 2 θ). The highest peak is defined as the 100% peak and the intensity of all the other peaks are reported as percentage.

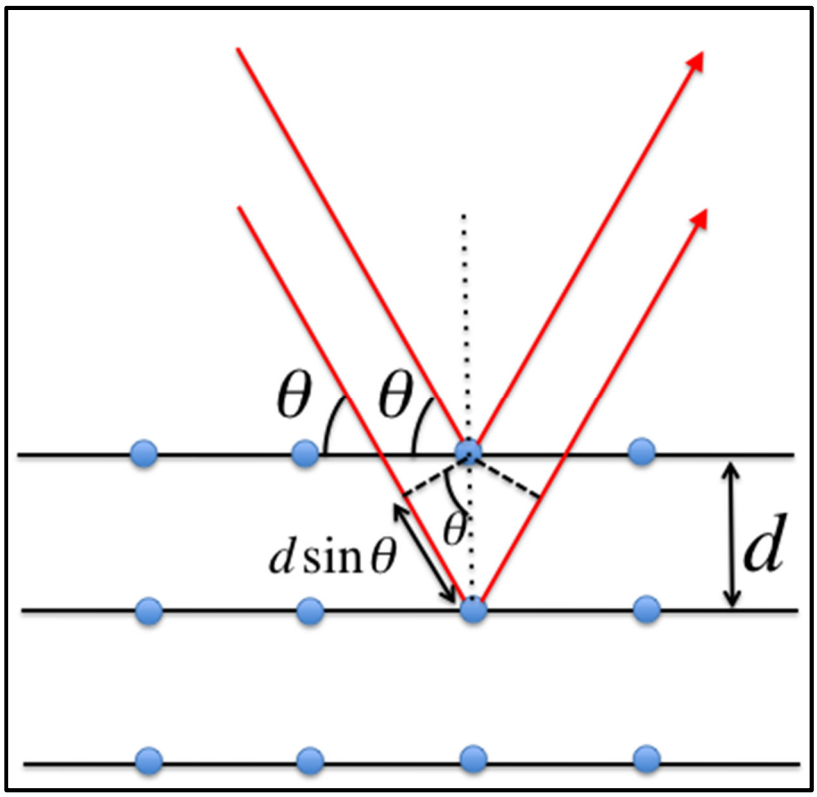

Figure 3 3: Incident and diffracted X-rays are in phase

Prior to XRD analysis, the samples were ground using a marble mortar and pestle before distributing 200mg of the ground sample powder over a 10mm diameter circular area of 25mm Magic® tape (Scotch Magic Tape, 3M, France) which was in turn folded over the sample and attached to the sample holder.

The prepared HA samples were analysed by XRD using a high resolution Powder Bruker D8 Diffractometer (Bruker ASX Gmbh, Karlsruhe, Germany, Figure 3.4), with CuKα monochromated beam (wavelength=0.154056 nm) produced at 40 kV and 40 mA. The scanning range 2 θ was performed from 20° to 60° using a step size of 0.05° and step duration of 1 second.

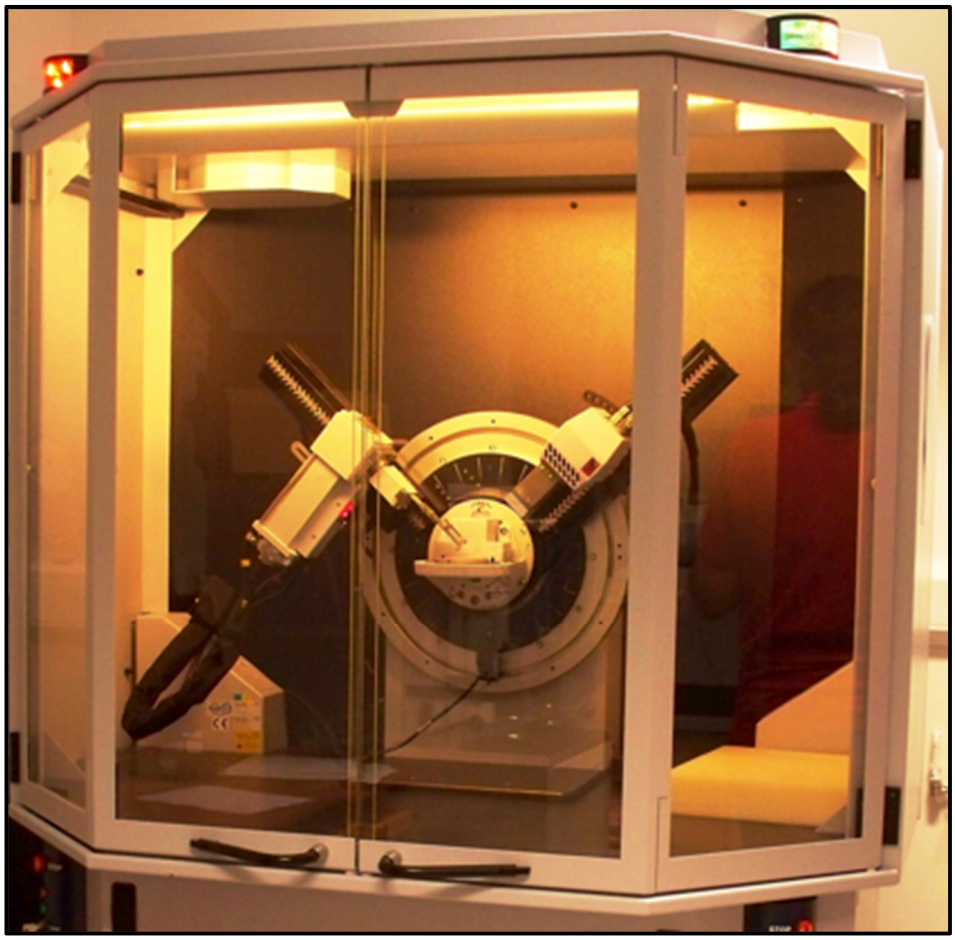

Figure 3. 4: Powder X-ray diffraction machine (Bruker D8 Diffractometer)

The sample was rotated about its axis during the entire measurement to minimise the influence of preferential crystal orientation. Baseline correct of the diffraction patterns was implemented using the Bruker DIFFRAC.SUITE software (Bruker ASX GMBH, Karlsruhe, Germany).

The XRD data was used to identify the phases, the crystallinity (what ratio of the ceramic is amorphous or crystallised), the purity of the HA powders as well as the details of their crystallographic properties (such as crystal size and lattice parameters).

Phase Identification

For the phase identification step, the X-ray diffraction patterns were directly compared to the files for HA from the Joint Committee for Powder Diffraction Standards (JCPDS, Card No. 09-432) as was supplied by the International Centre for Diffraction Data (ICDD).

The most common phases present within calcium phosphate based powders, such as *a*-TCP (09-348), β-TCP (09-169), DCPA (09- 80), DCPD (09-77), OCP (26-1056), TTCP (25-1137) were used. Similarly, the most comparable phases for Ag, silver phosphate (06-0505), silver metallic (04-0783), for Mg, Mg-β- TCP (01-70-1787), Brucite [$Mg(OH)_2$] (07- 0239) magnesium oxide (00-04683) and for Zn Parascholzite. (35-.0495), zinc oxide (36-1451) were identified and reported in the Results section.

Crystallinity

The crystallinity of the HA samples was measured by comparing the ratio of peak-to-background of the real samples to the one for a fully crystalline reference sample (163). The percentage of crystallinity was based on the XRD patterns obtained between 10° to 60°(2θ) and was calculated using the following equation (163):

$$X_c(\%) = \left(\frac{I_{300} - V_{112}/_{300}}{I_{300}}\right) \times 100 \qquad Eq.3.2$$

where I_{300} is the intensity of (300) diffraction peak and $V_{112/300}$ is the intensity of the hollow between 112 and 300 diffraction peaks of HA.

3.1.2 Crystal size (L_{002} reflection plane)

The crystal size, of the precipitates was estimated from XRD pattern using the Scherrer's formula (163). According to this equation, a single crystal dimension perpendicular to the (*h k l*) plane (D_{hkl}) (nm) can be estimated from the peak broadening as:

$$D = \frac{K\alpha}{FWHM.\cos\theta} \qquad Eq.3.3$$

where D is the crystal size in nm; *K* is the Scherrer constant (0.9 for hexagonal HA), α is the wavelength of the monochromatic X-ray beam (0.15418 nm); *FWHM* is the experimental *F*ull *W*idth at *H*alf *M*aximum intensity of the diffraction peak under the consideration peak; θ is the diffraction angle (°). In samples with apatite structures, the line broadening of the (002) reflection was used to evaluate the mean crystal size, which corresponds to the *c* crystallographic axis.

Lattice Parameters Determination

The spacing of the lattice points in a crystal is an important quantitative aspect of its structure and its investigation by X-ray diffraction. In case of the hexagonal crystal structure of HA, the lattice parameters were denoted by (*a*=*b*), and *c* and were determined from the relationship between the distance (*d*) of two adjacent planes and the (*h k l*) Miller Indices by using the equation below (163):

$$\frac{1}{d^2} = \frac{h^2 + k^2}{a^2} + \frac{l^2}{c^2} \qquad Eq.3.4$$

where *d* is determined by Bragg's law (*E* 4.1) by knowing the wavelength *(λ)* and diffraction angle (2θ). In this method, for each *(hkl)* XRD peak, lattice spacing of the *(hkl)* planes can be calculated by:

$$d_{(hkl)} = \frac{\lambda}{2\sin(\theta)} \qquad Eq.3.5$$

where θ is obtained from the XRD pattern. C axis parameter can be calculated from the *(00l)* peaks, once the c-axis parameter is calculated, a-axis parameter can be calculated by considering any *(hkl)* peaks. However, since any error in measuring the exact value of θ produces errors in $\sin\theta$ and subsequently in the calculated lattice parameter, it is important to choose the peaks which minimize this error. For the function of $\sin\theta$, the error in $\sin\theta$ would be the minimum if θ is close to 90°. Therefore, it is more accurate to use peaks near θ=90° to minimize the errors in $\sin\theta$. If there are more than one peak near θ=90°, all the peaks are considered and the average value for the lattice parameters are reported.

For this study, hexagonal unit cells (as in HA crystals) will result in the following equation for distance (*d*):

$$\frac{1}{d^2hkl} = \left[\frac{4}{3}(h^2 + k^2 + hk) + l^2\left(\frac{a}{c}\right)^2\right]\frac{l}{a^2} \qquad Eq.3.6$$

The following data were used for the analysis.

a=b, α=β=90°, and γ=120°, space group: $P6_3/m$

3.1.3 X-ray fluorescence

X-ray fluorescence (XRF) is an elemental analysis technique to understand the chemical composition of the samples and is based on measuring the emitted X-ray beams specific form each element after an X-ray beam is directed from an external source inside the X-Ray machine (164).

Samples were dried and powdered as described for XRD analysis. 1g of powder sample was evenly distributed over 2 μ m thick Mylar film held taut over a loose powder sample holder.

The atomic concentrations of Ca, P, Ag, Zn, and Mg in the precipitates were determined by Bruker S8 Tiger (Bruker ASX Gmbh, Karlsruhe, Germany).

Three replicates were carried out for each sample and the mean value was calculated. The reference samples of each ion was prepared by mixing known amount of cation (Nitrate salt) solid in the pure HA powder and using the mixed powder in the XRF machine to create a reference response for a known amount of cation. Standard curves were created by measuring the XRF response for 5 different concentrations of each cation (0.5%, 2%, 3% 4% and 12% wt% of $AgNO_3$, $ZnNO_3$ and $MgNO_3$ in pure HA) and used to calculate the accurate concentration of each component in the synthesized ion-substituted HA samples.

3.1.4 Fourier Transform Infrared Spectroscopy

Fourier transform infrared spectroscopy (FT-IR) is a chemical analysis technique that generates a molecular fingerprint of the samples. It is based on the vibrations of the atoms, which are subjected to a passing infrared radiation and measures the ratio of the incident radiation is absorbed at a particular energy (165). As the sample is exposed to different wavelengths of

infrared light, transitions between vibrational energy levels of various chemical bonds are detected, allowing for the functional groups within the molecules of the sample to be identified. The resulting spectra, which are a characteristic of infrared absorption/emission at different wavelength, can be used to define the chemical composition of the sample.

In this study, FT-IR was used for further confirmation of the chemical composition of the samples. FT-IR spectroscopy was carried out by a Nicolet nexus 470 FT-IR using a smart orbit diamond attenuated total reflectance (ATR) to confirm the presence of chemical group OH and PO_4. Sample preparation was consisted of mixing 2mg of each sample with 300mg of Potassium bromide (KBr), compressed to form a tablet and then placed on the diamond ATR specimen holder and analysed them from 400 to 4000cm^{-1} at 4 cm^{-1} resolution averaging 100 scans. Four spectra reading were done for each synthesised sample and absorbance spectrum were considered. A background reading was taken before collecting spectra from the samples and was subtracted from the sample spectra.

3.1.5 Raman Spectrometry

Raman spectroscopy is another non-destructive spectroscopic technique to obtain information about the structure and chemical composition of materials. Similar to FT-IR, a radiation source (such as UV light, near infrared beam) is used to excite the molecules through the absorption of a photon and measures the vibrational and rotational transition of the molecules and functional groups (166)(Figure 3.5). Raman spectroscopy is based on the change of polarisation of the molecule during the vibration while FT-IR technique relies on dipole moment change of the molecule. Hence, Raman spectroscopy can be used to analyse the molecules, which are symmetrical and have no dipole moment (like O_2).

Raman spectra of powdered samples (without any treatment) were obtained using a Renishaw InVia Raman microscope (Renishaw plc., Gloucestershire, UK) using a 532nm laser line at 10% power delivered to the sample via a x50 Plan-N objective lens with the detection range set to 300-1200cm^{-1}. The scan time was set to 10 seconds and 5 scans were gained and summed to produce the final spectrum for analysis using the Wire 3.0 software (Renishaw plc, Gloucestershire, UK.)

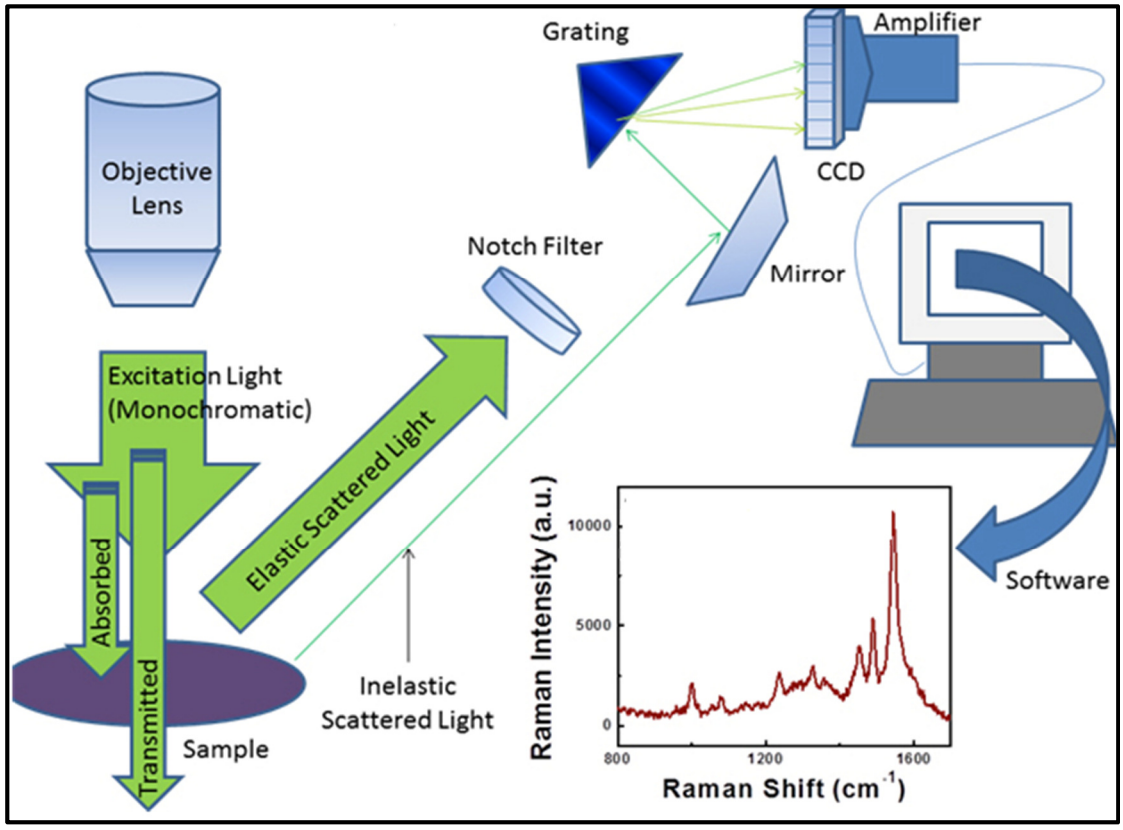

Figure 3.5: Adapted schematic diagram of Raman Spectroscopy taken from Department of Chemistry and Biochemistry website, University of Maryland.

3.1.6 Thermogravimetry (TG)

TG is used to study the change in mass of a sample as the temperature is varied. By controlling the atmosphere e.g. with O_2 or N_2, it may be possible to encourage or suppress oxidation reactions, thus controlling to some extent the nature of the thermal events occurring (167). When heated to 1000°C, many materials undergo weight changes giving characteristic curves. Where the changes can be linked to the particular thermal events, such as oxidation, or loss of water of crystallisation, the size of the step in the curve can be used for the quantitative analysis.

TG analysis was carried out in a NETZSCH-TG209 system under air atmosphere with the heating rate of 10°C/minute. 100mg of dried samples were grinded to make a fine powder.
The percentage weight loss is recorded and plotted as a function of time (in second) and temperature. The baseline values were corrected by carrying out a blank run and subtracting this from the plot obtained from the same machine.

3.1.7 Inductively coupled plasma mass spectrometry

Inductively coupled plasma mass spectrometry (ICP-MS) is a widely used analytical technique and is commonly applied for trace elemental analysis (168). ICP-MS operates on the basis of decomposing (ionising) the sample into neutral elements using a high temperature argon plasma, and separation and detection of the generated elements according to their mass to charge ratio (168). Samples are firstly converted to aerosols and then passed into a torch body and mixed with heated argon gas, producing an argon plasma flame. This produces atomised and ionised sample are transferred into a pumped vacuum system through a quadruple mass filter and are directed to a mass spectrometer, with a typical detection limit of 0.1 μg^{-1}.
For this study, an ICP-MS technique was used to measure the amount of released cations (Ag, Zn, and Mg) into the liquid phase. The solubilised cations were measured under two conditions:

a) Solubilised cations from the solid HA precipitates during washing, resuspension and centrifugation process. 5 ml of each supernatant was collected after each centrifugation step and the cations were measured by ICP-MS. The results from this section were used to carry out an accurate mass balance for the cations and determine how much of the cation were remained in the solid phase.

b) Release profile from the prepared disk samples after being placed in PBS buffer up to 21 *days*. This experiment was developed to measure the release profile of the cations and was used to better describe the concentration of the ions in the liquid phase and compare it to their antibacterial activity. Each disk sample (0.5 g of the powder was pressed at 155 Nm^{-2} force using a mechanically operated press machine and metallic dyes specially designed for making dense discs of 13 x 2 mm) of HA (as control) and of (Ag, Zn, and Mg)/HA composite were placed in polypropylene bottles and were filled with 20ml of potassium hydrogen phosphate buffer solution (pH=7.2) at time zero. The bottles were stayed stationary and incubated steadily at 37°C and 10 ml of the solution was collected after 3h, 6h, 12h, 24h, 48h, 72 h, 15 days and 21 days. 10 ml of fresh phosphate buffer was added to the bottle and gently mixed.

3.2 Cell culture

To assess the effect of ions on the proliferation and differentiation of cells well-characterised mouse osteoblast cell lines (2T3) were chosen. The main reasons for using these cells were that:

- 2T3 cells are easier to transfect than primary osteoblasts, which give very low transfection efficiencies, and

- They more closely resemble primary osteoblasts in terms of *in vitro* responses to various stimuli than many of the available human and murine cell lines (169).

Maintenance of osteoblast cells

Mouse osteoblast cell lines (2T3) were obtained from Professor Sabokbar's research group at University of Oxford. Cells used for the experiments were used from stocks passaged up to passage 21. These cells were in stored in cryogenic storage (-180°C) and whenever required were defrosted in a 37°C water bath before use. The vials (exterior) were wiped clean with 70% ethanol solution to remove any contamination and the content of the vial was then transferred with a sterile pipette into a 150 cm^2 tissue culture flask (T_{150}) (BD Bio-Sciences, UK). Fifteen ml of culture medium[1] was added to the cells which were incubated afterwards in a humidified incubator at 37°C and 5% CO_2. The growth medium was changed every 3 days until cells were confluent and ready for sub-culturing.

***In Vitro* cell Sub-Culture of 2T3 cells**

In order to sub-culture the cells, adherent confluent 2T3 cells had to be removed from the surface of T_{150} culture flasks. The most common approach for undertaking this task is by use of Trypsin/EDTA solution which is routinely used in *in vitro* tissue cell culture studies.

Firstly the culture media from flasks were discarded followed by the addition of 10 ml of 0.5% trypsin and 0.02 % ethylene diamine triacetic acid (EDTA) (Life Technologies, UK). After 5 minutes incubation at 37°C the flask was gently rotated to remove the ensure all the cells were

---

[1] *Osteoblast-like cells were cultured in Dulbecco's Modified Eagle's Medium (DMEM)- (Invitrogen Inc.) supplemented with 10% foetal bovine serum (FBS, Invitrogen) and 1% v/v antibiotics; penicillin & streptomycin (Invitrogen Inc.).*

detached from the flask. The resultant cell suspension was then gently aspirated with a sterile pipette before being mixed with 10 ml of culture media, the addition of which (due to the presence of FBS) stops the trypsin/EDTA activity as long term exposure of any cells to trypsin/EDTA can result cell death. The cell suspension was then transferred to a sterile universal and centrifuged at 1000 rpm for 5 minutes at room temperature. The supernatant was discarded and the resultant cell pellet was re-suspended in 4 ml of pre-warmed culture media. These cell suspension were either used to "passage/re-seed" further culture flasks or utilised for setting up the necessary experiments by counting the 2T3 cells.

Counting Viable Cells

When required, the suspended 2T3 cells (as described above) were used to set the necessary *in vitro* experiments using Trypan blue exclusion test. Firstly the number of viable cells was determined by adding 20µl of 2T3 cell suspension to 20µl of 0.4% (w/v) trypan blue solution which was homogenously mixed[2].

About 10 µl of stained cell suspension was transferred to the haemocytometer (Figure 3.6) and a microscope was used to view the viable cells for counting. The full grid on a haemocytometer contains 9 squares, each of which is 1 mm square and a chamber depth of 0.1 mm. Each square has a total volume of 0.1 mm^3 or 10^4 cm^3. The central square is divided into 25 small squares with triple lines and four corner squares are divided into 16 small squares. Each large square

[2] *The dye exclusion test is used to determine the number of viable cells present in a cell suspension. It is based on the principle that live cells possess intact cell membranes that exclude certain dyes, such as trypan blue, whereas dead cells do not. In this test, a cell suspension is simply mixed with dye and then visually examined to determine whether cells take up or exclude dye. A viable cell will have a clear cytoplasm whereas a nonviable cell will have a blue cytoplasm(170)*

has a surface area of 1.0mm^2, and the depth of the chamber is 0.1mm. As there are 1000 mm^3 per ml, each large square represents a volume of 0.0001ml, so that it is equal to 1/ 0.0001ml = 10,000 = (10^4). So the total numbers of cells per ml were calculated using the following equation:

Cells per ml = Average count per square x dilution factor x 10,000

Large cells are counted using the four large corner squares (and the middle one). Each is divided into nine 1mm^2 squares.

Thereafter 1x10^5 viable 2T3 cells were added in culture media to previously autoclaved HA discs (both ion substituted and non ion substituted) which had been placed in sterile 24-well cell culture plates containing media for 2 hours. Cells on HA discs were incubated in 5% CO_2 at 37°C for a period of 7 days, during which the samples were removed on a daily basis (1-7 days) to assess the effect of HA ± cations on 2T3 cells' cellular activity.

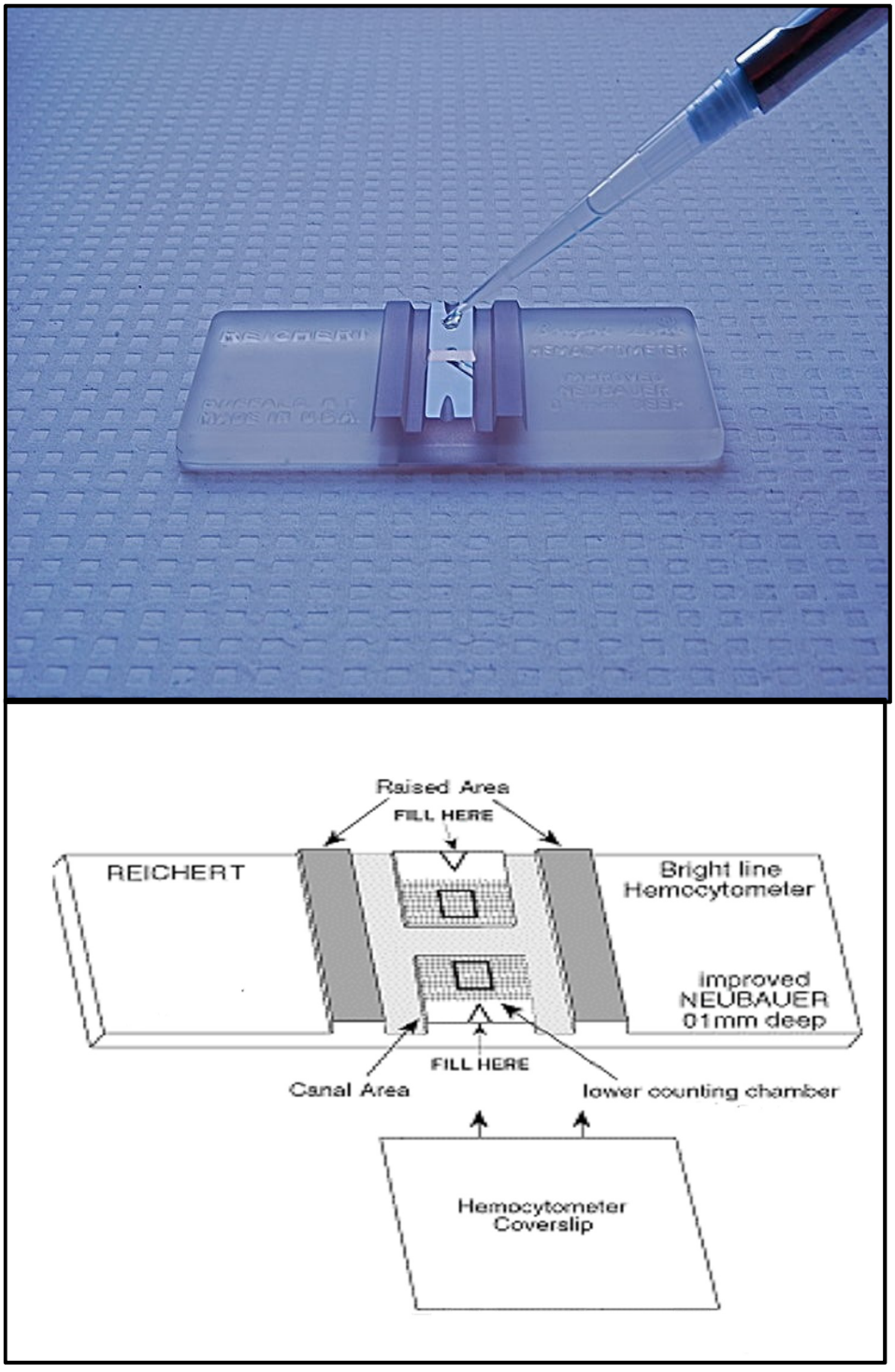

Figure 3.6: Haemocytometer used for the cell counting(171)

3.2.1 Osteoblast cellular activity in response to (Ag, Mg, and Zn)/HA

Osteoblast differentiation *in vitro* can be characterised in three stages: (a) cell proliferation, (b) matrix maturation, and (c) matrix mineralisation. *In vitro* matrix maturation and mineralisation are usually enhanced by growing the cells to complete confluency and by adding specific osteogenic factors. During proliferation stage (a), several extracellular matrix proteins (procollagen I, TGF-β, and fibronectin) can be detected. The matrix maturation phase (b) is characterised by maximal expression of alkaline phosphatase (ALP). Finally, at the beginning of matrix mineralisation (c), genes for proteins such as osteocalcin and osteopontins are expressed and once mineralization is completed, calcium deposition can be visualized using adequate staining methods. For the purpose of the current investigation, cell proliferation and matrix maturation of the 2T3 were assessed.

Cell Proliferation

The gold standard cell proliferation assay is ^{3}H-thymidine DNA incorporation during cell division (172). However, due to the high cost of the purchase of tritium and handling radio-labelled materials, it was decided to use the, Alamar Blue™ technique as an alternative for assessing the cell viability/proliferation (173). This approach is based on redox-sensitive growth indicator which quantitatively measures cell viability and proliferation using fluorescent or colourimetric detection strategies. The Alamar Blue™ reagent is a non-toxic, water-soluble that on its own is non-fluorescent, but it is effectively reduced by cytochrome-b5 reductase to a red fluorescence colour (resorufin) in the mitochondria of metabolically active cells and the dye is released into the cell medium (174) .

This approach is much more appropriate than ^{3}H as cell viability can be monitored in real time and the cells can be re-used for subsequent experimentations. For the present investigation 2T3 cells' proliferation was investigated using Alamar Blue™ (AbD Serotec, Oxford, UK) assay according to the manufacturer's instruction. Briefly, after 1 to 7 days cell culture incubation, the culture media from the 24-plates containing NS-HA or/and (Ag, Mg, and Zn) substituted hydroxyapatite were removed and the samples were washed three times with PBS. 500 µl of 10% Alamar Blue™ (at room temperature) was added to each well and incubated at 37°C and 5% CO_2 for 180 minutes. 100 µl of the Alamar Blue™ from each was then transferred to a sterile 96-well plate. Cells in the 24-well plates were then washed carefully with phosphate buffer saline to remove any excess the Alamar Blue™ and replaced with fresh culture media and returned back in the incubator for completion of the experiment.

The fluorescence level in the 96 well plate corresponding to the HA samples in 24-well plates was measured at 540 nm excitation and 590 nm emission using a FluorStar Optima plate reader. The measurement was repeated twice for each sample and thrice for individual experiment.

The background control fluorescence reading was assessed with the same number and type of cells but in the absence of any HA discs. Another set of cell-containing plates were used with control samples (NS-HA) and their absorbance were normalised against the mentioned background readings. Normalised control samples were compared with the ion-substituted samples to measure the efficacy of ions on the studied cells.

Standard curve were used as described by the assay kit supplier to convert te absorbance readings and concentration of ALP enzyme activity (coloured *p*-Nitrophenol).

In summary, two readings were taken from each of the three samples in each group – giving a

total of six readings per group. Also reading from an Alamar Blue™ only (blank) was measured and subtracted from all the reading values to obtain the real measurement of cell proliferation. This process was repeated for each measurement at each time point (days 1 to 7) and the Alamar Blue™ reduction for each cell density was obtained. For all cell densities, the relative fluorescence unit of Alamar Blue™ reduction was plotted against duration of the cell cultures.

3.2.2 Alkaline Phosphatase Activity Assay

Alkaline phosphatase is a non-specific de-phosphorylation metalloenzyme (Zn and Mg) which hydrolyses phosphate compounds at basic pH. It is found in all body tissues and is responsible to catalyse the splitting the organic phosphate esters to inorganic phosphates (175). ALP activity is regarded as a measurement of enzyme kinetics for transformation of p-nitrophenylphosphate into p-nitrophenol. ALP enzyme is known to be localised on the surface of osteoblast cells and secreted into the matrix in order to generate a basic medium for the formation of new bone (175). The activity of ALP enzyme has been shown to indicate the osteoblast maturation and its level maximises up to the mineralisation phase (176).

Osteoblastic phenotype was examined by the cell's response to BMP-2. Osteoblast- like cells typically up-regulate ALP and other phenotypic markers in response to BMP-2 when cultured and assessed *in vitro*. Osteoblast like cells 2T3 (7500) cells were seeded in triplicates in 24 well plates and treated with murine recombinant BMP-2 (100 ng/ml) over 2, 3 and 4 days. Plates were removed from incubators, media were aspirated and cells were washed with PBS and lysed in radioimmunoprecipitation lysis buffer (RIPPA) in 2% ready to use mammalian protease inhibitor cocktail (PI) on ice. Cell lysates were collected in labelled microfuge tubes, sonicated for 5 seconds, and centrifuged at 12000 rpm for 20 minutes. Supernatant was

collected and total protein content was measured by PIERCE BCA™ protein assay kit (Fisher Scientific-UK). ALP was measured by 4-methylumbelliferyl (4MU) substrate kit (Sigma-Aldrich). Briefly, 10µl of cell lysates were incubated with 100µl of freshly made 4MU (0.16mM in 50mM Tris pH= 6) in white 96 well plates (Fisher Scientific, UK) for 45 minutes in the dark at 37°C, following an addition of 100µl of 0.6M Na_2CO_3 to stop the reaction. Fluorescence was measured at 360 nm excitation, 450 nm emission and 435 nm cut off using a BMG Optima FluorSTAR® plate reader. ALP activities were calculated by preparing a standard curve of 0-20,000 pmol 4-methylumbelliferone (4MU) on the same plate and normalised to the total protein content of each relevant well. Murine 2T3 cells (1×10^4) were plated into 24 well plates in replicates in their culture growth medium to reach confluence. Differentiation was then induced (day zero) by osteogenic differentiation medium. 2T3 osteoblasts were maintained in osteogenic differentiation medium for 3 days, with media being changed twice on day zero and day two. Cultures were stopped at 12 hours intervals for the assessment of ALP activity.

3.3 Antibacterial Measurements

3.3.1 Agar diffusion study - Zone of Inhibition (ZI)

Ag and Zn substituted hydroxyapatite disks were prepared following the same procedure described in section 2.1. Under sterile conditions, a single colony of *S. epidermidis* 11047 (Fisher Scientific, UK) was cultured in 10ml Trypton Soya Broth (TSB) at 37 °C for 24 hours. This resulted in a bacterial suspension of ~10^8 cells/ml which was serially diluted to produce another suspension of ~10^5 cells/ml. 25 µl of this suspension was then spread across a Tryptone Soya Agar (TSA) (Oxoid, Hamps, England) plate using a sterile swab to form a lawn of bacteria covering the agar surface. Each disc samples placed in the center of the plate on the top surface of TSA agar medium. The plates were placed in a 37°C incubator for further 24 hours. The

same procedure was carried out to prepare *E. Coli ATCC* 4352 (Fisher Scientific, UK.

The Trypton Soya Broth (TSB) was prepared by addition of 18.5 g of TSB powder to 500 ml of deionized water and was sterilized by autoclaving at 121°C for 15 minutes to prepare a sterilized medium.

The Trypton Soy Agar (TSA), solid culture media, was used for cultivation of candidate bacteria. 40 g of powdered agar was added to 1 liter of distilled water and dissolved. The dissolved medium was sterilized by autoclaving at 121°C for 15 minutes.

The zone of inhibition (reported values are the diameter of zone) was measured and recorded for each plate at different times and results are summarized and compared for ach sample and bacteria strain.

3.3.2 Film adhering method (Quantitative)

In this technique, a known number of bacterial cell were cultivated on top of a sample disk (and control) for varying time intervals (hours) and then the whole disk was washed to remove and disperse any viable cells from the surface of the disk. Samples from the suspension were transferred to fresh agar plate to quantitatively measure the colony formation unit (CFU) and the effectiveness of antibacterial agent in the disk. Cultures of *E.coli ATCC* 4352(Fisher Scientific, UK) and *S.epidermidis* 11047 (Fisher Scientific, UK) were prepared by using freeze-dried ampoule of each bacteria (obtained from the Fisher Scientific, UK). Ampoules were broken open and the bacterial pellet revived by re-suspending in 500 µl of Trypton Soya Broth (TSB) (Oxoid, UK) and incubated at 37°C with 5% CO_2 overnight.

A method described by Kashani et al. was used for this measurement (177) . Cells were collected from a plate and were suspended in sterile TSB (5 ml). To prepare starter cultures for future experiments, 1 ml aliquots where stored at -80°C and used daily to inoculate 5 ml of fresh TSB. Growth was also measured by a spectrophotometer (Jenway, UK) using 1 ml cuvettes at 600 nm.

The OD at 600 nm of the *E.coli* and *S.epidermidis* was measured and adjusted using fresh solution to 0.05 ± 0.01 in 1 ml. The original bacterial suspension, adjusted to ~10^7 cells/ml, was added to the specimens.

To measure count cells, 20 µl of the test suspension was diluted ten-fold six times (10^{-6}) of the in phosphate buffered saline (PBS). When dilutions with each colony could be measured, the colony forming units (CFUs) per ml of original sample was calculated.

The samples then were transferred to 10 ml of sterile PBS after a set time, before dispersing the cover slips and suspend surviving bacteria in vortex. 100 ml of final suspension was pipetted into TSA, which was previously divided into three quadrants with different Dilution factors (DFs), such as 10^{-2}, 10^{-4} and 10^{-6}. Form each DF, three 20 µl spots were evenly spaced and CFUs were counted following 24 h incubation at 37 °C.

TO calculate the reduction, following formula was used:

$$\text{Reduction \% (CFU/ml)} = [(\alpha_t - \alpha_0)/\alpha_0] \times 100\%$$

Where α_t= mean CFU/ml for the treated coupon after the designated contact time and α_0 = mean CFU/ml for the untreated coupon after the designated contact time.

3.3.3 Statistical Analysis

All biological experiments were carried out in triplicates unless otherwise stated. Data were statistically tested for significance difference using parametric one-way analysis of variance (ANOVA) and Student's *T*-tests. Microsoft Excel 2003 was used for this purpose and the significant level (*p)* was set at $p<0.05$ unless otherwise stated.

CHAPTER 4
RESULTS

4 Results

4.1 X-ray Diffraction analysis

4.1.1 X-ray diffraction analysis of Non-Substituted Hydroxyapatite (NS-HA)

In order to understand the effect of ion substitution on the hydroxyapatite structure and the chemical and physical attributes, a sample of non-substituted hydroxyapatite (NS-HA) was prepared (using the same preparation method) and was used as the HA reference sample throughout this study. This non-substituted hydroxyapatite sample was analysed using all the analytical techniques described in Chapter 2.

As discussed earlier in Materials and Methods (Chapter 3), XRD was used for phase identification, measurement of the degree of crystallinity, crystal size and lattice parameters.

Phase Identification of NS-HA

The XRD patterns of NS-HA samples both sintered and non-sintered are shown in Figure 4.1 and provide an overview of the HA structure prepared by wet precipitation.

The overall diffraction patterns were in agreement with the current literature (62, 66, 178, 179) and showed the characteristic peaks of HA (66). Table 4.1 lists and compares the significant peaks of the synthesised HA sample with the Joint Committee on Powder Diffraction Standards (JCPDS), no. 09-0432 for stoichiometric HA.

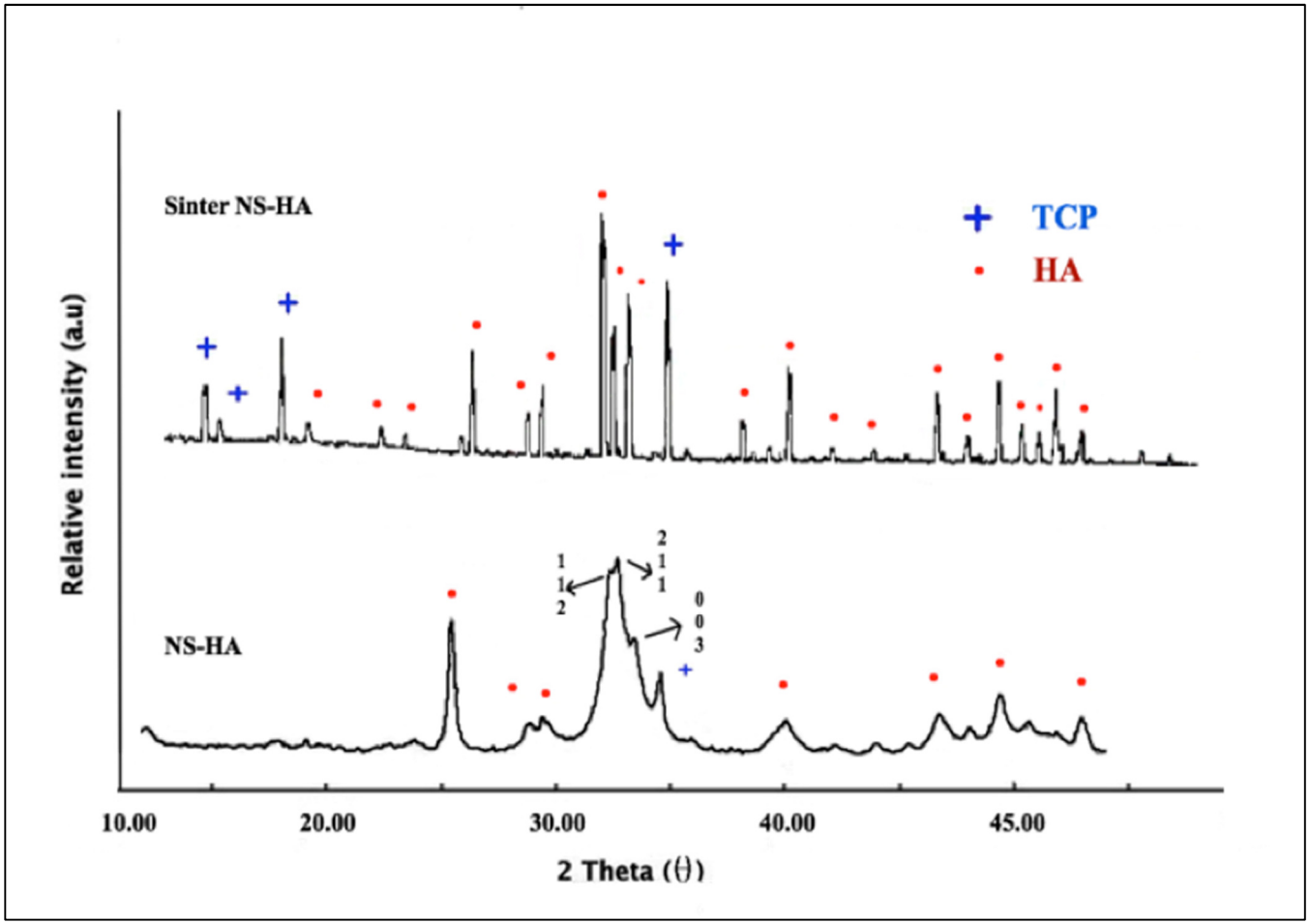

Figure 4. 1: The XRD diffraction patterns of sintered (1100 °C) and non-sintered hydroxyapatite.

Table 4. 1: Characteristic peaks of synthesised HA (non-substituted) and comparison with stoichiometric HA used as a reference.

Data from the X-Ray diffraction of NS-HA (Experimental results)			**Stoichiometric HA Card No. 09-0432**	
2Θ (°)	***d* (Å)**	**Miller Index of the Corresponding Reflection**	**d (Å)**	**Miller Index of the Corresponding Reflection**
16.84	5.26	(101)	5.25	(101)
18.78	4.72	(110)	4.72	(110)
21.6	4.1	(200)	4.07	(200)
22.97	3.87	(111)	3.88	(111)
25.9	3.44	(002)	3.51	(201)
28.22	3.16	(102	3.44	(002)
29.14	3.06	(210)	3.17	(102)
31.86	2.8	(211)	3.08	(210)
32.2	2.78	(112)	2.814	(211)
32.9	2.72	(300)	2.778	(112)
34.22	2.62	(202)	2.72	(300)
35.51	2.52	(301)	2.631	(202)
39.26	2.28	(212)	2.528	(301)
39.86	2.26	(310)	2.296	(212)
42.1	2.14	(311)	2.262	(310)
43.8	2.07	(113)	2.228	(221)
45.32	1.99	(203)	2.148	(311)
46.69	1.94	(222)	2.134	(302)
48.16	1.88	(312)	2.065	(113)
48.59	1.87	(320)	2.04	(400)
49.51	1.83	(213)	2	(203)
50.53	1.8	(321)	1.943	(222)
51.33	1.78	(410)	1.89	(312)
52.24	1.75	(402)	1.871	(320)
53.27	1.72	(004)	1.841	(213)

Data from the X-Ray diffraction of NS-HA (Experimental results)			Stoichiometric HA Card No. 09-0432	
2Θ (°)	***d* (Å)**	**Miller Index of the Corresponding Reflection**	**d (Å)**	**Miller Index of the Corresponding Reflection**
54.45	1.68	(104)	1.806	(321)
55.87	1.64	(322)	1.78	(410)
57.15	1.61	(313)	1.754	(402), (303)
58.17	1.58	(501)	1.722	(004), (411)

The prepared NS-HA samples in this study were sintered at 1100 °C, as described in the Materials and Methods section 3.1. As results suggest, slight HA decomposition to β-TCP was observed in samples (indicated by a small β-TCP peak at 2θ= 13.71 (104), 14.21 (006), 17.13 (110), 18.61 (113) and 34.37 (220) (JCPDS no. 09-0169 and JCPDS no. 09-0432)).

Table 4. 2: Present phases, crystallinity and crystal size for NS-HA.

HA Powder	Phase Present	Crystallinity (%)	Crystal Size (nm)
Commercial HA (Sigma Aldrich)	**HA**	**100**	
NS-HA	**HA, β-TCP**	**88.8±4.6**	**73±4.1**
Non-sintered NS-HA	**HA, β-TCP**	**61.75±5.3**	**88.76±4.8**

Crystallinity and crystal size of NS-HA

The degree of crystallinity was measured using the formula provided in Materials and Methods sections 3.1.1 and 3.1.2. The effect of sintering on crystallinity is summarised in Table 4.2 where the sintering of HA samples at 1100°C resulted in a considerable increase in crystallinity. This is evidenced through a substantial increase in peak heights and an associated drop in peak widths. Non-sintered NS-HA exhibited a crystallinity of 61.75 ±5.3 %, while sintered HA

exhibited crystallinity of 88.8 ±4.6 %; demonstrating that sintering increased crystallinity by 27 %.

Lattice parameters and crystal size of NS-HA

In order to determine the unit cell parameters of the substituted HA samples, the models previously reported by Dickens et al. (180) and Sudarsanan (181) were used as the starting conditions for the Rietveld refinement. It should be noted, that the Rietveld refinement technique was not sensitive enough to determine the ion concentration in each phase. Hence, only the unit cell parameters for both phases of HA (180) and β-TCP (181) were considered and compared against the values from the NS-HA sample.

Table 4.3 presents the lattice parameters of the powders, which were calculated using refined values for the NS-HA sample consisted of a mixture of HA and β-TCP phases. These values showed an excellent match to those input from the literature references.

Table 4. 3: Lattice parameters of HA and β-TCP in sintered (1100 °C) NS-HA.

	***a*-axis(Å)**	***c*--axis(Å)**
NS-HA	9.415±0.001	6.879±0.009
NS-β-TCP	10.439±0.005	37.399±0.008

For the sintered NS-HA sample, all the refined lattice data for the HA phase confirmed the presence of a hexagonal structure (space group $P6_3/m$) and the measured values were in good agreement with the crystal data for a single HA phase ($a = b = 9.424$ Å, $c = 6.879$ Å, $\alpha = \beta = 90°$, and $\gamma = 120°$) (182). A typical rhombohedral β-TCP structure (space group R3*c*) was

confirmed by the refined lattice data. The calculated values were very similar to those which are reported by Dickens *et al.* (180) for a single phase crystalline β-TCP ($a = b = 10.439$ Å, $c = 37.375$ Å, $\alpha = \beta = 90°$, and $\gamma = 120°$). The slight difference in the lattice parameters may be due to a possible deviation from stoichiometry, which is often the case for precipitated apatitic salts.

When the lattice parameter for the *a*-axis was compared to the ones for the stoichiometric HA (Ca/P=1.67) sample, which was used as reference, the precipitated HA exhibited a higher value for this crystal axis. This could be as a consequence of the higher Ca^{2+} for the HA reported here (Ca/P=1.8). This has previously been reported by Aizawa et al. (183), who suggested that the crystal planes of HA could be controlled by changing the Ca/P ratio during synthesis.

4.1.2 X-ray diffraction analysis of Silver-Substituted Hydroxyapatite (Ag-HA)

Phase Identification of Ag-HA

The XRD patterns of all silver substituted hydroxyapatite (1%, 5% and 10 % Ag-HA) samples are shown in Figure 4.2 and 4.3. The XRD patterns of all samples were very similar to that of NS-HA and in accordance with JCPDS no. 09-0432. However, two sharp peaks at $2\theta = 33.29°$ and 36.58° and a small peak at 27.16°, present in the X-ray diffraction pattern of 1% Ag-HA sample were in good agreement with (210), (211) and (110), crystal planes of the body centred cubic Ag_3PO_4, respectively. When the silver concentration increased to 5%, an additional peak at $2\theta = 20.82$ ° was present. This peak was associated with the (119) crystal plane of Ag_3PO_4.

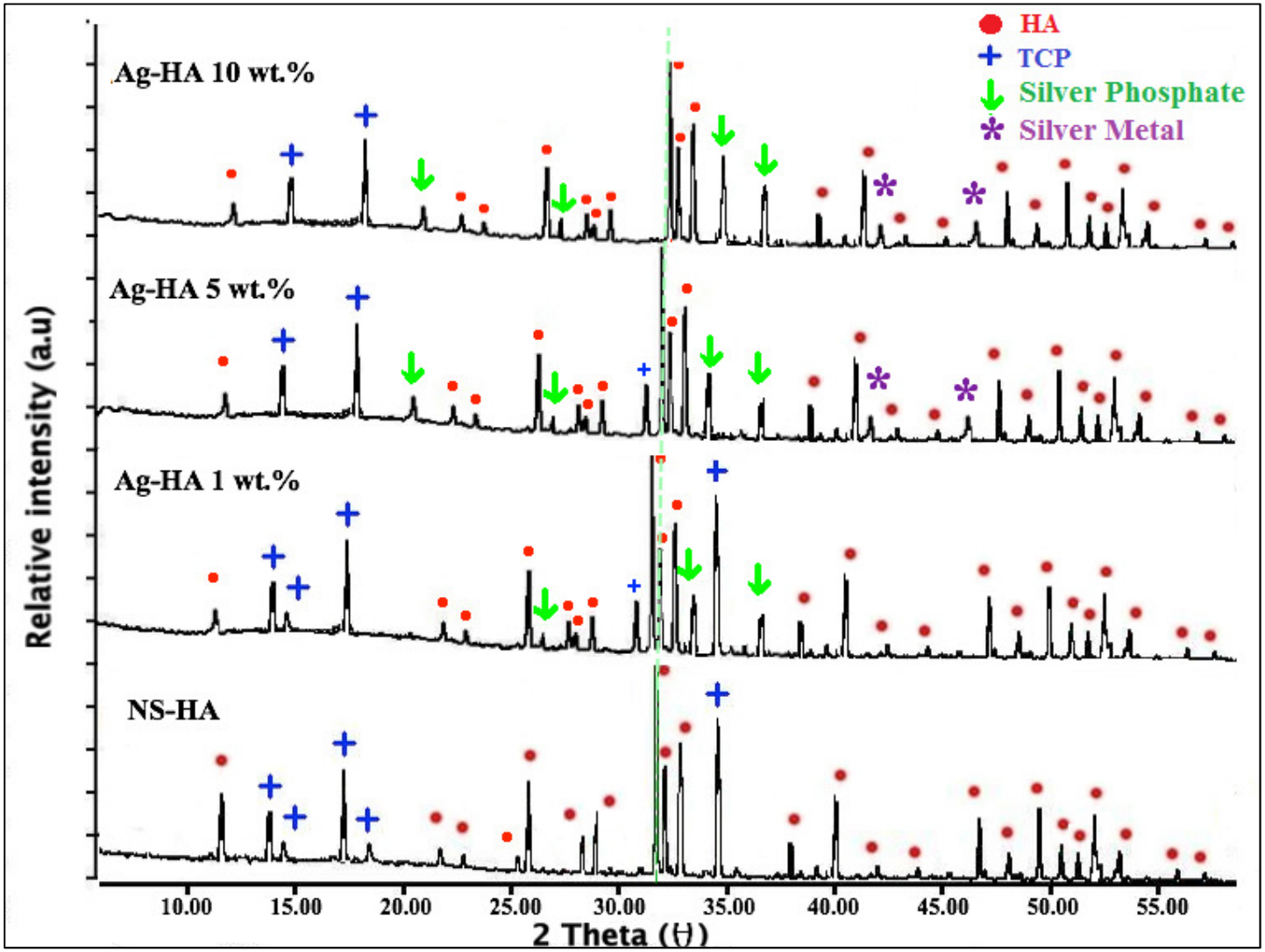

Figure 4. 2: The XRD diffraction patterns for sintered (1100 °C) silver substituted hydroxyapatite with different Ag concentrations. **:**

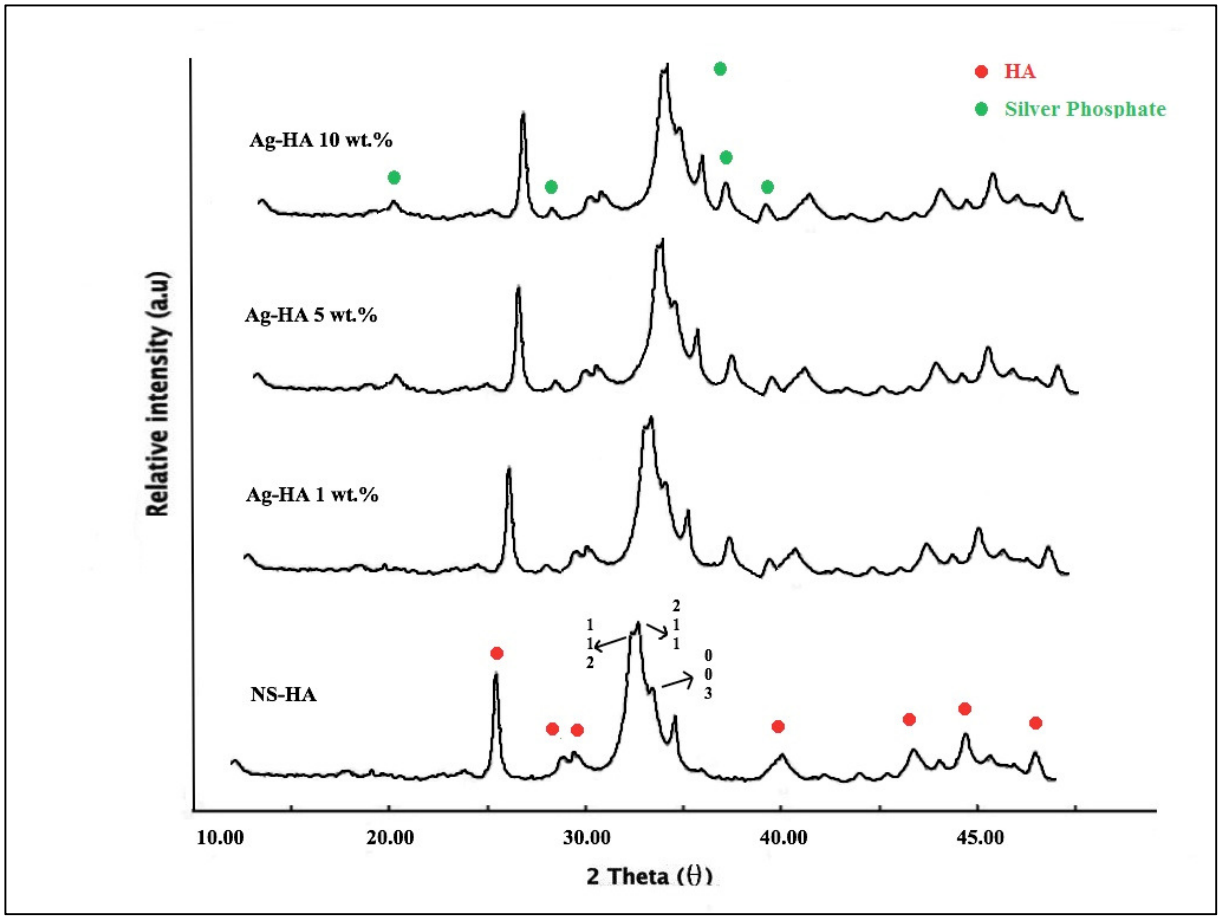

Figure 4. 3: The XRD patterns for non-sintered silver substituted hydroxyapatite with different Ag concentrations.

Silver phosphate (Ag_3PO_4) was observed in all silver added hydroxyapatite samples. It is worth mentioning, that with increasing silver content, the presence of Ag_3PO_4 is more pronounced as the peaks at 2θ= 33.29° and 36.58° become sharper especially in the case of 10% Ag-HA (Figure 3.2). A slight shift to a higher 2θ was also observed at 2θ = 33.29° and 36.58° with increasing silver from 5 to 10 wt.%.

In addition, two small peaks at 2θ = 40.30° and 45.31° may be associated with the hexagonal crystal planes of metal silver (102) and (103), respectively. These small peaks are present in 5 and 10 wt% silver concentrations and have also been reported in previous studies (184, 185).

Crystallinity and crystal size of Ag-HA

As the XRD patterns in Figure 4.2 showed, by introducing silver to hydroxyapatite in concentrations of 0 to 10 %, crystallinity marginally decreased. As presented in Figure 4.4, and Table 4.4, the crystallinity degree was about 88.8%±4.6 for NS-HA, and 85.85%±10.1, 86.72%±4.2 and 86.61±3.6 for Ag-HA 1 %, 5 %, and 10 % respectively (all sintered samples).

Table 4. 4: Present phases, crystallinity and crystal size for sintered (1100 °C) Ag-HA.

HA Powder	Phase Present	Crystallinity (%)	Crystal Size (nm)
NS-HA	HA, β-TCP	88.8±4.6	73±4.1
Ag-HA 1%	HA, β-TCP, Silver Phosphate	85.85±10.1	74±5.3
Ag-HA 5%	HA, β-TCP, Silver Phosphate, Silver Metal	86.72±4.2	78.31± 3.6
Ag-HA 10%	HA, β-TCP, Silver Phosphate, Silver Metal	89.31±3.6	79.1±6.1

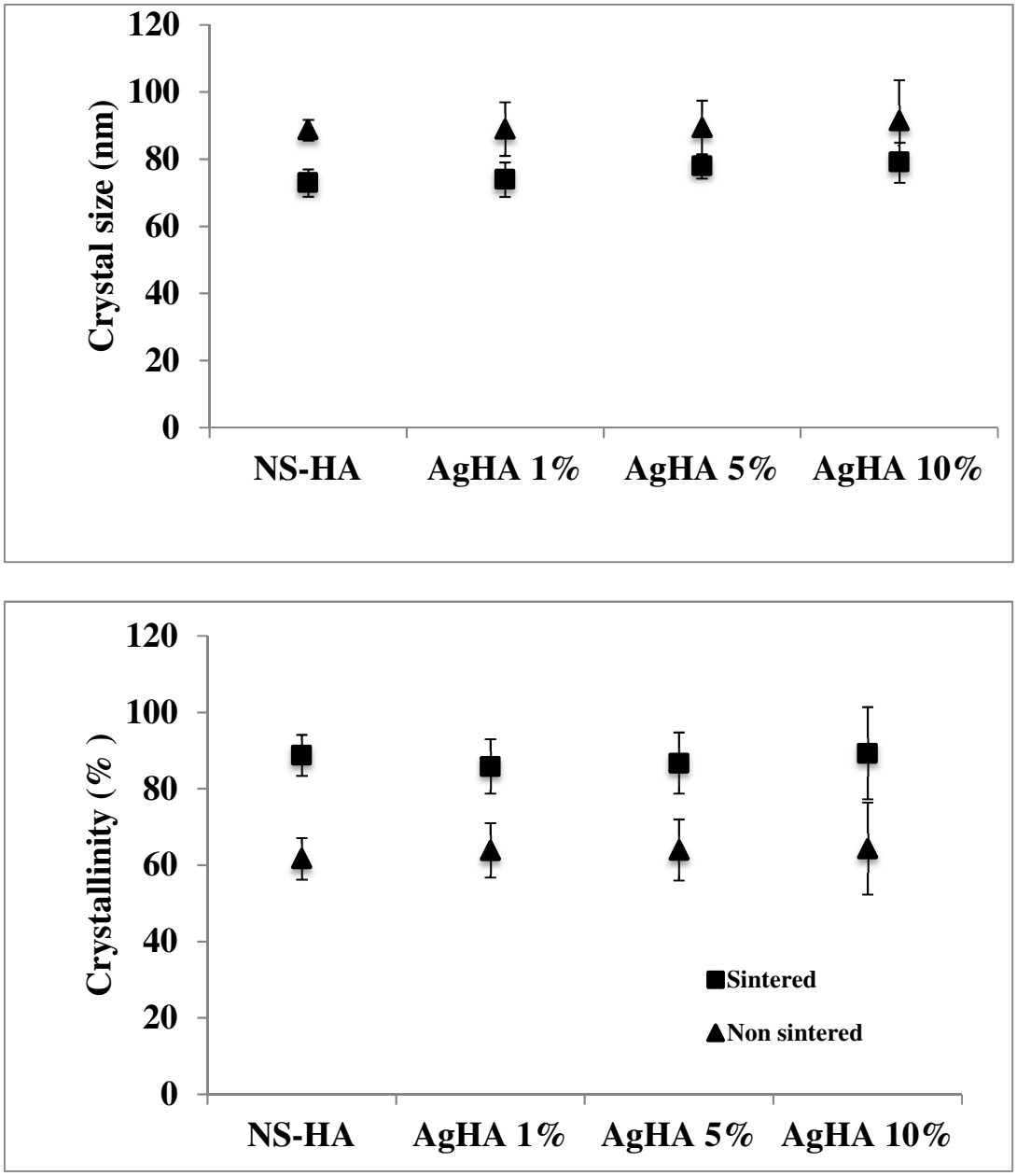

Figure 4. 4: Crystal size (top) and Degree of crystallinity (bottom) for silver substituted hydroxyapatites with different concentrations.

Lattice parameters of Ag-HA

The unit cell parameters of all Ag-HA samples are presented in Figure 4.5. The lattice parameters *a* and *c* increased with an increasing quantity of silver ions in the HA and β-TCP

phase, which suggested that Ag ions contributed to the change of the lattice parameters. It is not clear in what way silver ions can change the lattice parameters. Considering that silver ions are monovalent, it is difficult to say that silver ions can directly replace the divalent calcium ions as this would result to a charge unbalance within the crystal lattice.

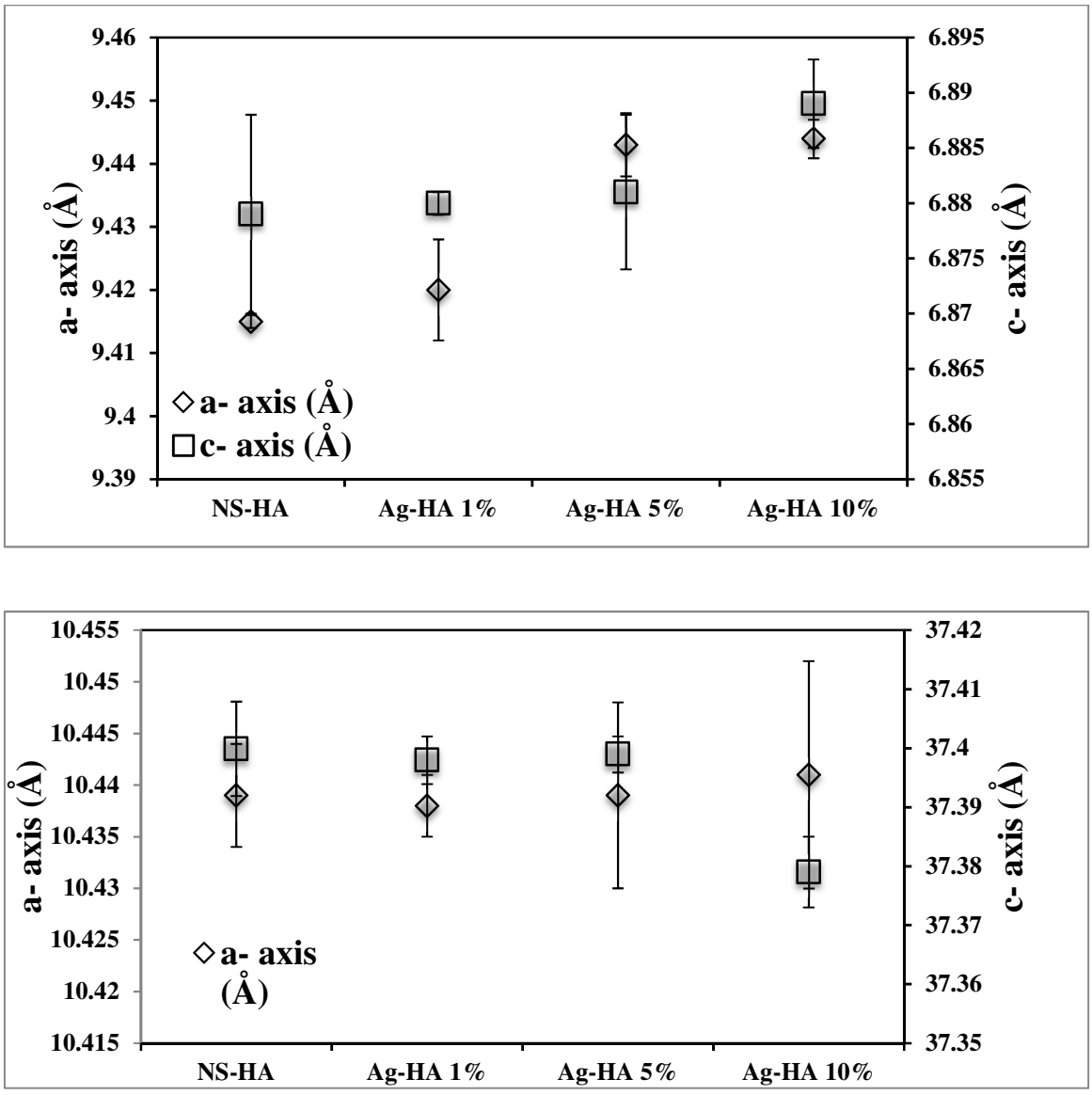

Figure 4. 5: Lattice parameters of HA crystal (top) and β-TCP crystal (bottom) in silver substituted hydroxyapatites with different concentrations.

Lattice parameters of both HA and β-TCP have changed, which may indicate Ag ions have replaced Ca^{+2} sites in both phases. The observed changes in the cell parameters also confirm that silver with the size of 0.128 nm has substituted the calcium (with the size of 0.099 nm) in the HA lattice.

4.1.3 X-ray diffraction analysis of Magnesium-Substituted Hydroxyapatite (Mg-HA)

Phase Identification of Mg-HA

The XRD patterns of all magnesium substituted hydroxyapatite (1%, 5% and 10 % Mg-HA) samples are shown in Figure 4.6 and Figure 4.7.

When Mg ions were added to HA, the XRD pattern was shifted clearly lower 2θ values comparing to NS-HA. In addition, a β-TCP phase was observed and also shifted to lower 2θ values.

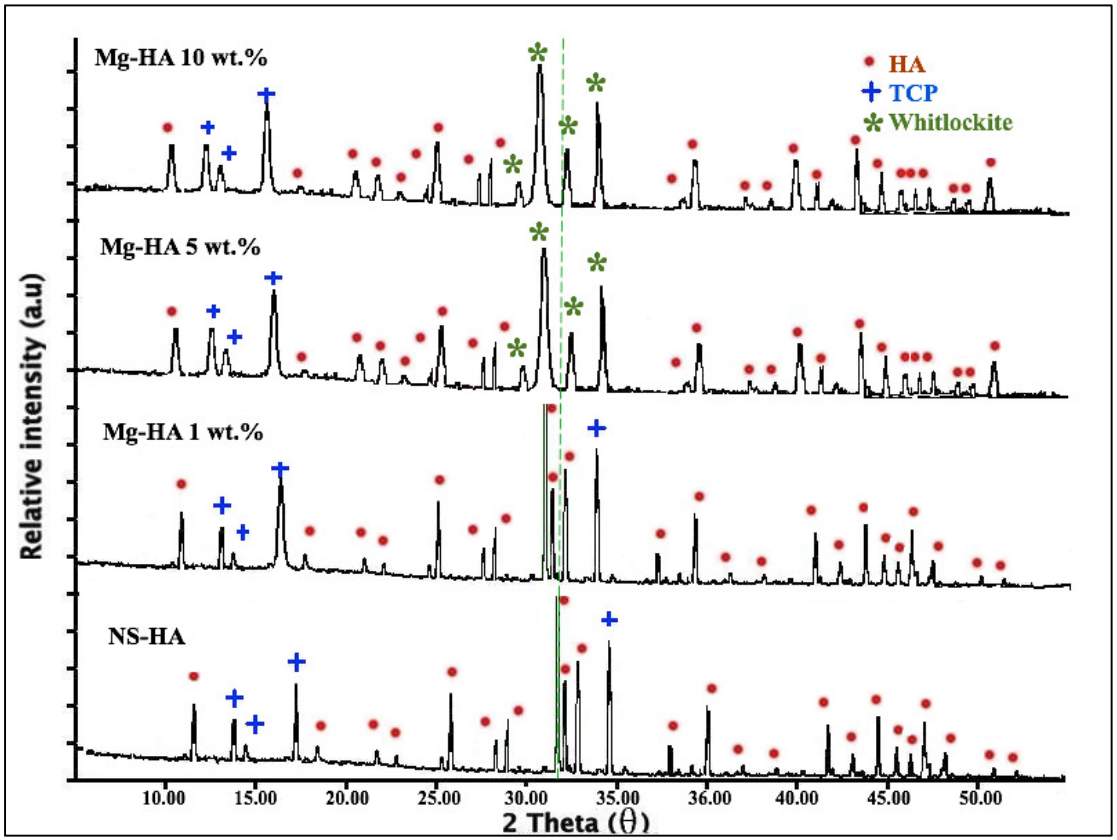

Figure 4. 6: The XRD diffraction patterns for sintered (1100 °C) magnesium substituted hydroxyapatite with different Mg concentrations.

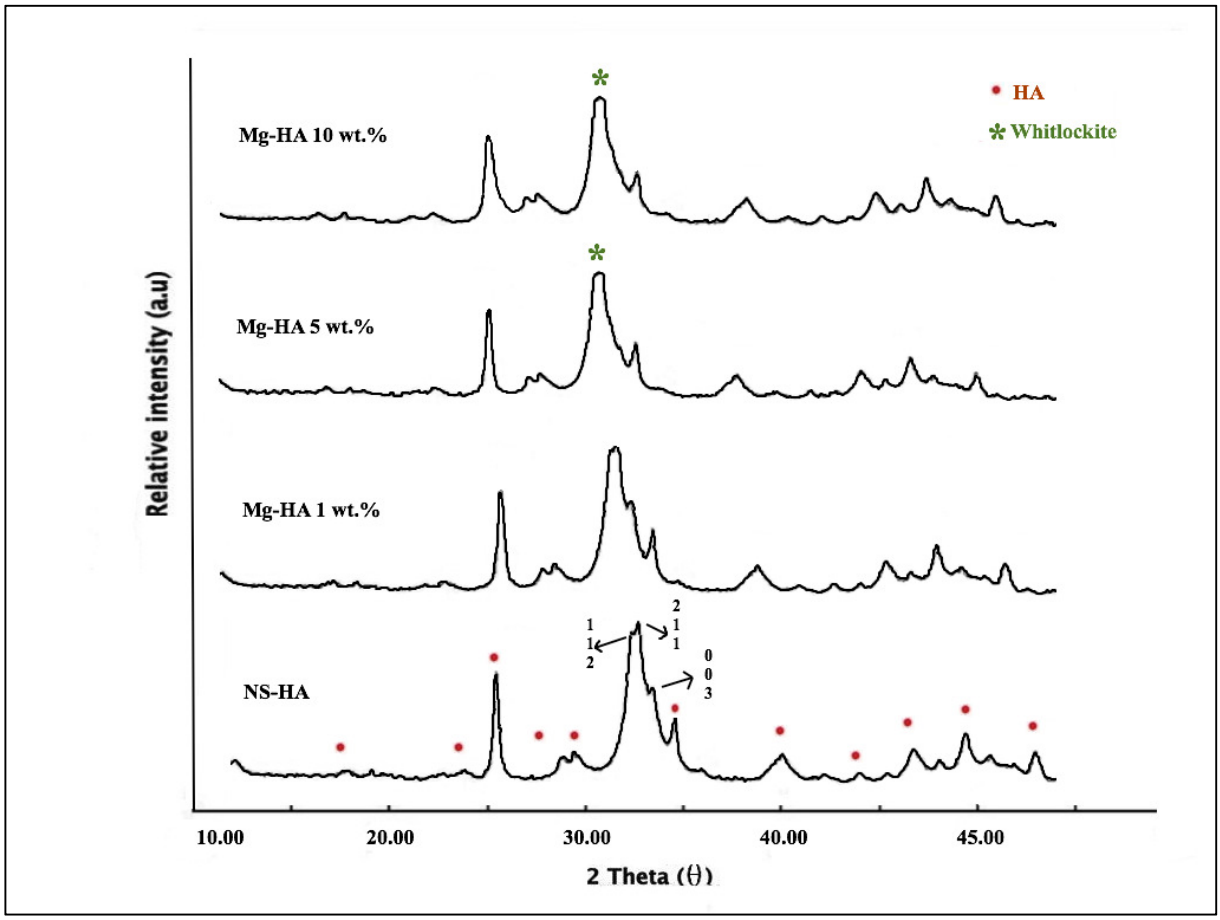

Figure 4. 7: XRD patterns for non-sintered magnesium substituted hydroxyapatite with different Mg concentrations.

All peaks became broader with increasing Mg substitution compared to NS-HA samples. Thus, it can be concluded that Mg ions which were engaged in the HA structure caused significant deformations in the crystal lattice. Also, the absence of unreacted MgO (JCPDS no. 00-04683) and Brucite ($Mg(OH)_2$) (JCPDS no.07- 0239) in all Mg-HA pattern may suggest that Mg ions were substituted in the HA and most likely replaced calcium ions in the crystal lattice. The location of the substitution is very difficult to observe from these data. When Mg concentration was increased to 5% and 10%, a new single Mg-Whitlockite ($Ca_9Mg(PO_4)$ $6(PO_3)OH$) phase ,

also called Mg-β-TCP (JCPDS no. 01-70-1787) was formed with representing peaks at 2θ= 31.30° in addition to the existing HA phases and β-TCP. In fact, one of the main characteristic planes, which is present at 31.81° (112) was shifted to a lower degree and converted to most characteristic Whitlockite phase at 30.00° (0210).

Table 4. 5: Present phases, crystallinity and crystal size for sintered (1100 °C) Mg-HA

HA Powder	Phase Present	Crystallinity (%)	Crystal Size (nm)
NS-HA	HA, β-TCP	88.8±4.6	73±4.1
Mg-HA 1%	HA, β-TCP,	83.2±7.8	68.5±4.6
Mg-HA 5%	HA, β-TCP, Whitlockite	64.8±10.2	49.3±5.4
Mg-HA 10%	HA, β-TCP, Whitlockite	63.5±4.31	43.6±4.31

A consistent shift to higher 2θ range was observed for the (0210) β-TCP plane with increasing Mg substitution. This shift is representative of a reduction in β-TCP lattice parameters. As explained earlier, the lattice contraction is due to the substitution of Ca^{2+} ions by the smaller Mg^{2+} ions.

Crystallinity and crystal size of Mg-HA

The XRD experimental data indicated that Mg could affect the crystallinity and crystal size of HA as reported in Figure 4.8. While there was a crystallized biphasic structure (β-TCP + HA) in the NS-HA samples, the peaks of HA and β-TCP became wider and their intensity reduced by introducing Mg ions, especially in the 2θ range between 28° to 32° and 45° to 55°. As

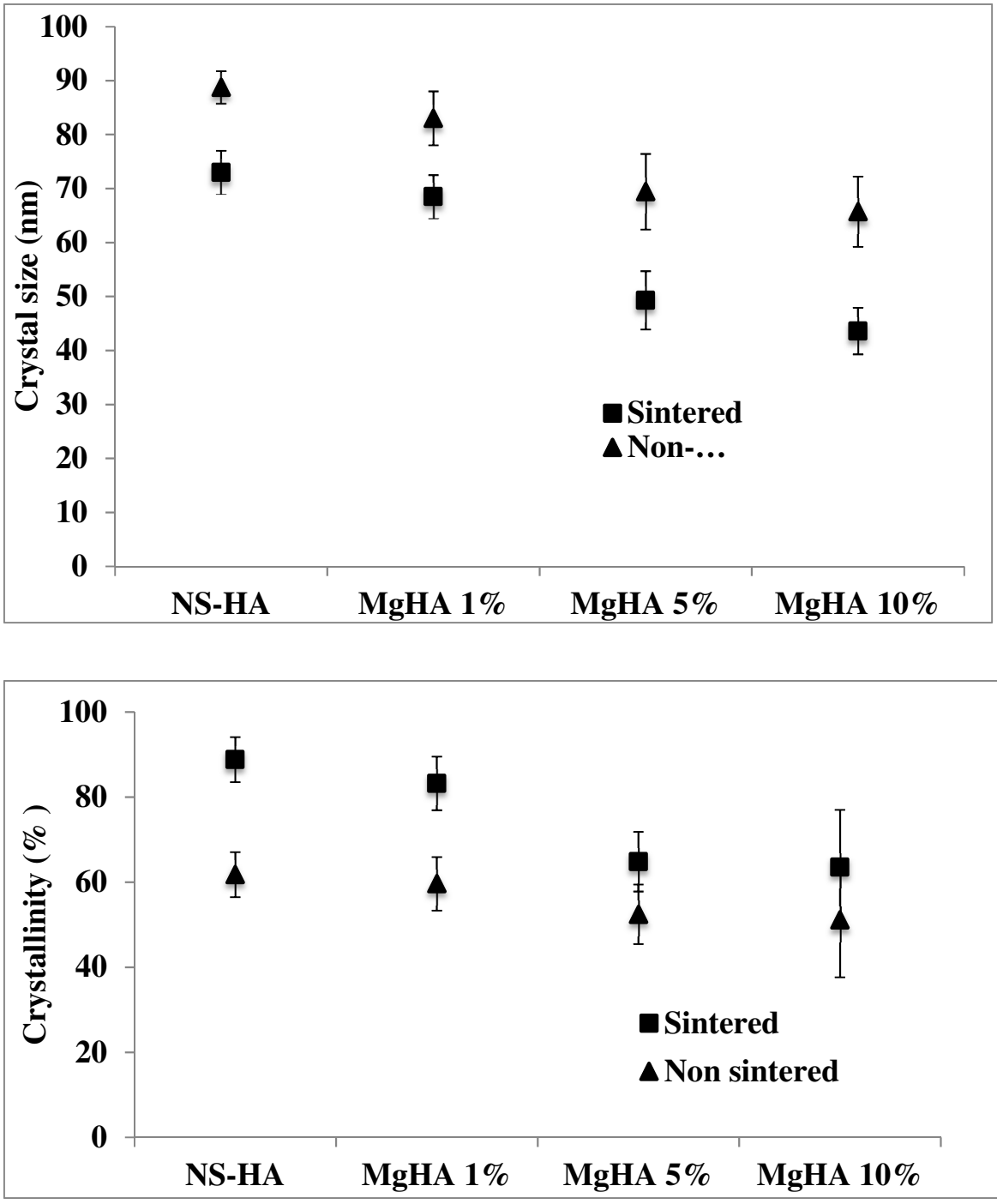

Figure 4. 8: Crystal size (top) and Degree of crystallinity (bottom) for magnesium substituted hydroxyapatites with different concentrations.

detailed earlier, the crystallinity degree was about 88.8% for NS-HA, and 83.2%, 64.8% and 63.5%, for Mg-HA 1 %, 5 %, and 10 %, respectively (all sintered samples). The results for the

degree of crystallinity and crystal size measurements of Mg-HA suggested that magnesium ions affected the crystal size by inhibiting the growth of the HA crystals (111).

Lattice parameters of Mg-HA

As shown in Figure 4.9, comparing the lattice parameter data obtained from Mg-HA samples with NS-HA indicated a decreasing trend in the values of *a* and *c*-axis parameter with the introduction of Mg^{2+} in both β-TCP and HA phases.

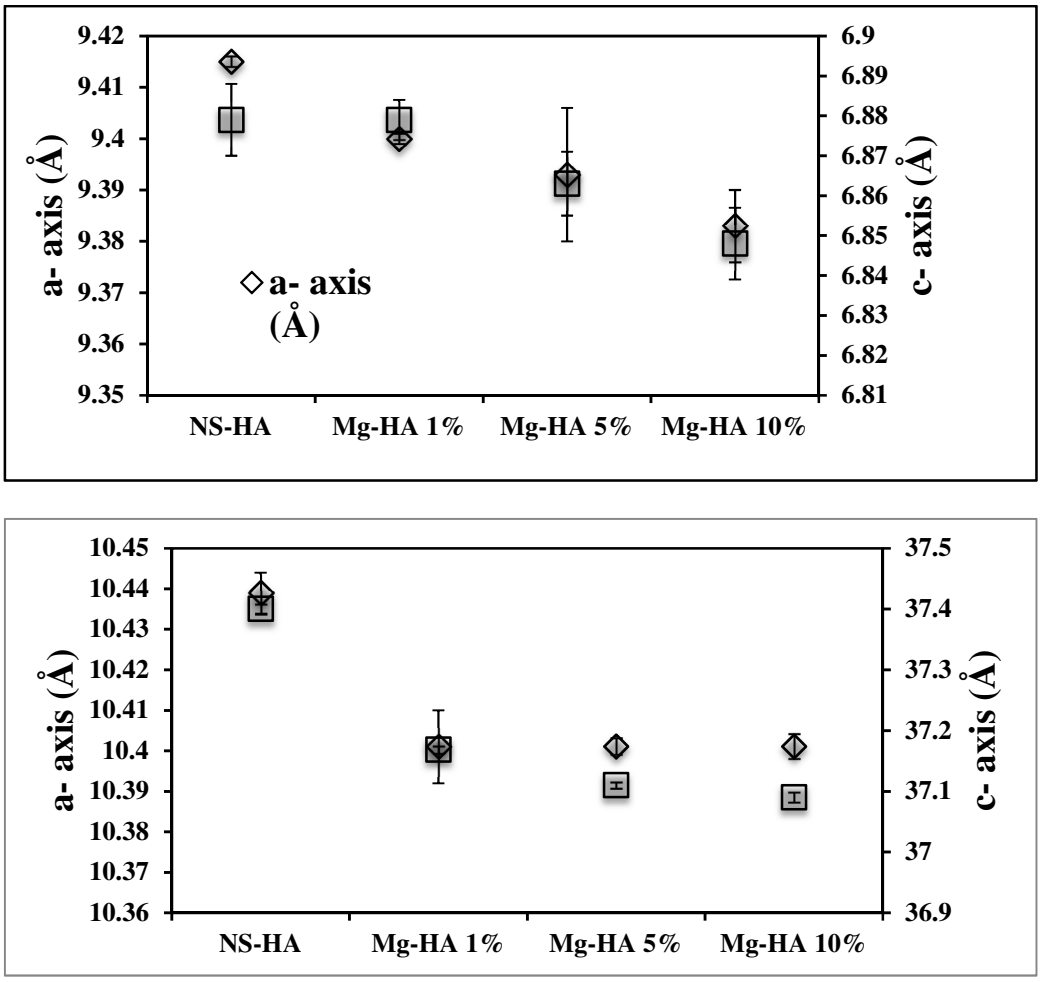

Figure 4. 9: Lattice parameters of HA crystal (top) and β-TCP crystal (bottom) in magnesium-substituted hydroxyapatites with different concentrations.

This suggested that there was a contraction of the cell volume after Mg^{2+} addition. The volume contraction was more pronounced in the case of the β-TCP phase, and therefore it might suggest higher concentration of Mg^{2+} in this phase. The reason for the observed contraction in both *a* and *c* axis could be explained by the substitution of the smaller ionic radii Mg^{2+} (0.072 nm) for Ca^{2+} ion (0.099 nm).

A comparison between the cell parameter values in samples with different Mg concentration indicated that at Mg 1 %, Whitlockite phase was not present suggesting that the majority of the Mg ions were accumulated in the HA phase. Another explanation could be that the range of Whitlockite was below the detectable range for XRD technique. As Mg concentration increased to (5 and 10 %), Whitlockite was detectable suggesting that Mg^{2+} ions were substituting Ca^{2+} ions in the β-TCP phase.

As described earlier, the *a* and *c*-axis parameter values decreased in the magnesium substituted HA phase for all Mg^{2+} ion concentrations. For the β-TCP phase, however, the *a* axis parameter decreased in the case of 1 % Mg but no further change was observed when more Mg^{2+} ions ware added. On the other hand, the *c*-axis parameter decreased in all magnesium substituted samples. This changing of the cell parameters may be due to the limited replacement capacity of Mg ions into the β-TCP crystal lattice.

4.1.4 X-ray diffraction analysis of Zinc-Substituted Hydroxyapatite (Zn-HA)

Phase Identification of Zn-HA

The XRD patterns of all zinc substituted hydroxyapatite (1%, 5% and 10 % Zn-HA) samples are shown in Figure 4.10 and Figure 4.11. The broad diffraction peaks in all Zn-HA samples suggest the formation of smaller apatite crystals than NS-HA. The peaks of β-TCP and HA

could be detected in Zn-HA 1% similar to NS-HA. However, HA and β-TCP peeks have been shifted to lower 2θ degree.

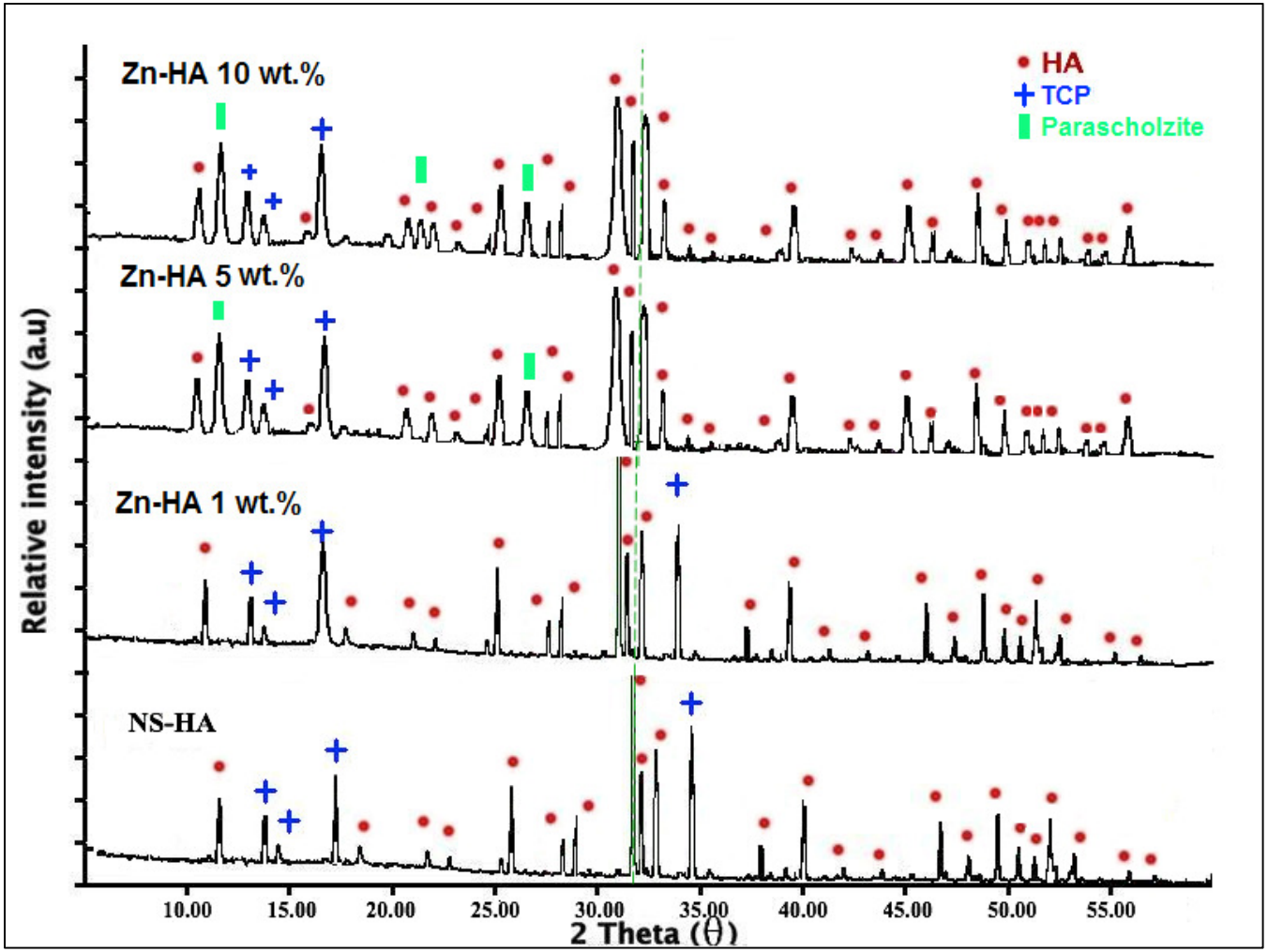

Figure 4. 10: The XRD diffraction patterns for sintered (1100 °C) zinc substituted hydroxyapatite with different Zn concentrations.

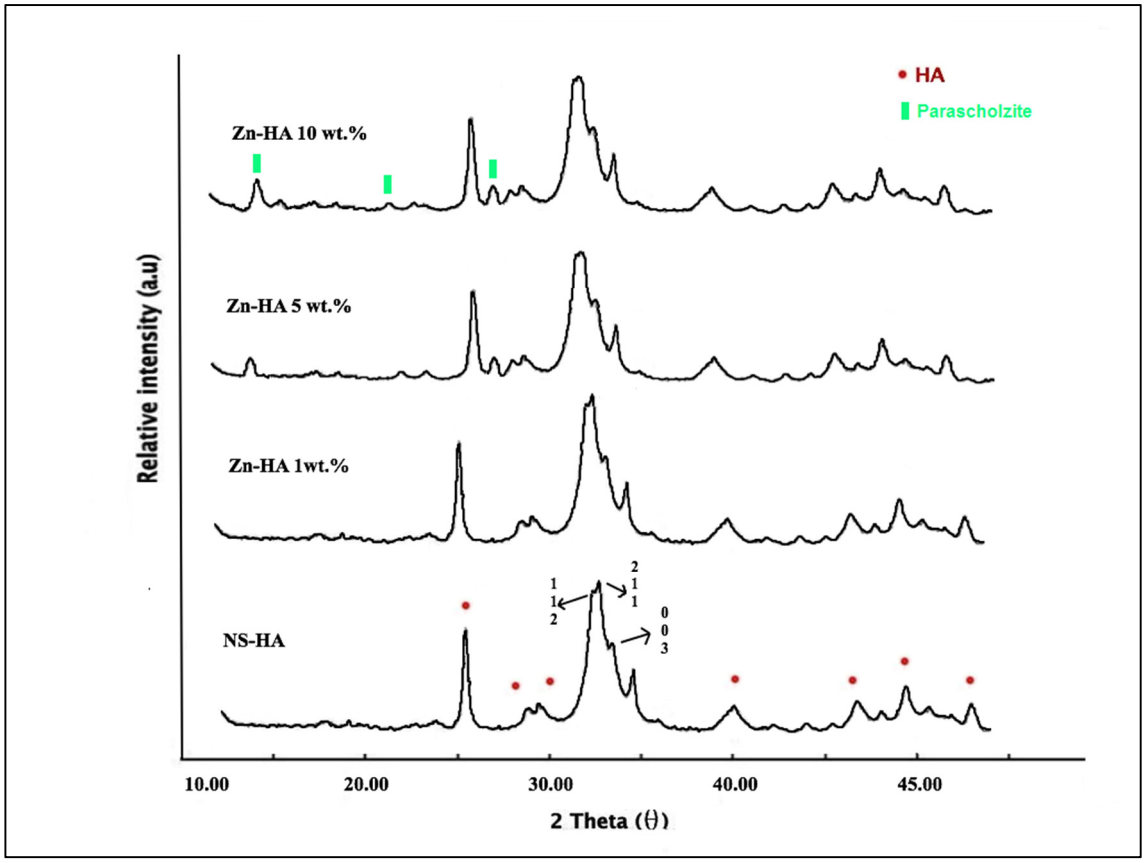

Figure 4. 11: XRD patterns for non-sintered zinc substituted hydroxyapatite with different Zn concentrations.

As shown in Figure 4.10 a new phase was identified at Zn concentration of 5 % associated with the presence of calcium zinc phosphate hydrate or Parascholzite. Parascholzite ($CaZn_2(PO_4)_2.2H_2O$) is a Zn-substituted TCP and its more pronounced in the case of Zn-HA 10% sample. More β-TCP phase at higher Zn concentrations suggested that more HA has been transformed to β-TCP in the form of Parascholizite at 1100 °C.

Table 4. 6: Present phases, crystallinity and crystal size for sintered (1100 °C) Zn-HA.

HA Powder	Phase Present	Crystallinity (%)	Crystal Size (nm)
NS-HA	HA, β-TCP	88.8±4.6	73±4.1
Zn-HA 1%	HA, β-TCP	85.12±8.6	72±4.9
Zn-HA 5%	HA, β-TCP, Parascholzite,	70.2±7.4	61.31±5.4
Zn-HA 10 %	HA, β-TCP, Parascholzite,	67.3±11.3	52.29±5.2

Crystallinity and crystal size of Zn-HA

As the XRD patterns in Figure 4.12 show, when Zn ions were added to hydroxyapatite, the patterns became broader suggesting that crystallinity and crystal size were decreased compared to NS-HA. The degree crystallinity was about 88.8% for NS-HA, and 85.12%, 70.2% and 67.3% for Zn-HA 1 %, 5 %, and 10 %, respectively (all sintered samples) (Table 4.6).

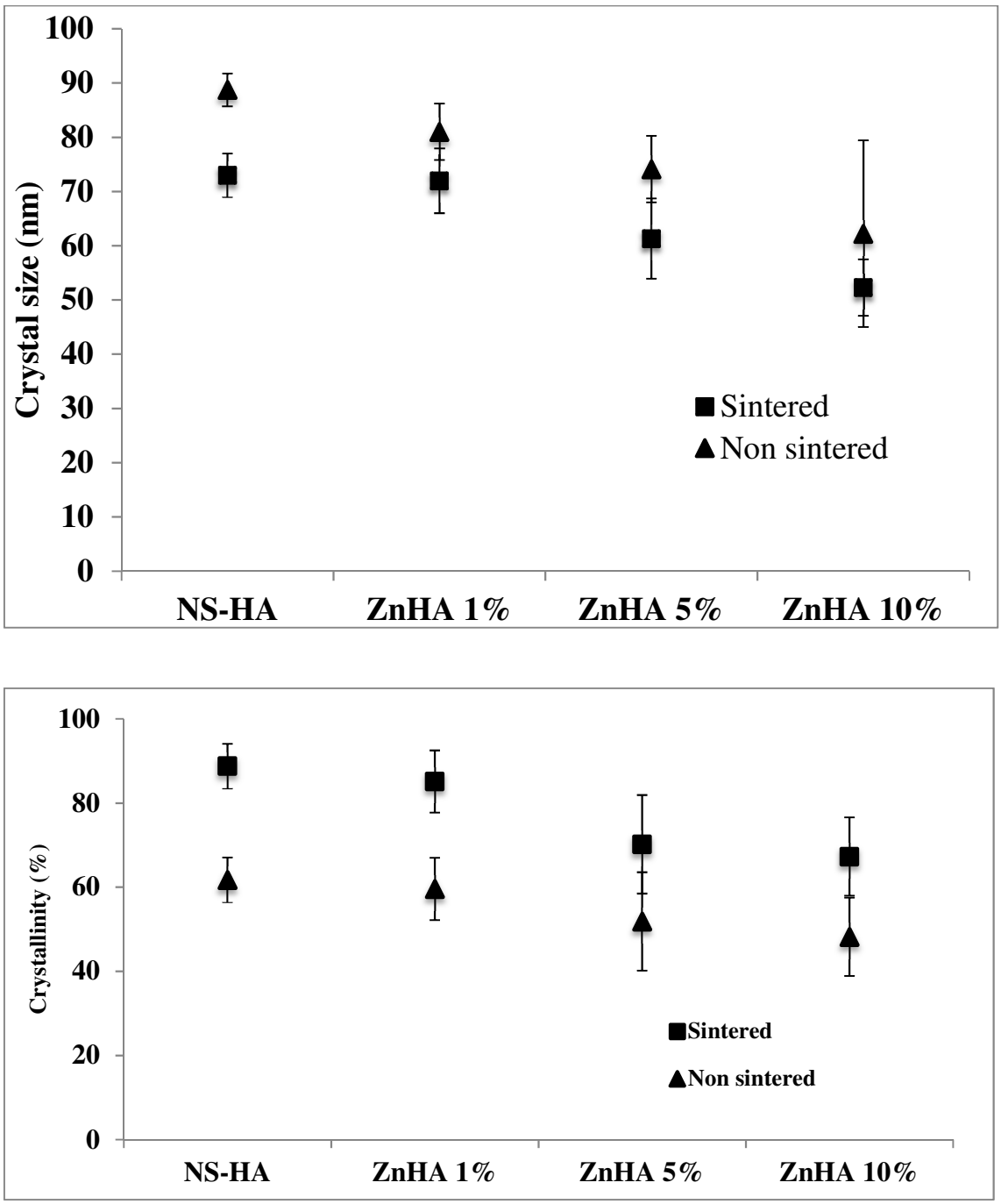

Figure 4. 12: Crystal size (top) and degree of crystallinity (bottom) for zinc-substituted hydroxyapatites with different concentrations.

The reduction in crystal size and crystallinity became more pronounced when Zn concentration increased from 5 and 10%. Similarly to magnesium substitution, results for

the degree of crystallinity and crystal size measurements of Zn-HA may indicate that zinc ions affected the crystal size by inhibiting the growth of the HA crystals.

Lattice parameters of Zn-HA

As Figure 4.13 which compares the lattice parameter data obtained from Zn-HA samples with NS-HA, indicates, there was decreasing trend in *a* and *c*-axis parameter values was observed with the introduction of Zn^{2+} in both β-TCP and HA phases.

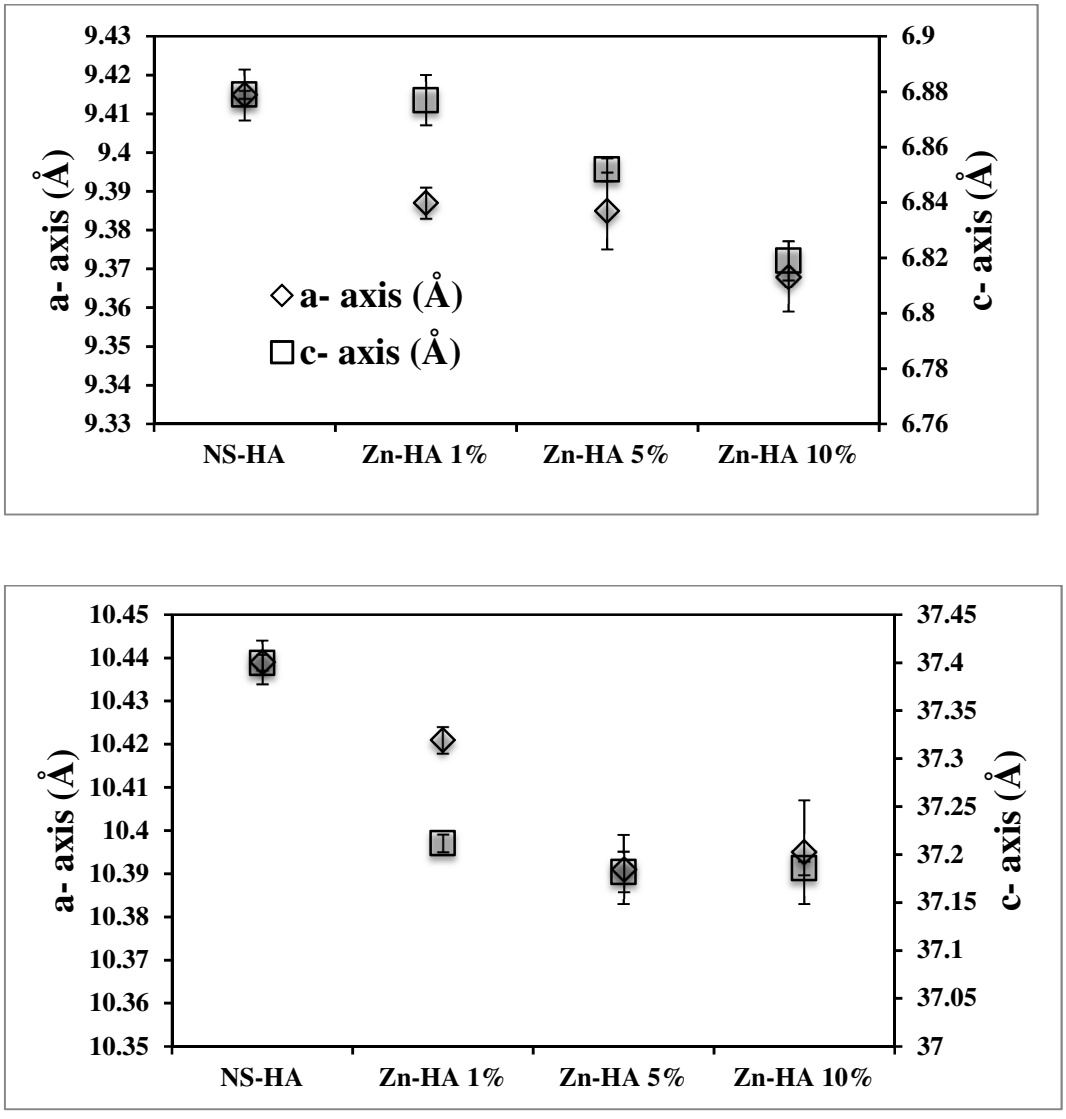

Figure 4. 13: Lattice parameters of HA crystal (top) and β-TCP crystal (bottom) in zinc-substituted hydroxyapatites with different concentrations.

Therefore, a contraction of calculated cell volumes was evident. A reason for this contraction in cell parameters can be the lower ionic radius of Zn^{2+} (0.0745 nm) when compared to Ca^{2+} ions (57, 186, 187).

4.2 Fourier transform infrared spectroscopy (FT-IR)

FT-IR is a versatile technique in analytical chemistry, which is based on the principles of molecular spectroscopy. This analytical tool detects the absorbance (or transmittance) of light energy, which is emitted on molecules at specific wavelengths (known as their resonance frequencies).

4.2.1 FT-IR for NS-HA

The FT-IR spectra for NS-HA samples are shown in Figure 4.14. The absorption band positions and their assignments are summarized in Table 4.7.

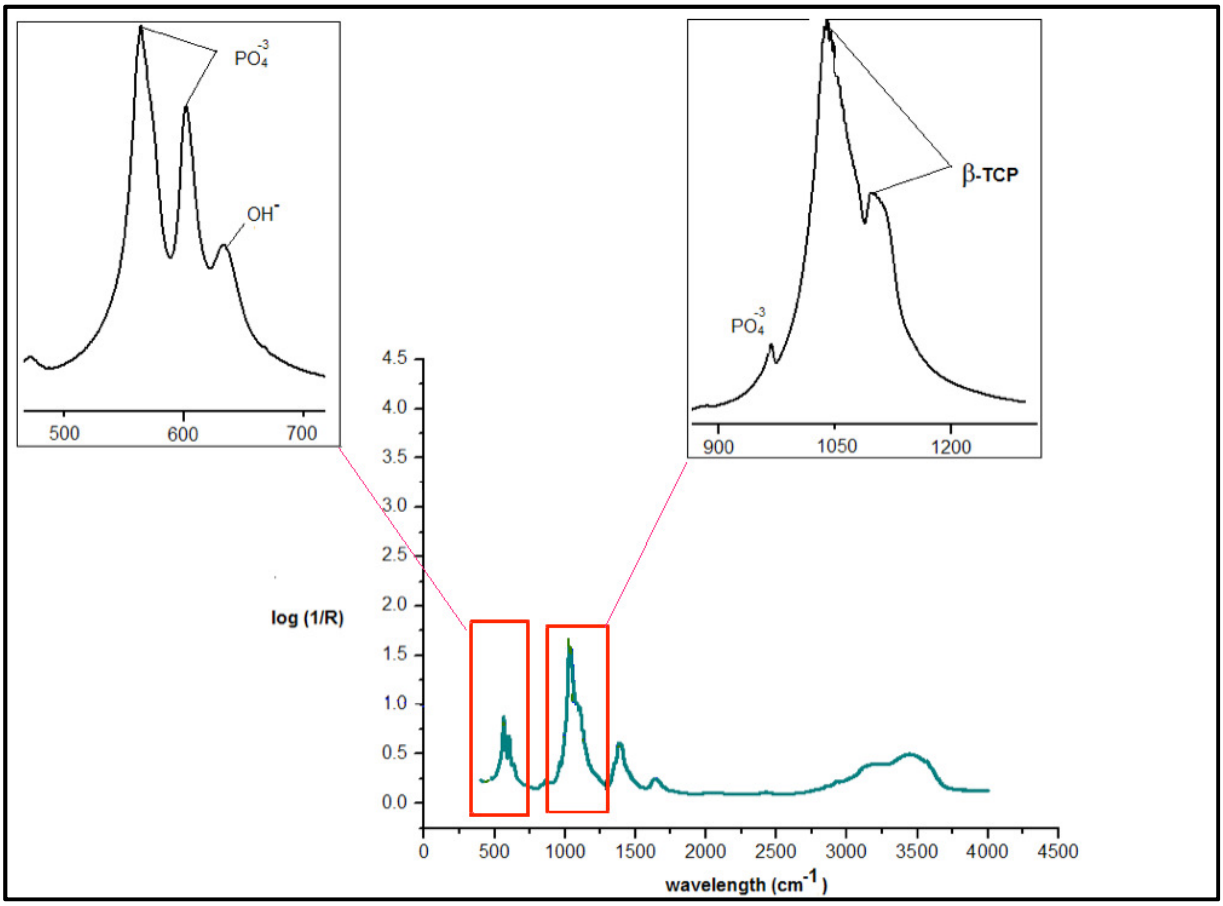

Figure 4. 14: FT-IR spectra of sintered Hydroxyapatite

As shown in Figure 4.14, the presence of apatite phase in the prepared powder can be proven by the presence of the fundamental vibrational modes of PO_4^{3-} group at 574, 609, 966 and 1020-1120 cm^{-1}. The bands at 630 and 3570 cm^{-1} are representative of OH^{1-} groups in the apatite phase and adsorbed water, respectively. The latter can be seen in the region around 3300-3600 cm^{-1} which is indicative of the "bound" water or hydration layer associated with HA crystals. It is known that this hydration layer contains high concentrations of calcium and phosphate ions (188).

While carbonate ions were not expected to be present in HA, a small peak of carbonate at 1430 cm^{-1} was formed due to the solubilisation of CO_2 in air in water and incorporation of resulting carbonate ions into the crystal lattice.

A small broad peak observed at 1422.6cm^{-1} is a characteristics peak for NH_4^+ groups and can be attributed to the ammonium residues which were still present in the sample after synthesis (189). There was no presence of nitrate ions indicated by the absence of characteristic peaks in the region between 1320 and 1480 cm^{-1}.

The studied experiments also confirmed that partially carbonated hydroxyapatites were formed. This was based on the observation of carbonate-specific bands in the range of 1460–1410 cm^{-1} and likely were incorporated from the carbonate groups present during the synthesis process.

Table 4. 7: Assignments of main bands observes in the Infrared absorption spectra of HA.

Peak (cm^{-1})	Assignment	References
3572	Stretching mode, ν_s, of hydroxyl groups OH^-	**(190), (191)**
2000	Harmonic overtone 2. ν_3 or combination band $\nu_1 + \nu_{3b}$	**(192), (193), (194)**
1630	Adsorbed water	**(195)**
1430	Stretching mode, ν_3, of B-type CO_3^{2-}	**(196)**
1087	Triply degenerated asymmetric stretching mode, ν_{3a}, of the P–O bond of phosphate groups PO_4^{3-}	**(197), (198)**
1046	Triply degenerated asymmetric stretching mode, ν_{3b}, of the P–O bond of phosphate groups PO_4^{3-}	**(193)**
1032 (shoulder)	Triply degenerated asymmetric stretching mode, ν_{3c}, of the P–O bond of phosphate groups PO_4^{3}	**(193), (194), (197)**
962	Non degenerated symmetric stretching mode, ν_1, of the P–O bonds in phosphate groups PO_4^{3-}	**(192), (193), (197), (198)**
880	Characteristic bending mode of A-type CO_3^{2-}	**(196)**
631	Librational mode, ν_L, of hydroxyl groups OH^-	**(199)**
602	Triply degenerated bending mode, ν_{4a}, of the O–P–O bonds in phosphate groups PO_4^{3-}	**(193), (194), (198)**
574 (shoulder)	Triply degenerated bending mode, ν_{4b}, of the O–P–O bonds in phosphate groups PO_4^{3-}	**(193), (194), (198)**
561	Triply degenerated bending mode, ν_{4c}, of the O–P–O bonds of the phosphate group	**(193), (194), (198)**
472	Double degenerated bending mode, ν_{2a}, of the O–P–O bonds in phosphate groups PO_4^{3-}	**(193), (198)**
462	Double degenerated bending mode, ν_{2b}, of the O–P–O bonds in phosphate groups PO_4^{3-}	**(193), (198)**
355 (shoulder)	Translational mode, ν_T, of hydroxyl groups OH^-	**(193)**
342 (shoulder)	Translational mode, ν_T, of hydroxyl groups OH^- (ν_3)	**(193), (199)**

4.2.2 FT-IR for Ag-HA

The FT-IR spectra of the silver (0 to 10%)-substituted hydroxyapatite samples are shown in Figure 4.15. The absorption band positions and their assignments are summarized in Table 4.7.

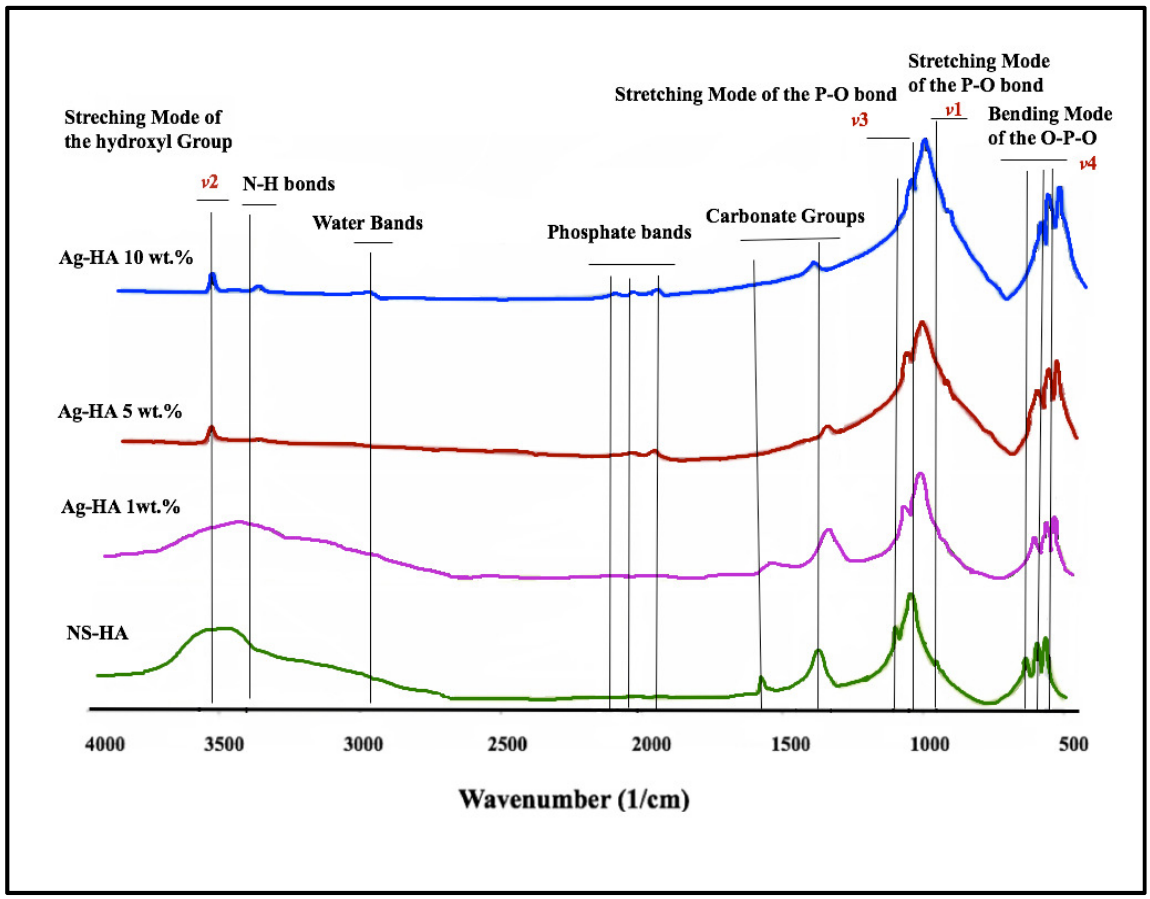

Figure 4. 15: FT-IR **Spectra of Silver Substituted Hydroxyapatite with different Ag ions concentrations.**

The characteristic HA peaks appeared in all apatite samples at 963, 1029, 1095 and 561-601 cm^{-1}(for PO_4^{-3}) and are in good agreement with previous studies (200, 201) (195). Similarly, characteristic OH^- peak at 3571 cm^{-1} was observed and was also in good

agreement with previous published work (200, 202, 203).The vibration band corresponding to the silver phosphate (bulk Ag_3PO_4 frequency 975 cm^{-1} and nano Ag_3PO_4 frequency 1017 cm^{-1}) which was reported by Thomas et al. (204) was not detected in the Ag-HA spectrum. However, the vibration around 1070 cm^{-1} was observed. The intense phosphate band of HA (1034 cm^{-1}) might be responsible for the obstruction of Ag_3PO_4 band.

The absorption bands at 873, 1300–1650 cm^{-1} of the Ag-HA are again attributed to the carbonate substitution in the HA lattice. In case of hydroxyl stretching band, they became more distinct at 3569 cm^{-1} in the Ag-HA 5% while the broad moisture peak was reduced significantly.

4.2.3 FT-IR for Mg-HA

Figure 4.16 shows the FT-IR spectra of HA samples with different Mg concentrations (1, 5 and 10 %).

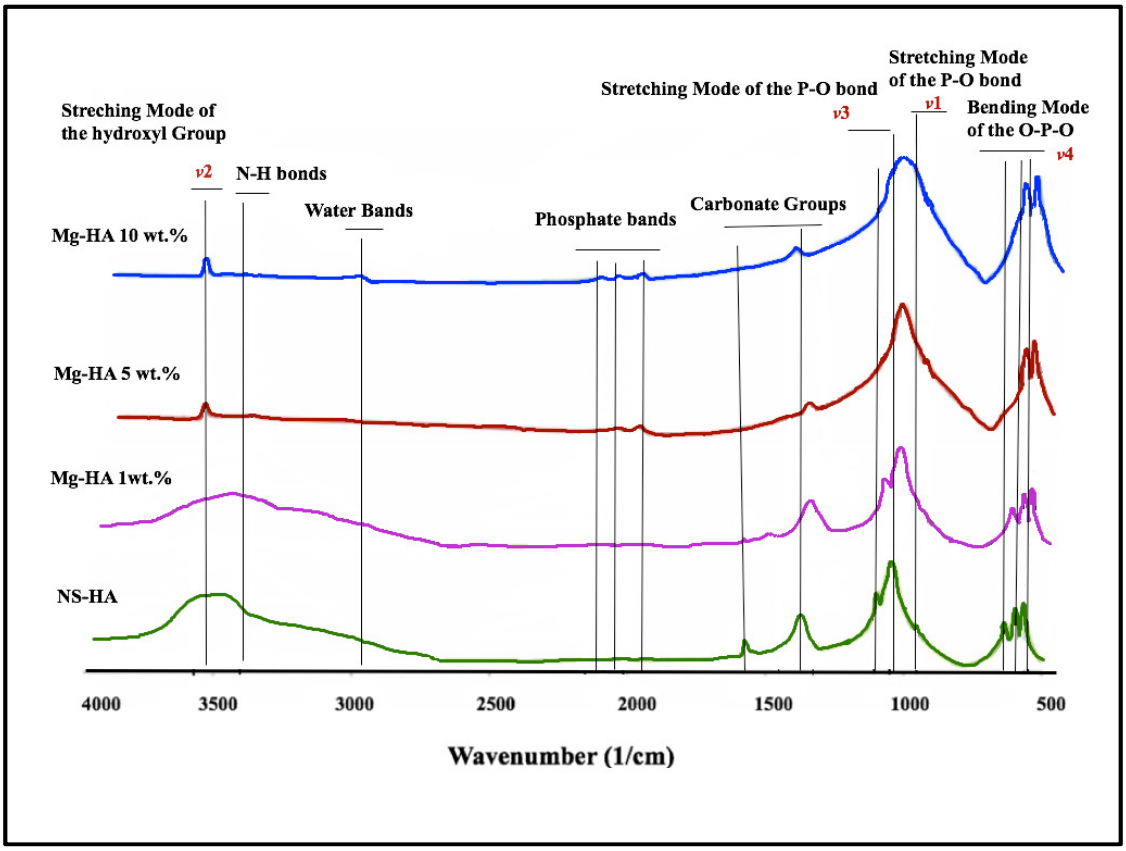

Figure 4. 16: FT-IR **Spectra of magnesium substituted Hydroxyapatite with different Mg ion concentrations.**

Introducing 1% Mg to HA, all the FT-IR absorption bands were present at similar positions to the ones in non-ion substituted HA. However, the bands associated with OH^- and N-H groups became broader. This indicates that Mg-HA 1 % substitution did not induce any significant changes in the apatite structure of HA. The same representative bands for PO_4^{-3} groups (574, 609, 966 and 1020–1120 cm^{-1}) and OH^- groups (around 3570 cm^{-1}) of apatite phase are still present in all the Mg-HA samples. Adsorbed water could also be identified in the same region (around 3300–3600 cm^{-1}) as well as carbonates (CO^{2-}_3) (around 1660 cm^{-1}), which is more pronounced in 5 and 10 % samples. Nitrates (NO^{1-}_3) were also present around 1320–1480 cm^{-1} resulting from the residual species in

the reaction (NO_3^{-1}, NH_4^{+}). Additionally, a peak at 1424 cm^{-1} can be attributed to CO_3^{-2} groups, which are common for the powders synthesised in the presence of air.

Increasing the Mg concentration to 5%, the FT-IR bands assigned to the four PO_4^{-3} modes appeared at similar wavenumbers as in HA. However, a reduction in the resolution at around 634 cm^{-1} can be assigned to OH^- liberation mode (83, 200, 203). In addition, the PO_4^{-3} peaks, which are present at around 1029 and 1059 cm^{-1} were, gradually merged into a broad peak centred at around 1062 cm^{-1}. These changes impled that the phase transformation from Mg substituted apatite to Mg substituted β-TCP (Whitlockite) was at its most when Mg content reached to 10 %.

At 10% Mg-HA, the FT-IR spectrum showed a similar pattern to that of 5 % sample but exhibited poorer resolution. In addition, the peak broadening was more significant when Mg concentration increased suggesting that the apatite structure was possibly distorted (114). The FT-IR spectra for samples with Mg substitution of 10% revealed a phosphate peak (range 1550–1450 cm^{-1}) that became broader with increasing magnesium content.

4.2.4 FT-IR for Zn-HA

Figure 4.17 shows the FT-IR spectra for the Zn substituted HA powder at different Zn concentrations.

Zn-HA samples at concentration of 1% showed a water broad peak, between 3155 and 3037 cm^{-1}, associated with water adsorption. No other significant changes were observed. It has also been reported that the CO_3^{-2} which is present in the region of 1570-1410 cm^{-1}(205) might have overlapped with the band in the region of 1575-1279 cm^{-1}, which was already ascribed to the presence of residual nitrates (206, 207), as described above.

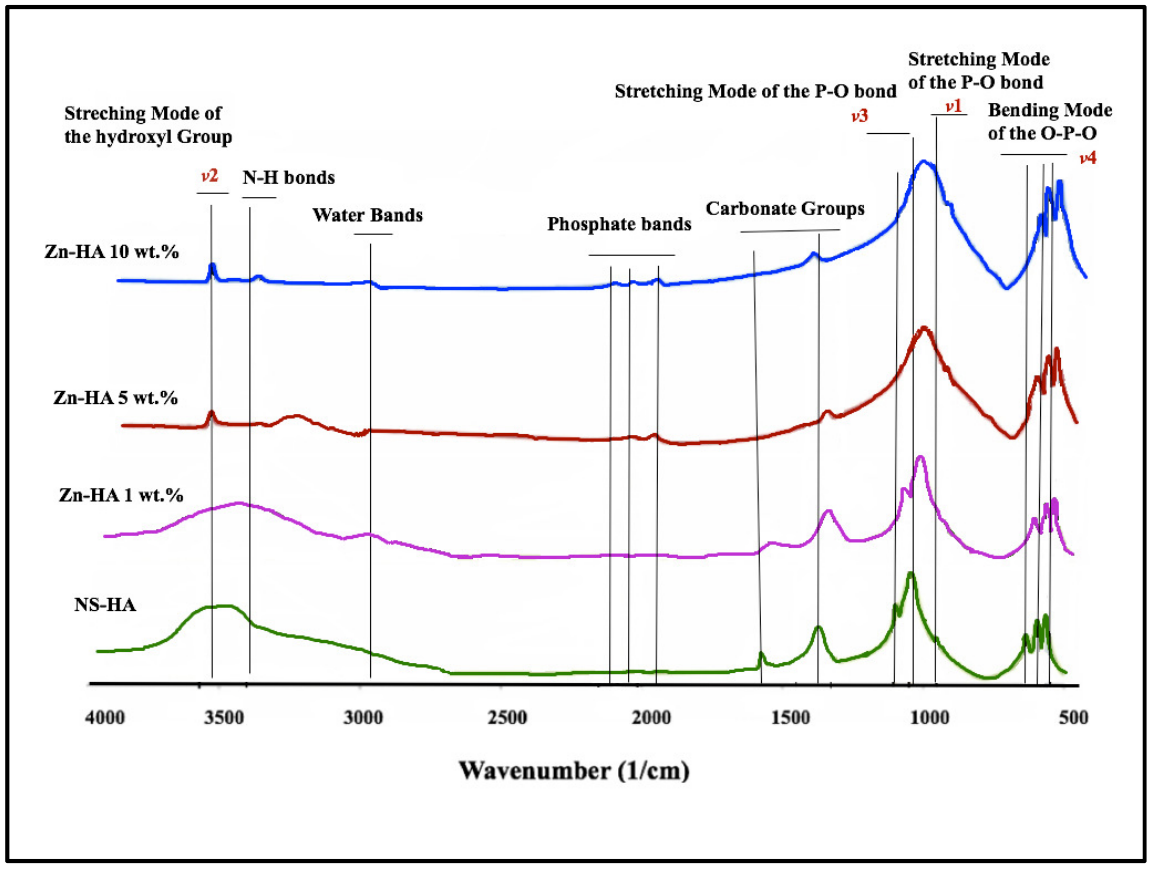

Figure 4. 17: FT-IR **spectra of zinc substituted hydroxyapatite with different Zn concentrations.**

By increasing Zn concentration from 1 to 5%, the PO_4^{-3} bending bands appeared at 562 and 600 cm^{-1} whilst the PO_4^{-3} stretching bands were centred at 1037 and 1089 cm^{-1}. The broad band between 3300 and 3700 cm^{-1} can be attributed to the presence of water molecules. Overlapping is possible in this region especially at 3571 cm^{-1} associated with the presence of OH^- groups. Also, carbonate CO_3^{-2} bands can be seen at 1414 and 1641 cm^{-1} similar to other prepared samples described earlier.

4.3 Raman spectroscopy

Complementary information can be obtained from FT-Raman spectroscopy. In addition to FT-IR, Raman analysis was also used to further explore the chemical structure of the prepared samples.

4.3.1 Raman analysis for NS-HA

Figure 4.18 shows the Raman spectra of sintered HA samples. The Raman peak positions and their assignments are summarized in Table 4.8.

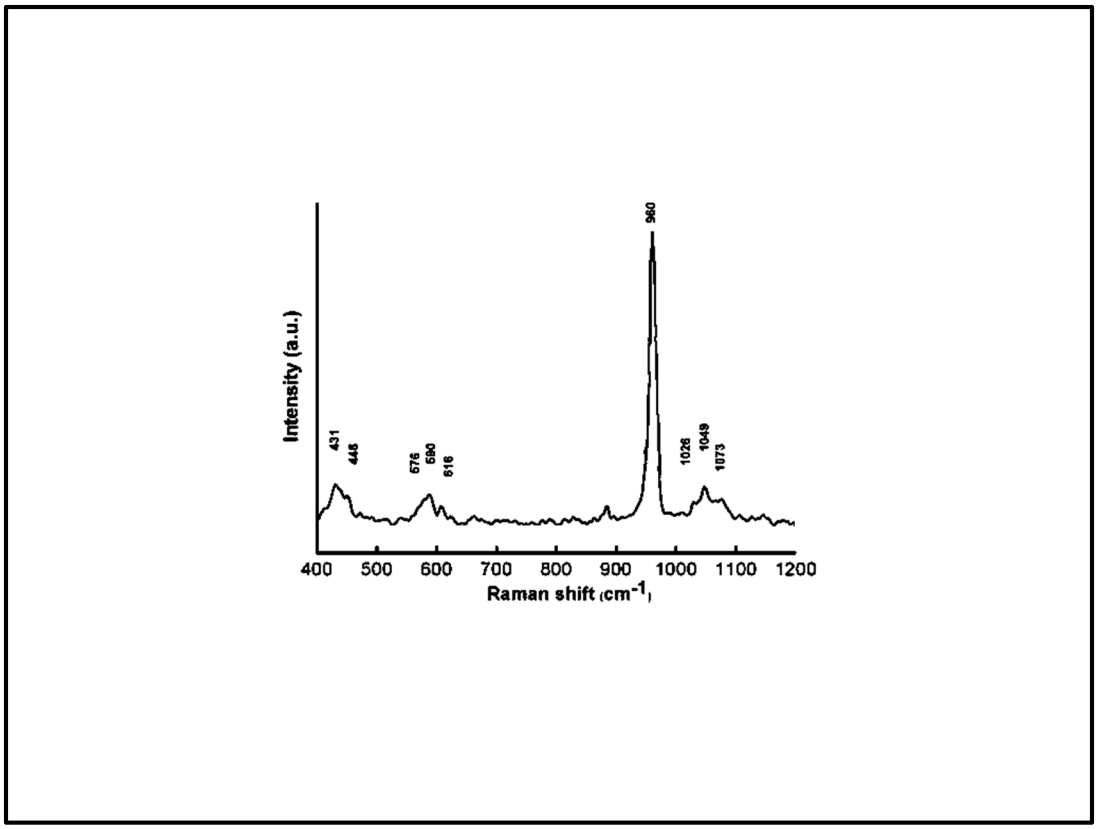

Figure 4. 18: Raman spectra of sintered NS- hydroxyapatite.

An intense peak was detected at around 960 cm^{-1} which can be assigned to $PO_4^{3-}(\nu_1)$ and is believed to be the characteristic peak of HA present in 963 and 961 cm^{-1} (208, 209).

Table 4. 8: Characteristic Raman peaks of HA observed in the Raman spectra and assignment.

Peak (cm^{-1})	Assignment	References
1076, 1054, 1046, 1030	Triply degenerated asymmetric stretching mode (ν_3) of the PO^{3-}_4 groups (P–O bond)	(210), (211), (212), (213)
961	Totally symmetric stretching mode (ν_1) of the tetrahedral PO^{3-}_4 groups (P−O bond)	(212, 214),(215)
620, 610, 594, 582	Triply degenerated bending mode (ν_4) of the PO^{3-}_4 group (O−P−O bond)	(211), (212),(215)
447, 433	Doubly degenerated bending mode (ν_2) of the PO^{3-}_4 group (O−P−O bond)	(210), (211), (212), (215)

The Raman spectrum clearly indicated that the peak with the highest intensity was associated with OH^- in HA. In addition, three other PO_4^{3-} modes were present in the regions of 447-430 cm^{-1} (PO_4^{3-}, v_2), 1076-1030-1048 and 1054 cm^{-1} (PO_4^{3-}, v_3), and 610-620-578 and 594 cm^{-1} (PO_4^{3-}, v_4).

The Raman peak at around 1076 cm^{-1} observed in all HA samples can be assigned to both PO_4^{3-} - v_3 mode (208, 209).

4.3.2 Raman analysis for Ag-HA

Figure 4.19 shows the Raman spectra of HA samples with different Ag concentrations (1,5 and 10 %).

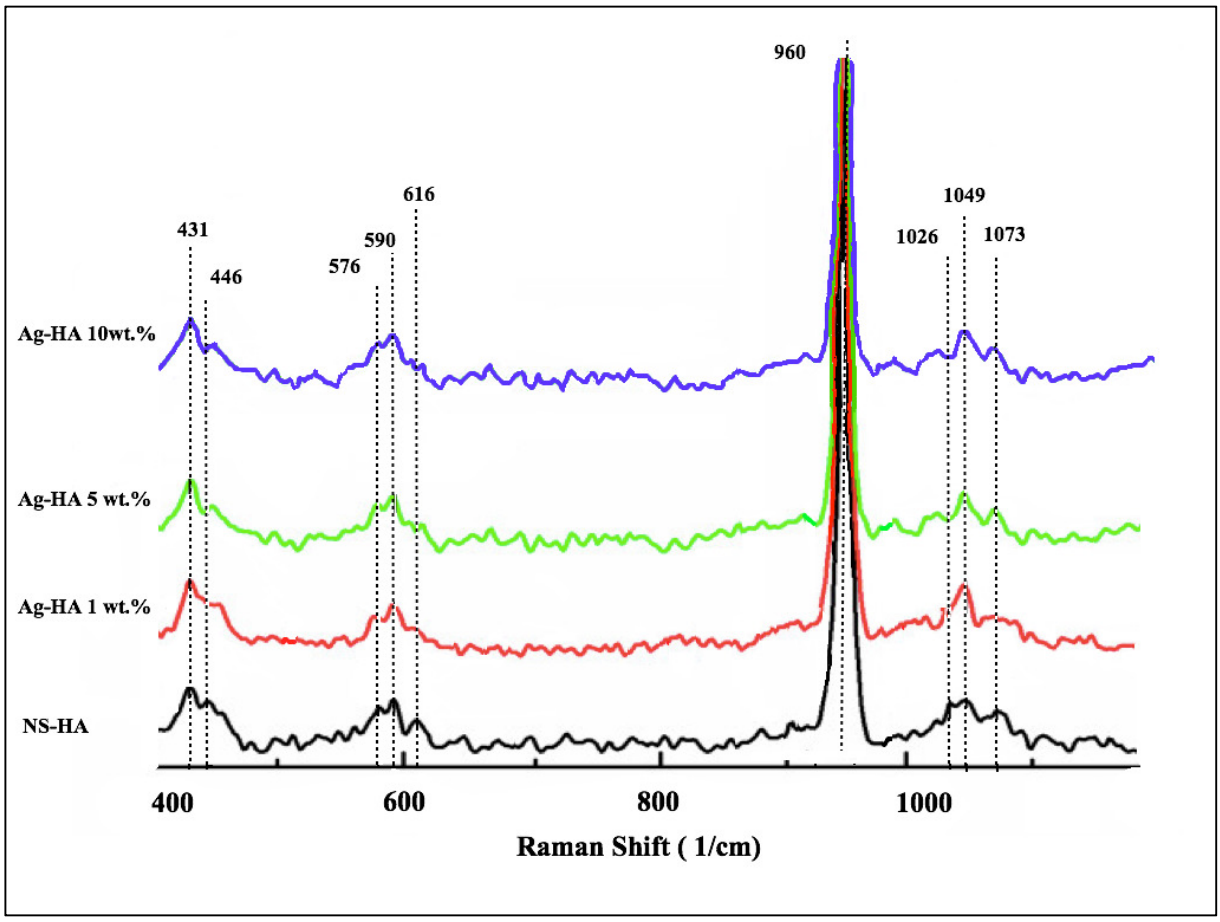

Figure 4. 19: Raman **spectra of silver substituted hydroxyapatite with different Ag ion concentrations**

Similar to the NS-HA sample, the symmetric stretching for P-O bonds (ν_1) was detected at (960 cm^{-1}). The vibrational bands at 429 cm^{-1} (ν_2) and 450 cm^{-1} (ν_2) were attributed to O-P-O bending modes. Both peaks at 1046 cm^{-1} (ν_3) and 1074 cm^{-1} (ν_3) were assigned to asymmetric ν_3 (P-O) stretching. As silver concentration increased to 5 %, the intensity of phosphate groups reduced.

It is worth noting, that pure metallic Ag is neither IR or Raman active and the formation of AgO and Ag_2O are not thermodynamically feasible up to the maximum sintering temperature of (1300°C) (216).

4.3.3 Raman analysis for Mg-HA

Figure 4.20 shows the Raman spectra of HA samples with different Mg concentrations (1, 5 and 10%). The Raman peak positions and their assignments are summarised in Table 4.9. The Raman spectra peaks in Mg-HA 1% sample were very similar to those observed in the NS-HA. Peaks at 1075 and 1046 cm^{-1} in the spectrum were believed to correspond to asymmetric stretching (ν_3) of the P–O bond in phosphate groups. The peak around 962 cm^{-1} corresponds to the symmetric stretching mode (ν_1) of the P–O bond in phosphate groups. This peak, however, is normally expected to be present at 961 cm^{-1} in hydroxyapatite (209). The small shift observed could be caused by the incorporation of the magnesium ions in the HA lattice.

Table 4. 9: Raman shifts observed and assignment for Mg-HA

Assignment	NS-HA		Mg-HA 1wt.%		Mg-HA 5wt.%		Mg-HA 10 wt.%	
	Peak (cm^{-1})	Ref	Peak(cm^{-1})	Ref	Peak (cm^{-1})	Ref	Peak(cm^{-1})	Ref
Triply degenerate asymmetric stretching mode (ν_3) of the PO_4 group (P–O bond)	1075(w),	(210),	1075(w),	(210),	1073(w),	(210),	1073(w),	(210),
		(211),	1046(m),	(211),	1046(m),	(211),	1046(m),	(211),
Totally symmetric stretching mode (ν 1) of the tetrahedral PO4 group (P–O bond)	958(vs)	(215)	962(vs),	(215)	971(vs)	(216)	971(vs)	(216)
Triply degenerate bending mode (ν 4) of the PO4 group (O–P–O bond)	610(w),	(211),	610(w),	(211),	612(w),59	(211),	612(w),	(211),
	587(m)	(215)	588(m)	(215)	1(m)	(215)	599(m)	(215)
Bending mode (ν 4) of the $HPO^{-2}{}_4$ group					555(w)	(212)	555(w)	(212)
P–O and O–P–O stretching and bending modes (ν 4) of the PO_4 group					633(w)	(215)	633(w)	(216)
Doubly degenerate bending mode (ν 2) of the PO4 group (O–P–O bond)	447(w),43	(210),	442(w),	(210),	442(w),	(210),	442(w),	(210),
	3(m)	(211)	432(m)	(211)	433(m)	(211)	433(m)	(211)

v: very, w: weak, m: medium, s: strong, Ref: references

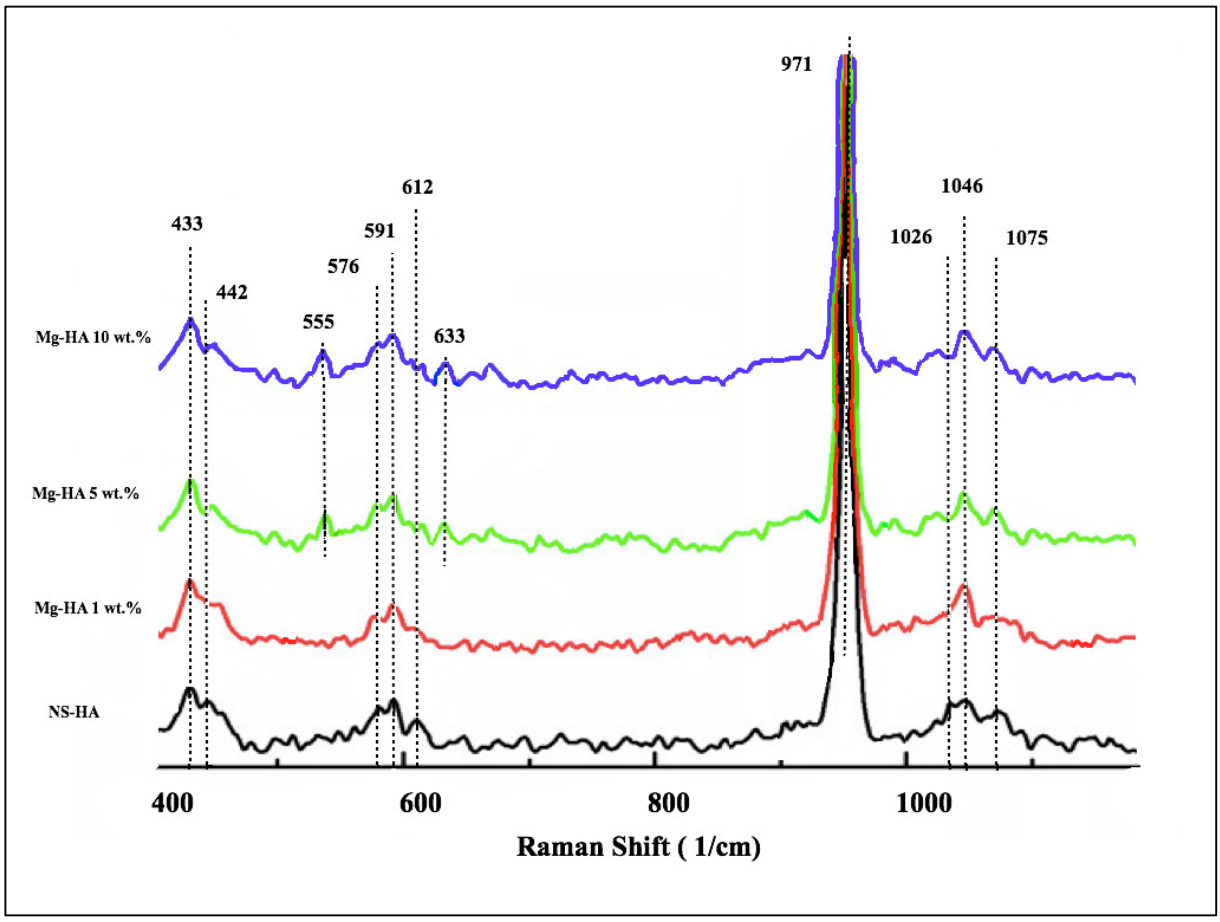

Figure 4. 20: Raman spectra for magnesium substituted hydroxyapatite with different Mg ion concentrations.

Peaks at around 610 cm^{-1} and 587 cm^{-1} correspond to the (ν_4). Peaks at around 442 cm^{-1} and 432 cm^{-1} correspond to the (ν_2) bending of the O–P–O linkage in phosphates in HA. The small shift observed in (ν_4) and (ν_3) in the spectra of Mg-HA 5 % and Mg-HA 10 %, which could be caused by the incorporation of the magnesium ions in the HA lattice and formation of TCP. Also Mg-HA 5% and Mg-HA 10 % samples each reveal a peak at 555 cm^{-1} and 633 cm^{-1} which

were associated with the bending modes of the O–P–O linkages in phosphates (e.g., Whitlockite).

4.3.4 Raman analysis for Zn-HA

Figure 4.21 shows the Raman spectra of HA samples with different Zn concentration (1, 5 and 10%). The Raman peak positions and their assignments are also summarized in Table 4.10

Similar to previous samples, the spectra for Zn-HA 1% were very similar to those observed for NS-HA. The asymmetric stretching peaks (ν_3) of the P–O bond in the phosphate group PO_4^{3-} were at 1076, 1055 and 1029 cm^{-1}. However, stretching peaks (ν_3) of P-O band of phosphate in 1030 cm^{-1} become more pronounced by adding Zn to the HA. The peak around 962 cm^{-1} was associated with the symmetric stretching mode (ν_1) of the P–O bond of the phosphate group PO_4^{3-}.

As discussed earlier, this peak is generally expected to be present at around 961 cm^{-1} in pure HA (209). Similarly, the shift could be due to the introduction of Zn into the HA lattice.

Peaks at around 610 cm^{-1} and 587 cm^{-1} correspond to the (ν_4). Peaks at around 447 cm^{-1} and 433 cm^{-1} correspond to the (ν_2) bending of the O–P–O linkages in phosphate in HA. The small shift observed in (ν_4) and (ν_3) in the spectra of Zn-HA 5 % and Zn-HA 10 %, which could be caused by the incorporation of the zinc ions in the HA lattice and formation of TCP. Also, Zn-HA 5 % and 10 % samples each reveal a peak at 555 cm^{-1}, which are corresponding to the bending modes of the O–P–O linkage in phosphate.

Table 4. 10: Raman shifts observed and assignment for Zn-HA

Assignment	NS-HA		Zn-HA 1wt.%		Zn-HA 5wt.%		Zn-HA 10 wt.%	
	Peak (cm^{-1})	**Ref**	**Peak (cm^{-1})**	**Ref**	**Peak (cm^{-1})**	**Ref**	**Peak (cm^{-1})**	**Ref**
Triply degenerate asymmetric stretching mode (ν_3) of the PO_4 group (P–O bond)	1075(w), 1046(m)	(211), (212)	1076(w), 1048(m), 1029(vw)	(211), (212), (213)	1077(w), 1046(m), 1030(vw)	(211), (212), (213)	1078(w), 1045(m), 1030(vw)	(211), (212), (213)
Totally symmetric stretching mode (ν 1) of the tetrahedral PO4 group (P–O bond)	958(vs)	(215)	962(vs)	(215)	970(vs)	(216)	971(vs)	(216)
Triply degenerate bending mode (ν 4) of the PO4 group (O–P–O bond)	610(w), 587(m)	(212), (216)	610(w), 588(m)	(212), (216)	611(w), 597(m)	(212), (216)	612(w), 599(m)	(212), (216)
Bending mode (ν 4) of the $HPO^{-2}{}_4$ group					555(w)	(213)	555(w)	(216)
Doubly degenerate bending mode (ν 2) of the PO4 group (O–P–O bond)	447(w),43 3(m)	(211), (212)	442(w), 433(m)	(211), (212)	440(w), 428(m)	(211), (212)	442(w), 433(m)	(211), (212)

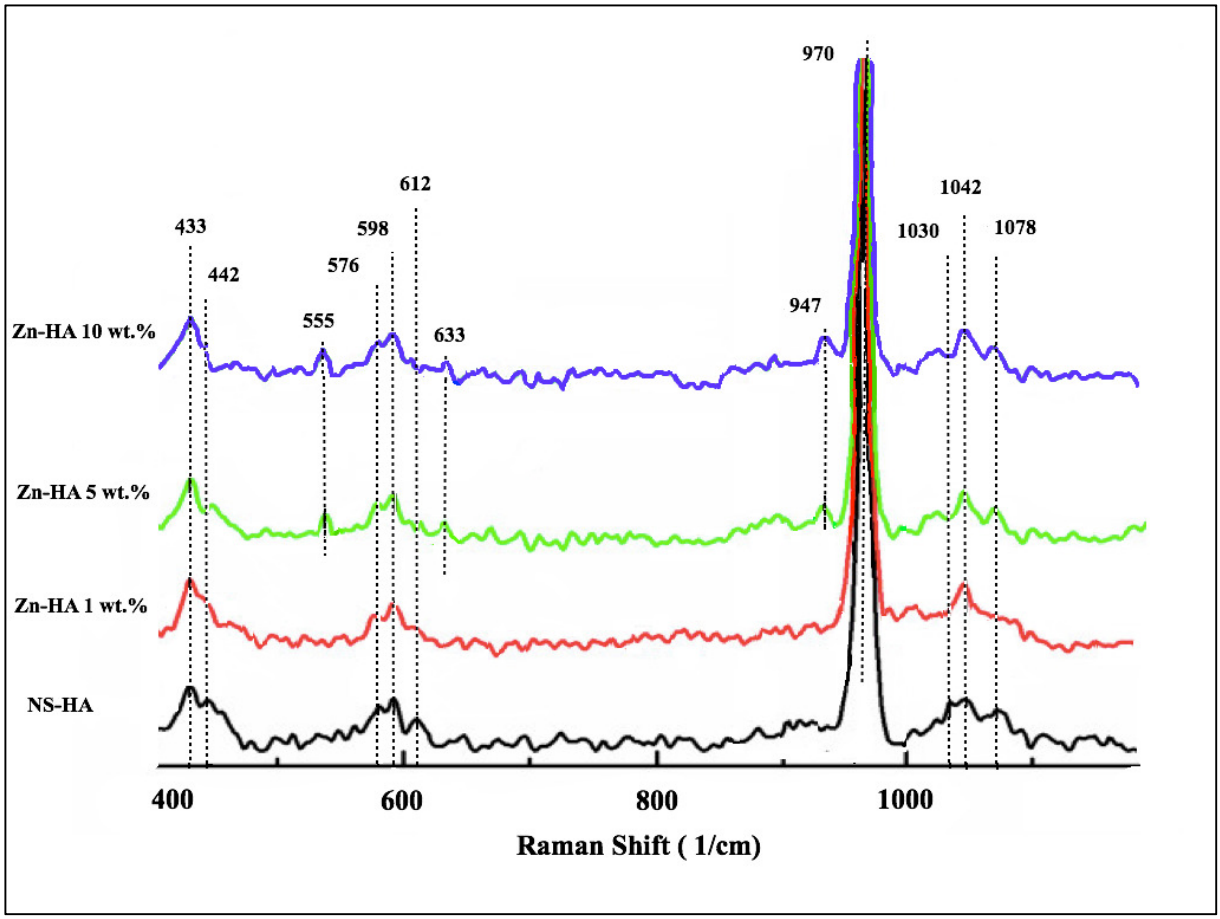

Figure 4. 21: Raman spectra of zinc substituted hydroxyapatite with different Zn ion concentrations.

4.4 Thermal Stability Analysis

This section provides information regarding the change in physical and chemical properties of apatite structure due to the sintering process at 1100 °C.

4.4.1 Thermogravimetric analysis of NS-HA

The thermogravimetric analysis (TGA) of the HA powder (NS-HA) was carried out between the room temperature and 1100°C (sintering temperature in this study) in order to understand the phase transformation within the sintered samples.

The TGA results for NS-HA sample are shown in Figure 4.22. The weight loss at the beginning of the TG plot from 25°C to 200°C corresponded to the removal of adsorbed water. At higher temperatures, the weight of NS-HA sample gradually decreased from 200 °C to 500 °C associated with the removal of water in the lattice. The weight loss trend continued (at a slower rate) from 500°C to 800°C and was associated to the transformation of HA to TCP.

The total weight loss was about 2.5 wt.% for NS-H sample. For comparison, a pure stoichiometric HA sample prepared by others show a weight loss of about 1.7 wt.% (217), and the difference is expected to be because of difference in both physical (initial adsorbed water) and chemical properties (different ratio of water in the HA structure) between the experiments.

4.4.2 Thermogravimetric analysis of Ag-HA

Figure 4.22 shows the TGA graph for the silver substituted hydroxyapatite with different concentrations (1, 5 and 10 %). Table 4.11, also shows all the weight loss data. The temperature where the weight loss peak (or slope change) appeared between 700-850 °C is a representation of how much the HA phase is stable. Similar to NS-HA samples, there are three stages of weight loss based on different temperature range. Up to 200 °C is the region where the adsorbed surface water is evaporated and normally the biggest weight loss can be observed. In case of Ag-HA sample, they all showed a sharp peak in this region.

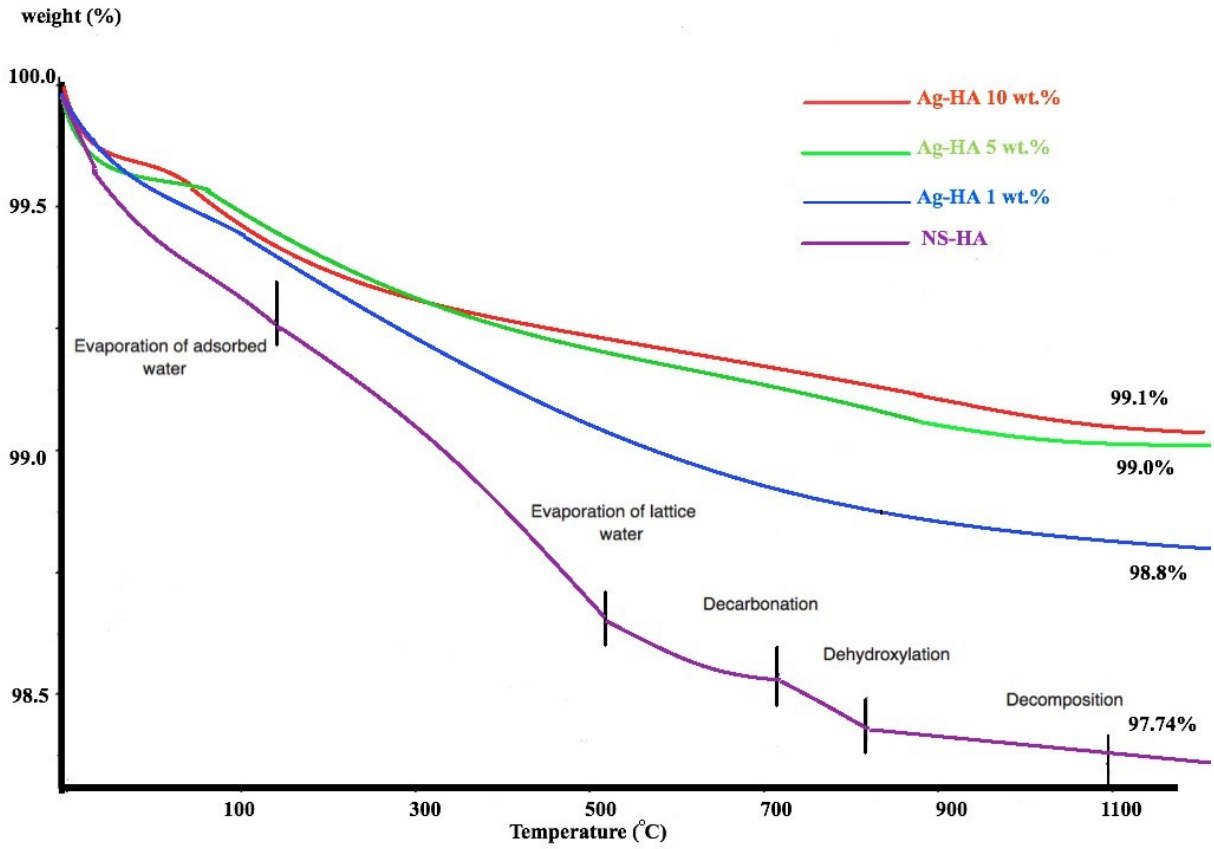

Figure 4. 22: TGA analysis of silver substituted hydroxyapatite with different Ag ion concentrations.

Table 4. 11 Weight loss for NS-HA and Ag ions substituted HA up to 1100 °C.

Sample	**Decomposition temperature (°C)**	**Total weight loss** (%)
NS-HA	688	2.5±1.4
Ag-HA 1 wt.%	Not determined	0.9± 0.1
Ag-HA 5 wt.%	Not determined	1±0.1
Ag-HA 10 wt.%	Not determined	1.2±0.2

The most prominent change indicates the stability of the sample is the weight loss between 600 and 1000°C. While it was difficult to measure and determine the decomposition temperatures from the results, based on the general profile of the curves, it was expected that the decomposition temperature are higher than NS-HA when Ag concentration increased. The total weight loss for the Ag substituted HA in the range of 25–1100 °C was about 7.9 wt.%. As expected, the residual weight slightly increased with the addition of Ag in the HA sample, as shown in Figure 4.22

4.4.3 Thermogravimetric analysis of Mg-HA

Figure 4.23 shows the TGA graph for the magnesium substituted hydroxyapatite with different concentrations (1, 5,10 %). Table 4.12 also shows all the weight loss data.

Table 4. 12: Weight loss for NS-HA and Mg ions substituted HA up to 1100 °C.

Sample	**Decomposition temperature (°C)**	**Total weight loss** (%)
NS-HA	688	2.5±1.4
Mg-HA 1 wt.%	750-810	7.3±2.9
Mg-HA 5 wt.%	735-798	10.5±3.0
Mg-HA 10 wt.%	720-791	11.4±4.1

A significant weight loss was observed for all magnesium substituted hydroxyapatite samples. In the temperature range between 25 and 400 ºC the weight loss is similar to NS-HA for all samples

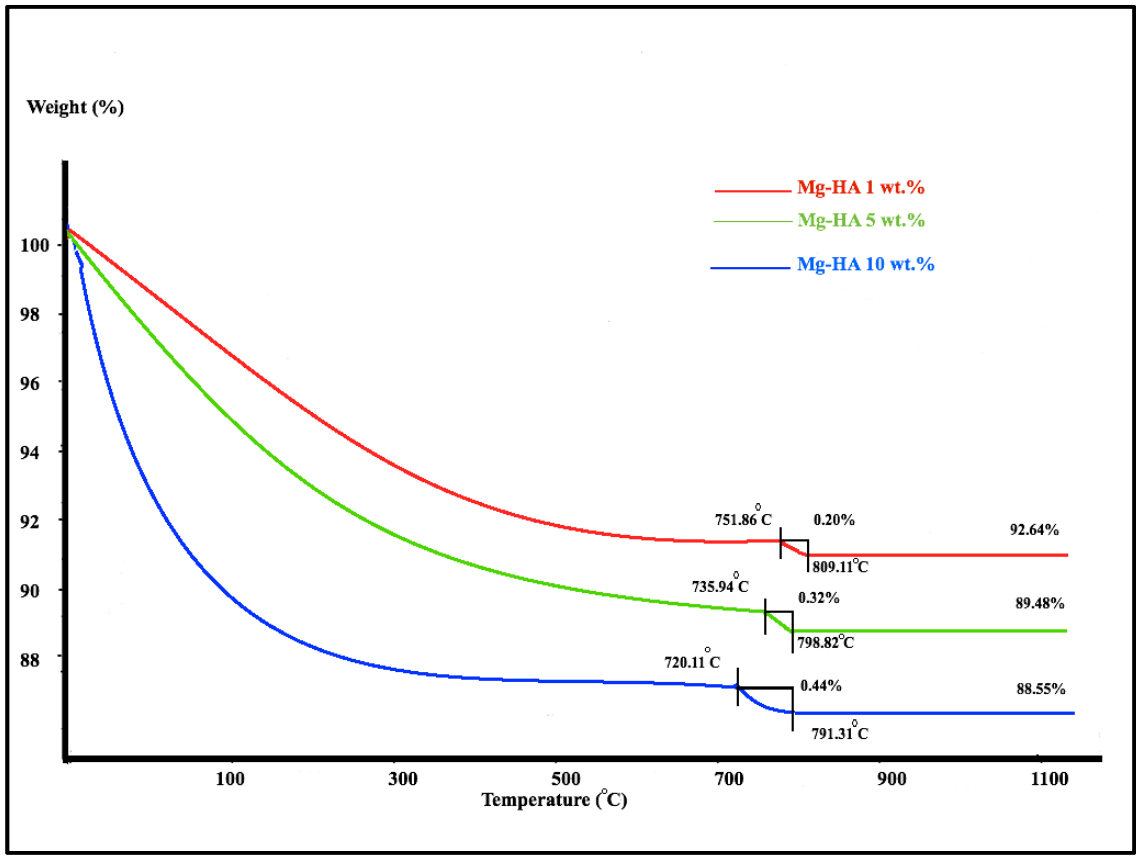

Figure 4. 23 : TGA analysis for magnesium substituted hydroxyapatite with different Mg ion concentrations.

The weight loss near the 690–800°C region was probably due to the loss of OH during the decomposition of HA to β-TCP. A decrease in the decomposition temperature with Mg content was indicated in the TG curves.

The total weight loss increased with increasing Mg concentration. Mg-HA 10 wt.% showed the highest weight loss 11.4%±4.1%. Three different thermal profiles for Mg-HA were observed.

The Mg-HA with 5% showed a sudden weight loss between 735.3°C to 798. 4°C which might indicate the decomposition into whitlockite (total weight loss about 10.5% ±3.00%). On the other hand, the Mg-HA sample with 10 % showed a weight loss at 720°C. As a conclusion, the thermal stability of Mg-substituted hydroxyapatite decreased by increasing the content of Mg into hydroxyapatite products and also Mg-HA partially transformed to Mg-substituted β-TCP or whitlockite.

4.4.4 Thermogravimetric analysis of Zn-HA

Figure 4.24 shows the TGA graph for the zinc substituted hydroxyapatite with different concentrations (1, 5 and 10 %). Table 4.13 shows all the weight loss data.

Table 4. 13: Weight loss for NS-HA and Zn ions substituted HA up to 1100 °C.

Sample	**Decomposition temperature (°C)**	**Total weight loss** (%)
NS-HA	688	2.5±1.4
Zn-HA 1wt.%	790-830	6.7± 0.5
Zn-HA 5wt.%	740-810	9.3±2.3
Zn-HA 10wt.%	735-790	10.5±4.9

There was a continuous weight loss of the samples with increasing the temperature. Again, the early weight loss between 25°C to 200°C was attributed to the adsorbed and bound (lattice) water while at higher temperatures, the weight loss was mainly due to the dehydroxylation of

hydroxyapatite (about 400 °C to 800°C) (218). The weight loss increased as the amount of zinc in the samples increased which might be linked to the formation of phases that include zinc or removal of a volatile species of zinc. As expected, the decomposition starting temperature at this concentration is about 790°C, which is very similar to NS-HA. However by increasing the Zn concentration, the decomposition temperatures drops to about 740 °C suggesting its lower thermal stability. The TG profile for different Zn concentrations showed, that the weight loss was more significant in samples with higher Zn concentrations (total weigh loss about 10.5% ±4.9). The amounts of both the adsorbed and lattice water increased with increasing Zn substitution. For the samples with higher Zn concentration, the effect of increasing lattice water might overcome that of the substitution by Zn with smaller ionic radius (132).

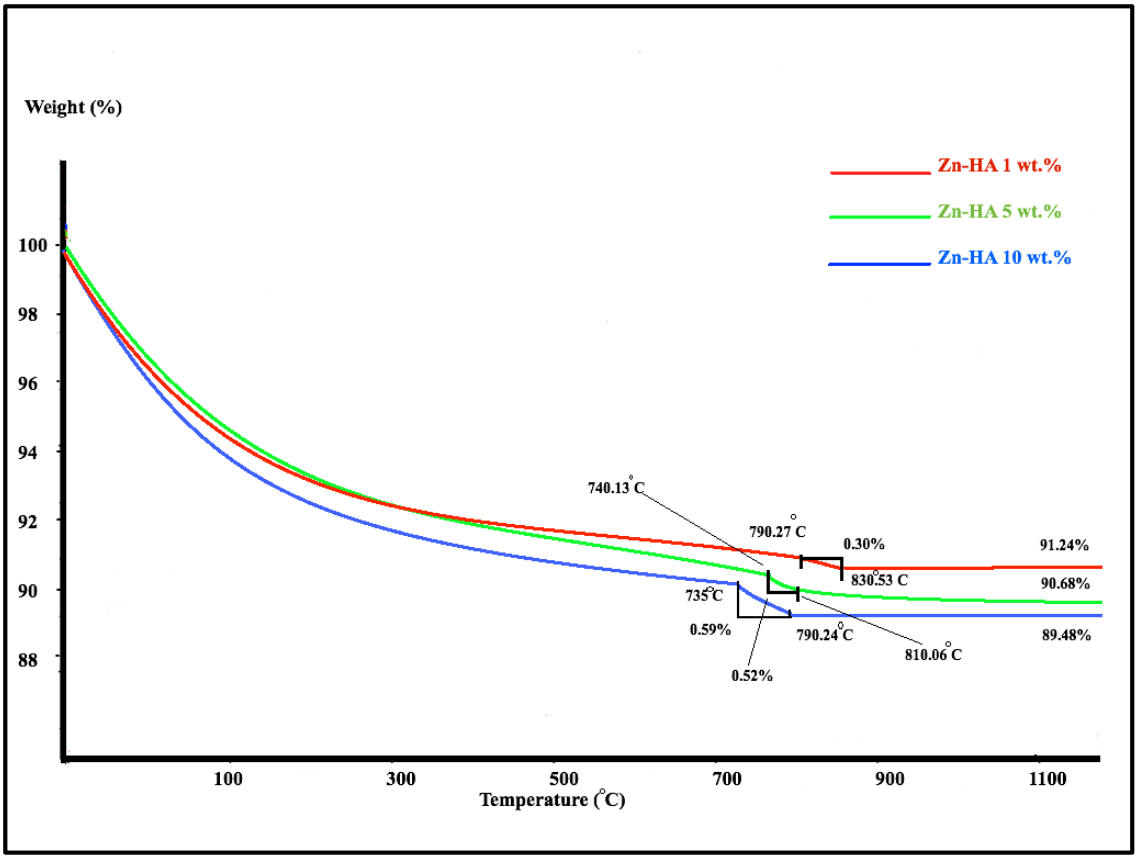

Figure 4. 24: TGA analysis of Zinc substituted hydroxyapatite with different Zn ions concentrations

4.5 ICP-MS Analysis

Analytical techniques such as XRD and FT-IR can only be used to obtain qualitative measurements and to confirm the inclusion of ions in the solid apatite structure. These techniques cannot give quantifying information about the degree of substitution in substituted apatite. Hence, Inductively Coupled Plasma-Mass Spectroscopy (ICP-MS) and X-Ray Fluorescence (XRF) methods were selected as two powerful tools to measure the substitution levels in the solid hydroxyapatite samples.

ICP-MS in particular can provide accurate measurement of ion concentration in the liquid phase, while it can also be used to indirectly determine the remaining ions in the solid phase knowing the initial concentration of ions in the starting reaction medium.

For all measurements, 3 samples for each case were used and each measurement was repeated 3 times using the ICP-MS machine. An average value was calculated and is presented here together with the standard deviation.

In order to find out the degree of substitution in the solid substituted hydroxyapatite samples ($I_{x,\ substituted}$), the mass balance equation below was used: (Equation 1).

$$I_{x,\ substituted} = I_{x,\ substrate} - (I_{x,\ sup\text{-}1} + I_{x,\ sup\text{-}2} + I_{x,\ sup\text{-}3}) \qquad Eq.\ 3.1$$

Where $\boldsymbol{I_{x,\ substrate}}$ is the concentration of ions present in the initial reaction solution, $I_{x,\ sup\text{-}1}$ is the concentration of residual ions in the first supernatant of the centrifugation step, $I_{x,\ sup\text{-}2}$ is the

concentration of the residual ions after the first wash and $I_{x,\ sup\text{-}3}$ is the concentration of residual ions after the second wash.

It was assumed, that the subsequent washing steps will remove any non-substituted or physically adsorbed ions, hence the difference will be the amount of substituted ions. As discussed in Section 3.2 (Materials and Methods), each measurement was performed using 10 ml samples taken from each step. The actual weigh of the available ions in each sample of Ag-HA, Mg-HA and Zn-HA was obtained and listed in Table 4. 15 and 4.16 respectively.

Table 4. 14: Ag ions concentration in silver substituted hydroxyapatite samples

Sample	Ag-HA 1%	Ag-HA 5%	Ag-HA 10%
$I_{x,\ substrate}$ (mg)	71.2	355.9	711.9
Ag not substituted (mg) ($I_{x,\ sup\text{-}1}$+ $I_{x,\ sup\text{-}2}$ + $I_{x,\ sup\text{-}3}$)	16.6	160.8	506.3
% of Ag which substituted in HA	76.6	54.8	28.9
wt. % of Ag in the final powder	0.99	3.4	3.6

Table 4. 15 Mg ions concentration in magnesium substituted hydroxyapatite samples.

Sample	Mg-HA 1%	Mg-HA 5%	Mg-HA 10%
$I_{x,\ substrate}$ (mg)	48.1	240.6	481.3
Mg not substituted (mg) ($I_{x,\ sup\text{-}1}$+ $I_{x,\ sup\text{-}2}$ + $I_{x,\ sup\text{-}3}$)	4.0	8.6	91.5
% of Mg which substituted in HA	91.7	96.4	81.0
wt. % of Mg in the final powder	0.3	1.7	2.19

Table 4. 16 Zn ions concentration in magnesium substituted hydroxyapatite samples.

Sample	Zn-HA 1%	Zn-HA 5%	Zn-HA 10%
$I_{x,\ substrate}$ (mg)	129.8	653.4	1309
Zn not substituted (mg) ($I_{x,\ sup\text{-}1}$+ $I_{x,\ sup\text{-}2}$ + $I_{x,\ sup\text{-}3}$)	15	24.5	119.2
% of Zn which substituted in HA	88.4	96.2	90.9
wt. % of Zn in the final powder	1.7	3.4	5.3

As discussed in the Materials and Methods section, the ion percentage used to differentiate each sample indicates the ion molar ratio of the selected ion to Ca, while the obtained values from the ICP-MS analysis shows the actual weight (and its ratio to the total weight of the powder) for each sample.

In the case of Ag-HA, the weight percentage of Ag ions in the 1% Ag-HA was almost 1 wt.%, for Ag-HA 5% it increased to 3.4 wt.% and for Ag-HA 10% it was 3.6 wt. %. In case of Mg-HA, the weight percentage of the Mg ion in the 1% Mg-HA was almost 0.28 wt.%, for Mg-HA 5% increased to 1.66 wt.% and for Mg-HA 10% was 2.2 wt. %. For Zn-HA, the weight percentage of the Zn ion in the 1% Zn-HA is almost 1.7 wt.%, for Zn-HA 5% that increases to 3.4 wt.% and for Zn-HA 10% that increases to 5.3 wt. %.

4.5.1 Release profile of substituted metal ions

ICP-MS analysis was also used to measure the amount of released ions from the disks placed in a liquid medium (PBS solution). The purpose of this study was to measure how much of the ions diffuse and solubilise in the liquid medium to almost resemble their release behaviour in

biological studies and human body. PBS buffer solution has a similar pH to human body =7.2 and the specimen was kept stationary (no stirring) to avoid any force mass transfer and dissolution of the samples. Stationary conditions also ensured the solid structure of the samples remained intact and were not disrupted through manipulation.

Release profile data are presented in two sections; a) Concentration (ppm) of the ion in the solution at each time interval b) Concentration (%) of the ion released as a ratio of the total ion available in the solid sample (disk). The total amount of ions was calculated based on the results presented in section 3.5.1.

Silver release profile from Ag-HA

Figure 4.25, shows the amount of released Ag ion (ppm and percentage of total Ag available in the solid) from Ag-HA samples after being submerged in PBS solution for up to 21 days.

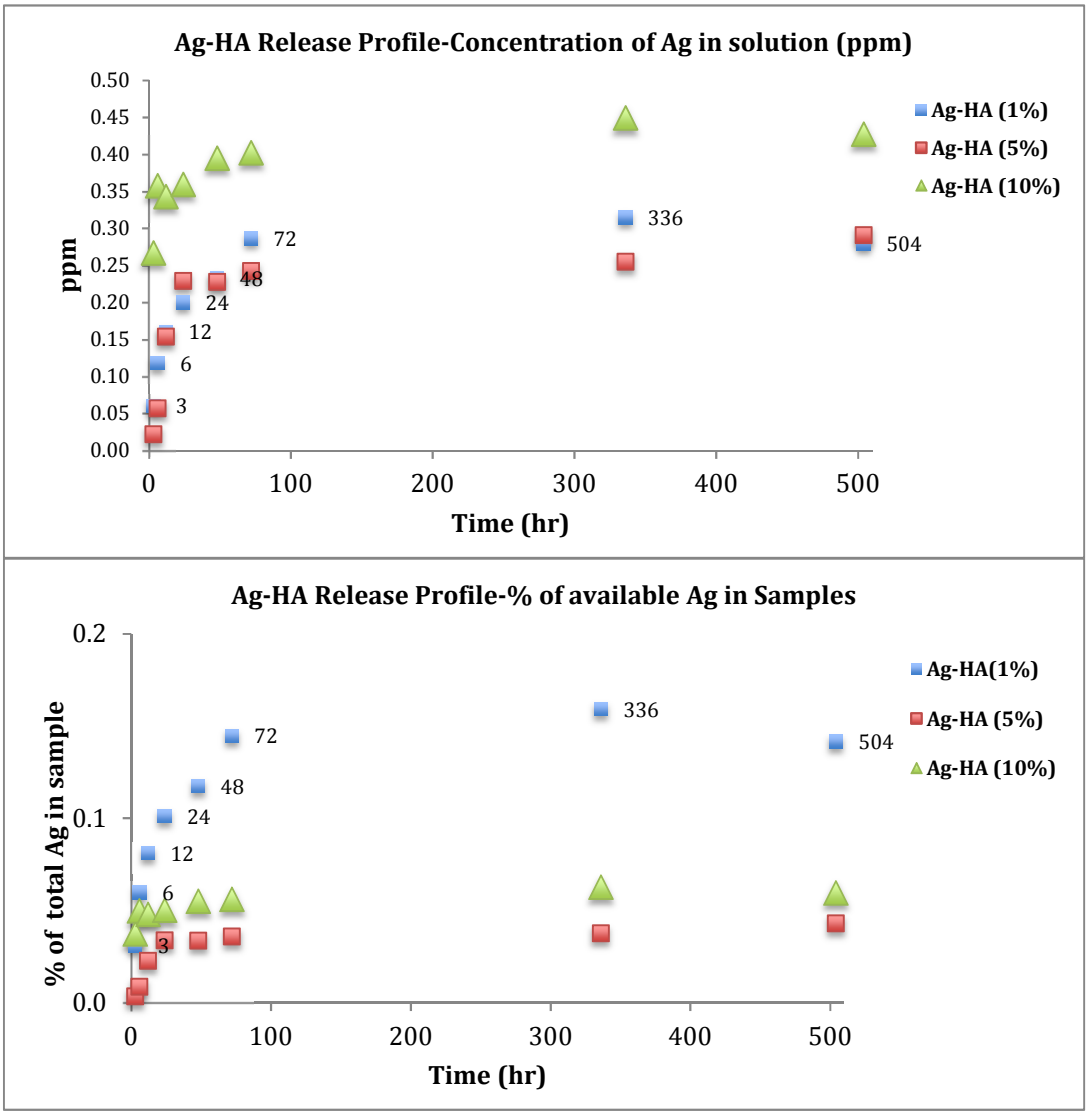

Figure 4. 25: Ag release profile from Ag-HA sample based on total Ag ion concentration in solution (top) and percentage of Ag in the powder which is released (bottom)

Ag ions were detected as soon as few hours (3 hours) after the solid samples were submerged in liquid phase. The results confirmed that there was a direct relationship between the amount of silver in the solid and the amount of ions released in the liquid phase. Ag ions were shown to be released to the medium gradually until they reached a peak concentration after 24-48 hours in all of the samples. For Ag-HA 1%, this value was 0.22 ppm (with slight increase to 0.24 ppm after 14 days). A similar profile was observed for Ag-HA 5% sample showing a concentration

of 0.23 ppm in the medium after 48 hours. For Ag-HA 10%, there was a maximum concentration of 0.40 ppm and it increased to 0.45 ppm after 14 days.

While Ag-HA 1% and Ag-HA 5% show an almost gradual release profile in the first 48 hours, a relatively burst release was observed for Ag-HA 10% sample. The concentration of Ag in the medium varied between 0.4 and 1.2 % of the total silver available in the solid for Ag-HA 10% and Ag-HA 1% respectively.

Magnesium release profile from Mg-HA

Figure 4.26, shows the amount of released Mg ions (ppm and percentage of total Mg available in the solid) from Mg-HA after being submerged in PBS solution for up to 21 days.

Similar to silver ions in Ag-HA samples, magnesium ion concentration was relative to its concentration in the solid samples and ions started to release as soon as the solid was submerged (3 hours) in PBS. As Figure 4.26 shows, a maximum 10 ppm of Mg^{2+} ions was released about 200 µg in 20 ml sample which was more compared to what was observed for Ag-HA samples and was equivalent of about 18% of the total Mg^{2+} ions available in Mg-HA 1%.

Similarly to Ag^{1+} ions, Mg^{2+} ions release followed a maximum release in the first days before it reached its highest concentration after 48 hours (4 days) 168 hours (7 days). The release profile for Mg^{2+} ions suggested that a burst release of Mg^{2+} ions was occurred in all samples showing that most of Mg^{2+} ions migrated from the surface of the solid particles and were transported into the liquid phase (PBS). Not much of Mg^{2+} ions were released at extended times, confirming that only very small amount of ions would diffuse through the solid (internal mass transfer), to the surface and then to PBS.

The concentration of solubilised Mg^{2+} ions was considerably higher than the ones observed for Ag ions. The highest concentration of Mg^{2+} ions was measured to be 8.79 ppm in the case of Mg-HA 1%, while in the case of Mg-HA 5% and 10% , the concentration was 9.64 and 10.35 ppm, respectively.

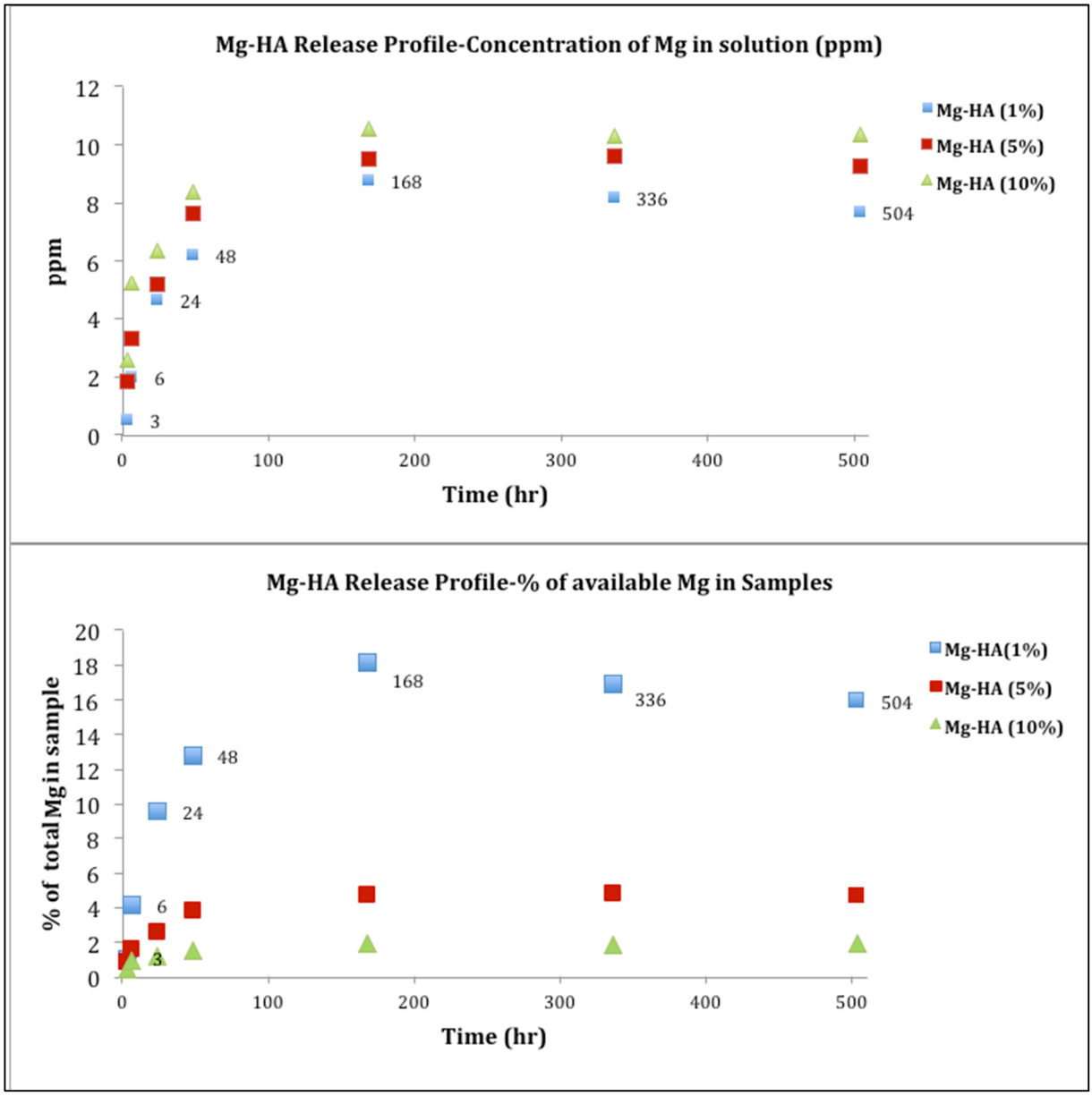

Figure 4. 26: Release profile of magnesium in magnesium substituted hydroxyapatite based on total Mg^{2+} ions concentration in PBS (top) and percentage of released Mg^{2+} ions from the samples (bottom).

Zinc release profile from Zn-HA

Figure 4.27, shows the amount of released Zn^{2+} ions (ppm and percentage of total Zn available in the solid) from Zn-HA samples after being submerged in the PBS solution for up to 21 days.

Similarly, to silver and magnesium ions, zinc concentration in liquid was changing relative to its concentration in solid sample. As Figure 4.27 shows, maximum 0.06 ppm of Zn was released (or 1.2 µg in 20 ml sample) which is less than what was observed in Ag-HA and Mg-HA samples. This was equivalent to about 0.007 % of total Zn substituted in Zn-HA 5% which is significantly lower than what was observed in Ag-HA and in particular Mg-HA samples.

Zinc concentration in liquid phase reached the maximum concentration after 24 hours for Zn-HA 1% and Zn-HA 10% and 48 hours for Zn-HA 5% hence showed a faster rate of release. The release profile for Zn ions (reaching its max level after 24 hours) and lower concentration of released Zn suggest that the release is mainly governed by the migration of the surface adsorbed ions. The concentration of solubilised Zn did not change after 48 hours, which again confirms the negligible mass transfer from the bulk material to the liquid phase.

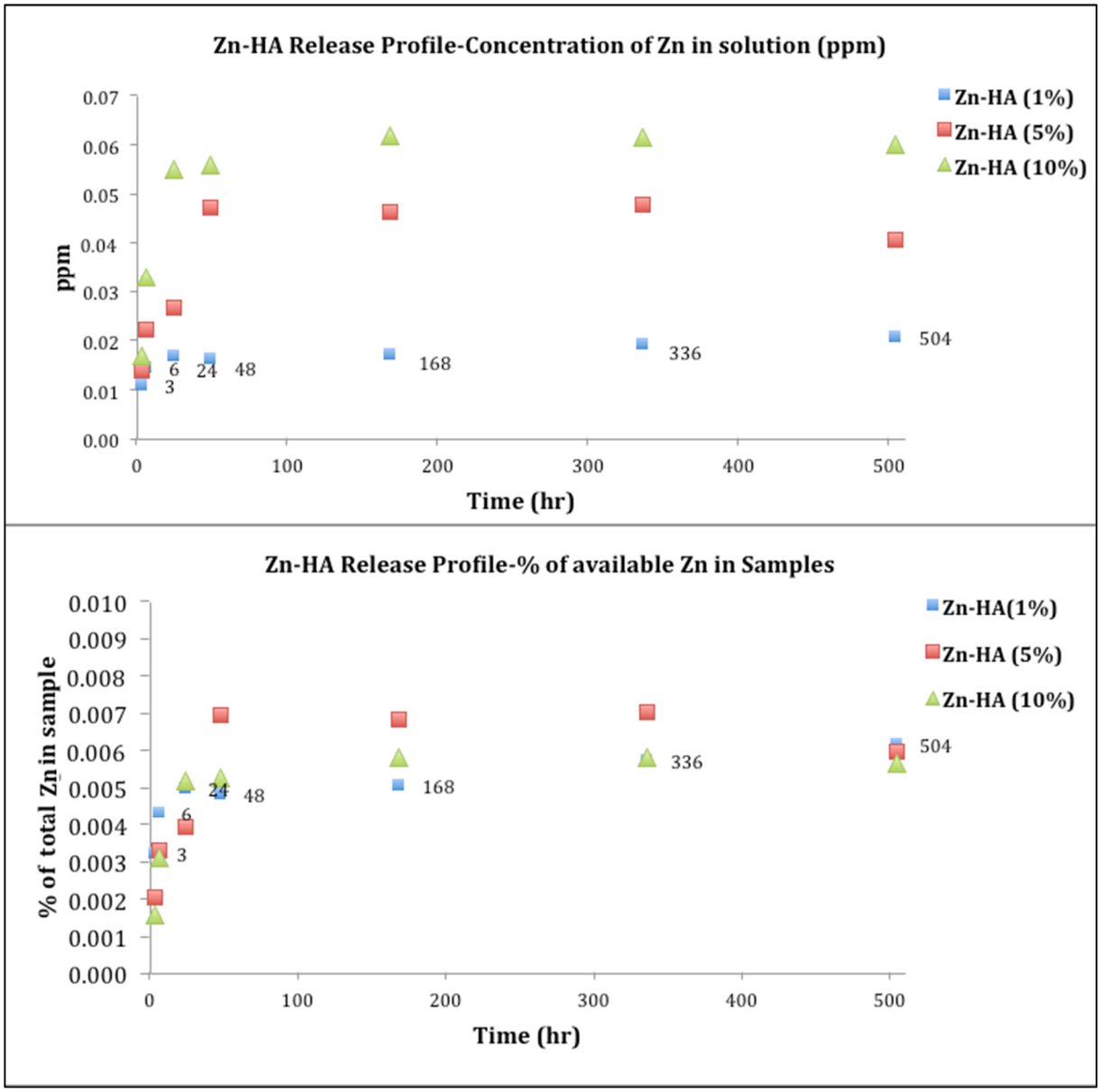

Figure 4. 27: Release profile of zinc in zinc substituted hydroxyapatite based on total Zn^{2+} ions concentration in PBS (top) and percentage of released Zn^{2+} ions from the samples (bottom).

4.6 X-ray Fluorescence Spectroscopy (XRF)

4.6.1 Characteristaion of Ag-HA by XRF

Table 4.17, shows the Ag ions content, Ca/P, (Ca+Ag)/P (as a ratio of total cations to phosphorus) and Ag/Ag+Ca (as ion substitution ratio) in Ag-HA samples measured by XRF.

Table 4. 17: XRF measurement for Ag-HA samples.

Sample	Pure HA	Ag-HA 1%	Ag-HA 5%	Ag-HA 10%
Ag (wt.%)-measured	0.0	0.57	2.89	4.23
Ca/P molar ratio	1.85	2.00	1.97	1.93
Ca+Ag/P molar ratio	1.85	2.01	2.02	2.01
Ag/Ag+Ca	0.0	0.48	2.53	3.68

The ratio of Ca/P in NS-HA and Ca+X/P (where X is cation substituted for Ca in HA) was set to 1.8. Ca/P ratio. The stoichiometric HA is 1.67, but as discussed in chapter 3 (section 3.1) the ratio of 1.8 was selected to obtain a higher calcium content in the HA with better bone-implant interaction.

The Ca/P ratio in the prepared NS-HA (1.85) was similar to the ratio in the reactants (1.8) and the slight increase could be due to the replacement of phosphorus with carbonate ions as a result of atmosphereic CO_2 solubilised in the aqueous reaction medium.

In the Ag-HA samples, the total substitution was 0.57, 2.89 and 4.23 wt.% in the solid HA which was almost in the same range as the values obtained from the ICP measurements in section 4.5.

Silver substitution, or the amount of silver replacing calcium ions in Ag-HA 1, 5 and 10 wt.% was 0.48, 2.53 and 3.68 %, respectively.

The Ca+Ag/P ratio increased from 1.85 in NS-HA to about 2 when Ag^{1+} ions were introduced

to the structure.

4.6.2 Characterisation of Mg-HA by XRF

Table 4.18, shows the XRF measurements of the Mg content in solid Mg-HA and also the calculated values for Ca/P ratio, Ca+Mg/P (as a ratio of total cations to phosphorus) and Mg/Mg+Ca (as a measure of Mg substitution).

Table 4. 18: XRF measurement for Mg-HA samples.

Sample	**Pure HA**	**Mg-HA 1%**	**Mg-HA 5%**	**Mg-HA 10%**
Mg (wt.%) incorporated	0.0	0.22	0.99	2.55
Ca/P molar ratio	1.85	1.9	1.95	1.88
Ca+Mg/P molar ratio	1.85	1.91	2.02	2.07
Mg/Mg+Ca	0.0	0.88	3.61	9.07

In case of Mg-HA samples, the XRF analysis showed that the total concentration of Mg in Mg-HA was 0.26, 1.11 and 2.86 wt.% in Mg-HA 1, 5 and 10% samples, which was again similar to wt.% ratios of Mg which was obtained from ICP measurements. Magnesium substitution, or the amount of Mg ion which has replaced and substituted Ca in HA structure was 1.02, 4 and 9.92% for Mg-HA 1, 5 and 10% samples. These results suggest that Mg substitution in HA structure was very similar to the stoichiometric values which was calculated for the amount of chemicals as reactants. Ca+Mg/P ratio increased from 1.85 to about 2 when Mg was introduced to the HA structure, which can be explained with similar effects discussed for Ag-HA above.

4.6.3 Characterisation of Zn-HA by XRF

Table 4.19, shows the XRF measurements of the Zn content in solid Zn-HA and also the calculated values for Ca/P ratio, Ca+Zn/P (as a ratio of total cations to phosphorus) and Zn/Zn+Ca (as a measure of Zn substitution).

Table 4. 19: XRF measurement for Zn-HA samples.

Sample	**Pure HA**	**Zn-HA 1%**	**Zn-HA 5%**	**Zn-HA 10%**
Zn (wt%) measured	0.0	0.56	2.80	4.23
Ca/P molar ratio	1.85	1.93	1.85	1.87
Ca+Zn/P molar ratio	1.85	1.94	1.92	1.99
Zn/Zn+Ca	0.0	0.77	3.96	5.90

For Zn-HA samples, XRF measurement shows that total concentration of Zn in Zn-HA was 0.56, 2.8 and 4.23 wt. % in Zn-HA 1, 5 and 10% samples, which was again similar to wt.% ratios of Zn which was calculated from ICP measurements. Zinc substitution, or the amount of Zn ion which has replaced and substituted Ca in HA structure was 0.77, 3.96 and 5.9 % for Zn-HA 1, 5 and 10 % samples. As Table 4.16 shows, Zn substitution in HA structure was 5.9 % (in Zn-HA 10% sample) even when there was excess Zn available in the medium. Ca+Zn/P ratio increased slightly from 1.85 to 1.92 when Zn was introduced.

4.7 Cell Biology

In order to ascertain the biological activity and cellular responses to the ion-substituted HA samples animal cell lines were employed to investigate their impact on cell viability, cell proliferation and cell differentiation. The results from these assays enabled us to establish the behaviour of HA selected ions and potentially elucidate their responses *in vivo*. The *in vitro* cell investigation is well established and commonly used in biomaterial testing as indicated in following section.

4.7.1 Cell Proliferation results

Cell proliferation can be directly attributed to the level of cell growth and multiplication and when negatively impacted, can also be representative of the chemical toxicity(219). Comparison with NS-HA samples show the effect of addition of ions on the studied tests. All the results in this section are normalised for response of NS-HA of 100.

Proliferation results are presented using absorbance values which are directly related to the number of living cell. As absorbance values increases, more number of cells are formed.

Cell Proliferation on NS-HA samples

Figure 4.28 illustrate the changes in osteoblast cell proliferation on samples of NS-HA during 6 days of incubation in culture media. As results indicated, there was a steady increase in 2T3 proliferation from 2 days to 6 days in culture conditions in the presence of NS-HA discs. Cell proliferation was significantly ($p<0.05$) increased by 20%, 38% and 52% in day 2, 4 and 6 respectively. These preliminary results, represent a favourable response by the studied cells with hydroxyapatite disks.

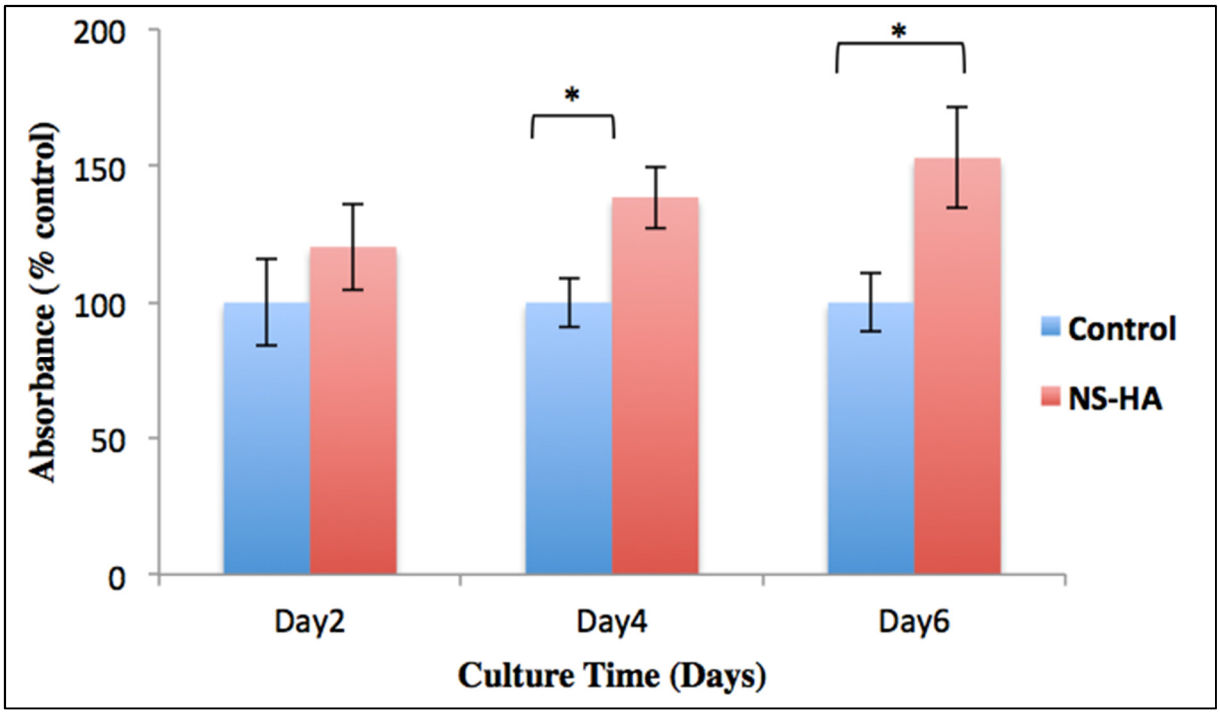

Figure 4. 28: Cell growth (mouse osteoblast cell lines (2T3)) vs. time (over 6 days culture) from the AlamarBlue™ assay (blank wells is control). Mean values (±standard error values) from 3 independent experiments. * (p<0.05).

Cell Proliferation on Ag-HA samples

Figure 4.29 shows the changes in osteoblast cell proliferation on Ag-HA at three different ratio (1, 5 and 10%) samples during 6 days of incubation in culture media. Ag-HA samples, as prepared following the method described in Section 3, were used to investigate the effect of silver substitution on cell proliferation. In case of 1 % Ag-HA, proliferation increased by 10% cell when compared to NS-HA 2 days incubation. However, cell proliferation increased by 18% in these cultures after 4-days incubation and this difference reached significance ($p<0.05$). A similar pattern of significant increase ($p<0.01$) was noted after 6 days incubation with a 19% increase in the extent of cell proliferation as compared to control cultures.

For Ag-HA 5 % samples, cell proliferation rate was almost similar to Ag-HA 1% samples. Hence, 8% cell proliferation increase was observed up to day 2 when compared with NS-HA sample. Although cell proliferation on Ag-HA 5 % was slightly lower than the results obtained from incubation of Ag-HA 1 % at days 4 and 6, cell proliferation increased by 17%% and 18% in these cultures after 4 and 6 days incubation respectively compared to NS-HA and this difference reached significance ($p<0.05$).

Cell proliferation on Ag-HA 10 %, was significantly lower than the NS-HA ($P<0.05$), Ag-HA 1% ($p<0.05$) and Ag-HA 5% ($p<0.05$) during all days. Cell proliferation on Ag-HA 10% decreased by 34%, 35% and 38% in these cultures after 2, 4 and 6 days respectively compared to NS-HA and this difference reached significance ($p<0.01$).

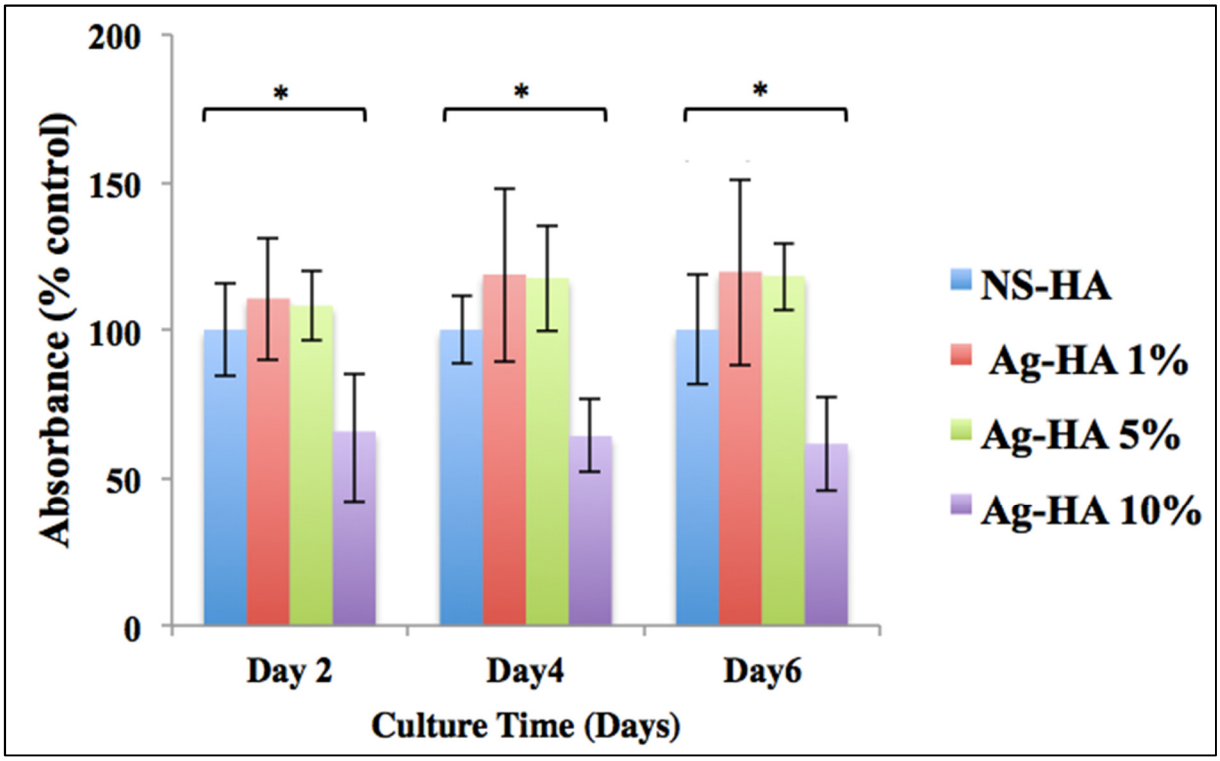

Figure 4. 29: Cell growth (mouse osteoblast cell lines (2T3)) vs. time (over 6 day culture) from the AlamarBlue™ assay for Ag-HA (NS-HA is control). Mean values (±standard error values) from 3 independent experiments *(p<0.05) and **(p<0.01).

As shown in section 4.5.2 (release profile measurement), the total concentration of Ag ion which is present in the medium after 6 days are as table below:

Table 4. 20: Concentration of Ag ions due to unassisted release (ppm) over period of 2, 4 and 6 days.

	Day 2	Day4	Day6
Ag-HA 1%	0.21	0.30	0.31
Ag-HA 5%	0.23	0.30	0.31
Ag-HA 10%	0.40	0.45	0.46

Based on the values presented in Table 4.20 and the results from cell proliferation assessment, when the concentration of Ag ion increases to more than (between 3 and 4) ppm (which corresponds to 10% Ag sample) cell proliferation is negatively affected and cell proliferation reduced.

Cell Proliferation on Mg-HA samples

Figure 4.30 presents the results of the osteoblast proliferation assay for on Mg-HA (1, 5 and 10 %) samples versus the NS-HA control sample.

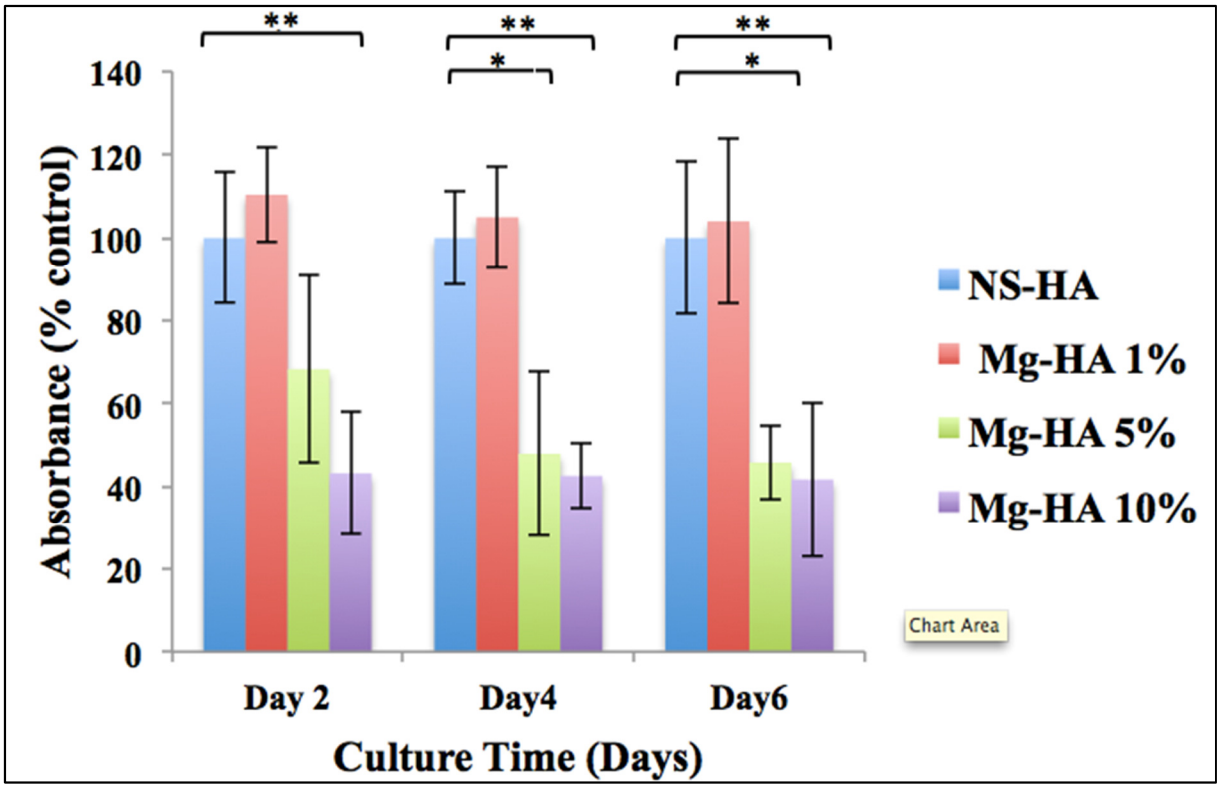

Figure 4. 30: Cell growth (mouse osteoblast cell lines (2T3)) vs. time (over 6 days culture) from the AlamarBlue™ assay for Mg-HA (NS-HA is control). Mean values (±standard error values) from 3 independent experiments *(p<0.05) and **(p<0.01).

Mg-HA 1% samples increased cellular activity in terms of cell proliferation by 10% on day 2 compared to NS-HA sample. Although proliferation rate slightly decreased on day 4 and 6, it was still higher than control by 5% and 4% respectively. In case of Mg-HA 5 and 10% cell proliferation have showed sharp decrease in all time pointed. For Mg-HA 5%, cell proliferations decreased significantly by 31%, 52% and 54% in day 2, 4 and 6 respectively. A similar pattern was observed for Mg-HA 10 wt.% with a significant decline ($p<0.01$) by 56%, 57% and 58% in day 2, 4 and 6 respectively.

Based on the release profile values presented in Table 4.21 and the results from cell proliferation assessment, when concentration of Mg ion increases to more than 8 ppm (which corresponds to 5% Mg sample) cell proliferation was negatively affected and cell proliferation reduced.

Table 4. 21: Concentration of Mg ions due to unassisted release (ppm) over period of 2, 4 and 6 days.

	Day 2	Day4	Day6
Mg-HA 1%	6.22	8.01	8.03
Mg-HA 5 %	7.06	9.05	9.02
Mg-HA10 %	8.02	10.03	10.05

Cell Proliferation on Zn-HA samples

Figure 4.31 shows the osteoblast cell proliferation on NS-HA and Zn-HA (1, 5 and 10 %) samples during 6 days of incubation in culture media. On day 2, proliferation on the surface of Zn-HA 1% increased but the difference was not statically significant. However, on the same day, osteoblast cell proliferation with Zn-HA 5 % and 10 % were 5% and 17% higher than the one for NS-HA respectively. On day 4, cell proliferation on the surface of Zn-HA 1% was 5% higher than the NS-HA sample. On the same day, Zn-HA 5 and 10 % samples showed 15% and 37% increase in cell proliferation respectively ($p<0.05$). On day 6, cell proliferation increased by 9%, 21% and 41% with Zn-HA 1, 5 and 10 % respectively.

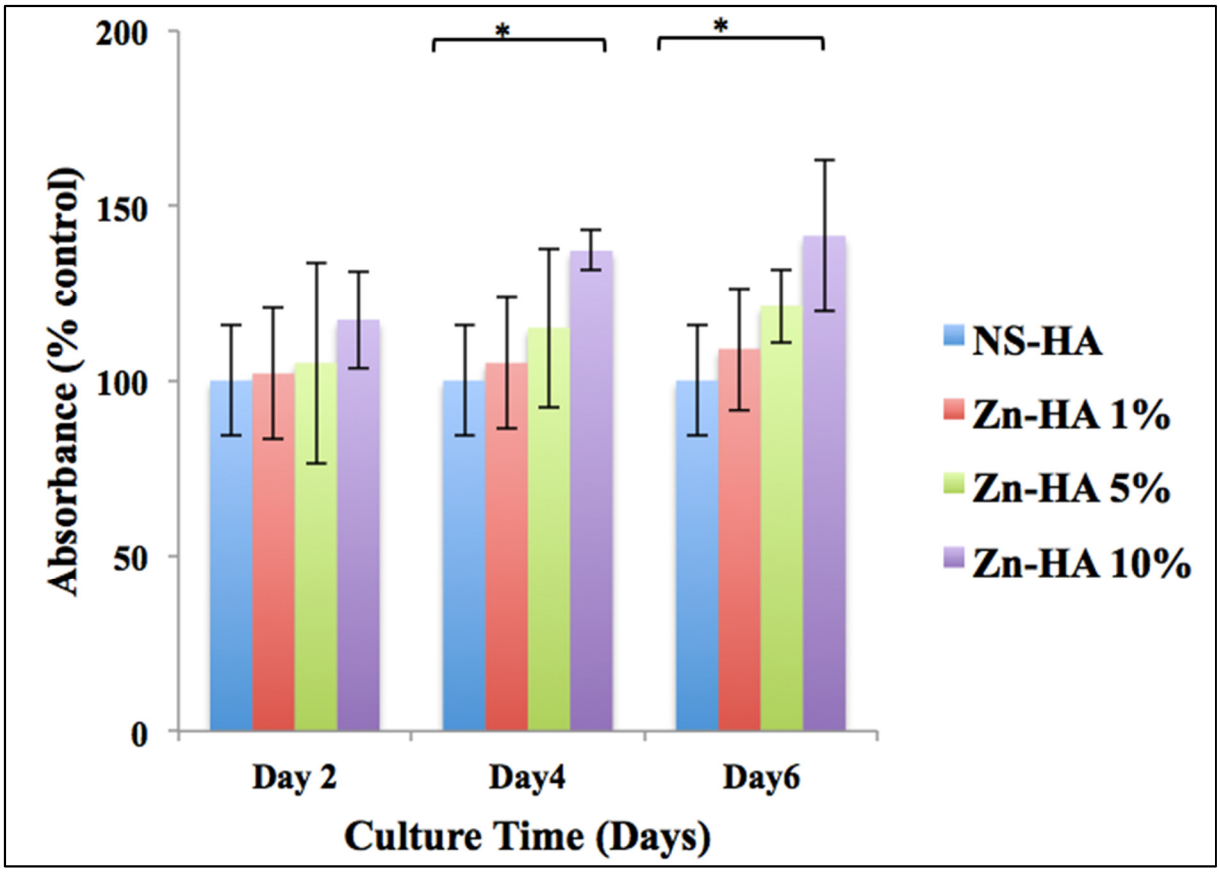

Figure 4. 31: Cell growth (mouse osteoblast cell lines (2T3)) vs. time (over 6 day culture) from the AlamarBlue™ assay for Zn-HA (NS-HA is control). Mean values (±standard error values) from 3 independent experiments *(p<0.05).

Based on the values presented in Table 4.22 and the results from cell proliferation assessment, all selected Zn concentration (with maximum 0.08 ppm concentration) can enhance cell proliferation.

Table 4. 22: Concentration of Zn ions due to unassisted release (ppm) over period of 2, 4 and 6 days.

	Day 2	Day4	Day6
Zn-HA 1%	0.02	0.03	0.03
Zn-HA 5 %	0.05	0.07	0.08
Zn-HA10 %	0.06	0.08	0.08

4.7.2 Alkaline Phosphatase (ALP) Activity quantification

When studying the biocompatibility of the implants, cell proliferation may not provide conclusive result to assess the suitability of the implants. A new set of measurement based on ALP activity was designed to investigate the effect of ion substitution on the cell differentiation. ALP is a hydrolyse enzyme secreted by osteoblasts, and is responsible for removing phosphate groups from nucleotides, proteins, and alkaloids. Therefore, ALP is a useful marker for osteoblast activity.

ALP Activity on Ag-HA samples

The level of ALP protein expression by 2T3 cell cultured on HA and Ag-HA (1, 5, and 10 %) samples are illustrated in Figure 4.32. The onset of ALP activity for all samples was observed at day 7 of incubation.

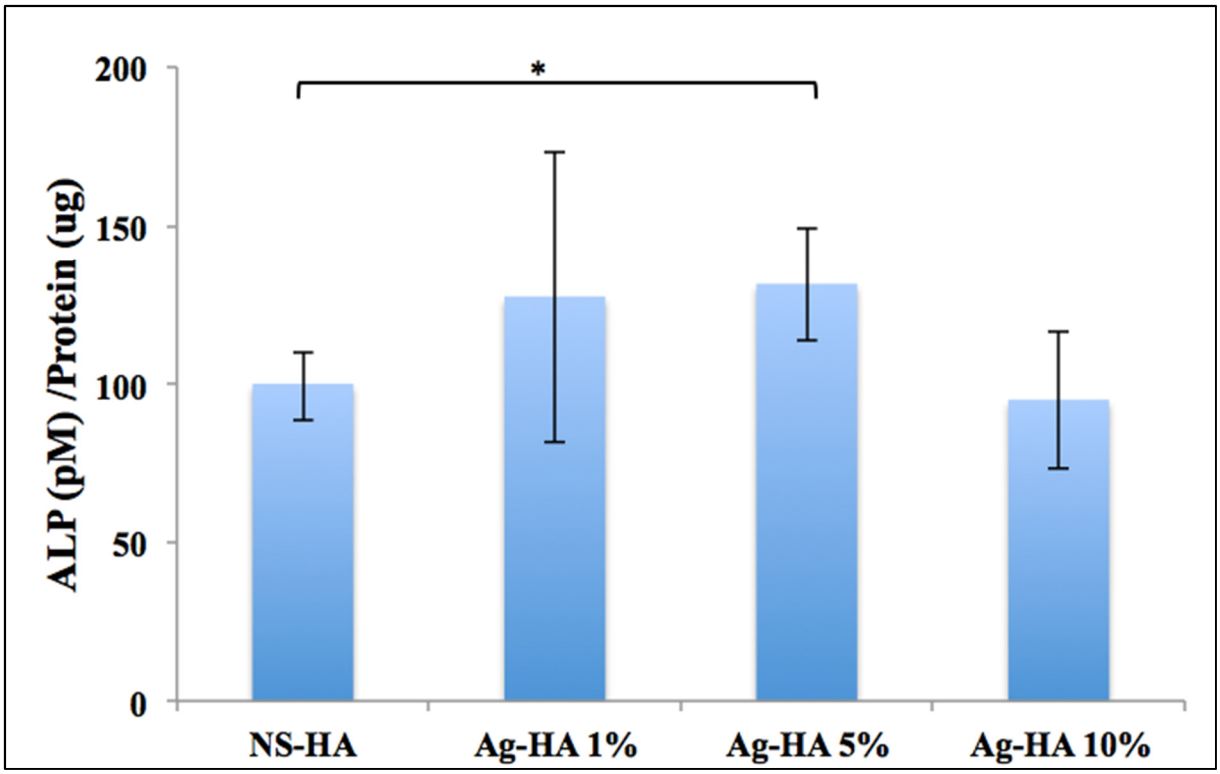

Figure 4. 32: ALP/ Protein values representing osteogenic differentiation of 2T3 cells after subsequent culture at day 7 for NS-HA and Ag-HA. Mean values (±standard error values) from 3 independent experiments. *(p<0.05).

A steady increase in the ALP activity at the time points was observed for 2T3 cell cultured on Ag-HA 1 and 5 % when compared with NS-HA, by 27% and 31% respectively. In case of Ag-HA 1 wt.%, ALP activity was more distributed. The activity for Ag-HA 10% decreased by 5%.

ALP activity produced by 2T3 cultured on Ag-HA 5 % was statistically the highest whilst for Ag-HA 10 wt.%, it showed the lowest activity on day 7. This suggests that the incorporation of silver of more than 5 % did not affect the bone differentiation of 2T3.

ALP Activity on Mg-HA samples

The level of ALP protein expression by 2T3 cell cultured on NS-HA and Mg-HA (1, 5, and 10 %) samples are illustrated in Figure 4.33.

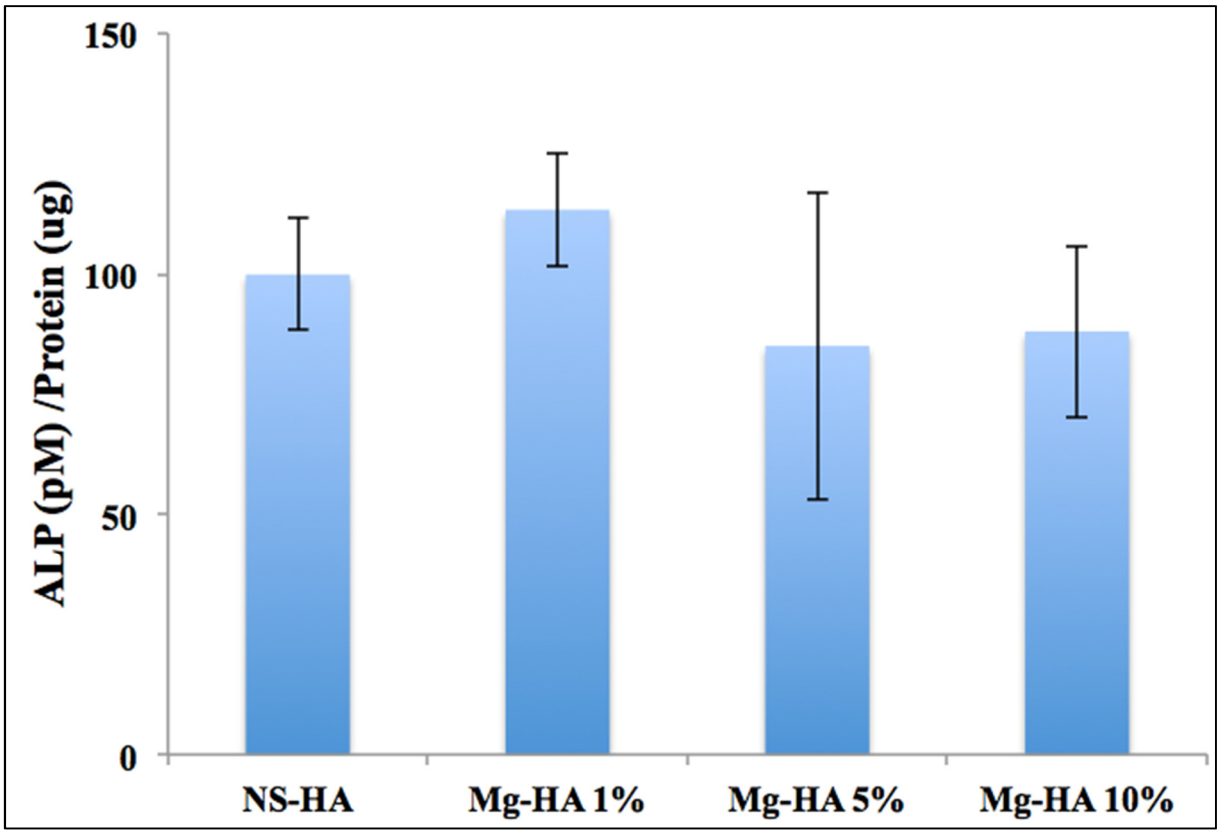

Figure 4. 33: ALP/ Protein values representing osteogenic differentiation of 2T3 cells after subsequent culture at day 7 for NS-HA and Mg-HA. Mean values (±standard error values) from 3 independent experiments.

A gradual increase in the ALP activity was observed on day 7 by increasing Mg concentration from 0 to 1 wt.%. For Mg-HA 5 %, the activity was the lowest while for Mg-HA 1 % it showed the highest on day 7. In other words, incorporating magnesium in hydroxyapatite by more than 1 wt.% can decrease differentiation by 15% and 12% in Mg-HA 5 and 10 % respectively. While

the difference between 1% sample and 5% and 10% sample were more pronounce, the difference between ALP activity for Mg-HA 10 % and 5 % was not significantly higher. It can be concluded that the substitution of Mg has a relatively positive effect on bone differentiation of 2T3 but is dose-dependent. This slight increase is believed to be the result of Mg and Ca ions release from Mg-HA into the cell culture medium.

ALP Activity on Zn-HA samples

The level of ALP protein expression by 2T3 cell cultured on NS-HA and Zn-HA (1, 5, and 10 %) samples are illustrated in Figure 4.34.

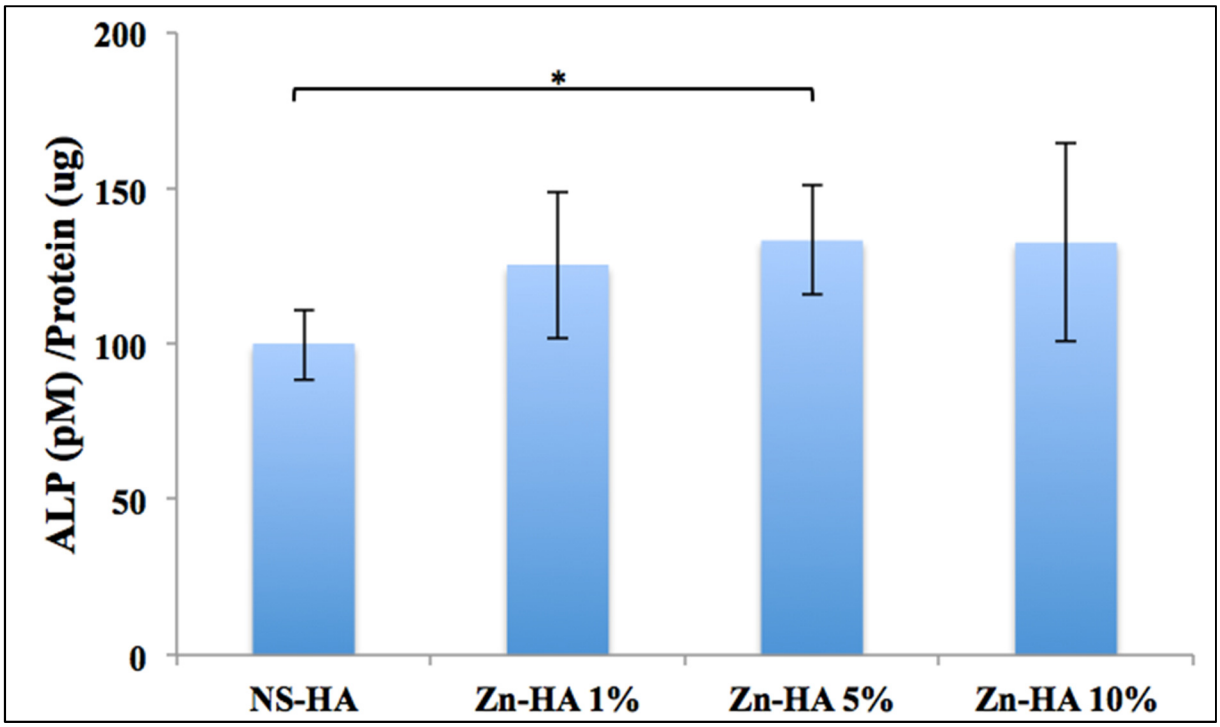

Figure 4. 34: ALP/ Protein values representing osteogenic differentiation of 2T3 cells after subsequent culture at day 7 for NS-HA and Zn-HA. Mean values (±standard error values) from 3 independent experiments. *(p<0.05).

A gradual increase in the ALP activity was observed for 2T3 cell cultured with Zn-HA samples as the concentration of Zn increased. ALP activity for Zn-HA 1 % sample increased only by 25% while for Zn-HA 5 % it increased by 33% and for Zn-HA 10% it increased by 32%. The difference between ALP activity of Zn-HA 5 % and 10 % was not significantly different ($p>$ 0.10) . This suggests that the incorporation of Zn positively affect the bone differentiation of 2T3 cell culture at the levels studied.

4.8 Antimicrobial efficacy tests

4.8.1 Agar diffusion study (Zone of Inhibition (ZI))

Agar diffusion study with Ag-HA

Figure 4.35 shows the change in the size of the zone of inhibition (ZI) against time and different concentrations of loaded silver samples in two bacterial cultures. Bacterial growth was inhibited in all Ag-HA samples, suggesting that solid disks exhibit antibacterial properties when compared to the NS-HA (control) sample. The size of the ZI increased with times suggesting that the release profile of silver (Ag) ions was not fast and sudden under such conditions.

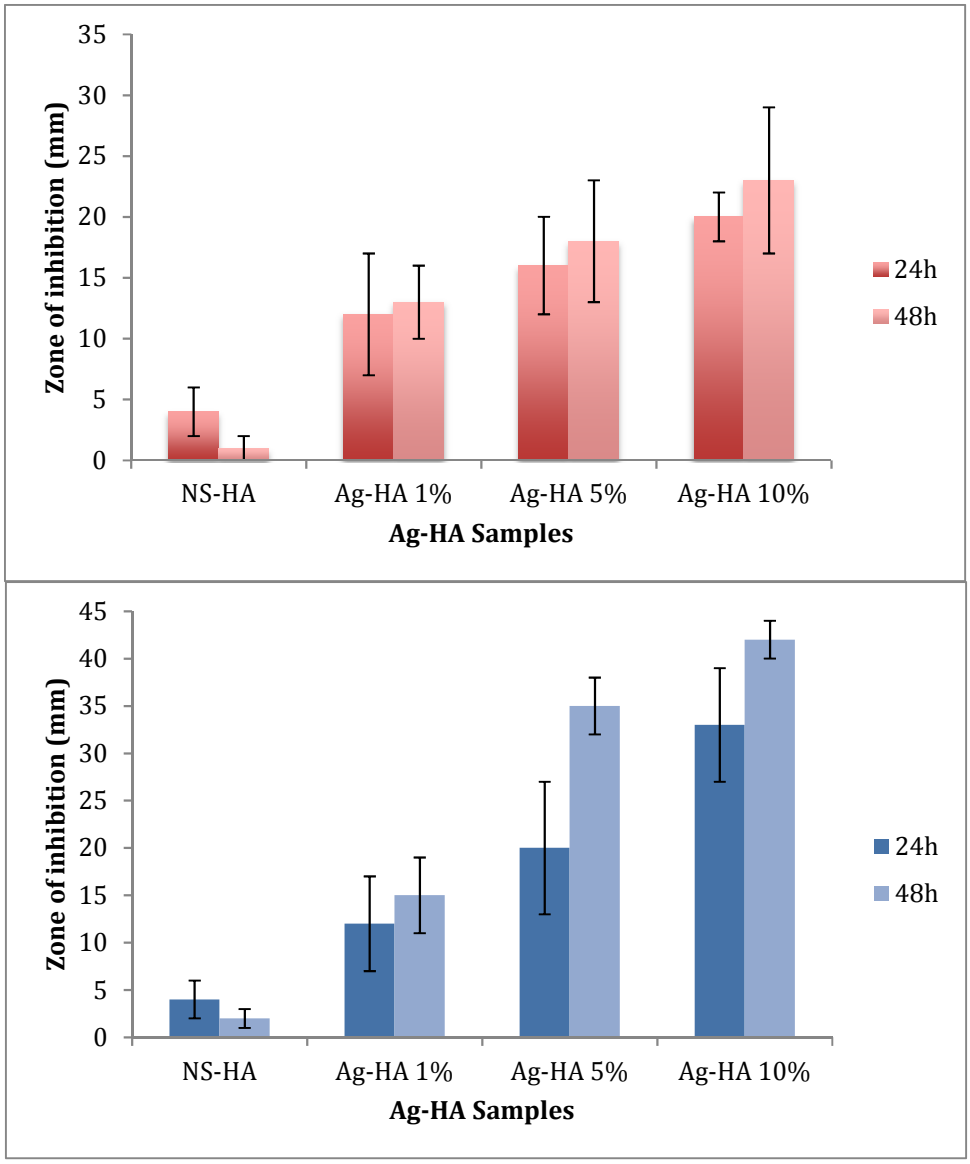

Figure 4. 35: Zone of inhibition of Ag-HA samples against *S.epidermidis* (top) and *E.coli* (bottom).

Agar diffusion study with Zn-HA

The diameter of the ZI is larger against *Escherichia coli* (*E.coli)* than *Staphylococcus epidermidis (S.epidermidis)* in all Ag concentrations. By increasing the Ag concentration, larger ZI ($p < 0.05$) was observed against both bacteria. Figure 4.36 shows the size of the ZI in agar plates obtained with Zn-HA samples and confirms bacterial inhibition in 5% and 10% Zn-HA

when compared to the NS-HA (control) sample. However, the results showed no significant difference in 1% Zn-HA in two cultures after 24 hours.

The diameter of the ZI was larger against *S.epidermidis* than in *E.coli* in all zinc (Zn) concentrations. When the Zn concentration increased, larger ZI ($p<0.05$) was obtained against both microorganisms. However, no significant difference was observed in the diameters of the ZI for 5% and 10% Zn-HA samples in 24 hours against *S.epidermidis* ($p>0.1$). However, antibacterial activity recovered and increased at 48 hours ($p<0.01$).

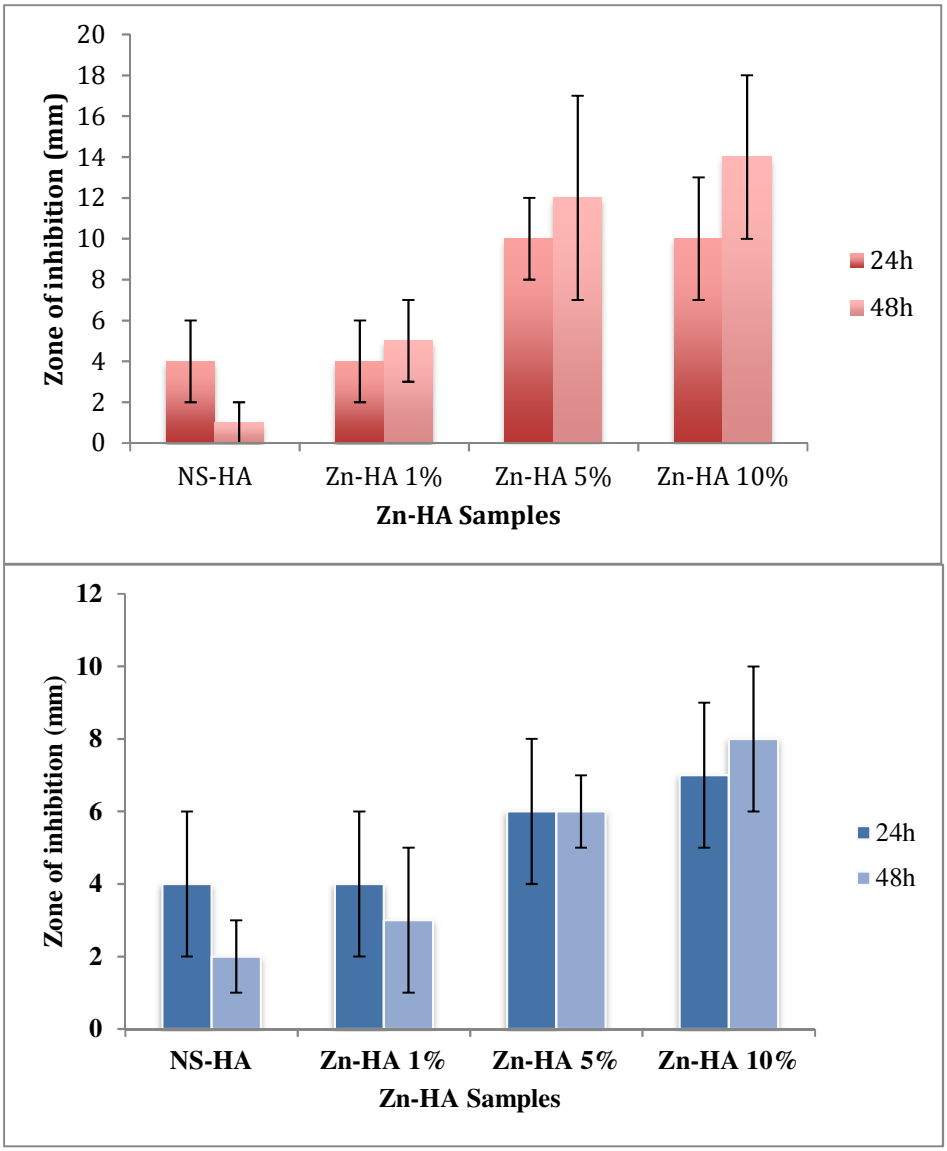

Figure 4. 36: Zone of inhibition of Zn-HA samples against *S.epidermidis* (top) and *E.coli* (bottom)

4.8.2 Film Adhering Method (Quantitative analysis)

The quantitative tests provided a more detailed measurement of the antibacterial activity in the studied samples. In the film adhering method, higher inhibitory rates suggest that the studied specimen possesses higher antibacterial activity.

Film adhering method with Ag-HA

As Figure 4.37 shows, the Ag-HA samples had significant growth inhibition against both bacteria in comparison to the control sample in all three different ratios.

The graph reveals that, even with the lowest Ag content (1 %), antibacterial properties can be obtained against both Gram positive and Gram negative bacteria. For the high Ag content (10 %) sample, the colony formation units (CFU) reduction reached 80% after 143 hours. Similar to the ZI experiments, the Ag efficiency was shown to be dose-dependent and was more pronounced against Gram-negative bacteria (*E.coli*) than Gram-positive bacteria (*S. epidermidis*).

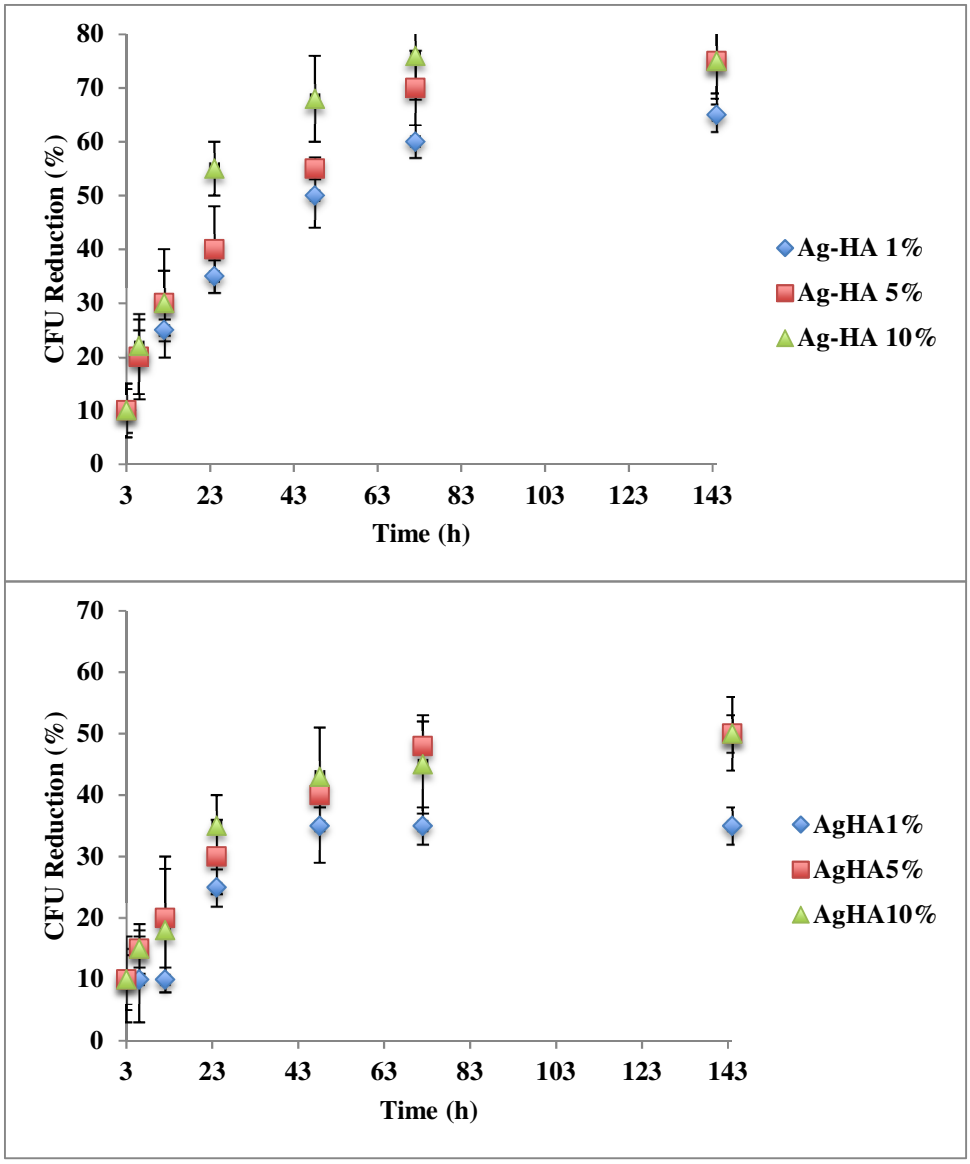

Figure 4. 37: CFU Reduction (%) of Ag-HA samples against *E.coli* (top) and *S.epidermidis* (bottom).

Film adhering method with Zn-HA

The CFU reduction values for the Zn-HA samples (Figure 4.38) confirm that there is a significant growth inhibition in comparison with the NS-HA (control) samples. However, the CFU reduction was lower in comparison to the Ag-HA plates.

The Zn-HA samples were not able to remove completely the colonies of *E.coli* and *S.epidermidis* in any studied concentration of Zn even after 143 hours. The Zn-HA also shows to be more effective against *S.epidermidis* and its antibacterial properties increases at higher ion concentrations. The lowest Zn concentration (1 %) still shows a CFU reduction with both bacteria cultures. The graph reveals that the highest growth reduction was reached after 72 hours with both positive and negative bacteria and in different Zn concentrations.

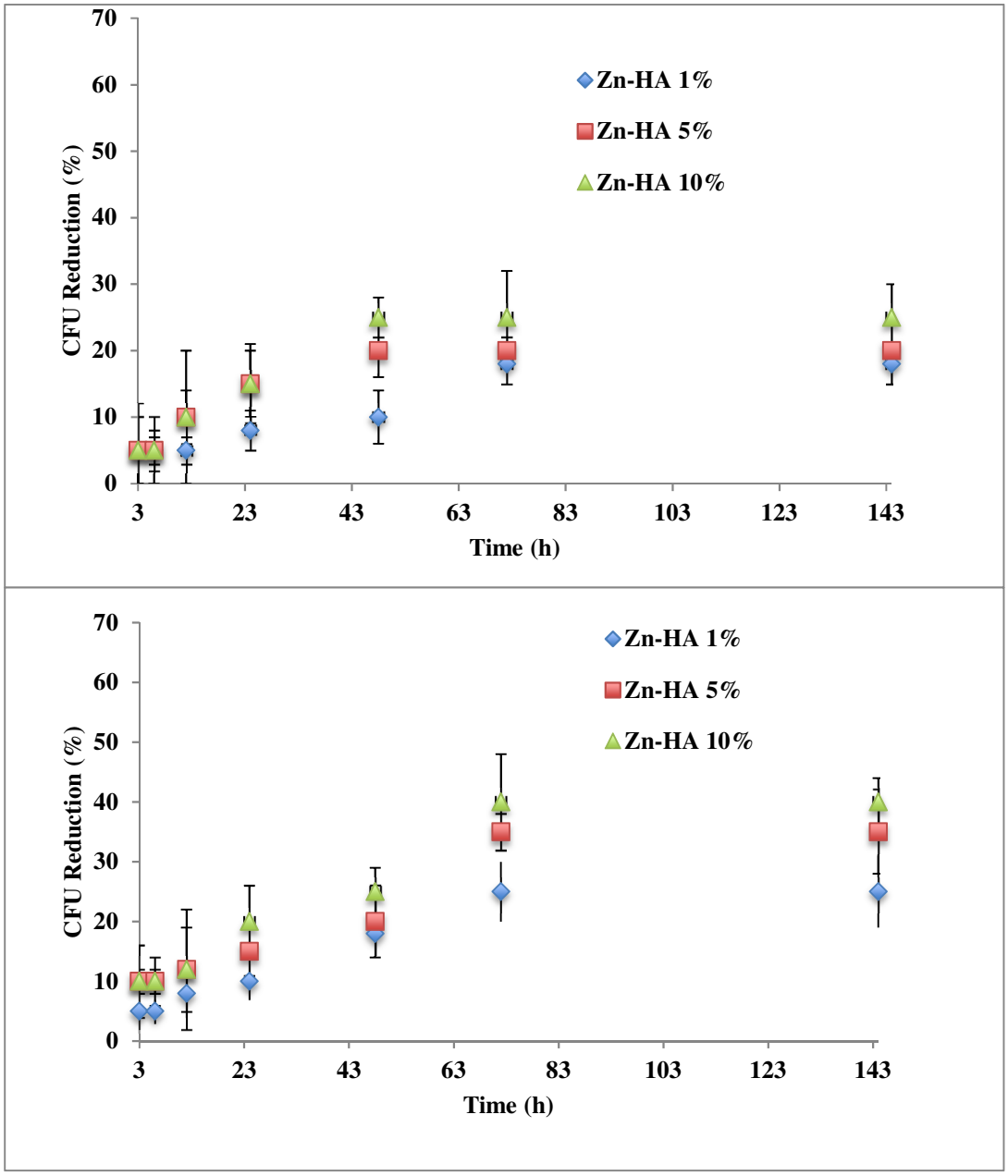

Figure 4. 38: CFU Reduction (%) of Zn-HA samples against *E.coli* (top) and *S.epidermidis* (bottom).

CHAPTER 5
DISCUSSION

5 Discussion

5.1 X-ray Diffraction

XRD technique was used for phase identification, measuring the degree of crystallinity, crystallite size and also the calculation of lattice parameters.

5.1.1 X-ray diffraction analysis of Non-Substituted Hydroxyapatite (NS-HA)

Phase Identification of NS-HA

As shown in Figure 4.1**,** the XRD pattern obtained for NS-HA showed the characteristic peaks for calcium phosphates, consistent with the International Centre for Diffraction Data (ICDD) files for the same material. The overall diffraction pattern of the sample was in agreement with the results of previous studies (62, 66, 178, 179). The NS-HA sample in this study was sintered at 1100°C. As diffraction profiles show, a small amount of HA decomposed to β-TCP.

Highly crystalline hydroxyapatite is expected to be synthesised when HA is sintered at 1100 °C (220, 221), while at higher temperatures (>1100 °C), β-TCP phase is synthesised from the partial spontaneous decomposition of HA (222). The calcination was set up for 2h, for prevention of further decomposition)The advantage of β-TCP, and in general all TCP phases, for biological applications is their relatively higher mechanical strength and better bioresorption rates when compared to HA (223).

The decomposition of HA can be associated with the formation of oxyapatite intermediate phase ($Ca_{10}(PO_4)_6O\square$), where □ denotes a non-charged vacancy in the HA lattice. This phase begins to form with the gradual loss of radical OH^- (dehydroxylation) in the matrix when HA is heated in air to above 1200°C (224). As a result, one of the lattice sites originally occupied

by two OH groups will be occupied by an oxygen while the other is left vacant (224). The formation of oxyapatite is believed to follow the reaction mechanism below:

$$Ca_{10}(PO_4)_6(OH)_2 \Rightarrow Ca_{10}(PO_4)_6\,O.\square + H_2O \qquad \text{Eq. 5.1}$$

where $\square$ denotes a non-charged vacancy in the HA lattice. Oxyapatite is stable although it can undergo further decomposition to form tricalcium phosphate (TCP) and tetracalcium phosphate (TTCP) at higher temperatures.

There are several possible explanations why HA has decomposed in this study. A longer sintering time could lead to higher dehydration and decomposition rates of HA at lower temperatures (1100°C), as also suggested by Wang et al. (225). Furthermore, the presence of moisture in the sintering atmosphere can affect the rates of decomposition up to 1300°C. Wang et al.'s experiments were carried out at relative humidity of 80% (225), while experiments in this study, air humidity during the material processing steps was expected to be about 50% (based on the official seasonal average measurement obtained from the UK Meteorological Office website), which may have contributed to the minor instability in the HA phase in case of this study. Possible inaccuracy in the stoichiometry of reaction can also impact the composition of phases, since secondary phases start to form at Ca/P ratios of above 1.8 (Ca/P=1.8 was used for all samples in this study) (226).

The method used for the preparation of HA samples (wet precipitation) can also impact the stability of HA phases. Based on results from Ramesh et al. (226), HA synthesis by precipitation can decompose to TCP at about 800°C, while no follow-on decomposition phase (α-TCP) was present.

Special attention was given to the selection and purity of the reactants. This was to ensure the absence of intervening ions such as chloride (Cl^-), potassium (K^+), or sodium (Na^{+2}), which can impact the quality of the final product. Chloride (Cl^-) ions are shown to impact the morphology and crystallinity of the final HA by substituting hydroxyl groups (227). Similarly, potassium (K^+) ions can substitute calcium ions and negatively impact the bulk structure of the final sample (228). Hence, NH_4OH was used as the source of hydroxyl groups (OH) rather than KOH. The presence of Na^{+2} ions was also avoided in the reaction medium since previous studies suggest that their presence will easily lead to their incorporation into the crystal lattice and formation of non-stoichiometric HA (66, 227). The XRD results in this study confirm that none of these elements were present in the final HA samples.

In addition, the NO_3 ion was also absent from the final HA as expected, due to its large size which limits its ability to substitute hydroxyl groups (229). NH_4^+ ions were not observed mainly because of several washing steps used following the synthesis step. CaO has been shown to have negative impact on the biological response and success of implants, due to its dissolution in the surrounding environment and pH increase resulting in the inhibition of bone growth (230), though no peak referring to CaO was observed in any of the prepared samples. The presence of CaO can be attributed to little or no carbonation of HA during the reaction synthesis (66, 231).

Crystallinity and crystal size of NS-HA

The degree of crystallinity of HA is one of the critical elements which correlates to its thermal stability and rate of dissolution in physiological environment (232).

Sintering of HA samples at 1100°C resulted in a considerable increase in degree of crystallinity. There was a substantial increase in the height and sharpness of peaks, corresponding to an increase in crystallinity levels. Non-sintered HA possessed a crystallinity of 61.75 ±3.2 %, while sintered HA attained levels of crystallinity of 88.8 ±5.7 %; an increase of about 27%. All the powders produced in this study, including NS-HA and Mg-HA, Zn-HA and Ag-HA for all ion ratios had a crystallinity degrees lower than 95%, the minimum requirement as set out by FDA (233). An explanation for this relatively low crystallinity could be the short time available for calcination (2 hours). It is expected that by increasing this time, the final product would attain a higher degree of crystallinity.

Another explanation could be the non-optimised ripening time which was not used in this study, which is believed to have a strong contribution to the crystallinity of the final powder (234). During the ripening stage, which initiates in the reactions but continues until the crystals are physically separated from the solution, crystals undergo the nucleation and growth stages in a supersaturated solution. This is considered to impact the crystal size and its morphology. Producing highly crystalline HA was not the objective of this study and ripening time was not controlled during the experimental work. Reaction temperature, kinetics and unknown interactions between different ions in the solution are also expected to affect the crystallinity of the product as suggested in other studies (179, 234, 235), which were not studied in this study. To control the crystallinity as a quality attribute for a biomedical material, however, all these parameters are expected to be identified, controlled and optimised during the reaction.

There are key parameters which can influence the final crystal size in the 002 plane. For example, using an inert atmosphere (e.g. a nitrogen purged medium) is shown to have a major

effect on the size of the crystals in this plane. As shown by Smiciklas et al. (179), an increase in crystallite size was observed when an inert atmosphere was used.

Another factor is the two-way interaction between the reaction temperature and the ripening time, as highlighted previously. Both Pang et al. (234) and Smiciklas et al. (179) reported that crystal size increases by increasing the reaction temperature and ripening time in this plane.

While the above-mentioned parameters are known to impact crystallinity and size of the crystals, again, it was not the purpose of this research to optimise these parameters. However, they were expected to remain constant in this study, and any change to crystal size and crystallinity was due to the change in the type and concentration of added metal cations.

Lattice parameters and crystal size of NS-HA

The reported values for lattice parameters are consistent with the available lattice data for HA and β-TCP phases reported in the mentioned references (and purchased standard HA) as starting values. The slight difference in lattice parameters in the prepared NS-HA may be due to some deviation from the reaction stoichiometry. Generally, an increase in the lattice parameter *c* with a reduction in lattice parameter of *a* indicates either (236):

1. A change in the Ca/P ratio in the HA;
2. A change in the Ca/OH ratio in the HA; or
3. Substitution of OH groups by CO_3^{2-} groups.

Cases (1) and (2) can be described as a change in the composition on account of precipitation of the impure phases (e.g. β-TCP) present in the HA, and are discussed in section 4.6 for XRF analysis. Case (3) suggests that HA may have reacted with carbonate ions present in the solution

originating from CO_2 in the air, as opposed to the inert environment which may used during the preparation of reference HA.

The HA crystal consists of two types of crystal planes, each with different charges: positive charge for the *a*-planes and negative charge for the *c*-planes (236). Controlled orientation may be obtained by changing the morphology of the HA crystals. As an example, by increasing the surface charge of the HA, hexagonal-shaped HA starts to grow along the *c*-axis so that the (*a*=*b*)-plane is wider than the *c*-plane.

When the lattice parameter in the *a*-axis was compared to those for the stoichiometric HA sample (the reference and had Ca/P=1.67), the higher Ca^{2+} concentration of HA sample (as a higher Ca/P ratio (=1.8) was used in these experiments) resulted in a higher *a* value, the expected outcome which was also reported by Aizawa et al. (183).

5.1.2 X-ray diffraction analysis of Silver-Substituted Hydroxyapatite (Ag-HA)

Phase Identification of Ag-HA

The XRD patterns of all samples were very similar to that of NS-HA. However, two sharp peaks at 2θ = 33.29° and 36.58°, and also a small peak at 27.16°, were present in the XRD pattern of Ag-HA 1% sample which belongs to Ag_3PO_4. When Ag concentration increased in Ag-HA 5%, an additional Ag_3PO_4 peak at 2θ= 20.82 ° became visible.

A study by Ipekoglu et al. (237) reported Ag_3PO_4 peaks for 5 and 10 wt.% Ag-HA samples. It was expected that the majority of silver at lower concentrations was incorporated directly as Ag^+ ions into the HA structure, with less chance for it to react with the phosphate ions and form silver phosphate. However, as silver concentration increased in 5 and 10 wt.% samples, more silver was available leading to the formation of silver phosphate.

In addition, hexagonal crystal planes of metallic silver were observed in the XRD pattern of Ag-HA. Similar observations were reported in other studies where silver substituted hydroxyapatite was synthesised and studied (184, 185). However, the intensity of the small peaks associated with the presence of metallic silver was much lower than that found in JCPDS no. 04-0783, which may be explained by an increased degree of silver substitution and thus a lower concentration of residual metallic silver residue.

Crystallinity and Crystal Size of Ag-HA

As XRD patterns shows, by introducing silver to hydroxyapatite in concentrations of 1 to 10 wt.%, HA peaks became only slightly sharper, suggesting that a marginal rise in crystallinity after silver incorporation. The XRD pattern also shows that the powders obtained by co-precipitation exhibit an apatite structure with good crystal characteristics. Similar results were obtained by Ciobanu et al. (238), who prepared silver doped hydroxyapatite without forming a new phase. They reported an increase in lattice parameters but showed a minor reduction in crystallinity when silver concentration increased from 0.05 to 0.3 (238). Stanic et al. (138) used Ag_2O as the source of silver and similarly showed an increase in lattice parameters but again a slight decrease in crystallinity of final Ag-HA in comparison to pure HA.

In another study by Nirmala et al. (239), TEM was used to assess the incorporation of Ag particles and also to measure the crystal size. While a high crystalline sample was formed, they showed that Ag particles were mostly attached on the surface of HA crystals. Although they did not measure the crystallinity but reported no significant change in the peak sharpness in the sample's XRD pattern after Ag was incorporated up to 5 wt. %. While there is a good agreement in terms of having a highly crystalline Ag-HA, results from this study show a different crystal size in the final product, which is expected to be due to different experimental methods.

Lattice parameters of Ag-HA

When cations are substituted into the HA lattice, they tend to change the lattice parameters and cause the HA structure to be disordered. Depending on the size and charge of the cation, the unit cell can become bigger or smaller. This change can be observed even in the XRD pattern, as represented by broader or narrower peaks.

Lattice parameters *a* and *c* increased with an increasing amount of silver ions in HA and β-TCP phase, which indicate that Ag ions are included in the HA lattice and may have replaced Ca^{+2} sites in both phases.

Similar expansion on the *a* and *c* axes was observed in a study by Ipekoglu et al. (237), where they prepared Ag substituted HA using a microwave technique. They claim that this led to Ag replacing Ca^{+2} sites, due to an increase in the unit cell parameter.

The observed change in the cell parameters is a result of inclusion of Ag ions (size of 0.128 nm) in the HA structure made of Ca cations (size 0.099 nm), resulting in a change of crystal structure. This theory is consistent with previous work by Rameshbabu et al. (240), which also assumed that silver had substituted calcium ions following a similar synthesis route and reported an increase in lattice parameters. Janackovic et al. (241) used a neutralization method for synthesis of monophase silver-doped HA nanoparticles and observed an increase in lattice parameters when silver was increased to maximum of 0.25 mol.%. Similar results were reported by Ciobanu et al. (238), who doped nanocrystalline HA with silver in different ratios (0.05, 0.2, and 0.3 wt.%) and found a constant increase in the lattice parameters for HA phase only. However, they did not measure the lattice parameters in other calcium phosphate phases (238).

Deformation in crystal structure by increasing unit cell parameters can even be observed with lower amounts of silver, as reported by Lim at al. (242). They only substituted 0.5 wt.% of Ag into the HA structure, lower than what was achieved as discussed in the XRF section, and still indicated an expansion in lattice cell parameters in Ag-HA.

5.1.3 X-ray diffraction analysis of Magnesium-Substituted Hydroxyapatite (Mg-HA)

Phase Identification of Mg-HA

When Mg ions were added to HA, the XRD pattern shifted to lower 2θ values compared to NS-HA, and the presence of β-TCP phase was more significant. However, the resulting peaks became slightly broader compared to NS-HA samples, which may imply that Mg ions were engaged in the HA structure leading to deformations of the crystal lattice. By increasing the Mg content, all peaks became broader, suggesting lower crystallinity with less grain growth because of Mg ion substitution.

The 2θ values derived from the XRD patterns of Mg-HA (5 and 10%) samples showed a considerable shift with respect to stoichiometric hydroxyapatite, becoming more similar to Whitlockite. In fact, one of the main characteristic planes present at 31.81° shifted to a lower degree representing the formation of Whitlockite. Previous studies have also indicated that Mg-Whitlockite can form through precipitation reactions when relatively low temperatures (range 37 - 95 °C) and acidic or neutral pH were used (13, 243, 244). As Mg-Whitlockite was also present in non-sintered hydroxyapatite, its formation cannot be attributed to the sintering process, though it is expected that the presence of Mg ions contributed most to the formation of Mg-Whitlockite. Fadeev et al. (123) also reported that increasing Mg content to more than 1

wt.% and calcination temperatures up to 1000°C can promote transformation of HA to Whitlockite.

The results in Figure 4.6 are in agreement with the existing literature and confirmed the formation of Magnesium substituted β-TCP with increasing magnesium substitution (13). According to Ryu et al. (245), when Mg is introduced, it substitutes the Ca^{2+} cations resulting in lattice contraction and respective displacement of β-TCP reflections towards lower 2θ angles. The effect of the magnesium incorporation became more evident with increasing magnesium content (114, 245). This shift was representative of the reduction in lattice parameters of β-TCP, which was caused by larger radii atoms (Ca^{2+}) being replaced by smaller radii (Mg) atoms.

Brucite ($Mg(OH)_2$) has been reported to be present in Mg-HA products synthesised in other studies (114)(245). No Brucite was observed in the XRD pattern of this study, which can be due to the use of different reaction precursors ($MgNO_3$ instead of $Mg(OH)_2$). Another explanation could be that brucite peaks overlap with HA peaks and therefore it would be difficult to identify it using XRD. It is also suggested that the calcination of Brucite will generate MgO peaks, but this was also absent from the studied samples.

There are different values for the maximum amount of magnesium that can replace and substitute calcium in the HA structure when synthesised using precipitation and hydrolysis methods. RZ et al. (246) reported a maximum of 0.3 wt.% Mg, while other similar studies have quoted less than 1 wt.% (111, 247, 248). Mayer et al. (249) precipitated HA powders containing up to 1.5 wt.% of Mg without simultaneous carbonate substitution. Golden and Ming managed to synthesise Mg-HA powders with up to 2 wt.% of Mg from aqueous solutions (250). Okazaki et al. (251), substituted up to 5 wt.% of Mg in HA using a precipitation method but with a total

loss of crystallinity. It is worth mentioning that a total replacement of Ca^{2+} with Mg^{2+} in HA powders has also been reported using precipitation at high pH solutions (252, 253).

However, an excess of Mg is shown to have a negative effect on the bioactivity of certain biomaterials (254). While there are some degrees of substitution for Mg^{+2} ions, surface adsorption in other secondary phases like Brucite and Magnesium Oxide is also present.

The position of Mg in the HA lattice is not clearly known. Mg can occupy one of the two crystallographic calcium sites or both, referred to as Ca(I) and Ca(II), which are present in different reaction conditions (118).

Crystallinity and Crystal Size of Mg-HA

The experimental data within this study indicated that Mg affects the crystallinity and crystal size of HA Table 4.5, and this effect is more pronounced at higher Mg concentrations. While there was a crystallised biphasic structure (β-TCP + HA) in the NS-HA sample, the peaks of HA and β-TCP became wider and their intensity reduced after Mg ion was introduced, especially in the 2θ range between 28° and 32° and between 45° and 55° Figure 4.6. The same effect was reported after Mg addition in other studies, and similar XRD pattern and degree of crystallinity were obtained (255-257).

The crystallinity degree was 88.8% for NS-HA while it decreased to 83.2%, 64.8% and 63.5% for Mg-HA 1%, Mg-HA 5%, and Mg-HA 10% respectively (all sintered samples). A similar trend was present in other studies where the degree of crystallinity decreased when Mg concentration was increased (13, 114, 258). However, Kim et al. (259) reported no change in HA phase profile when a mixture of Mg and Si was added with Mg ion concentration of up to 1 wt.%. Bertoni et al. (248) used a wet precipitation technique with addition of 1, 5 and 10

mol.% of Mg ions and crystal size decreased even at lowest concentration (1 mol.%). Ren et al. (217) measured the crystallinity and phase behaviour of up to 20 mol.% Mg ions in HA, and reported similar results in terms of decreasing crystallinity as well as the presence of a Whitlockite phase at higher Mg concentrations. They also indicated that the total concentration of Mg in solid phase was no more than 7 mol.% when a 20 mol.% solution was prepared.

Change in crystal size for Mg-HA 1% suggest that magnesium ions affect crystal size by inhibiting the growth of HA crystals, as also noted by LeGeros et al. (111). Caccioti et al. (260), also concluded that the presence of Mg ions within the HA lattice decreases the degree of crystallization.

Lattice parameters of Mg-HA

Both *a* and *c*-axis parameters in β-TCP and HA phase samples decreased after the introduction of Mg^{2+} to the reaction, suggesting contraction of cell volumes after Mg^{2+} addition. As this contraction is more pronounced in β-TCP phase, it can be concluded that a higher ratio of Mg^{2+} ions were incorporated in this phase. Identical results were reported by Bigi et al. (13), who proposed that Mg^{2+} is more likely to enter into the β-TCP rather than the HA phase. In another study, Mg was introduced to hydroxyapatite using hydrothermal method, and a similar effect was obtained from the refinement of the Whitlockite cell parameters and the unit cell volume for 1.5% Mg-HA was approx. 3480 Å. As Mg content changes from 1.5 to 4%, unit cell volume dropped by about 52 Å (261).

The main reason for contraction on both *a* and *c* axes is the substitution of Mg^{2+} (ionic radii of 0.072 nm) for Ca^{2+} ions (ionic radii 0.099 nm).

As mentioned previously, no Whitlockite phase was present at Mg 1%, and the majority of Mg^{2+} ions were accumulated in the HA phase. As Mg concentration increased to both 5 and 10 %, the Whitlockite started to form, suggesting that Mg substitution has shifted towards the β-TCP phase. However, it is impossible to establish the relative magnesium content in the amorphous phase or on the crystal surface. Posner et al. (262) suggested that magnesium prevents the transformation of amorphous calcium phosphate into HA by distorting the hydroxyapatite pre-nuclei structures, inhibiting further HA growth as a result of a structural mismatch. A similar mechanism may explain the inhibiting role of magnesium on the crystallisation or crystal growth of HA. Regardless of the location of Mg in the HA structure (either on the surface, being present as defects or formed within the amorphous phase), Mg can promote the formation of magnesium substituted hydroxyapatite (following a similar pattern as in Whitlockite).

It was also shown that based on measurements of the lattice parameters for HA samples, systematic cell volume reduced when levels of substituted magnesium changed from 1 to 10 wt. %.

As described earlier, *a* and *c*-axis parameters decreased in HA phase in all Mg concentrations. In case of β-TCP phase, however, the *a* axis parameter decreased when 1 wt.% Mg was added and it did not change even with more addition of Mg. The value of *c*-axis dropped after addition of 1, 5 and 10% Mg. This changing in the profile of cell parameters may be due to the limited replacement capacity of Mg^{2+} ions within the β-TCP network. Hesaraki et al. (263) reported that the maximum capacity of β-TCP for Mg replacement is about 15 mol.%. However, in another study, maximum replacement of Mg^{2+} on Ca^{2+} sites was reported to be about 10 mol.%, and a steady contraction of *c*-axis was also observed (264).

The exact location and quantity of Mg substitution, whether replacing Ca^{2+} ions or being adsorbed on the surface, or even being incorporated as defects are still under debate. Neuman et al.(265) stated that a high percentage of Mg ions were adsorbed on the surface of apatite crystal when HA crystals were precipitated under physiological conditions. However, Riman et al. (114) suggested that Mg^{2+} ions were not detected on the surface of HA. LeGeros et al. (246), indicated that Mg substitution in an apatite lattice significantly affects the degree of crystallinity and solubility of HA.

Experimental evidence from Ren et al. (217), suggests that magnesium does substitute the calcium in apatite. Also, their experimental data from ab initio simulations predicted that Mg ion occupancy on Ca (I) sites was energetically favored. In contrast to Ren at al.'s results, Laurencin et al. (118) claimed that the preferential incorporation of Mg is in the Ca(II) triangles along a single OH channel, which could have a direct impact on the properties and reactivity of Mg-HA. Their evidence from the computational data indicates that deformation of the HA lattice mainly occurs closer to the Mg sites, since the Mg/O bonds are much shorter than Ca/O ones. Also, their calculations confirmed that at higher Mg concentration, there is a preference for an ordered pattern of Mg ions in alternating positions in the Ca(II) triangles along a single OH channel.

5.1.4 X-ray diffraction analysis of Zinc-Substituted Hydroxyapatite (Zn-HA)

Phase Identification of Zn-HA

The broad diffraction peaks in all Zn-HA samples, particularly in 5 and 10 wt.% samples may suggest smaller apatite crystals. For Zn-HA 1% sample, the phase pattern remained unchanged when compared to NS-HA. The same peaks of β-TCP and HA could still be detected and no other phase (such as calcium oxide or α-TCP) was detected. Absence of any secondary phase

in the diffraction pattern was also indicated by Thian et al. (266), as they introduced a maximum of 1.6 wt.% Zn using a precipitation technique. All HA and β-TCP peaks however were shifted to lower 2θ, indicating the deformation of crystal planes.

A new phase was detected at Zn-HA of 5%, which was comparable to calcium zinc phosphate hydrate or Parascholzite. Parascholzite can be classified as a Zn-substituted TCP, and its intensity increased in Zn-HA 10 wt.% while the intensity of HA phase decreased. β-TCP phase became stronger when the Zn concentration increased to 5 and 10 wt.%, suggesting that the Zn-HA had been transformed into Parascholzite, as also suggested by Li et al. (135).

Crystallinity And Crystal Size of Zn-HA

By introducing Zn ions to the hydroxyapatite, all the peaks became broader, suggesting decreased crystallinity and crystal size in comparison to the NS-HA sample. This reduction trend was more pronounced when the Zn concentration increased to 5 and 10 wt.%.

An identical trend was observed after addition of Zn in previous studies (15, 127, 135). It is suggested that the presence of Zn in the solution strongly inhibits the crystallisation of HA, and the single crystalline HA phase was only achievable at a Zn concentration of up to 25 mol.%. Ren et al. (126) reported comparable results after using a similar precipitation technique to this study (126). LeGeros et al. (267) reported the same effect with the addition of Zn, suggesting that even lower concentrations of Zn (< 1 wt.%) may lead to the inability of the structure to host greater amounts of Zn.

Concerning crystal growth inhibition, Ren et al. (126) proposed that this behaviour is likely to be caused by a mismatch between the ion sizes of calcium and zinc, which generates a distortion in crystal structure. They also reported that samples with higher Zn content were far harder to

compact, due to higher agglomeration rates when crystal size decreases and surface area increases. Their results were further confirmed by scanning electron microscopy, which indicated that "particle sizes" increases with the addition of zinc ions to the HA structure.

Miyaji and co-workers also reported similar changes in the HA structure, crystallite size and crystallinity after increasing the Zn concentration (268). They synthesized Zn-substituted HA using precipitation method (at pH= 8.0, temperature= 90°C) and measured the lattice parameters using XRD and an internal standard. They showed that the maximum Zn concentration that can be substituted in HA is 15 mol.% and also measured the change in lattice parameters. In case of *a,* it decreased for Zn concentrations of up to 5 mol.% and increased at higher concentrations (10 mol.%). In case of lattice parameter *c,* it monotonically decreased as Zn concentration increased in the sample.

Hayakawa et al. (269) prepared Zn-containing HA particles using an ion-exchange reaction process using zinc nitrate, involving HA particles with aqueous solutions containing various amounts of zinc nitrate, which showed a minor change in degree of crystallinity (without mentioning whether it increased or decreased), particle size and specific surface area. The lattice parameters of HA decreased with an increase in Zn concentration for up to 3 mol.% in their research (269).

Lattice parameters of Zn-HA

Comparing lattice parameters of Zn-HA with pure HA, it was evident that both *a* and *c*-axis parameters decreased after the introduction of Zn^{2+} in both β-TCP and HA phases which suggest contraction in cell volume. This contraction in cell parameters is again due to the lower ionic radii of Zn (0.745 Å) when compared to Ca ions (57, 186, 187).

The decrease in the lattice parameters on both *a* and *c* axes, is consistent with observations by Li et al.(135). Ren et al. (126) also reported a reduction in cell parameters and indicated that both *a* and *c* axes decreased when Zn was added for up to 1 mol.%. However, they reported a slight increase in the lattice parameters when the Zn concentration exceeded 10 mol.%. Miyaji et al. (268) showed that the lattice parameter *a* decreased first when Zn content increased up to 5 mol.%, but increased for Zn of more than 5 mol.% and became almost constant over 10 mol.% Zn. The lattice parameter *c* decreased constantly with increasing Zn concentration. The size of reduction in *c* decreased over 10 mol.% Zn (268).

Results reported by David et al. (270) slightly differ from the findings in this study. They used either the nitrate route with (two different temperatures of 20°C ± 1 and 9°C ± 1) or the hydroxide route, after which they observed a reduction in the *a* lattice but an increase in the *c* lattice. These variations may be due to different reaction temperature to what was used in this study (90°C followed by sintering at 1100°C). Miyaji et al. (132) reported that lattice parameter *a* may increase, as H_2O substitutes the OH sites in the zinc-doped hydroxyapatite.

5.2 Fourier transform infrared spectroscopy (FT-IR)

FT-IR was used as a complementary technique to X-ray diffraction analysis and confirmed the chemical changes in HA after the addition of ions.

5.2.1 FT-IR study of NS-HA

As Figure 4.14 shows, the presence of apatite phase in the final powder can be established by the presence of fundamental vibrational modes of PO_4^{3-} group. The bands at 630 and 3570 cm^{-1} are representative of OH group in the apatite phase while the adsorbed water can be seen in

the region around 3300-3600 cm^{-1}. The presence of carbonate CO_3^{2-} groups at 1430 cm^{-1} can be due to the adsorption of soluble carbon dioxide originating mainly from air during the aqueous precipitation as the experiemnts were not carried out in an inert environment.

As ammonium solution was used for pH adjustment during HA synthesis, it is believed that some residual trace of ammonia was left which was apparent as a small broad peak at 1422.6 cm^{-1} and is the characteristics peak for NH_4^+ group. A similar peak and explanation was observed following HA synthesis in a study by Kang et al. (189).

The presence of nitrates (NO_3) was clear from the peaks in the region around 1320-1480 cm^{-1} as also was pointed out by Raynaud et al. who used a similar synthetic route for preparation and used FT-IR for chemical analysis (207).

FT-IR analysis showed that partially carbonated hydroxyapatites has been formed, based on a strong carbonate-specific bands in the range of 1460–1410 cm^{-1} indicating that carbonate groups have substituted PO_4^{3-} in the hydroxyapatite lattice.

A small peak at 1635 cm^{-1} and a stretched band between 3000-3600 cm^{-1} is expected to be caused by “bound” water or hydration layer, which was present in all the FT-IR spectra and is associated with HA crystals. It is long been known that this hydration layer contains high concentration of calcium and phosphate ions (188). Neuman et al. (271) have shown that ions in the hydration layer are readily exchangeable in the bulk solution. The same peaks were identified in the results obtained by Pak et al. (272) and Avnimelech et al. (273) for HA samples.

5.2.2 FT-IR for Ag-HA

The characteristic PO_4^{-3} group peaks appeared in all apatite samples. This is in good agreement with previous studies (200, 201) (195). The characteristic OH^- peaks were also present and is in agreement with the literature (200, 202, 203). Although not much difference was observed between the HA spectrum with and without silver, the presence of Ag_3PO_4 band around 1070 cm^{-1} was clear. Jelinek et al. (274), reported a small change in the slope of the band in the region of 4000-2000 cm^{-1} in the case of silver doped HA using KrF excimer laser deposition.

Fowler et al. (193) also reported a linear downshift in the internal PO_4^{-3} modes with FT-IR analysis of apatite samples with the decreasing cationic radii and also concluded that this phenomenon is caused by decreased anion-anion repulsion and higher anion-anion separation (193) .

Nirmala et al. (239) reported the change in FT-IR spectrum when they synthesised bioresourced hydroxyapatite containing silver nanoparticles and detected the characteristic transmittance bands for phosphate ion at 845,1045, 1458, 568 and 601 cm^{-1}.

The absorption bands at 873 and 1400 cm^{-1} of the Ag-HA were attributed to the carbonate ion in HA. For hydroxyl groups, they are more apparent at 3569 cm^{-1} at 5 wt.% Ag while the broad hydration layer peak was reduced significantly. In another study by Lim et al. (242), similar results were obtained when Ag introduced to HA using wet precipitation method at concentration range of 0.3, 0.7, 1.6, 3.0, 4.5, and 10 wt. %. They also detected a stretching band between 3200 and 3700 cm^{-1} in the autoclaved Ag-HA which corresponds to bound water molecules.

5.2.3 FT-IR for Mg-HA

After introducing 1 wt.% Mg to HA, all the FT-IR absorption bands were present at similar positions to the ones in NS-HA. This indicates that Mg substitution did not change the apatite structure in HA. The same representative bands for PO_4^{3-} group (574, 609, 966 and 1020–1120 cm^{-1}) and OH groups (630 and 3570 cm^{-1}) of apatite phase are still present in all the Mg-HA samples.

FT-IR patterns tend to coincide with the XRD results as the intensity of OH and PO_4^{3-} bands was reduced after the introduction of Mg in the structure. Adsorbed water could also be detected in the same region (around 3300–3600 cm^{-1}) as well as carbonates (CO_3^{2-}) around 1660 cm^{-1}, which is more pronounced in 5 and 10 wt.% samples. Nitrates (NO_3) were also present around 1320–1480 cm^{-1} resulting from the residual species in the reaction (NO_3^{-1}, NH_4^{+}) and has already been reported elsewhere (207). A peak at 1424 cm^{-1} can be attributed to CO_3^{-2} group which is common for the powders synthesised under air atmosphere.

According to LeGeros et al. (275), the PO_4^{-3} group (B-type substitution) and the OH^- group (A-type substitution) of HA can be substituted by CO_3^{-2} groups. B-type PO_4^{-3} substitution, which is believed to occur mainly during wet chemical synthesis of calcium phosphates has a characteristic vibration band at 1428 cm^{-1} (275).

Increasing the Mg concentration to 5 wt.%, the FT-IR bands assigned to the four PO_4^{-3} modes appear at similar wavenumbers as in HA. However, a reduction in the resolution at around 634 cm^{-1} can be assigned to OH^- librational mode (83, 200, 203), which may indicate the presence of Mg-Whitlockite. The formation of Whitlockite was previously discussed in XRD results in Section 4.1.3. In addition, the PO_4^{-3} peaks, which are present at around 1029 and 1059 cm^{-1} assigned to (195, 200, 201), are merged into a peak at 1062 cm^{-1}. This pattern show that the

phase transformation from Mg substituted apatite to Mg substituted β-TCP (Whitlockite) is more pronounced at higher Mg contents.

FT-IR spectrum in 10w t.% Mg-HA resembles the pattern at 5 wt.% sample with lower separation between the peaks. In addition, the peak broadening is more significant when Mg concentration increases suggesting that the apatite structure is possibly distorted (114).

As mentioned earlier, when magnesium content raised from 1 to 5 wt.%, there was a reduction in the intensity of hydroxyl peaks at 3570 and 633 cm^{-1}which is consistent with the onset of Whitlockite formation. The FT-IR spectra for Mg-HA 10 wt.% revealed a phosphate peak (range 1550–1450 cm^{-1}) that grows wider when MG concentration increases. This also matches with the crystallinity reduction in Mg-Whitlockite (as presented in Table 4.2).

The results in this study were in good agreement with previous studies. Mg-HA has been reported to have lower intensity of OH^- vibration modes at 630 and 3570 cm^{-1}, as well as broad PO_4^{-3} bands when compared with pure HA (13, 114). While the impact of Mg addition was stronger at higher Mg content, these effects were mostly observed in samples prepared by wet chemical precipitation and can be explained by the increased lattice disorder due to PO_4^{-3} substitutions (111, 114, 256).

The position of the CO_3^{-2} derived bands indicates that CO_3^{-2} for PO_4^{-3} substitution (B-type) was dominant in the Mg-HA powders while OH^{-2} groups are replaced by CO_3^{-2} when during wet precipitation route (276) (111).

5.2.4 FT-IR for Zn-HA

Zn-HA samples at concentration of 1 wt.% showed a new broad peak in the region of 1517-1306 cm^{-1} and two water bands at around 3155 and 3037 cm^{-1}. Zn at this concentration did not show any other significant change to the FT-IR spectra. It has also been reported that the CO_3^{-2} which is present in the region of 1570-1410 cm^{-1}(205) might have overlapped with the band in the region of 1575-1279 cm^{-1} originating from residual nitrates (206, 207). CO_3^{-2} is most likely present in Zn-HA like other experiments, especially when the CO_3^{-2} at 871 cm^{-1} was present in the FT-IR spectrum(205).

By increasing Zn concentration to 5 wt.%, the PO_4^{-3} bending bands appeared at 562 and 600 cm^{-1} whilst the PO_4^{-3} stretching bands were centred at 1037 and 1089 cm^{-1}. The broad band between 3300 and 3700 cm^{-1} again is for hydration layer, which overlap and covers the hydroxyl band at 3571 cm^{-1}.

5.3 Raman spectroscopy

5.3.1 Raman analysis for NS-HA

As Figure 4.18 shows**,** an intense peak was detected at around 960 cm^{-1} which can be assigned to $PO_4^{3-}(v_1)$ and is believed to be the characteristic peak of HA present in 963 and 961 cm^{-1} (208, 209). This observation supports previous results from XRD and FT-IR analysis, which showed the presence of the apatite phase.

The Raman spectra clearly indicates that the highest intensity belongs to O–H peak in HA phase. It has been reported by De Aza et al. (215) that the intensity of this peak is directly relative to the crystallinity of the sample. As sintered HA shows higher crystallinity when compared to non-sintered HA, the intensity of this $PO_4^{3-}(v_1)$ is more pronounced. In addition, three other PO_4^{3-} modes are present in the region of 447-430 cm^{-1} (PO_4^{3-}, v_2), 1076-1030-1048

and 1054 cm^{-1} (PO_4^{3-}, v_3), and 610-620-578 and 594 cm^{-1} (PO_4^{3-}, v_4), which are also shown in Figure 4.18 for HA samples.

Penel et al. (209) pointed out that the Raman peak at 1070 cm^{-1} does not correspond to the PO_4^{3-} (v_3) mode solely, as the A-type and B-type CO_3^{2-} (v_3) modes were also present at a similar peak position at 1107 and 1070 cm^{-1}, respectively. This may suggest that some Carbon Dioxide may have been included during synthesis. Additionally, the Raman peak at 1076 cm^{-1} can be caused by both PO_4^{3-} (v_3) mode (208, 209) and B-type CO_3^{2-} (v_1) mode (209) (Figure 4.19).

5.3.2 Raman analysis for Ag-HA

Similar to NS-HA sample, the symmetric stretching for P-O bonds (ν_1) was detected at (960 cm^{-1}). The vibrational bands at 429 cm^{-1}(ν_2) and 450 cm^{-1}(ν_2) can be attributed to the O-P-O bending modes. Both peaks at 1046 cm^{-1} (ν_3) and 1074 cm^{-1} (ν_3) were assigned to asymmetric ν_3 (P-O) stretching. The ν_4 frequency (589 and 608 cm^{-1}) can be addressed mainly to O-P-O bending character. As silver concentration increased to 5 %, the intensity of vibration peak reduced but in general, most phosphate bands became broader after addition of silver ions, responsible for increasing disorder in the structure. Again, these results compliment the findings from the XRD and FT-IR analysis.

It worth noting that pure metallic Ag is neither IR nor Raman active and the formation of AgO and Ag_2O are not thermodynamically feasible up to the maximum sintering temperature (1300°C) (216). Also the Ag–O bonding from either AgO or Ag_2O phase could not be detected by FT-IR within its detection range of 400–4000 cm^{-1}.

5.3.3 Raman analysis for Mg-HA

Raman spectra peaks in Mg-HA 1 wt.% sample were almost identical to ones present in the NS-HA. Peaks at around 1075 and 1046 cm^{-1} in the spectrum are believed to correlate to asymmetric stretching (ν_3) of the P–O bond in phosphate. However, the small shift can be due to the non-stoichiometric HA and also incorporation of Mg in HA. The peak around 970 cm^{-1} is expected to have been caused by the symmetric stretching mode (ν_1) of the P–O bond in the phosphate group. This peak, however, is normally expected to be present at 961 cm^{-1} in hydroxyapatite (209). The small shift observed can be caused by the incorporation of the magnesium ions in the HA lattice. Moreover, based on the unit cell lattice parameter results, which were obtained from the XRD data (Section 3.1.3), the unit cell volume decreased with higher magnesium content (because of larger calcium ion being replaced by the smaller magnesium ion).

The resulting compressive stresses after the change in the unit cell volume can be responsible for the observed shift in the peak position (277). A similar peak broadening in Raman spectra was reported by Sprio et al. (278), after the addition of Mg to HA and was explained by the less ordered structure. This peak broadening effect can also be caused by the segregation of Mg ions outside the HA lattice (278) or the accumulation of CO_3^{2-} ions within the sample. Specifically, it has been reported that the phosphate peak became broader when CO_3^{2-}concentration was increased (279).

There are two factors which may influence the vibration behaviour of phosphate ions: 1) P-O bonds may experience weaker intra-molecular interaction due to new inter-ionic Mg–O interactions and 2) the repulsion potential of the lattice, which is inversely proportional to the

unit-cell volume. These two factors are believed to contribute to the broadening of the phosphate peak in these samples, as also described in a study by Chaudhry et al.(280).

Two peaks at 610 cm^{-1} and 587 cm^{-1} correspond to the (ν_4), whereas the peaks at around 442cm^{-1} and 432 cm^{-1} correspond to the (ν_2) bending of the O–P–O linkage in phosphate groups in HA. The small shift observed in (ν_4) and (ν_3) in the spectra of Mg-HA 5 wt. % and Mg-HA 10 wt.%, which can be caused by the incorporation of magnesium ions in the HA lattice and formation of TCP. Also Mg-HA 5 and 10 wt.% samples each revealed a peak at 555 cm^{-1} and 633 cm^{-1} which corresponds to the bending modes of the O–P–O linkage in phosphate ions in Whitlockite (281). These results are also in agreement with the appearance of the Whitlockite phase in the XRD profile as shown in Figure 4.6 and Figure 4.7.

5.3.4 Raman analysis for Zn-HA

Similar to previous samples, the spectra for Zn-HA 1 wt.% are very similar to those observed for NS-HA. This indicating, that the HA structure can tolerate the presence of 1wt.% of Zn, and XRD results have already supported this conclusion.

The asymmetric stretching peaks (ν_3) of the P–O bond in phosphate are again present at around 1076, 1055 and 1029 cm^{-1}. However, stretching peaks (ν_3) of P-O band of phosphate in 1030 cm^{-1} are more pronounced by adding Zn in HA. The peak around 961 cm^{-1} is lost likely caused by the phosphate group. As discussed earlier, this peak is generally expected to be present at around 963 cm^{-1} in pure HA (209). Similarly, the shift can be explained by the addition of Zn into the HA lattice and as unit cell measurement suggests (as described in section 4.1.4), a similar drop in unit cell volume was resulted with the increase in Zn content (because smaller Zn ion replaced the larger calcium ion). Peaks at around 610 cm^{-1} and 587 cm^{-1} correspond to

the (ν_4). Peaks at 447 cm^{-1} and 433 cm^{-1} also correspond to the (ν_2) bending of the O–P–O linkage in phosphate in HA. The small shift observed in (ν_4) and (ν_3) in the spectra of Zn-HA 5 % and 10 wt.%, which can be caused by the incorporation of the zinc ions in the HA lattice and formation of TCP. Also, Zn-HA 10 wt.% samples each reveal a peak at 546 cm^{-1}, which are caused by bending modes of the O–P–O linkage in phosphate.

Gomez et al. have reported the new modes (ν_1) at 940 cm^{-1} which is believed to be for a new component, (282). The new modes (ν_1) indicate a loss of order (due to statistic disorder in the hexagonal channel) when Zn inserts the HA crystal structure. By increasing the Zn concentration, a new band appeared at 3410 cm^{-1}, which is attributed to the Zn insertion in HA crystal unit. This confirms that Zn is directly responsible for the deterioration of HA crystallinity. However, these two new modes have not been detected in present study.

Disorientation in HA crystal observed by Gomes et al. but has been reported to occur at lower concentration of Zn (1 wt.%) (283). Their results from Raman spectra of Zn substituted samples show the presence of a third [OH] stretching mode at 3584 cm^{-1}.

5.4 Thermal Stability Analysis

5.4.1 Thermogravimetric analysis of NS-HA

The TG analysis of the HA powder (NS-HA) was carried out between the room temperature and 1100°C (sintering temperature in this study) in order to understand the phase transformation within the sintered samples. There are three regions of interest corresponding to HA structure which are applicable to the temperature range studied in this research:

1. Up to 200°C, which corresponds to the removal of structure-adsorbed water. Adsorbed water is characterised by its removal between 25 to 200°C and weight loss with no impact on lattice parameters (284).
2. Between 200°C and 400 °C, which corresponds to the lattice water. Within this temperature range, contraction of *a*-lattice dimensions occurs during heating (284).
3. At higher temperatures (above 400 °C), the hydroxyapatite gradually dehydrates, which leads to the release of OH^- ions and the subsequent transformation to oxyhyrdroxyapatite (OHA). The HA dehydration does not occur instantly but over a wide temperature range, which is suggested to be dominantly dependent of the partial H_2O pressure during the heating step. If performed under vacuum, HA loses its OH at a lower temperature, about 850°C. If HA is heated in H_2O stream, the structure of HA is then preserved up to 1100°C (285).

For NS-H samples, the weight loss at the beginning of the TG plot between 25°C and 200°C corresponds to the removal of adsorbed water (about 0.9 % ± 0.021 weight loss). At higher temperatures (between 200 °C to 500 °C), the weight of NS-HA sample gradually decreased which corresponds to the removal of lattice water (about 0.77% ± 0.027% weight loss). Rootare et al. (286) carried out detailed studies of vapour phase adsorption of water on HA and concluded that the water monolayer that is in contact with the HA surface (lattice water) was more strongly bound than the additional water.

The weight loss trend continues (at a slower rates) from 500°C to 800°C which corresponds to the transfer of HA to OHA (about 0.59% ± 0.13%). Consequently, partial decomposition of HA to TCP happen as described above. The total weight loss was about 2.5 wt.% for NS-H sample.

5.4.2 Thermogravimetric analysis of Ag-HA

The temperature where the weight loss peak (or slope change) appears between 700-850 °C is a representation of how much the HA phase is stable. Based on the results from XRD analysis (see section 4.1.2), the stability of the HA phases increases by addition of more silver ions. Hence, it is expected that the weight loss peak appears at higher temperatures when the ion concentration increases in the HA samples

In case of Ag-HA sample, a sharp peak was present in region of up to 200 °C. The main stage which corresponds to the stability of the sample is the region between 600 and 1000°C. This is when the further removal of hydroxyl groups occurs and the early decomposition of hydroxyapatite lattice onsets. However, it is expected that the decomposition temperature was higher than NS-HA when Ag concentration increased. This result is consistent with the findings in XRD analysis (Section 3.1.2), confirming the increased stability of HA phase by addition of silver. The total weight loss for the Ag substituted HA in the range of 25–1100°C was maximum about 1.2 wt. %. Also the residual weight increased slightly as Ag was added in the HA sample, as Figure 4.22 shows.

5.4.3 Thermogravimetric analysis of Mg-HA

As it is expected, a series of weight losses were observed in the TGA curves for Mg-HA samples. The weight loss in all different Mg-HA samples are very similar to NS-HA in 25°C to 400°C region.

The weight loss within 690–800 °C region is probably due to the loss of OH during decomposition of HA to β-TCP. TG curves suggest that the decomposition temperature decreases with increasing Mg content. As XRD data confirmed (Section 4.1.3), by introducing

more Mg to HA structure, Whitlockite phase was formed which causes more Mg destabilization in the apatite structure. The TG curves presented in Figure 4.23 supports the presence of Mg within apatite structure, as the surface adsorption of Mg cannot influence the decomposition temperature of HA structure.

The total weight loss increased with increasing Mg concentration as opposed to Ag samples. Mg-HA 10 wt.% showed the highest weight loss of about 8 wt.%. The thermal decomposition of apatite to (β-TCP) can be seen by the slope change in the TGA graph because of the OH loss associated with apatite phase change. Above 600–700 °C, nonstoichiometric Mg-HA decomposes usually with the formation of whitlockite and water (111, 287). However, at higher Mg concentrations, formation of $Ca_4Mg_5(PO_4)_6$ or β-$Ca_2P_2O_7$ has also been reported (287).

As Figure 4.23 shows, TGA curves for Mg-HA also shows three different thermal profiles. The Mg-HA with 5 wt.% showed a sudden weight loss between 735°C to 798°C which is believed to indicate the decomposition into whitlockite (total weight loss about 10.52%). On the other hand, the Mg-HA sample with 10 % showed a weight loss at 720°C which could be due to the presence of larger quantities of Mg^{2+} and lower crystallinity (114, 287), which was also confirmed by XRD results (Section 4.1.3). As a conclusion, the thermal stability of Mg-substituted hydroxyapatite decreases by increasing the content of Mg into hydroxyapatite products and also Mg-HA partially transforms to Mg-substituted β-TCP or Whitlockite when more Mg was added.

5.4.4 Thermogravimetric analysis of Zn-HA

As Figure 4.24 showed, the weight loss is more significant in samples with higher Zn concentrations (total weigh loss about 10.52%). The amounts of both the adsorbed and lattice

water increase with increasing Zn substitution. Miyaji et al. reported that the lattice parameter *a* decreases with increasing the amount of lattice water (132). The value for lattice parameter *a* decreased by the increase of Zn concentration (Section 4.1.4), which can be explained by the combined effects of the ionic radius of Zn and the lattice water. For the samples with higher Zn concentrations, the effect of increasing lattice water might overcome that of the substitution by Zn with smaller ionic radius (132).

Similar to previous samples, there is a continuous weight loss in the samples as temperature rises. The significance of the weight loss during the last stage increased as the amount of zinc in the samples increased, which might be linked to the formation of other phases or removal of a volatile species of zinc.

As expected, the TCP formation for the lowest Zn content (1 %) sample occurs at a higher temperature suggesting its higher thermal stability. The temperature when the destabilisation begins is about 790°C, which is very similar to NS-HA. By increasing the Zn concentration, the decomposition temperature drops to about 740 °C suggesting its lower thermal stability. Results from the XRD analysis (Section 4.1.4) also confirmed that the parascholzite formation was very similar in samples with 5 and 10 % concentrations.

5.5 Measuring the substituted ions in solid samples

Ion substitution using the wet precipitation technique consists of a reaction between mixing soluble precursors and the formation and precipitation of a generated calcium phosphate phase. The soluble ion reactants in the reaction medium also drive the substitution of Ca cations in the HA structure. The concentration of the substituted ions may be assumed to be the same as the

initial concentration of ions in the reaction solution. However, this may fail to be the case with the used technique in this research because:

1) The total uptake of ions in the solid can be affected by the reaction conditions and possible structural considerations, which may limit the number of ions impregnated in the HA crystal.

2) The final powder is washed several times with distilled water to remove any non-reacted reaction residues that may have left on the powders. This was of particular importance in this study, as these samples were to be used in biological and microbiological studies where any the intention was to minimise any interference from chemicals other than the solid phase hydroxyapatite.

A review of existing published research where similar biomaterials were used to measure the biological response indicated that most of the studies assumed a "nominal" concentration of the ion in the solid phase of hybrid hydroxyapatite formulation.

Measurement of the ions substituted in the solid phase was of special importance for this research, in order to explain the correlation between the biological response and the ion concentration in the final biomaterial. The existing values for ion toxicity levels and any impact on cellular activity (such as proliferation, differentiation and mineralisation) are assumed to be mainly due to the additional ions. In addition, the release profile data will be more meaningful if the concentration of ions in the solids are known.

It worth to note that because of the non-selective nature of wet precipitation technique and the poor control of synthetic reaction, there is always the possibility of secondary phases formation or surface adsorption of ions. Analytical techniques such as XRD and FT-IR can only be used to obtain qualitative measurements and to confirm the inclusion of the ions in the solid apatite

structure. These techniques cannot accurately measure the concentration of the substituted ions. Hence, Inductively Coupled Plasma-Mass Spectroscopy (ICP-MS) and X-Ray Fluorescence (XRF) methods were selected as two techniques to measure more accurate levels of ion substitution in the prepared powders.

XRF is the selected method for quantification of different elements using their characteristic secondary X-ray patterns within the solid structure. XRF is a gold standard technique in studying ion-substitution in hydroxyapatite ceramics which enables the determination of total ion incorporation in the HA structure. Knowing the content of the substituted ions, it is possible to elucidate the chemical composition and Ca/P ratios within the HA structure, and investigate how much of the selected ion was substituted.

To minimise any possible matrix or surface effects during XRF measurement, quantification of ion substitution was accompanied by ICP-MS technique. While XRF can be used for solid specimens, ICP is predominantly for liquid samples. However, as explained in Section 4.5.1, mass balance calculation was used to measure the total ions remaining in the solid phase. Results from these two techniques reported almost identical values for the amount of ion incorporation in each sample.

5.5.1 Measuring of degree of ion substitution by XRF

For all samples, XRF measurement confirmed the presence of metal cations in the HA powder. While washing of the solid powder should have removed most of the non-substituted ions trapped in the loose structure or surface-adsorbed cations, the detected metals were assumed to refer to ones incorporated in the HA structure.

The XRD pattern indicated that lattice parameters have changed, confirming the substitution of

selected cations in the lattice structure of the HA. XRF measurements, as shown in Tables 4.17, 4.18 and 4.19, also confirm that the Ca/P ratio of the resulting HA has changed from that of the starting material, suggesting a change in the reaction stoichiometry.

In case of Ag-HA, XRF measurement in Table 4.17 confirmed that silver was incorporated in HA and that its concentration increased as more silver ions were available in the reaction medium.

The higher ratio of cations to phosphorus can be due to the change in the stoichiometry of the HA structure, or to the depletion of phosphate ions in the HA structure due to the presence of carbonate ions. It is also possible that some of the Ag ions were only adsorbed on the surface of HA or being incorporated as defects, suggesting that the actual Ag in the structure is less than what was measured. The substitution of Ag ions was confirmed earlier by changes in the lattice parameters, though the extent of the substitution may not be as high as levels measured by the XRF. XRF cannot distinguish between ions adsorbed on the surface and those which are just incorporated as defects or ones which are substituted in the structure.

The amount of Ag substitution in the solid was almost half of what was expected; a maximum of 4.23 wt. % of Ag was substituted. While the ratio of cations (Ag/Ag+Ca) during reaction was adjusted to 1, 5 and 10 mol.% in the reaction medium, the actual amounts of Ag/Ag+Ca were 0.48, 2.53 and 3.68 mol.% in the respective samples. Ca/P and Ca+Ag/P molar ratio increased to about 2 as Ag was introduced into the structure, which suggests a change in the stoichiometry of the reaction. Also, some of the phosphate may have been replaced by other anions (such as carbonate ions) resulting in fewer phosphorus ions being available in the solid.

Other studies have also indicated lower levels of Ag in the solid phase than expected. Lim et

al. added 0.3, 0.7, 1.6, 3.0, 4.5, and 10.0 wt.% of Ag to the reaction medium, but the resulting solids showed 0.2, 0.3, 0.5, 0.9, 1.0 and 1.1 wt.% respectively, suggesting a maximum of about 1 wt.% Ag substitution (242).Oh et al. (288) also used the wet precipitation route for preparation of Ag-HA, but could not incorporate more than 32% of the starting material into the final solid structure.

Loss of Ag ions during the powder washing steps, which aimed to remove impurities and reaction residues, might also contribute to a lower concentration of Ag in the final sample. Ag ions also have a larger ionic radius than Ca, which is expected to obstruct the Ag being fully incorporated during HA synthesis, resulting in lower levels of Ag incorporation in the solid (242).

With regards Mg-HA samples, both XRF and XRD assays confirmed the incorporation of Mg in the HA structure. The XRD pattern in particular confirmed that Mg was substituted in the HA lattice, as the lattice parameters changed after Mg was introduced into the medium. As Table 4.18 shows, the expected values for Mg incorporation for both molar ratio and wt.% ratio were very similar to what was expected in the final powder. Mg concentration (wt.%) in the HA reached a maximum of 2.43 wt.% in Mg-HA 10% (vs. 2.55 wt.% expected), which was 9.07% in terms of molar concentration (Mg/Mg+Ca).

The content of Mg in Mg-HA ceramic and the level of its incorporation has been the subject of many discussions within the research community, and different levels of Mg incorporation have been reported. LeGeros et al. (111) indicated that incorporation of Mg in synthetic HA is limited to 0.4 wt.%, while Yasukawa et al. (124) reported that 31 mol.% of Mg (or the ratio of Mg/Mg+Ca) is the maximum of Mg in HA phase through wet precipitation before an

amorphous phase being formed. The maximum amount for Mg incorporation was not more than 10 atom.% in the study conducted by Bigi et al. (13).

It has also been suggested that Mg has a tendency to stay on the surface of HA crystals during wet precipitation (surface adsorption) rather than being fully substituted in the HA structure (13). XRF analysis alone cannot determine the location of ion accumulation, whether on the surface, being present as defectsor at different regions of the crystal. Other techniques such as XPS are capable of determining the ion concentration at various depths of crystals (29), but were not used in this study because of limited technical resources. It is not possible for us to determine what ratio of Mg was being surface adsorbed or substituted within the structure, but it is expected to be a combination of these two cases.

Similar to Ag-HA preparation, the ratio of cations to phosphorus ions (Ca+Mg/P) was adjusted to 1.8, but this ratio increased to 1.91, 2.02 and 2.07 for Mg-HA of 1, 5 and 10 mol.% samples.

Most studies, however, confirm that increasing the Mg content will decrease crystallinity and lead to amorphous phases, such as Whitlockite (29) (217), similar to the results as discussed in Section 4.1.3 for XRD analysis of Mg-HA. The presence of Whitlockite phase in Mg-HA 5 and 10 mol.% samples were also observed, as discussed earlier.

For Zn-HA samples, the values for Zn substitution are summarised in Table 4.19 and they confirm that Zn was incorporated in the HA structure, but not at levels observed with Mg ions. Zn concentration in Zn-HA 1% was 0.56 wt.% (vs. 0.65 expected), for Zn-HA 5 wt.% it was 2.8 wt.% (vs. 3.2 wt.% expected), and for Zn-HA 10% it was 4.23 wt.% (vs 6.32 wt.% expected). These values, however, were consistent with the values obtained from ICP-MS analysis for Zn incorporation in Zn-HA (Section 4.5.1).

Different levels of Zn incorporation in HA have been reported in different studies. Ren et al. reported up to 20 mol.% (Zn/Zn+Ca) of incorporation using the wet precipitation technique, by setting the Zn concentration to 20 mol.% in the solution. However, they reported that an amorphous phase was formed at this high concentration of Zn (126). However, could not detect more than 0.7 wt.% of Zn while they expected to have a maximum of 5 wt.% (289). Li et al. (21) suggested that at Zn concentrations of more 0.13 wt.%, a new phase of Zn-TCP was formed, which was in agreement with the results of observing a TCP phase at 5 and 10 mol.% (the equivalent of 2.8 and 4.23 wt.%).

The Ca+Zn/P ratio for Zn-HA 1, 5 and 10 % was higher than what was set in the reaction (1.8), similar to Ag-HA and Mg-HA. The higher ratio of cations to phosphorus can be explained by either less phosphate ions in the HA structure (for example, because of carbonate substitution instead of phosphate) or by the surface adsorption of Zn instead of substitution in the HA lattice. Again, it was not possible to fully quantify how much Zn was substituted in the lattice, but the change in lattice parameters and the provided XRD profile confirm that Zn substitution in the HA phase has occurred.

5.5.2 Measuring ion substitution with ICP-MS

The discrepancy between the molar and weight ratio is directly related to the molecular weight of each ion. It is expected that when Ag with a MW=107 is substituted in the HA structure in similar molar ratios, it results in a higher weight ratio in comparison to Zn.

The overall results suggest that no matter how high the concentration of ion alters in the solution, there is a limit to how many ions can be substituted in the hydroxyapatite structure.

This limit based on the results was calculated to be 3.5 wt.% for Ag, 2.2 wt.% for Mg and 5.3 wt.% for Zn. The hydroxyapatite structure did not take up relatively more Ag (only increased by 10%) when the concentration of Ag was doubled from 5 to 10 wt.% in the solution. In absence of advanced analytical assays, one explanation for this limitation may be the larger size of Ag ions in the lattice compared to Ca, Mg or Zn and difficulty to fit in HA lattice.

With regard to Mg-HA, the lower MW of Mg ions explains the lower values for Mg weight ratio, as explained earlier. When the molar ratio of Mg in the solution increased, the wt.% ratio of the Mg in the HA lattice increased at almost the same order. When the concentration of Mg was increased 5-fold (5%) and 10-fold (10%) in the solution from the 1% sample, the wt.% of substituted Mg also increased by factors of 5.9 and 7.8 respectively.

In case of Zn-HA samples, increasing the concentration of Zn by factors of 5 and 10 resulted in 2 and 3.1 times increase in the Zn wt.% incorporated in the HA lattice.

5.5.3 Release profiles for Ion-substituted HA

The maximum concentration of ions in the medium plateaued in the range of 0.04, 10 and 0.01 ppm for Ag, Mg and Zn samples respectively. In terms of total number of ions released, these concentrations are only a minor fraction of the ions substituted in the solids, except for Mg (see Figures 4.25, 4.26 and 4.27).

The release profiles for the three different samples follow a similar pattern and confirm that:

a) For all samples, a direct relationship exists between the concentration of ions in the solid sample and the amount of ions released.

b) Most of the ion contents are released during an initial burst from the solid sample. This was less evident for Mg-HA, which showed a more sustained release. This burst release may also suggest that there is a considerable levels of surface adsorption of ions to solids in all the samples. d

The ion release data can be used to estimate the relationship between final ion concentration in the liquid phase and the solid phase. Using these data, it is possible to synthesize an HA sample with the right amount of substituted ions in the solid for the expected concentration in the liquid phase, which can give the optimum biological response (for example, in terms of antibacterial activity). After 21 days, there was only a slight sign of visible disintegration of the solid. The surface area will directly affect the final concentration of the ions in liquid; however, this parameter was not investigated in this study, and all samples were prepared in identical disk shape.

Assuming that solid structure and morphological parameters remain the same in all the samples, it is expected that ion solubilisation was controlled by the following mechanisms (Figure 5.1):

1) Diffusion, from the solid surface to the liquid and then to the bulk of the liquid;

2) Dissolution, during which the solid is solubilised in the liquid and ions are released while diffusion occurs at the same time.

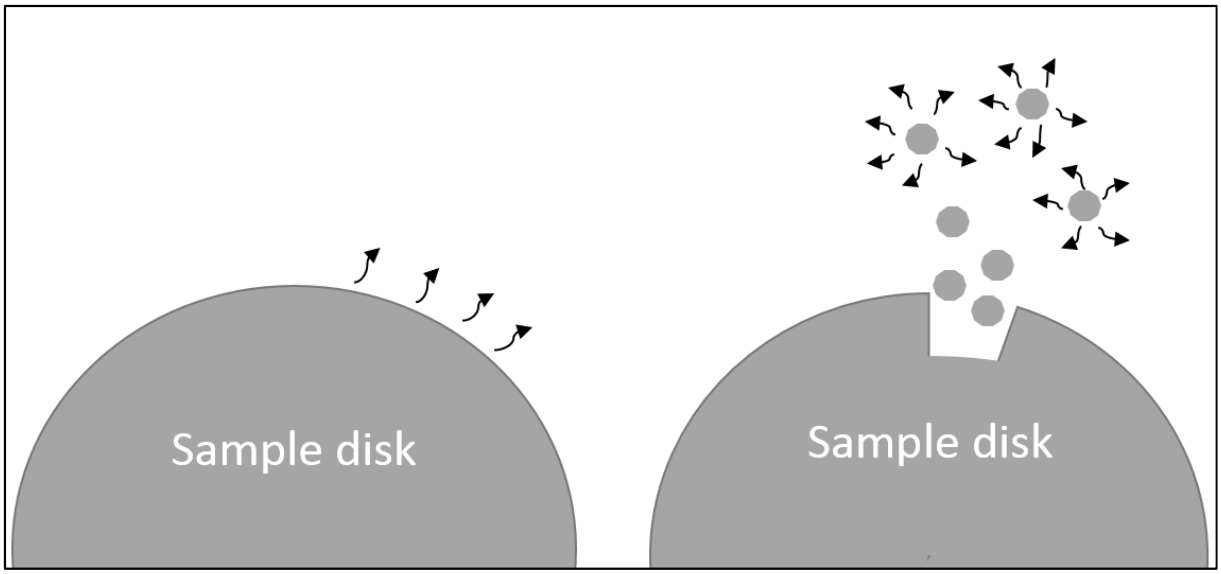

Figure 5. 1: Proposed mechanisms for the release of metal ions from solid disks. Diffusion (left) and Dissolution and diffusion (right)

Mass transfer and diffusion within the solid structure towards the surface is believed to be limited, hence ion diffusion mostly occurs from the outer surface of the disks to the immediate layer of liquid surrounding the solid. By depletion of the ions in the surface, the concentration of the ions in the liquid phase will reach a plateau, which normally is a small fraction of the total ions available in the whole disk of solid.

The dissolution mechanism, on the other hand, is expected to result in a higher quantity of ions being released. The resulting higher number of solid particles will increase the total surface area, resulting in higher rates of diffusion in the liquid phase. The dissolution mechanism is expected to be present in the solid samples which are readily soluble in the liquid phase. As an example, TCP phase in calcium phosphates is believed to have much higher solubility when compared to HA phase. As a result, when TCP phase is present in the solid structure, higher solubility and higher concentration of ions are expected to occur in that sample.

As explained earlier, other parameters may influence the rate of solubilisation such as morphology, crystal size, crystallinity, density and Ca/P ratio but were not studied in this research (138).

The measured release profile is strongly affected by the surface area of the solid, and the surface of the disk is much smaller than the powder coating which is disturbed on the surface of the implant. The size of the crystals then becomes important factor, as finer particles will have more surface area and a higher release of metal ions will occur. These parameters were expected not vary significantly within the range of samples prepared in this study. Sample disks were compacted with high force to ensure that they sustain their solid structure when submerged in the experiments, and thus the effects of particle size on mass transfer is expected to be minimum. However, it is expected that the proposed model for mass transfer to have limitation to fully simulate the mass release profile from powder coatings in real samples.

As a general observation, Ag-HA and Zn-HA samples showed a burst release during which almost all the ions were released in the first 48 hours. For Mg-HA, the burst release was less pronounced and Mg tended to show a more sustained release.

A burst release in the prepared solid structures may be due to the following reasons:

a) During sample preparation, some of the ions were accumulated on the surface of the powder or may have been adsorbed by weak physical bonds or as defects, which are released only when submerged for extended times. This fraction of ions may have remained on the solid surface even after being washed several times during sample preparation steps.

b) A burst release can also be attributed to the release of ions from crystals on the surface which ions substituted in their lattice. While most ions on the surfaces or defect fractions are

solubilised, the concentration remains constant and no more ions are solubilised from the surface (as a result of the diffusion mechanism described earlier).

In case of Ag, the maximum concentration of silver ions was reached at 0.4 ppm from 10% Ag-HA sample after an initial burst release. 0.4 ppm of silver in the liquid was equivalent to less than 0.2% of total Ag in the solid specimen.

Mg-HA, however, followed s slightly different pattern when compared to Ag-HA and Zn-HA (Figure 4.26). Firstly, the concentration of Mg in the liquid was much higher when compared to Ag and Zn (almost 100 times), and secondly, Mg release followed a more extended release profile, as it reached its maximum concentration after more than 100 hours compared to 24 to 48 hours in Ag-HA and Zn-HA.

The main factor which may explain the high concentration of Mg in liquid are either the 1) higher surface adsorption of Mg ion on the surface of HA, or 2) higher solubility of Mg-HA in liquid because of higher dissolution of solid in the liquid phase. Based on the solubilisation mechanisms explained earlier, it is expected that Mg-HA solubilisation is mainly governed by the second mechanism since:

a) The mass balance calculation (discussed in Section 4.5) indicated that the concentration of substituted Mg varies between 0.3, 1.7 and 2.2 wt.% in 1, 5 and 10 % Mg-HA respectively. When compared with Ag-HA and Zn-HA, there is a similar range of ion concentration in the solid. Hence, if the diffusion was the main mechanism (a function of ion concentration on the surface of the solid), there should have been a similar range of ion concentration in the liquid for Mg-HA as well.

b) Morphology, physical conditions and fluid dynamics, which may change the diffusion mechanism, were identical in all experiments.

c) XRD results in Section 4.1 confirmed the presence of TCP phase in Mg-HA samples. TCP phase is known to have higher solubility and less stability compared to HA phase (discussed in the literature survey in Section 2.3: Calcium phosphates), suggesting that the dissolution mechanism will predominate over diffusion in this sample. As TCP phase solubilises in solution, any Mg-ion contained within that phase will be released, which may explain the high concentration of Mg ions in the liquid phase.

The higher ratio of Mg ion release may also be due to a higher amount of Mg adsorption on the surface of the solid Mg-HA samples or incorporated as defects, but no specific surface measurement techniques (such as XPS) were available to confirm this hypothesis.

In respect of Zn-HA, it showed lower rates of ion release (similar to Ag-HA) accompanied by a burst release within the first 24 hours. The maximum concentration of Zn in liquid was 0.06 ppm, predominantly from the surface of the solid. Lower rates of Zn release can support the idea that the majority of the ions are substituted within the HA structure and there was no strong surface adsorption. These results were also in agreement with XRD confirming Zn substitution in the HA structure.

The small fraction of β-TCP phase was observed in the XRD profile of Zn-HA of 5 and 10% samples (Figure 4.10). This, however, did not seem to have much effect on the solubility of Zn-HA samples.

5.6 Cell Biology

5.6.1 Cell Proliferation

Metallic compounds are known to initiate adverse responses in humans or experimental animals in an excessive amount that may represent their toxicity level (219, 290). However, even a chemical generally regarded as toxic (such as Ag) shows no toxic effect in a small concentration, while a vital substance (such as Mg or Zn) may trigger adverse responses at high concentrations. In case of the metal ions selected in the current research, there are no inclusive studies to measure and compare the relationship between the concentration of these ions and the resultant toxicity and biological responses. Furthermore, the level of released ions from the implanted devices cannot easily be determined *in vivo*. Therefore, *in vitro* experiments were developed with the objective of measuring the relationship between the concentration of metallic compounds and biological responses of cells. Generally, it is expected that an ideal bioactive implant will offer active interaction with cells and stimulate cell growth (291).

As indicated in Figure 4.28, there was a steady increase in 2T3 proliferation from 2 days to 6 days in the presence of NS-HA discs. These preliminary results, which represent a favourable response from the studied cells, confirm the biocompatibility of hydroxyapatite in terms of cellular response

The same behaviour in osteoblast cell lines has been reported by Qu et al. (292) but only after 3 days incubation. They demonstrated that cells cultured with ceramics with higher crystallinity initiate a higher proliferation until they reach the highest proliferation rate within 3 days.

Regardless of any contribution from the incorporated metal ions, there are three main factors that can lead to different cellular responses in the studied experiments:

1) Physical properties, such as the morphology of the specimen, agglomeration of the

particles and crystal size (including degree of crystallinity), can change the response of the studied cells. As explained by Evans et al., cell interaction and, ultimately, any positive and negative impacts are directly related to the cell-particle interaction, which can be affected by physical attributes of the solid sample independent of the chemical nature of the particles (293).

2) Chemical properties, such as the material's composition and variation in its chemistry, which can change the chemical ingredients in the culture media in favour of or against cellular activity. In case of HA samples, the rate of calcium phosphate dissolution is correlated with the ratio of Ca/P ions and, consequently, the pH of the surrounding environment (293). The dissolution rate (both in body fluids or *in vitro*) is more critical when the crystallinity degree is lower, as it results in higher ratios of dissolution. The resulting alkaline pH would lead to a cytotoxic effect inhibiting DNA, and protein synthesis and cell proliferation in cell cultures.
3) Biological properties, the osteoblast cells used in this study had different origins, which may result in the varied responses observed compared to Qu et al. Lang et al. (294) reported that the human osteoblast-like cells reacted slightly more sensitive to toxic substances on tested materials compared to rat osteoblast-like cells.

Based on the results from Ag-HA samples, it can be concluded that silver can promote cell proliferation but can have negative effects at higher concentrations of the study (10 wt.%), *in vitro*. Although Ag has been shown to have a broad antibacterial effect; high concentrations of Ag have been reported to be cytotoxic against human cells. The results showed that 10% Ag-HA samples expressed adverse effects against osteoblast cells by dropping their proliferation

rate at all time intervals. In addition, by increasing silver to 10%, the degree of the crystallinity of final samples decreased, and consequently, the solubility of HA should have increased. Because no unfavourable effect was observed in the NS-HA sample, it can be concluded that Ag ions can be the main factor in the reduction of cell proliferation. This conclusion, however, assumes that any change to HA structure because of Ag incorporation had a minimum impact on the biological response. As discussed earlier in Section 2.4.4, silver's toxic mechanism can be explained by electrostatic interactions with the cell membrane followed by their entry into the cytoplasm and subsequent interactions with DNA and proteins (295).

Based on the data presented in Table 4.20 and the results from the cell proliferation assessment, when the concentration of the Ag ion increases to 0.3 ppm (which is expected to be achieved by the 5 wt.% Ag-HA sample in the cell culture medium), cell proliferation is negatively affected. Yamamoto et al. (296), compared the cytotoxicity of silver in HA samples to MC3T3-E1 osteoblast cells. It was shown, that 0.298ppm of Ag^+ reduces the proliferation of osteoblast cells by 50%. At a concentration of 1.07 ppm Ag^+, only a small percentage of osteoblast cells could proliferate, and when the concentration of Ag increased to 2.14 ppm and higher, zero osteoblast cells survived (296). However, the results obtained from the present study indicate that a maximum silver concentration of 0.3 ppm (with the Ag-HA 5% sample) can increase the rate of 2T3 cell lines up to 19% before reaching a plateau. Moreover, a silver concentration of 0.4 ppm (as was expected to be released from the Ag-HA 10% sample) can reduce the proliferation of the studied cell line by 35% after 6 days incubation.

However, the effect of silver in HA in the attachment rate of mouse osteoplastic (MC3T3-E1) cell lines (an initial step to cellular response) has been examined in another study by Sandukas et al. (297), who suggested that the optimum concentration of Ag is between 1%wt. to 3% wt.,

the equivalent of 0.78 ppm to 1.7 ppm in the medium. Sandukas et al. (297), however, suggested that higher concentrations of silver (0.7 ppm) do not show any negative effect (compared to 0.3ppm in this study). They did not measure the proliferation rate of their cells, instead concentrating on the adhesion and spreading of cells on the surface of Ag doped HA. The surrounding liquid for measuring the Ag concentration was different, which may affect Ag release quantities, but they reported a similar burst release from hydroxyapatite after 172 h (297).

In another study, the viability of the human mesenchyme stem cell (hMSCs) line on Ag-HA was studied, and positive results were reported in terms of the biocompatibility and antibacterial activity of hydroxyapatite with 0.5 wt. % of Ag which was equivalent to a maximum 0.5 ppm release(242). In the same study, it was also reported that actual silver's incorporation into hydroxyapatite was lower than expected, which the XRF and ICP results also confirmed (Section 4.5 and 4.6). In addition, they showed the proliferation of the candidate cell line on 0.05ppm silver to be similar to hydroxyapatite after seven days. These finding, however, suggests a sharp release profile of silver in 3 days followed by a minor release in the following days.

Lim et al. (242), showed that the slow release of Ag in 7 days (0.5ppm) is favourable in terms of antibacterial properties, while the results suggest that 0.3 ppm silver in 3 days is effective regarding higher cell proliferation. Conversely, plateau release of silver after 3 days helps in retaining the antibacterial properties of samples.

Similarly, Chen et al. (108), reported that the HA coating with a silver concentration of <5% is not toxic to the murine fibroblast L929 cell line, but the antimicrobial activity is >90%.

However, they did not report any measurement of actual concentrations of silver in the medium and how it can be related to the activity of the murine fibroblast L929 cell line.

The results, supported by the detailed results from the material characterisation and release profile measurement, directly relate to the characteristics of a solid sample. In addition, the concentration of released ions from the samples to the observed cellular activity. The results suggest that silver hydroxyapatite substitution in 1% and 5% (equal to a maximum 0.3 ppm of Ag release) can promote osteoblast cell proliferation by up to 18%, while introducing more than 5 wt.% (equal to 0.4 ppm) can adversely affect cell proliferation. Hence, it should be prohibited from use in implantable devices. Notably, cell line, culture time period and proliferation assay can affect conclusions regarding the maximum safe concentrations of silver in hydroxyapatite.

The data from an AlamarBlue™ assay with Mg-HA samples showed that 2T3 cells could proliferate on Mg-HA, as also demonstrated by the proliferation assay and confirming positive cellular responses to this material at concentrations of 1%, which was expected to be equivalent to 8.00 ppm of Mg ion in the medium. This suggests that the Mg ion could promote cellular proliferation more effectively than NS-HA. It can also be concluded that Mg-HA at a maximum of 1% concentration is biocompatible, and no obvious adverse effects were noted in the nominated concentrations and against the studied cells.

Previous studies have reported that ion-dissolution products containing Ca and Mg from bioactive glasses and ceramics could stimulate cell proliferation (298, 299). It is also reported that the release of Mg ions from Mg alloys should not cause toxicity and may have beneficial effects on cell responses in the local tissue (300). As expected, there is a limit to the amount of Mg amount that can be incorporated into biomaterials, as reported by Serre et al. (15). In these

studies, collagen sponges and magnesium-enriched apatite were used, and the authors reported cytotoxic effects of samples contained 20 wt.% magnesium and 80 wt.% calcium on human osteoblast-like cells *in vitro* (254). In this study, Mg and Ca ions were released from the Mg-HA into the medium solution as discussed in ICP and XRF Section 4.5. and 4.6. The higher level of ion release was highlighted as measured by ICP in Section 4.5 and is expected to be due to the lower degree of crystallinity of Mg-HA samples. Hence, the chemical composition of the medium (which contains a mixture of Mg and Ca ions) may have contributed to the improved cellular responses to Mg-HA disks.

Sader et al.(299), cultivated human osteoblast cells over a sintered tablet of 2% mol Mg substituted β-TCP for maximum of 7 days. The result was improved cell proliferation. However, the findings from this study indicated a maximum of 1% mol of Mg incorporation in HA (which was expected to be equal to 6.22 ppm Mg in the medium) can increase proliferation. Another study by Tavares et al. (301), indicated that less than 1ppm Mg in β-TCP can be cyto-compatible. Landi et al. (125), implanted HA granules containing 5.7 wt.% of Mg in rabbit femoral bone defects. They indicated that the osteoconductivity and resorption of the material was higher compared with commercial HA. Another study indicated that the presence of even 6.8% mol of Mg in tricalcium phosphate discs had no effect on osteoclast apoptosis(302), while others have suggested that the presence of Mg in the TCP structure stabilised the cell-material interface and consequently, enhanced cell attachment and growth(303).

Cell proliferation and protein adhesion to the surface of biomaterial can be affected by surface modifications and their chemistry. Osteoblast cells interact with biomaterial and bind directly through a process mediated by receptors from the integrin group (304). The presence of Mg^{2+} in the biomaterial structure can enhance the stabilisation of the osteogenic phenotype by

improving the integrin receptors intracellular signalling. Mg has been suggested to enhance cellular activity, as it is mitogenic for osteoblast cells and, when diminished, can inhibit cellular growth *in vitro* (24). Ryan et al. (305), have shown that magnesium can have a positive impact on cell proliferation and collagen formation. Landi et al. (28), showed that osteoconductivity increases with Mg-doped hydroxyapatite (Mg-HA) when compared with pure HA and can lead to more favourable conditions for bone growth due to surface characteristics such as composition and nano-dimensions. Zreiqat et al. (306), reported that bone cell adhesion on magnesium-enriched alumina was increased in comparison to Mg-free alumina. The concentrations of both the integrin receptor and collagen I extracellular matrix protein were increased when cells were grown on Mg-containing alumina indicating that Mg can impact the cell attachment process (306). Bone cell attachment and cell growth on magnesium-enriched apatite and collagen have been studied, and reported positive results in both cases (307, 308).

The data obtained from the AlamarBlue™ assay regarding the Zn-HA study showed that 2T3 cells could proliferate on the Zn-HA. The results from this study clearly suggest that the addition of Zn ions to hydroxyapatite promotes cell proliferation in certain concentrations and at certain time points. However, the possible cytotoxicity of Zn is still under review in biomaterial research trying to minimise tissue cytotoxicity while maintaining a good inhibitory effect against bacteria. Zinc has been shown to induce cellular toxicity via the production of ROS and disruption of the energy metabolism at high concentrations (309).

In this study, with the dissolution of Zn-HA, zinc can be gradually released into the surrounding medium (to a maximum of 0.06 ppm concentration) at a level that is well below the established toxic concentrations of zinc (12 ppm) (296). Other studies have reported that the incorporation of Zn into hydroxyapatite in low concentrations (1.6 wt.%) can enhance cell growth and

differentiation (310, 311). However, these studies did not report the concentrations of the Zn ion that were released from the prepared implant.

Some studies have reported the presence of zinc oxide in the final sample and suggested that it has a higher solubility rate than the Zn-TCP and HA phases and can contribute to biological activity (296). The dissolution of zinc oxide will contribute to a higher concentration of zinc in the medium. This zinc concentration was more than twice of the level required to inhibit the MC3T3-E1 cells culture by 50% (296). Therefore, the reported cytotoxicity was mainly due to the presence of zinc oxide. No zinc oxide was observed in Zn-HA samples in the XRD pattern (see Section 4.1) and did not contribute to any of the observed responses to this compound. In a similar study by Ito et al. (312), they suggested that the zinc content must be less than 1.20 wt. % (3.53 ppm) to prevent any negative effect, when the Zn-TCP/HAP composite ceramics were applied to the MC3T3-E1 cell culture. They also suggested that adding Zn to TCP can change its phase to HA, which can affect the solubility and ionic composition of culture media (312).

5.6.2 Alkaline Phosphatase (ALP) activity quantification

Osteoblast cells undergo a temporal sequence of gene expression during the development of a fully differentiated osteoblastic phenotype. The sequence includes: proliferation, differentiation and mineralisation periods (313). The proliferation phase is characterised by an increase in cell number and by the synthesis of the extracellular matrix. This is followed by the expression of high levels of ALP (differentiation phase). Measure the ALP activity then indicates the level differentiation to cells which deposit calcium minerals.

A number of different parameters have been selected to monitor the behaviour of osteoblast cells in the early stages of colonisation. Besides proliferation, the ability of the cells to differentiate on the biomaterials also indicates cell viability and indirectly shows whether the materials are biocompatible (314). ALP activity has been used as an early marker of the functionality and differentiation of osteoblasts during *in vitro* experiments (315). The number of attached cells was measured at different periods to evaluate if the surface can support the attachment and proliferation of osteoblast cells. The level of ALP was assumed to be a reliable marker of cellular differentiation since it is a product of osteoblast cells**.**

Cells from a single culture were used to reduce any effects arising from the cell origin or because of the maturation period. ALP is a non-collagenous protein regulating cellular metabolism through the hydrolysation of phosphate esters and indicates evidence of new bone formation, the onset of mineralisation and ECM matrix remodelling (316).

The data obtained from ALP activity on the Ag-HA study showed that 2T3 cells could differentiate on the Ag-HA in limited concentrations of silver. Accordingly, bone differentiation of 2T3 cultured on 1% and 5 % Ag-HA samples was superior (by 27% and 31% respectively) compared to NS-HA, indicating the biological benefits of substituting silver in apatite. In another study, which was done by Liu et al.(317), silver nanoparticles were used, and the cytotoxicity and genotoxicity of silver nanoparticles were determined. In the aforementioned study, the uptake of silver nanoparticles and its effect on the osteogenic differentiation of human mensenchymal stem cells were investigated *in vitro.* The results indicated that silver nanoparticles cause cytotoxicity in hMSCs. Furthermore, it demonstrated that the uptake of silver nanoparticles did not affect alkaline phosphatase activity (317). However, the observed results suggest that Ag-HA 10% (with a silver concentration of between

3.00 and 4.00 ppm in the medium) can decrease ALP activity by 5% when compared to NS-HA.

Mahmood et al. (318), evaluated the concentration of 20 µg/ml Ag nanoparticles on cell calcification and bone matrix formation in MC3T3-E1 bone cells after 6 days of incubation. They reported more mineralisation and ALP expression in the MC3T3-E1 cells incubated with Ag particles than the cells treated in the Ag-free medium. The exposure of cells to the Ag nanoparticle was suggested to affect the genes responsible for osteogenic differentiation (318). Their results support the findings in this study with regards the increased ALP expression in the presence of Ag. Albers et al. (319), found that ionic silver had a strong impact on ` murine osteoblast differentiation and viability. They noted that silver ions can alter cell differentiation and viability on a scale that depends on the size of the Ag particles.

The advantage of using magnesium in bone implant biomaterials is its enhanced biodegradability and enhanced mechanical properties (300, 320, 321). In addition, Mg deficiency is known to be a risk factor for osteoporosis (24, 300). However, the contribution of magnesium to the levels of cell differentiation is not clearly defined yet. Some studies indicated that low extracellular magnesium promotes cell differentiation (322), while others have reached opposite conclusions (323).

These results showed that the ALP activity of the cells on the Mg-HA exhibited higher levels of expression by 15% than those on the NS-HA at 7 days, indicating that the Mg facilitated cell differentiation. It must be noted that the effect of Mg on the differentiation of osteoblast cells is dose-dependent. As these results also confirmed, ALP activity decreased at higher Mg concentrations for 5% and 10% Mg-HA samples. Lee et al. (324), evaluated the effects of Mg

ions on osteoblastic differentiation in hBMSC. They examined the differences between magnesium chloride, calcium chloride and strontium chloride to measure hBMSC proliferation and ALP activity. Their results showed that the treatment of human BMSC with Mg for 14 days enhances ALP activities. In addition, both ALP levels and proliferation were increased after Mg treatment.

Several studies involving human cells, however, indicate that both high and low concentrations of magnesium could have harmful effects on bone metabolism and homeostasis (325). Leidi et al. (322), tried to focus on the effect of low (0.1mM) and high (5.0 mM) concentrations of the Mg ion on osteoblast-like SaOS-2 cells and the differentiation of normal human osteoblast cells. These results were consistent with this study, suggesting that a high concentration of magnesium decreases both the mineralisation and the activity of ALP.

In another study by Cai et al. (323), that is consistent with our finding, magnesium was incorporated into a fluorinated HA coating. It was shown that a 1.5% concentration of Mg ions increases MG63 cells attachment, has a significant stimulating effect on osteoblastic cell responses and results in higher cell proliferation and faster cell differentiation. It waso showed that a maximum concentration of 1% Mg in HA (expected to be equivalent to 8 ppm of Mg in the medium) has positive effects on osteoblast cell differentiation.

In a recent study, MC3T3-E1 cell differentiation was investigated with a magnesium coated titanium implant prepared by a plasma spray technique (326). Authors reported that Mg has a favourable effect on osteoblastic and osteoclastic cell differentiation and that Mg may accelerate the bone remodelling process and substantially activate osteoclast differentiation (326). However, they did not mention the effective concentration of Mg in their medium.

In a similar study, the Alkaline phosphatase activity of MC3T3-E1 was analysed after 7 days on magnesium-hydroxyapatite coated titanium prepared by radio frequency (RF) and direct current (DC) magnetron sputtering (327). The authors suggest that the presence of Mg and Mg-HA coatings can stimulate the differentiation of the target cells into osteoblastic MC3T3-E1 cells with potentially higher rates of osseointegration (327).

Results from this study indicated that the ALP activity of the cells on the Zn-HA exhibited significantly higher levels of expression than those on NS-HA at 7 days, suggesting that Zn accelerated cell differentiation. As our results have shown 1, 5 and 10% of Zn can increase cell differentiation by increasing 25%, 33% and 32% respectively, as demonstrated by the ALP activity of 2T3 cells.

The literature suggests that Zn incorporation into implants promotes bone formation around the implant and decreases the inflammatory response (328). Its stimulatory effect on bone formation and mineralisation has been reported with both *in vivo* and *in vitro* studies (328, 329). It was shown that the Zn^{2+} ion results in osteoclastic inhibition (128). However, it worth noting that high amounts of Zn^{2+} doping (up to 15‑20% mol) can inhibit HA phase formation (126).

It was noted that a concentration of 0.06 ppm observed for Zn-HA 10% can increase the differentiation of the 2T3 cell after 7 days. Badr et al. (330), reported higher levels of alkaline phosphatase in a rat calvarium-derived osteoblastic cell cultured on 5 wt.% zinc-containing glass powder combined with calcium. They reported that biphasic calcium phosphate shows enhanced mechanical and biological properties by incorporating small quantities (0.5-5 wt.%) of zinc-containing bioactive glass particles (330). No measurement was carried out for the

amount of zinc released form their powder formulation, while differentiation improved up to 10% Zn-HA sample, which was the equivalent of 0.06 ppm of the zinc released ion.

Seo et al. (331), evaluated the ALP activity of MC3T3-E1 cells against different concentrations of Zn at different culture times. They concluded that 15 μM and 25 μM zinc (equivalent to 0.7 and 1.2 ppm) showed the highest effects in increasing the ALP activity at the end of the proliferation phase and the start of the mineralisation stage. However, their data are consistent with findings in this study, as it was showed that their lowest studied zinc concentration (1μM or 0.06 ppm) increases ALP activity. A similar result with identical concentrations (0.06 ppm) in a 10% Zn-HA sample was also observed.

In another study, the effect of zinc on SaOS-2 human osteoblastic cells on ALP synthesis was investigated. It was concluded that Zn can increase ALP activity in the range of 1 μM to 10 μM and decrease in 50 μM (332). A similar pattern was observed by Yang et al. (333), who reported that a Zn-HA coating with a Zn/(Ca+Zn) molar ratio of 1.04% significantly enhances the differentiation of MC3T3-E1 on day 7, with the potential benefit of enhancing implant osseointegration. Uysal et al. (334), reported that 2%mol Zn ions incorporated into the HA crystal resulted in an increase in the ALP activity of the Saos-2 cell line after 7 days when compared to the pure HA. Moreover, they claimed that the incorporation of zinc can change the physical properties of final the HA, as its grain size has potential impact on the differentiation levels.

5.6.3 Concluding statements

The results from the cell biological studies confirmed that ions (Ag, Mg and Zn) substituted hydroxyapatite promote greater osteoblast cell proliferation and differentiation in comparison

with NS-HA samples. However, the biological response was limited by the concentrations of Ag, Mg and Zn ions.

It can be claimed that silver substituted in hydroxyapatite can promote the proliferation and differentiation of mouse osteoblast cell lines (2T3) by 19% and 27% respectively, which corresponds to the Ag-HA 1% sample (0.3 ppm in the medium). Between 0.3 ppm and 0.4 ppm of silver shows no desirable effect on proliferation and differentiation. Zn-HA 10 wt.% with a maximum release of 0.06 ppm Zn resulted in a 41% increase rate of proliferation and 33% differentiation at the same time of incubation. However, Mg-HA 1 wt.% with 6.22 ppm can increase the rate of proliferation with up to 10% and differentiation by 13%.

Adding any cation to the hydroxyapatite structure can change the physical and chemical characteristics of the crystals, and each can individually affect the final biological response of HA.

There was a decreasing degree of crystallinity after ion substitution (at different levels for each ion and concentration) for all the studied ions, which is believed to result in a higher degree of solubility in the liquid and potential impact on the chemistry and pH of the medium compared to the NS-HA sample. It was showed that substitution could influence the calcium phosphate stoichiometric as well as the chemical phases present in the final crystal structure. In the case of Mg and Zn substitution, in addition to the HA phase, it was reported that with TCP phase, the solubility of crystal and subsequently the pH and composition of the medium will be affected. Moreover, the rate of calcium phosphate dissolution is correlated to the ratio of Ca/P ions and again the pH of the surrounding environment (293). It is expected that the pH will become more alkaline by dissolving the HA material, which can have a cytotoxic effect on cell

proliferation in cell cultures. The dissolution rate (both in body fluids or *in vitro*) is more critical when the crystallinity degree is lower, as it results in higher ratios of dissolution.

The method of introducing metal cations to HA can affect its microstructure in terms of particle charge, grain size, crystal size and roughness. All these parameters are expected to impact surface characteristics (such as wettability) and as a result the cell attachment on the surface. However, the main focus of this work was on the effect of ion addition and its presence in the medium against the cellular activity.

The substitution of cations can occur on the Ca (I) or Ca (II) position (or between them) or even on the surface of HA with different cellular responses. Regardless of the mechanism of ion incorporation, the outcome of biological assessments to the total ions released and present in the medium can be correlated.

5.7 Microbiological assays

With increasing rate of microbial organisms becoming resistant to the existing antibiotics, many studies have tried to develop new and effective antimicrobial reagents free of resistance and with less cost. Such problems have led to the resurgence in the use of metal based antiseptics which are applicable to broader spectrum of bacteria with far lower susceptibility to induce resistance than common antibiotics(335).

As discussed in Section 2.4.4, both silver and zinc have long been known for their antibacterial properties (96) against an exceptionally broad spectrum of bacteria, including gram-positive and gram-negative, as well as viruses and fungi (97, 98). Within metals with antibacterial

activity, silver has the highest efficiency even at a very diluted concentration (as low as 35 ppb range) within which there is no known toxic effect for mammalian cells (99, 100). In addition, microorganisms have a relatively poor ability to develop immunity to silver. Therefore, it has been widely used in many forms as an antibacterial agent, both in medicine (e.g., for the treatment of flash burns, catheters, the coverage of implant materials, urinary tract infections, dentistry(92) (101) and in other fields like clothing, home appliances and water treatment (336) (337).

The main purpose of microbiological assay was to measure how the prepared samples "perform" *in vitro* in terms of antibacterial action against two strains of bacteria. The efficacy of the ion-substituted samples was measured and reported considering results from following three main assays which were carried out in this thesis:

1) The exact measurement of ion content in solid samples from ICP-MS and XRF studies, which can be used to correlate to the observed antibacterial effect.

2) The concentration of ions and their rate of change in the medium (release profile). Having the release profile results, it was possible to correlate the antibacterial activity to the concentration of ions known to be present for each sample.

3) Placing the disks in bacterial culture to understand growth inhibition of cells and measure the antibacterial activity.

While it is possible to outline the antibacterial strength of the samples with either of the mentioned experiments (zone of inhibition or film adhering technique) as in most previous studies (108, 338), each technique come with inherent limitations. For example, zone of

Inhibition technique is based on the release of ions in a semi-solid gel-like medium where the mass transfer is somehow more limited to the surrounding medium when compared with *in-vivo* conditions. Likely, the mass transfer and inhibition of bacterial growth is largely dependent on the thickness of agar layer and dimensions of the disk, which is placed on the agar surface. To overcome these limitations, the spread plate/film adhering methods were developed to accompany the zone of inhibition study, to understand how the release will be like in the liquid medium and how the activity will change.

In general, the substantial data from these experiments conclude that each of Silver or Zinc can inhibit the growth of selected microorganisms with varying degrees based on type and concentration of the metal in solid and also the type of bacteria studied.

Further discussions to review the three main studies, i.e. zone of inhibition, spread plate method and adhering film are provided below.

5.7.1 Measuring antibacterial activity

The antibacterial action during the mentioned assays occurs in two main steps;

1) Ion transfer from the disk to the surface of the bacteria
2) Ion interaction with the cell, either through attraction or reaction with the cell or through diffusion into the cell.

The ions are expected to reacts in a similar way regardless of which mechanism the ions used to reach to the cells. However, in each of the mentioned technique, it was believed that different mechanisms may have been followed during the ion transfer phase. It was expected that ion

transfer from the solid to the outer medium (agar or liquid phase) should have a significant impact on the observed results in this section of work. Hence, it is critical to explain and compare these mechanisms to make the right conclusion.

Two main mechanisms can be considered on how metal ions in solid specimen can interact with the bacterial cells. The first mechanism is based on the attraction of microorganisms to the surface of the disk by electrostatic forces, where there is a direct interaction between the bacterial cell membrane and the metal ions (102, 103). This mechanism is expected to occur mainly in the film adhering method. However, in the second mechanism, Ag ions are first released from the surface of the solid and diffuse through the surrounding medium until they reach and react with the cells(84). Second mechanism is like diffusion and similar to general ion release profile, and is believed to be more dominant in the ZI study.

On the other hand, molecular movement was expected to control the ion transfer in the ZI techniques. Ion diffusion within the agar gel controls the rate of the antibacterial activity until the ions reach the surface of the bacteria.

In the film adhering technique, solid samples were shaken in the bacterial suspension (forced convection). Hence, two stages can be proposed during which ion interaction happens in the film adhering method:

1) First, ions are released from the solid disk into the liquid solution. A similar release profile to what was occurred in ICP measurement assays (section 4.7) should be present in this method. However, as samples were shaken during the film adhering experiments, it is expected that the ion transfer from solid to liquid phase to be larger because of the disturbed liquid medium. The solid disks remained intact at the end of film adhering experiment, suggesting that diffusion regime should be dominant throughout this stage.

2) Ion interaction with the suspended cells in the liquid was at a different rate than what occurs during agar-based experiments. As there is an agitated medium, it was expected that a higher number of cells being affected with ions. Consequently, higher values for antibacterial activity may be observed in this test but while all samples are compared together, a better comparison can be provided.

Measuring antibacterial activity of Ag-HA samples

Strong inhibition in bacteria growth was observed in the Ag-HA samples in the studied culture plates. While the negative control (NS-HA) showed minor antibacterial activity which diminished after 24 hours, Ag ions indicated noticeable antibacterial activity in both ZI measurement and film adhering assays. Minor antibacterial activity of NS-HA can be due to the release of calcium and/or phosphate ions or other reaction residues with a potential of unbalancing the pH of the medium. A similar effect was exoected in all ion-substituted samples.

Based on the results from the Ag release profile measurement (Section 4.5.2), the concentration of Ag in the liquid medium was expected to be about 0.25 ppm, 0.3 ppm and 0.4 ppm for Ag-HA of 1, 5 and 10 %, respectively. The ZI experiments showed that these concentrations have been effective to some extent in the inhibition of bacterial growth for both Gram- negative and Gram-positive bacteria.

Antibacterial activity was measured for up to 48 hours. Considering the release profile of Ag (Section 4.5.2), a burst release of Ag ions was expected during the first 24 hours, suggesting that most of the Ag should have been released. The release profile experiments were carried out in a liquid medium, in contrast to the semi-solid agar structure in the antibacterial assays.

However, the diffusion was assumed to be in a similar range in the liquid and semi-solid agar medium. For ZI tests in an agar medium, the Ag ions were able to diffuse from the solid surface and penetrate into the agar. Similarly, for the film adhering method, the ions were transferred from the surface of the disks to the attached layer of the bacterial cells.

The type of experimental method to measure the antibacterial activity will affect the final results, although the results in this study were in general agreement with previous works from other research groups (339, 340). The Ag-HA samples in all the different ratios showed antimicrobial activity in a similar pattern to what was reported by Sondi et al. (341).

Ag has been shown to be effective against bacteria at a concentration of 12 ppm (85), and it has been shown to be more effective than Cu^{+2} and Zn^{+2} when it was substituted in hydroxyapatite (342). In fact, Fenga et al. (85), reported that the minimum inhibitory concentration against bacteria (defined as the removal of 90% of the bacteria) for Ag was about 0.8 ppm (1.3 ppm for $AgNO_3$), which is slightly higher than what was observed for the concentration of Ag being released from the sample. The results showed that even at a lower concentration of Ag, a high ratio of bacterial removal (based on the film adhering method) is achievable.

The diameter of the ZI increased as the concentration of Ag increased in the solid structure, but the effect of Ag was more pronounced in the *E.coli* culture compared to the one for *S. epidermidis*. Previous studies reviewing the mechanism of action of Ag ions referred to the thicker peptidoglycan layer of Gram-positive bacteria compared to Gram-negative ones (20-80 nm in Gram-positive bacteria compared to 2-3 nm outer membrane and 8-10 nm in Gram-negative bacteria (343)). This can protect the cell from the influx of Ag ions, resulting in a higher resistance against the Ag inhibitory effect (344, 345). The peptidoglycan layer is a

specific membrane feature of bacterial species and is not present in mammalian cells. In one previous study by Jun et. Al., however, a slightly different response in *E.coli* was observed when compared to *S.epidermidis* against Ag ions (346). In their results, the inhibitory effect of Ag was lower in *S.epidermidis* when compared to *E.coli* microorganisms.

The mechanism of the antibacterial action of Ag ions is not fully understood yet (all explanations are reviewed in Chapter 1), while the interaction of the Ag ions and the cell membrane is predominantly the major factor in most hypotheses. Some studies suggested that the positive charge of the ion is critical for its action against the negatively charged particles on the bacterial cell membrane (347-349). In contrast, Sondi et al. (341), reported that "negatively" charged Ag particles also show antimicrobial activity on Gram-negative bacteria and its efficacy is solely determined by its concentration, which it was confirmed in the results. The charge of the Ag ions in this study was not measured but was expected to be positive based on the formulation and the neutral pH of the environment.

Increasing the inhibitory effect by increasing the Ag concentration has been shown to be associated with the formation of "pits" in the cell wall of the bacteria (341). The Ag particles were shown to accumulate in the bacterial membrane and increase the cell permeability, resulting in cell lysis. Amro et al. (349), suggested that metal depletion may cause the formation of irregularly shaped pits in the outer membrane and may change the membrane permeability, which is caused by the progressive release of lipopolysaccharide molecules and membrane proteins (349) Sondi et al. (341), speculated that a similar mechanism may cause the degradation of the membrane structure of *E. coli* during treatment with Ag particles..

Measuring antibacterial activity of Zn-HA samples

The advantages of using inorganic particles (e.g. Zn) as antimicrobial agents are their greater effectiveness on resistant strains of microbial pathogens, less toxicity and heat resistance (350). While it has been suggested that Zn ions act as a bacteriostatic agent rather than a bactericide (351), the inhibitory effect of zinc loaded hydroxyapatites against bacteria, including *E. coli*, *Staphylococcus aureus*(*S. aureus*), *Candida albicans* (*C. albicans*), and *Streptococcus mutan* have been previously confirmed (352). Zn is also a crucial molecule for human cells, particularly bone cells, and can exhibit strong activity at very low concentrations (353, 354). Zn is known to be in the active centre of more than 300 enzymes involved in bone metabolism (355).

The antibacterial activity of Zn-HA formulation (as in 1, 5 and 10% samples) were tested following two different methods. Its antibacterial activity was evident in all the employed techniques when compared with the NS-HA control.

Similar to the Ag-HA samples, the antibacterial property of Zn increased with a higher concentration in the solid sample. The presence of a ZI clearly indicates that Zn ions are released from the solid specimen into the agar and have an antibacterial effect against both strains. Similar to what Rizwan et al. (356), reported, increasing the concentration of Zn in hydroxyapatite leads to higher rates of growth inhibition. However, when compared to the Ag-HA, the ZI was slightly smaller, particularly in the *S.epidermidis* culture plates. One explanation for the lower antibacterial activity could be due to the lower rates of Zn released from the Zn-HA samples. As results of Zn-HA release profile suggest, the maximum concentration of Zn in the medium reaches only 60 ppb for 10% Zn-HA after 48 hours. Even

at such low Zn concentrations, the bacterial growth was inhibited as indicated in both ZI study and film adhering method. Previous works have confirmed effective bioactivity and antibacterial properties with the hydroxyapatites sample doped with small amounts of Zn ions (less than 1%) (140, 141, 357). At a slightly higher concentration (1.3%), Zn ions shown to increase the level of osteoblast responses (311). Studies on a hydroxyapatite doped with Zn were synthesized using the wet method and a hexahydrate Zn nitrate of Zn $(NO_3)_2{\cdot}6H_2O$ (wherein the Zn ion content was 1.6%), have shown its real impact on the reduction of *S.aureus* bacteria (310). It is critical to remember that for the optimum formulation, one needs to consider Zn cytotoxicity levels against human cells. Cytotoxicity effect has been reported to initiate for hydroxyapatites containing Zn ions when Zn concentrations is more than 1.2% wt. in the solid (310, 312) .

The minimum inhibitory concentration (MIC) for zinc nitrate ($ZnNO_3$) is not fully determined against *E.coli* or *S.epidermidis,* in contrast for zinc oxide (ZnO), which is a very common additive in cosmetic and topical formulations. ZnO is expected to be partially dissolved and generate Zn^{+2} ions, which are reported to partly contribute to its antibacterial activity(358). For ZnO, the MIC against *E.coli* varies in different studies, from as low as 0.1 ppm (359) to 400 ppm (350). $ZnNO_3$ is fully dissolved in water, and is expected that the released Zn^{+2} ions are responsible for any antibacterial activity (358).

The size of the ZI was different according to the type of bacteria and the concentrations of Zn. The results also confirm that the effect of Zn ions is more pronounced against *S.epidermidis* bacteria, which is different from what was observed for Ag-HA samples. Results from previous studies also do not provide a conclusive explanation if Zn ion is more effective against Gram-

negative or Gram-positive bacteria. While some studies reported a higher antibacterial property for Zn against Gram-negative bacteria (343), in another case a different pattern was reported (360). Several factors have been attributed to the different response of Gram-positive and Gram-negative bacteria against Zn ions. These factors are different cell wall structure, membrane or the outer layer in each bacteria strain and different resistances to oxidant compounds and defence mechanisms to tackle oxidative stresses (351, 361, 362).

The mechanism of action of Zn as an antibacterial agent is described to be similar to Ag ions. When Zn reaches the microbial cell membrane, it will be strongly adsorbed and penetrate into the bacterial cell wall. The bacteria lose their proliferation capacity due to protein denaturation and the destruction that ultimately occurs (343). Zn also has been reported to bind to the membranes of the microorganisms, consequently prolonging the lag phase of the growth cycle and increasing the generation time of the organisms, so that it takes each organism more time to complete the cell division (362). Zn is also found to block the secretory effect of the cholera toxin and the *E.coli* heat-labile enterotoxin, which acts by cyclic adenosine monophosphate (363).

Hybrid formulation of hydroxyapatite, which consists of mixing a common antibiotic with Zn ions, has been used to resolve the problem of local availability of the antibacterial agent and to provide a higher concentration of the antibiotic in the bone tissue (364). In the mentioned work, hydroxyapatite was doped with Zn ions as carriers for the controlled release of ciprofloxacin, which exhibits antibacterial activity against *S.aureus* and *Pseudomonas aeruginosa*. It was shown that both the ciprofloxacin and Zn ions co-release. The Zn not only increases the total antibacterial activity, but also it resulted in a higher amount of ciprofloxacin release from the

hybrid material as it reduces the crystallinity and increase the surface area of the nano grains. Using a similar formulation can result in higher efficiency of the therapy with lower doses of ciprofloxacin and a reduction in the formation of resistant strains.

5.7.2 Concluding statement

The results from the microbiology studies confirmed that Ag and Zn hydroxyapatite present antibacterial activity against two candidate bacterial strains. However, the antibacterial activity has been controlled by the concentration of the ion and type of bacteria.

Ag-HA samples had significant growth inhibition against both bacteria in comparison to the control sample in all three different ratios. The Ag antibacterial activity was shown to be dose-dependent and was more pronounced against Gram-negative bacteria (*E.coli*) than Gram-positive bacteria (*S. epidermidis*).

Zn-HA also showed clear growth inhibition in comparison with the NS-HA (control) samples and the level of reduction in bacteria growth was lower when compared to Ag-HA samples. Zn-HA also shows to be more effective against *S.epidermidis* and similar to Ag-HA, its antibacterial properties increases at higher ion concentrations.

CHAPTER 6
CONCLUSION

6 Conclusion

For decades, calcium phosphate has been used to mimic bone structure or enhance biocompatibility of implants in various formulations. Selected cations of Silver, Magnesium and Zinc were incorporated in HA to add their beneficial antibacterial activity and bio-functionality and reviewed their key characteristics through a multidisciplinary approach.

The results proved that antibacterial activity is a positive attribute observed after addition of these cations but the type and concentration of these ions can impact other critical properties of the HA with potential impact on the final structure. The aim of this study, however, was to define how the most critical attributes were affected and conclude a meaningful review and fill the knowledge gap between material characteristics, biological response and antimicrobial activity of this type of material.

Following section highlights the conclusion of the present study.

6.1 The extent of ion substitution

The selected cations were substituted in the HA structure but not necessarily in the ratios similar to the stoichiometric concentrations present in the starting reaction pool. Two different methods were used to measure and validate this hypothesis, as it is essential to know the exact amount of the present ion in the final formulation. The concentration of the incorporated cations in the powder (molar and wt%) were calculated and compared.

In case of Ag-HA, it contained almost half of the expected silver while for other two cations, in particular for Mg-HA, the final values for ion incorporation were closer to the initial ratios. While XRD analysis confirmed that these cations have been substituted in the HA structure to

some degree, no definitive conclusion can be made to confirm how much of these cations are actually substituted in the HA structure and how much being either adsorbed on the surface, being incorporated as defects or formed a second phase.

6.2 Changes in crystal properties

We reported the changes in structural phase analysis and mapped clearly how the addition of cations impact the crystal phases, which ultimately can affect the micro- and macro-properties of the powder. Higher Ag concentration increased the crystallinity and crystal size slightly while for Mg and Zn, both crystallinity and crystal size decreased suggesting a contraction in the cell unit volume and inhibition in crystal growth. The change in crystallinity and crystal size can affect the nano grain size and ultimately the surface area and higher rates of release of drugs from the particles.

6.3 Chemical structure

Phase analysis of the final powders confirmed the formation of a strong β-TCP phase at higher Mg concentrations and most of the Mg was present in this phase resulting in the formation of Whitlockite. The presence of β-TCP phase was shown to affect the macro-properties of the powder (solubility and thermal stability as the only ones studied in this research) which can impact the overall stability of the powder. FT-IR and Raman Spectroscopy confirmed the formation of the HA and TCP phases and also indicated the presence of carbonate ions which suggest the importance of the reaction environment and CO_2 in the atmosphere throughout the reaction.

6.4 Solubility and release properties

We showed that there is a direct correlation between the amount of cation incorporated in the powder and the amount of ions released in the liquid phase. There is an initial burst release step for all the samples, which lasts average about 24 hours followed by a more sustained lower rate release. Maximum release of Ag and Zn was reached after 72 hours suggesting the poor solubility of the powder and mass transfer in these two formulations.

As expected, the morphology and surface area of the final material will change the release profile. However, it was expected that the mass transfer from the solid HA phase to the surface should be very poor and most of the solubilised ions are ones which are released from the surface of the powder. In addition, it is proposed that the availability of more soluble phase (β-TCP in Mg-HA) may have influenced the higher rates of Mg release. Different rates of solubility from different phases of calcium phosphate can suggest the possibility of tuning and fabricating “engineered” particles with controlled rates of releases of different agents released from different phases.

6.5 Antimicrobial activity

The results proved that there is a direct relationship between the release profile in each sample and the observed antibacterial activity. The observed antibacterial activity can be attributed solely to the presence of the cations in the powder as all the samples were compared with a control sample of non-substituted HA. Based on the defined concentration of each cation in the solid and liquid phase, it was concluded that the observed antibacterial activity to the concentration of cation in the medium assuming other parameters remained unchanged. Using this principal, it is possible to predict the final antibacterial activity against these bacterial strains by knowing the amounts of each cations in the starting reaction medium.

6.6 Cell experiments

For any newly developed biomaterial formulation, it is critical to measure its performance against selected biological activity screenings to ensure it is safe and compatible in principal. The biological response of the prepared material was measured by how the cation concentration affects the cell proliferation and cell differentiation responses in selected cell line. While cell proliferation was increased in the lower ranges of cation concentration, it was negatively affected at higher ratio samples where the expected concentration of cation in liquid phase was exceeding the cation's cytotoxicity level. Similar results were obtained for osteoblast differentiation as at higher ratios of Mg-HA, negative results were observed.

We suggested that biocompatibility may be affected with the change in crystal properties of the powder which highlights how different parameters may be interrelated and impact the success of a biomaterial.

6.7 Recommendation for future work

Using extra analytical techniques for material characterisation can provide further understanding of the final powder and how the calcium phosphate and its chemical and crystal properties may change by addition of cations. In particular, solid NMR can help to define the new and existing molecular bonds at greater detail.

Mechanical properties of the bulk material and parameters like compressive and tension strength and strain, porosity and density can be useful to predict the in situ behaviour and how they are changed with different formulations. Also release profile and solubility can be evaluated under simulated conditions which there is circulated medium similar to what occurs in the body.

Also, elemental analysis assays at the surface of material (like EDS) can determine the extent of the surface adsorption of cations on powder and differentiate it from the chemicals that are incorporated within the crystal lattice.

Furthermore, new formulations can be used by mixing different ratios of cations at selected optimum concentration and generate a hybrid formulation with possibly inventive properties.

To better define antibacterial activity, other pathogenic bacterial strains can be used against these powders. Using the prepared hybrid material as discussed earlier may be able to control various bacterial strains in particular the strains which are becoming more resistant to common antibiotics.

Using more detailed biological assessments, such as mineralisation and gene expression can also help to understand the behaviour of the material in the body and provide a better picture its overall success.

7 References

1. Dobzyniak M, Fehring T, Odum S. Early failure in total hip arthroplasty. Clin Orthop Relat Res. 2006;447:76-78.
2. Fehring TK, Odum S, Griffin WL, Mason JB, Nadaud M. Early failures in total knee arthroplasty. Clin Orthop Relat Res. 2001 (392):315-322.
3. Losina E, Barrett J, Mahomed NN, Baron JA, Katz JN. Early failures of total hip replacement: effect of surgeon volume. Arthritis Rheum. 2004;50(4):1338-1343.
4. Moioli E, Clark P, Xin X, Lal S, Mao J. Matrices and scaffolds for drug delivery in dental, oral and craniofacial tissue engineering. Advanced Drug Delivery Reviews. 2007;59(4-5):308-324.
5. Popat K, Eltgroth M, Latempa T, Grimes C, Desai T. Decreased Staphylococcus epidermis adhesion and increased osteoblast functionality on antibiotic-loaded titania nanotubes. Biomaterials. 2007;28(32):4880-4888.
6. Chua P, Neoh K, Kang E, Wang W. Surface functionalization of titanium with hyaluronic acid/chitosan polyelectrolyte multilayers and RGD for promoting osteoblast functions and inhibiting bacterial adhesion. Biomaterials. 2008;29(10):1412-1421.
7. Suchanek W, Yoshimura M. Processing and properties of hydroxyapatite-based biomaterials for use as hard tissue replacement implants. J MaterRes. 1998;13(1):94-117.
8. Regí M, Calbet J. Calcium phosphates as substitution of bone tissues. Progress in Solid State Chemistry. 2004;32(1-2):1-31.
9. Simionescu R, Kennedy D. Prevention of Infection in Prosthetic Devices. In: Johnson F, Virgo K, Lairmore T, Audisio R, editors. The Bionic Human: Humana Press; 2006. p. 159-185.
10. Bernard L, Hoffmeyer P, Assal M, Vaudaux P, Schrenzel J, Lew D. Trends in the treatment of orthopaedic prosthetic infections. J Antimicrob Chemother. 2004;53(2):127-129.
11. Gillespie W, Walenkamp G. Antibiotic prophylaxis for surgery for proximal femoral and other closed long bone fractures. . Cochrane Database Syst Rev. 2010;17(1).
12. Chu V, Crosslin D, Friedman J, Reed S, Cabell C, Griffiths R, et al. Staphylococcus aureus bacteremia in patients with prosthetic devices: costs and outcomes. . Am J Med. 2005;118(12):1416.e1419–1416.e1424.
13. Bigi A, Falini G, Foresti E, Gazzano M, Ripamonti A, Roveri N. Magnesium influence on hydroxyapatite crystallization. J Inorg Biochem. 1993;49:69-78.
14. Sebti S, Tahir R, R.Nazih R, Boulaajaj S. ComparisonofdifferentLewisacidsupported on hydroxyapatite as new catalysts of Friedel–Crafts alkylation. Appl Catal A: Gen. 2001 (218):25-30.
15. Fujii E, Ohkubo M, Tsuru K, Hayakawa S, Osaka A, Kawabata K, et al. Selective protein adsorption property and characterization of nano-crystalline zinc-containing hydroxyapatite. Acta Biomater. 2006;2(1):69-74.
16. Suzuki T, Hatsushika T, Hayakawa Y. Synthetic hydroxyapatites employed as inorganic cation-exchangers. J chem Soc Faraday Trans. 1981;1(77):1059-1062.
17. Campoccia D, Montanaro L, Arciola CR. The significance of infection related to orthopedic devices and issues of antibiotic resistance. Biomaterials. 2006;27(11):2331-2339.

18. Zheng X, Chen Y, Xie Y, Ji H, Huang L, Ding C. Antibacterial Property and Biocompatibility of Plasma Sprayed Hydroxyapatite/Silver Composite Coatings. J Therm Spray Tech. 2009;18(3):463-463.
19. Chen W, Oh S, Ong A, Oh NY, Liu Y, Courtney H, et al. Antibacterial and osteogenic properties hydroxyapatite coating produced using of silver-containig a sol-gel process. J Biomed Mater Res. 2007;82(4):899-896.
20. Samani S, Hossainalipour S, Tamizifar M, Rezaie H. In vitro antibacterial evaluation of sol–gel-derived Zn-, Ag-, and (Zn+Ag)-doped hydroxyapatite coatings against methicillin-resistant Staphylococcus aureus. J Biomed Mater Res A. 2013;101(1):222-230.
21. Li X, Sogo Y, Ito A, Mutsuzaki H, Ochiai N, Kobayashi T, et al. The optimum zinc content in set calcium phosphate cement for promoting bone formation in vivo. Mater Sci Eng. 2009;29(3):969-975.
22. Otsuka MM, S.; Matsuda, Y.; Ito, A.; Layrolle, P.; Naito, H.; Ichinose, N. . Calcium level-responsive in vitro zinc release from zinc-containing tricalcium phosphate (ZnTCP). J Biomed Mater Res. 2000;52(4):819-824.
23. Landi E, Logroscino G, Proietti L, Tampieri A, Sandri M, Sprio S. Biomimetic Mg-substituted hydroxyapatite: from synthesis to in vivo behaviour. J Mater Sci Mater Med. 2008;19(1):239-247.
24. Rude R, Gruber H. Magnesium deficiency and osteoporosis: animal and human observations. J Nutr Biochem. 2004;15(12):710-806.
25. Matsumoto N, Sato K, Yoshida K, Hashimoto K, Toda Y. Preparation and characterization of beta-tricalcium phosphate co-doped with monovalent and divalent antibacterial metal ions. Acta Biomater. 2009;5(8):3157-3164.
26. Lansdown A. Critical observations on the neurotoxicity of silver. Crit Rev Toxicol. 2007;37(3):237-249.
27. Lansdown A. Silver in health care: antimicrobial effects and safety in use. Curr Probl Dermatol. 2006;33:17-34.
28. Landi E, Logroscino G, Proietti L, Tampieri A, Sandri M, Sprio S. Biomimetic Mg-substituted hydroxyapatite: from synthesis to in vivo behaviour. J Mater Sci Mater Med. 2008;19:239-247.
29. Suchanek W, Byrappa K, Shuk P, Riman R, Janas V, TenHuisen K. Preparation of magnesium-substituted hydroxyapatite powders by the mechanchemical-hydrothermal method. Biomaterials. 2004;25(19):4647-4657.
30. Tampieri A, Celotti G, Landi E, Sandri M. Magnesium doped hydroxyapatite: synthesis and characterization. Key Eng Mater 2004;264-268:2051-2054.
31. Williams D. On the nature of biomaterials. Biomaterials. 2009;30(30):5897-5909.
32. Pilliar R, Deporter D, Watson P, Pharoah M, Chipman M, Valiquette N, et al. The effect of partial coating with hydroxyapatite on bone remodeling in relation to porous-coated titanium-alloy dental implants in the dog. J Den Res. 1991;70(10):1338-1345.
33. Widmer AF. New developments in diagnosis and treatment of infection in orthopedic implants. Clin Infect Dis. 2001;1(33):S94-106.
34. Anthony R, Berendt B, Smith P. Prosthetic joint infection. Current Infectious Diseases Reports. Current Infectious Diseases Reports. 1999;1(3):267-272.

35. Collins D, McKenzie J. Infections at the site of a hip implant. Clinical Orthopaedics. 1991;269:9-15.
36. Tattevin P, Cremieux A, Pottier P. Prosthetic joint infection: when can prosthesis salvage be considered? Clin Infect Dis. 1999;2:292-295.
37. Goldenberg D. Septic arthritis. The Lancet. 1998;351:197-202.
38. Ribeiro M, Monteiro F, Ferraz M. Infection of orthopedic implants with emphasis on bacterial adhesion process and techniques used in studying bacterial-material interactions. Biomatter. 2012;2(4):176-194.
39. Goodman S, Yao Z, Keeney M, Yang F. The future of biologic coatings for orthopaedic implants. Biomaterials. 2013;34(13):3174-3183.
40. Petrosillo N. Epidemiology of Infections in the New Century. In: Signore A, Quintero A, editors. Diagnostic Imaging of Infections and Inflammatory Diseases: John Wiley & Sons, Inc.; 2013. p. 1-14.
41. Uçkay I, Buchs NC, Seghrouchni K, Assal M, Hoffmeyer P, Lew D. Bacterial Osteomyelitis: The Clinician's Point of View. Diagnostic Imaging of Infections and Inflammatory Diseases: John Wiley & Sons, Inc.; 2013. p. 15-26.
42. David MZ, Daum RS. Community-Associated Methicillin-Resistant Staphylococcus aureus: Epidemiology and Clinical Consequences of an Emerging Epidemic. Clin Microbiol Rev. 2010;23(3):616-687.
43. Goyal N, Miller A, Tripathi M, Parvizi J. INSTRUCTIONAL REVIEW: GENERAL ORTHOPAEDICS Methicillin-resistant Staphylococcus aureus (MRSA). Bone Joint J. 2013;95(B):4-9.
44. Campoccia D, Montanaro L, Speziale P, Arciola CR. Antibiotic-loaded biomaterials and the risks for the spread of antibiotic resistance following their prophylactic and therapeutic clinical use. Biomaterials. 2010;31(25):6363-6377.
45. Calhoun J, Mader J. Musculoskeletal Infections: CRC Press; 2003. 680 p.
46. Hanssen A. Local antibiotic delivery vehicles in the treatment of musculoskeletal infection. Clin Orthop Relat Res. 2005 (437):91-96.
47. Norden C, shaffer M. Treatment of experimental chronic osteomyelitis due to staphylococcus aureus with vancomycin and rifampin. J Infect Dis. 1983;147(2):352-357.
48. Hetrick E, Schoenfish M. Reducing implant-related infections: active release strategies. Chem Soc Rev. 2006;35:780-789.
49. Takezawa Y. Studies on physico-chemical properties of self-setting apatite cement. Gifu Shika Gakkai Zasshi. 1989;16(2):500-519.
50. Otsuka M, Nakahigashi Y, Mastsuda Y, Fox J, Higuchi W. A novel skeletal drug delivery system using self-setting calcium phosphate cement. 7. Effect of biological factors on indomethacin release from the cement loaded on bovine bone. J Pharm Sci. 1994;83(11):1569-1573.
51. Alt V, Bitschnau A, Osterling J, Sewing A, Meyer C, Kraus R, et al. The effects of combined gentamicin-hydroxyapatite coating for cementless joint prostheses on the reduction of infection rates in a rabbit infection prophylaxis model. Biomaterials. 2006;27(26):4627-4634.
52. Patel S. Optimising calcium phosphate cement formulations to widen clinical application. University of Birmingham2011.

53. Verron E, Khairoun I, Guicheux J, Bouler J. Calcium phosphate biomaterials as bone drug delivery systems: a review. Drug Discov Today. 2010;15(13–14):547-552.
54. Dorozhkin SV. Calcium Orthophosphates as Bioceramics: State of the Art. Journal of Functional Biomaterials. 2010;1(1):22-107.
55. Dorozhkin S. Biphasic, triphasic and multiphasic calcium orthophosphates. Acta Biomater. 2012 Mar;8(3):963-977.
56. De Groot K. Clinical applications of calcium phosphate biomaterials: A review. Ceramics International. 1993;19(5):363-366.
57. Bohner M, Theiss F, Apelt D, Hirsiger W, Houriet R, Rizzoli G, et al. Compositional changes of a dicalcium phosphate dihydrate cement after implantation in sheep. Biomaterials. 2003;24(20):3463-3474.
58. Uskokovic V, Uskokovic D. Nanosized hydroxyapatite and other calcium phosphates: chemistry of formation and application as drug and gene delivery agents. J Biomed Mater Res B Appl Biomater. 2011;96(1):152-191.
59. Kalita SJ, Bhardwaj A, Bhatt HA. Nanocrystalline calcium phosphate ceramics in biomedical engineering. Materials Science and Engineering: C. 2007;27(3):441-449.
60. Bow J, Liou S, Chen S. Structural characterization of room-temperature synthesized nano-sized β-tricalcium phosphate. Biomaterials. 2004;25(16):3155-3161.
61. Vallet-Regi M. Ceramics for Medical Applications. J Chem Soc, Dalton Trans. 2001 (2):97-108.
62. Kweh S, Khor K, Cheang P. The Production and Characterisation of Hydroxyapatite (HA) Powder. Journal of Materials Processing Technologies. 1999;89-90:373-377.
63. Palazzo B, Iafisco M, Laforgia M, Margiotta N, Natile G, Bianchi CL, et al. Biomimetic Hydroxyapatite–Drug Nanocrystals as Potential Bone Substitutes with Antitumor Drug Delivery Properties. Advanced Functional Materials. 2007;17(13):2180-2188.
64. Iafisco M, Palazzo B, Marchetti M, Margiotta N, Ostuni R, Natile G, et al. Smart delivery of antitumoral platinum complexes from biomimetic hydroxyapatite nanocrystals. Journal of Materials Chemistry. 2009;19(44):8385-8392.
65. Cao W, Hench L. Bioactive materials. Ceramics International. 1996;22(6):493-507.
66. Koutsopoulos S. Synthesis and Characterisation of Hydroxyapatite Crystals: A Review Study on the Analytical Methods. J Biomed Mater Res. 2002;62(4):600-612.
67. Elliott J. Structure and Chemistry of the Apatites and Other Calcium Orthophosphates 1ed: Elsevier; 1994. 389 p.
68. Boanini E, Gazzano M, Bigi A. Ionic substitutions in calcium phosphates synthe sized at low temperature. Acta Biomater. 2010;6(6):1882-1894.
69. Puajindanetr S. Characterisation and Sintering of Precipitated Hydroxyapatite 1993.
70. Yang Y, Kim K, Ong J. A review on calcium phosphate coatings produced using a sputtering process—an alternative to plasma spraying. Biomaterials. 2005;26(3):327-337.
71. Geesink R, Hoefnagels N. Six-year results of hydroxyapatite-coated total hip replacement. J Bone Loint Surg Br. 1995;77(4):534-547.
72. Soballe K, Overgaard S. The current status of hydroxyapatite coating of prostheses. J Bone Joint Surg Br. 1996;78(5):689-691.

73. Ducheyne P, Qiu Q. Bioactive ceramics: the effect of surface reactivity on bone formation and bone cell function. Biomaterials. 1999;20(23-24):2287-2303.
74. Thummler F, Oberacker R. Introduction to Powder Metallurgy. Maney Publishing for IOM3, the Institute of Materials, Minerals and Mining; 1993.
75. Yong P, Macaskie L, Sammons R, Marquis P. Synthesis of nanophase hydroxyapatite by a Serratia sp. from waste-water containing inorganic phosphate. Biotechnol, Lett. 2004;26(22):1723-1730.
76. Jiangling L. Structural Characterisation of Apatite like Materials. UK: University of Birmingham; 2009.
77. Bernard L, Freche M, Lacout J, Biscans B. Preparation of Hydroxyapatite by Neutralization at Low Temperature - Influence of Purity of the Raw Material. Powder Technology. 1999;103(1):19-25.
78. Tagai H, Aoki H. Preparation of synthetic hydroxyapatite and sintering of apatite ceramics." 'Mechanical Properties of Biomaterials. University of Keele 1980.
79. Rhee S. Synthesis of Hydroxyapatite via Mechanochemical Treatment. Biomaterials. 2002;23(4):1147-1152.
80. Cacciotti I, Bianco A, Lombardi M, Montanaro L. Mg-substituted hydroxyapatite nanopowders: synthesis, thermal stability and sintering behaviour. J Eur Ceram Soc. 2009;29(14):2969-2978.
81. Habibovic P, Barralet J. Bioinorganics and biomaterials: bone repair. Acta Biomater. 2011;7(8):3013-3026.
82. Dvorak M, Siddiqua A, Ward T, Carter D, Dallas S, Nemeth E, et al. Physiological changes in extracellular calcium concentration directly control osteoblast function in the absence of calciotropic hormones. Proc Nati Acad Sci USA. 2004;101(14):5140-5145.
83. Bigi A, Boanini E, Capuccini C, Gazzano M. Strontium-substituted hydroxyapatite nanocrystals. Inorganica Chimica Acta. 2007;360(3):1009-1016.
84. Samani S, Hossainalipour S, Tamizifar M, Rezaie H. In-vitro antibacterial evaluation of sol-gel-derived Zn- , Ag-, and (Zn + Ag)-doped hydroxyapatite coatings against methycillin-resistant S. aureus. J Biomed Mater Res A. 2013;101(1):222-230.
85. Fenga Q, Kim T, Wua J, Parkb E, Kimb J, Limb D, et al. Antibacterial effects of Ag-HAp thin films on alumina substrates. Thin Solid Films 1998;335(1-2):214-219.
86. Chung R, Hsieh M, Huang K, Perng L, Chou F, Chin T. Anti-Microbial Hydroxyapatite Particles Synthesized by a Sol–Gel Route. J Sol-Gel Sci Technol. 2005;33(2):229-239.
87. Oh K, Kim K, Jeong Y, Park E, Kim S, Kwon J, et al. Cytotoxicity and antimicrobial effect of Ag doped hydroxyapatite. European Ceramic Society. 2004;264-268:2107-2110.
88. Costescu A, Ciobanu C, Iconaru S, Ghita R, Chifiriuc C, Marutescu L, et al. Fabrication, Characterization, and Antimicrobial Activity, Evaluation of Low Silver Concentrations in Silver-Doped Hydroxyapatite Nanoparticles. Journal of Nanomaterials. 2013;2013(5):9.
89. Joanna K, Groszyk E, Różycka D. Substituted Hydroxyapatites with Antibacterial Properties. BioMed Research International. 2014;2014:15.
90. Visurraga J, Gutie´rrez C, Plessing V, Garcia A. Metal nanostructures as antibacterial agents. Science against microbial pathogens: communicating current research and technological advances. 2011.

91. Dastjerdi R, Montazer M. A review on the application of inorganic nano-structured materials in the modification of textiles: focus on anti-microbial properties. Colloids and Surfaces B: Biointerfaces,. 2010;79(1):5-18.
92. Simchi A, Tamjid E, Pishbin F, Boccaccini A. Recent progress in inorganic and composite coatings with bactericidal capability for orthopaedic applications. Nanomed. 2011;7(1):22-39.
93. Hajipour M, Fromm K, Ashkarran A, Aberasturi D, Larramendi I, Rojo T, et al. Antibacterial properties of nanoparticles,. Trends in Biotechnology,. 2012;30(10):499-511.
94. Hajipour M, Fromm K, Ashkarran A, Aberasturi D, Larramendi I, Rojo T, et al. Antibacterial properties of nanoparticles. Trends Biotechnol. 2012;30(10):499-511.
95. Kandile N, Howida T, Mansoura I, Hemat M. Silver Nanoparticles Effect on Antimicrobial and Antifungal Activity of New Heterocycles. Bull Korean Chem Soc. 2010;31(12).
96. Klasen H. Historical review of the use of silver in the treatment of burns. I. early uses. Burns. 2000;26(2):117-130.
97. Lara H, Garza-Trevino E, Ixtepan-Turrent L, Singh D. Silver nanoparticles are broad-spectrum bactericidal and virucidal compounds. J Nanobiotechnology. 2011;9(30):30-38.
98. Wright J, Lam K, Hansen D, Burrell R. Efficacy of topical silver against fungal burn wound pathogens,. Am J Infect Control. 1999;27(4):334-350.
99. Hardes J, Ahrens H, Gebert C, Streitbuerger A, Buerger H, Erren M, et al. Lack of toxicological side-effects in silver-coated megaprostheses in humans. Biomaerials. 2007;28(18):2869-2875.
100. Gosheger G, Hardes J, Ahrens H, Streitburger A, Buerger H, Erren M, et al. Silver-coated megaendoprostheses in a rabbit model—an analysis of the infection rate and toxicological side effects. Biomaterials. 2004;25(24):5547-5556.
101. Darouiche R, Raad I, Heard S, Thornby J, Wenker O, Gabrielli A, et al. A comparison of two antimicrobial-impregnated central venous catheters. Catheter Study Group. N Engl J Med. 1999;340(1):1-8.
102. Kora A, Arunachalam J. Assessment of antibacterial activity of silver nanoparticles on Pseudomonas aeruginosa and its mechanism of action. world J Microbiol Biotechnol. 2011;27(5):1209-1216.
103. Oh K, Kim K, Jeong Y, Choa Y. Effect of fabrication processes on the antimicrobial properties of silver doped nano-sized HAp. Key Engineering Materials. 2003;240-242:583-586.
104. Chen W, Liu Y, Courtney H, Bettenga M, Agrawal C, Bumgardner J, et al. In vitro anti bacterial and biological properties of magnetron co- sputtered silver- containing hydroxyapatite coating. Biomaterials. 2006;27(32):5512-5517.
105. Feng Q, Cui T, Kim T, Kim J. Ag-subsituted hydoxyaptite coating with both antimicrobial effects and biocompatibility. Journal of Materials Science Letters. 1999;18(7):559-561.
106. Karlov A, Shakhov V, Kolobov J. Definition of silver concentration in calcium phophate coatings on titanium implants ensuring balancing of bactericidity and cytotoxicity. Bioceramics. 2000;192(1):207-210.

107. Shirkhanzadeh M, Azadegan M, Liu G. Bioactive delivery systems for the slow release of antibiotics: incorporation of Ag+ ions into micro-porous hydroxyapatite coatings. Materials letters. 1995;24(1-3):7-12.
108. Chen Y, Zheng X, Xie Y, Ding C, Ruan H, Fan C. Anti-bacterial and cytotoxic properties of plasma sprayed silver-containing HA coatings. J Mater Sci Mater Med. 2008;19(12):3603-3609.
109. Alt V, Bechert T, Steinrucke P, Wagener M, Seidel P, Dingeldein E, et al. An in vitro assessment of the antibacterial properties and cytotoxicity of nanoparticulate silver bone cement Biomaterials. 2004;25(18):4383-4391.
110. Aimonova O, Racquel Z, LeGeros R, Sinyayev V. Antimicrobiologic property hydrated amorphous calcium phosphates containg silver. Bioceramics. 2005;17:439-442.
111. LeGeros R. Calcium phosphates in oral biology and medicine. Monogr Oral Sci. 1991;15(1):201.
112. Castiglioni S, Cazzaniga A, Albisetti W, Maier J. Magnesium and Osteoporosis: Current State of Knowledge and Future Research Directions. Nutrients. 2013;5(8):3022-3033.
113. Belluci M, Giro G, Barrio R, Pereira R, Marcantonio E, Orrico S. Effects of magnesium intake deficiency on bone metabolism and bone tissue around osseointegrated implants. Clin Oral Implants Res. 2011;22(7):16-21.
114. Suchanek W, Byrappa K, Shuk P, Riman R, Janas V, TenHuisen K. Preparation of magnesium-substituted hydroxyapatite powders by the mechanochemical–hydrothermal method. Biomaterials. 2004;25(19):4647-4657.
115. Zhao S, Jiang Q, Peel S, Wang X, He F. Effects of magnesium-substituted nanohydroxyapatite coating on implant osseointegration. Clin Oral Implants Res. 2013:34-41.
116. Gibson I, Bonfield W. Preparation and characterization of magnesium/carbonate co-substituted hydroxyapatites. J Mater Sci Mater Med. 2002;13(7):685-693.
117. G. Dolci RM, R. Rrati, and G. Valdre, . Odontostomatologic use of apatite-based nanostructured materials,. 1998.
118. Laurencin D, Almora-Barrios N, Leeuw N, Gervais C, Bonhomme C, Mauri F, et al. Magnesium incorporation into hydroxyapatite. Biomaterials. 2011;32(7):1826-1837.
119. Fuierer T, LoRe M, Puckett S, Nancollas G. A mineralization adsorption and mobility study of hydroxyapatite surfaces in the presence of zinc and magnesium ions. Langmuir. 1994;10(12):4721-4725.
120. Kannan S, Lemos I, Rocha J, Ferreira J. Synthesis and characterization of magnesium substituted biphasic mixtures of controlled hydroxyapatite/B-tricalcium phosphate ratios. J Solid State Chem. 2005;178(10):7.
121. Chiranjeevirao S, Hemmerle J, Voegel J, Frank R. A method of preparation and characterization of magnesium-apatites. Inorganica Chimica Acta. 1982;67:183-187.
122. Patel P. Magnesium calcium hydroxylapatite solid solutions. Journal of Inorganic and Nuclear Chemistry. 1980;42:1129-1132.
123. Fadeev I, Shvorneva L, Barinov S, Orlovskii V. Synthesis and structure of magnesium-substituted hydroxyapatite. Inorganic Materials. 2003;39(9):947-950.
124. Yasukawa A, Ouchi S, Kandori K, Ishikawa T. Preparation and characterization of magnesium-calcium hydroxyapatites. J Mater Chem. 1996;6:1401-1405.

125. Landi E, Logroscino G, Proietti L, Tampieri A, Sandri M, Sprio S. Biomimetic mg-substituted hydroxyapatite: from synthesis to in vivo behaviour. J Mater Sci Mater Med. 2008;19(1):239-247.
126. Ren F, Xin R, Ge X, Leng Y. Characterization and structural analysis of zinc-substituted hydroxyapatites. Acta Biomater. 2009;5(8):3141-3149.
127. Bigi A, Foresti E, Gandolfi M, Gazzano M, Roveri N. Inhibiting effect of zinc on hydroxylapatite crystallization. J Inorg Biochem. 1995;58:49-58.
128. Moonga B, Dempster D. Zinc is a potent inhibitor of osteoclastic bone resorption in vitro. J Bone Miner Res. 1995;10(3):453-457.
129. Yamaguchi M, Mochizuki A, Okada S. Stimulation of bone resorption by comparatively high dose of zinc in rats. J Pharmacobiodyn. 1982;5(7):501-504.
130. Hayakawa S, Ando K, Tsuru K, Osaka A, Fujii E, Kawabata K, et al. Structural characterization and protein adsorption property of hydrox- yapatite particles modified with zinc ions. J Am Ceram Soc. 2007;90(2):565-569.
131. Ergun C, Webster T, Bizios R, Doremus R. Hydroxylapatite with substituted magnesium, zinc, cadmium, and yttrium. i. structure and microstructure. J Biomed Mater Res. 2002;59(2):305-311.
132. Miyaji F, Kono Y, Suyama Y. Formation and structure of zinc-substituted calcium hydroxyapatite. MaterResBull. 2005;40(2):209-220.
133. Boanini E, Gazzano M, Bigi A. Ionic substitutions in calcium phosphates synthesized at low temperature. Acta Biomater. 2010;6(6):1882-1894.
134. Tripathy N, Patel P, Panda A. Preparation, IR, and lattice constant measurements of mixed (Ca + Cu + Zn) hydroxylapatites. J Solid State Chem. 1989;80(1):1-5.
135. Li M, Xiao X, Chen C, Huag L. Structural characterization of zinc-substituted hydroxyapatite prepared by hydrothermal method. J Mater Sci Mater Med. 2008;19(2):797-803.
136. Tang Y, Chappell H, Dove M, Reeder R, Lee Y. Zinc incorporation into hydroxylapatite. . Biomaterials. 2009;30(15):2864-2872.
137. Wang L, Nancollas G. Calcium Orthophosphates: Crystallization and Dissolution. Chem Rev. 2008;108(11):4628-4669.
138. Stanic V, Dimitrijevic S, Antic-Stankovic J, Mitric M, Jokic B, Plecas L, et al. Synthesis, characterization and antimicrobial activity of copper and zinc- doped hydroxyapatite nanopowders. Applied Surface Science. 2010;256(20):6083-6089.
139. Wolschendorf F, Ackart D, Shrestha T, Dove L, Nolan S, Laminchhane G, et al. Copper resistance is essential for virulence of Mycobacterium tuberculosis. Proc Natl Acad Sci U S A. 2011;108(4):1621-1626.
140. Yang Y, Zhang L, Xu K. Effect of storing on the microstructure of Ag/Cu/HA powder. Ceramics International. 2009;35(4):1595-1601.
141. Kawamura H, Ito A, Miyakawa S, Layrolle P, Ojima K, Lchinose N, et al. Stimulatory effect of zinc-releasing calcium phosphate implant on bone formation in rabbit femora. J Biomed Mater Res. 2000;50(2):184-190.
142. Grandjean-Laquerriere A, Laquerriere P, Jallot E, Nedelec J, Guenounou M, Laurent-Maquin D, et al. Influence of the zinc concentration of sol-gel derived zinc substituted hydroxyapatite on cytokine production by human monocytes in vitro. Biomaerials. 2006;27(17):6.

143. Orlovskii V, Komlev V, Barinov S. Hydroxyapatite and Hydroxyapatite-based Ceramics. Inorganic Materials.38:973-984.
144. Martin R, Burr D, sharkey N. Skeletal Tissue Mechanics. Illustrated ed. New York: Springer; 1998.
145. Cox S, Jamshidi P, Grover L, Mallick K. Preparation and characterisation of nanophase Sr, Mg, and Zn substituted hydroxyapatite by aqueous precipitation. Mater Sci Eng, C Mater Biol Appl. 2014;1(35):106-114.
146. Clarke B. Normal Bone Anatomy and Physiology. Clin J Am Soc Nephrol. 2008;3:131-139.
147. Tovar A. Bone Remodelling as a Hybrid Cellular Automaton Optimization process. Indiana: University of Notre Dame in Partial Fulfillmen; 2004.
148. Rho J, Kuhn-Spearing L, Zioupos P. Mechanical properties and the hierarchical structure of bone. Med Eng Phys. 1998;20(2):92-102.
149. Reznikov N, Shahar R, Weiner S. Bone hierarchical structure in three dimensions. Acta Biomater. 2014;10(9):3815-3826.
150. Weiner S, Wagner H. The Material Bone: Structure-Mechanical function Relations. Annual Review of Materials Science 1998;28:271-298.
151. Martin R, Burr D, sharkey N. Skeletal Tissue Mechanics. illustrated ed. New York: Springer 1998. 392 p.
152. Reznikov N, Shahar R, Weiner S. Three-dimensional structure of human lamellar bone: the presence of two different materials and new insights into the hierarchical organization. Bone. 214;59:93-104.
153. Hing K. Bone repair in the twenty-first century: biology, chemistry or engineering? Philos Trans, A Math Phys Eng Sci.362(1825):2821-2850.
154. Junqueira L, Carneiro J. Basic Histology 12 ed: McGraw-Hill Medical; 2010.
155. Fratzl P, Groschner M-V, G., Vogl G, Plenk H, Eschberger J, Fratzl-Zelman N, et al. Mineral crystals in calcified tissues: a comparative study by SAXS. J Bone Miner Res. 1992;7(3):329-334.
156. Gelinsky M, Bernhard A, Eckert M, Hanke T, Konig U, Lode A, et al. Biomaterials based on mineralised collagen—an artificial extracellular bone matrix. Japan: Springer 2007.
157. Martin R, Burr D, sharkey N. Skeletal Biology. In Skeletal Tissue Mechanics. illustrated ed. New York: Springer; 1998. 392 p.
158. Omelon S, Georgiou J, Henneman Z, Wise L, Sukhu B, Hunt T, et al. Control of Vertebrate Skeletal Mineralization by Polyphosphates. PLoS ONE. 2009;4(5):5634.
159. Sommerfeldt D, Rubin C. Biology of bone and how it orchestrates the form and function of the skeleton. Eur Spine, J. 2001;10:86-95.
160. Suryanarayana C, Grant Norton M. X-Ray Diffraction: A Practical Approach. Illustrated ed: Springer; 1998.
161. Slosarczyk A, Paszkiewicz Z, Paluszkiewicz C. FTIR and XRD evaluation of Carbonated Hydroxyapatite Powders Synthesised by Wet Methods. J Molecular Structure. 2005;744-747:657-661.
162. Heimann R. Plasma-Spray Coating: Principles and Applications. 2 ed. New York: John Wiley & Sons; 2008.

163. Cullity B, Stock S. Elements of X-Ray Diffraction. 3, Illustrated ed: Prentic Hall; 2001.
164. Hoffmann P. Atomic and nuclear analytical methods. XRF, Massbauer, XPS, NAA and ion-beam spectroscopic techniques. Anal Bioanal Chem. 2008;391(6):2103-2104.
165. Ferraro J, Krishnan K. Practical Fourier transform infrared spectroscopy : Industrial and laboratory chemical analysis San Diego: Elsevier; 2012.
166. Ferraro J, Nakamoto K. Introductory Raman Spectroscopy. London: Academic Press; 2012. 370 p.
167. Meenan B, McClorey C, Akay M. Thermal analysis studies of poly(etheretherketone)/hydroxyapatite biocomposite mixtures. J Mater Sci. 2000;11(8):481-490.
168. Fifield F, Kaeley D. Principles and Practice of Analytical Chemistry. illustrated ed. US: Springer; 2013. 521 p.
169. Ghosh-Choudhury N, Windle J, Koop B, Harris M, Guerrero D, Wozney J, et al. Immortalized murine osteoblasts derived from BMP-2-T- antigen expressing transgenic mice. Endocrinology. 1996;137(1):331-339.
170. Strober W. Trypan blue exclusion test of cell viability. Curr Protoc Immunol. 2001 May;3.
171. Adds J, Larkcom E. Tools, Techniques and Assessment in Biology: A Course Guide for Students and Teachers: Nelson; 1999.
172. Sidman R, Miale I, Feder N. Cell proliferation and migration in the primitive ependymal zone; An autoradiographic study of histogenesis in the nervous system. Exp Neurol. 1959;1(4):322-333.
173. Ahmed S, Gogal R, Walsh J. A new rapid and simple non-radioactive assay to monitor and determine the proliferation of lymphocytes: an alternative to [3H]thymidine incorporation assay. . J Immunol Methods. 1994;170(2):211-224.
174. Anoopkumar-Dukie S, Carey J, Conere T, O'sullivan E, van Pelt F, Allshire A. Resazurin assay of radiation response in cultured cells. Br J Radiol. 2005;78(934):945-947.
175. Samizadeh S. Bone Formation on Calcium Phosphate Bone Substitute Materials: University College London; 2010.
176. Stein G, Lian J, Owen T. Relationship of cell growth to the regulation of tissue-specific gene expression during osteoblast differentiation. FASEB J. 1990;4(13):3111-3123.
177. Kashani MAMP. Effect of Cation Substitutions in an Ionomer Glass Composition on the Setting Reaction and Properties of the Resulting Glass Ionomer Cements: University of Birmingham; 2013.
178. Santos M. Synthesis Control and Characterization of Hydroxyapatite Prepared by Wet Precipitation Process. Synthesis Control Materials Research. 2004;7(4):625-630.
179. Smiciklas I, Onjia A, Raicevic S. Experimental Design Approach in the Synthesis of Hydroxyapatite by Neutralization Method. Separation and Purification Technology. 2005;44(2):97-102.
180. B D, Schroeder L, WE B. Crystallographic studies of the role of Mg as a stabilizing impurity in β-Ca3(PO4)2. The crystal structure of pure β-Ca3(PO4)2. J Solid State Chem 1974;10(3):232-248.

181. Sudarsanan K, Young R. significant precision in crystal structural detail: holly springs hydroxyapatite. Acta Crystallographica section B. 1969;25:1534-1543.
182. Sudarsanan K, Young R. Significant precision in crystal structural details. Holly Springs hydroxyapatite. Acta Crystallographica section B. 1969;25:1534-1543.
183. Aizawa M, Ueno H, Itatani K, Okada I. Syntheses of calcium-Deficient Apatite Fibres by a Homogeneous Precipitation Method and their Characterizations. Journal of European Ceramic Society. 2006;26(4-5):501-507.
184. Díaz M, Barba F, Miranda M, Guitián F, Torrecillas R, Moya J. Synthesis and Antimicrobial Activity of a Silver-Hydroxyapatite Nanocomposite. Journal of Nanomaterials. 2009:4110-4129.
185. Jadalannagari S, Deshmukh K, Ramanan S, Kowshik M. Antimicrobial activity of hemocompatible silver doped hydroxyapatite nanoparticles synthesized by modified sol–gel technique. Applied Nanoscience. 2014;4(2):133-141.
186. Kannan SG-N, F.; Neubauer, J.; Ferreira, J.M.F. . Synthesis and structure refinement of zinc-doped beta-tricalcium phosphate powders. J Amer Ceram Soc. 2009;92:1592-1595.
187. Kannan S, Goetz-Neunhoeffer F, Neubauer J, Rebelo A, Valério P, Ferreira J. Rietveld structure and in vitro analysis on the influence of magnesium in biphasic (hydroxyapatite and beta-tricalcium phosphate) mixtures. J Biomed Mater. 2009;90(1):404-411.
188. Robertson W, Morgan D. Effect of pyrophosphate on the exchangeable calcium pool of hydroxyapatite crystals. Biochim Biophys Acta. 1971;230(3):495-503.
189. Kang S. Sintering: Densification, Grain Growth and Microstructure: Butterworth-Heinemann; 2004. 280 p.
190. Freund F KR. Distribution of fluorine in hydroxyapa- tite studied by infrared spectroscopy. J Chem Soc, Dalton Trans. 1977;11:1136-1140.
191. Wienand L, Dallemagne M, Duyckaerts G. Hydrogen bonding in apatitic calcium phosphates. Nature. 1961;190:164-165.
192. Baddiel C, Berry E. Spectra-structure correlations in hydroxyapatite and fluorapatite. Spectrochemica Acta Part B-atomic Spectroscopy. 1966;22(8):1407-1416.
193. Fowler B. Infrared studies of apatites. I. Vibrational assignments for calcium, strontium, and barium hydroxyapatites utilizing isotopic substitution. Inorg Chem. 1974;13(1):194-207.
194. Joris S, Amberg C. Nature of deficiency in nonstoichiometric hydroxyapatites. II. Spectroscopic studies of calcium and strontium hydroxyapatites. J Phys Chem B. 1971;75:3172-3178.
195. Palard M, Champion E, Foucaud S. Synthesis of silicated hydroxyapatite Ca10(PO4)6-x(SiO4)x(OH)2-x. Journal of Solid State Chemistry. 2008;181(8):1950-1960.
196. Chickerur N, TTUN M, Brown W. A mechanism for incorporation of carbonate into apatite. Calcif Tissue Int. 1980;32(1):55-62.
197. Gadaleta S, Paschalis E, Camacho N, Betts F, Mendelhson R, Boskey A. Fourier Transform Infrared Spectroscopy of Synthetic and Biological Apatites. Amjad Z, editor. New York: Plenum Press; 1995.
198. Klee W, Engel G. Infrared spectra of the phosphate ions in various apatites. J Inorg Nucl Chem 1970;32(6):1837-1843.

199. Arends J, Christoffersen J, Christoffersen M, Eckert H, Fowler B, Heughebaert J, et al. A calcium hydroxyapatite precipitated from an aqueous solution; an international multimethod analysis. J Crystal Growth. 1987;84(3):512-532.
200. Prakash K, Ooi C, Kumar R, Khor K, Cheang P. Effect of super saturation level on the size and morphology of hydroxyapatite precipitate. Emerging Technologies - Nanoelectronics; Singapore: IEEE; 2006. p. 345-349.
201. Sammons R, Thackray A, Ledo H, Marquis P, Jones I, Yong P, et al. Characterisation and sintering of nanophase hydroxyapatite synthesised by a species of Serratia. Journal of Physics: Conference Series. 2007;93(1):1-7.
202. Mobasherpour I, Heshajin M, Kazemzadeh A, Zakeri M. Synthesis of nanocrystalline hydroxyapatite by using precipitation method. Journal of Alloys and Compounds. 2007;430(1-2):330-333.
203. Furuzono T, Walsh D, Sato K, Sonoda K, Tanaka J. Effect of reaction temperature on the morphology and size of hydroxyapatite nanoparticles in an emulsion system. Journal of Materials Science Letters. 2001;20(2):111-114.
204. Thomas M, Ghosh S, George K. Characterization of nano-structured silver orthophosphate. Materials Letters. 2002;56(4):386-392.
205. Gibson I, Bonfield W. Novel synthesis and characterization of an AB-type carbonate-substituted hydroxyapatite. J Biomed Mater Res. 2002;59(4):697-708.
206. Siddharthan A, Seshadri S, Sampath Kumar T. Rapid synthesis of calcium deficient hydroxyapatite nanoparticles by microwave irradiation. Trends in Biomaterials and Artificial Organs. 2005;18(2):110-113.
207. Raynaud S, Champion E, Bernache-Assollant D, Thomas P. Calcium phosphate apatites with variable Ca/P atomic ratio I. Synthesis, characterisation and thermal stability of powders. Biomaterials. 2002;23(4):1065-1072.
208. Silva C, Pinheiro A, Miranda M, Góes J, Sombra A. Structural properties of hydroxyapatite obtained by mechanosynthesis. Solid State Sciences. 2003;5(4):553-558.
209. Penel G, Leroy G, Rey C, Bres E. MicroRaman spectral study of the PO4 and CO3 vibrational modes in synthetic and biological apatites. Calcif Tissue Int. 1998;63(6):475-481.
210. Sauer G, Zunic W, Durig J, Wuthier R. Fourier transform Raman spectroscopy of synthetic and biological calcium phosphates. Calcif Tissue Int. 1994;54(5):414-420.
211. Tsuda H, Arends J. Raman spectra of human dental calculus. J Dent Res. 1993;72(12):1609-1613.
212. Griffith W. Raman studies on rock-forming minerals. Part II. Minerals containing MO3, MO4, and MO6 groups. J Chem Soc (A). 1970 (0):286-291.
213. de Aza P, Guitian F, Santos C, de Aza S, Cusco R, Artus L. Vibrational investigation of calcium phosphate compounds. 2. Comparison between hydroxyapatite and beta-tricalcium phosphate. Chem Mater. 1997;9(4):916-922.
214. O'Shea D, Bartlett M, Young R. Compositional analysis of apatites with laser-Raman spectroscopy: (OH, F, Cl) apatites. Arch Oral Biol. 1974;19(11):995-1006.
215. de Aza PN, Guitián F, Santos C, de Aza S, Cuscó R, Artús L. Vibrational Properties of Calcium Phosphate Compounds. 2. Comparison between Hydroxyapatite and β-Tricalcium Phosphate. Chemistry of Materials. 1997 1997/04/01;9(4):916-922.

216. Nath S, Kalmodia S, Basu B. Densification, phase stability and in vitro biocompatibility property of hydroxyapatite-10 wt% silver composites. J Mater Sci Mater Med. 2010;21(4):1273-1287.
217. Ren F, Leng Y, Xin R, Ge X. Synthesis, characterization and ab initio simulation of magnesium-substituted hydroxyapatite. Acta Biomater.6(7):2787-2796.
218. Sopyan I, Ramesh S, Nawawi N, Tampieri A, Sprio S. Effects of manganese doping on properties of sol–gel derived biphasic calcium phosphate ceramics. Ceramics International. 2011;37(8):3703-3715.
219. Yamamoto A, Honma R, Tanaka A, Sumita M. Generic tendency of metal salt cytotoxicity for six cell lines. National Research Institute for metals, Science and Technology Agency. 1999;19:193-199.
220. Ryu H, Young H, Hong K, Chang B, Lee C, Chung S. An improvement in sintering property of B-tricalcium phosphate by addition of calcium pyrophosphate. Biomaterials. 2002;23(3):909-914.
221. Bouler J, LeGeros R, Daculsi G. Biphasic calcium phosphates: Influence of three synthesis parameters on the HA/B-TCP ratio. Biomed Mater Res. 2000;51(4):680-684.
222. Sudarsanan K, Young R. Significant precision in crystal structural details. Holly Springs hydroxyapatite. Acta Crystallographica section B. 1969;25:1534-1543.
223. Famery R, Richard N, Boch P. Preparation of a- and b-tricalcium phosphate ceramics, with and without magnesium addition. Ceram Int 1994;20(5):327-336.
224. Zhou J, Zhang X, Chen J, Zeng S, De Groot K. High temperature characteristics of synthetic hydroxyapatite. J Mater Sci Mater in Med. 1993;4(1):83-85.
225. Wang P, Chaki T. Sintering behaviour and mechanical properties of hydroxyapatite and dicalcium phosphate. J Mater Sci Mater in Med. 1993;4(2):150-158.
226. Ramesh S, Tan CY, Hamdi M, Sopyan I, Teng WD, editors. The influence of Ca/P ratio on the properties of hydroxyapatite bioceramics2007.
227. Neuman W, Toribara T, Mulryan B. Synthetic hydroxyapatite crystals I. Sodium and potassium fixation. Arch Biochem Biophys. 1962;98(3):384-390.
228. Nordström E, Karlsson K. Carbonate-doped hydroxyapatite. J Mater Sci: Mater Med. 1990;1(3):182-184.
229. Heughebaert J, Zawacki S, Nancollas G. The growth of nonstoichiometric apatite from aqueous solution at 37°C: I. Methology and growth at pH 7.4. J Colloid Interface Sci. 1990;135(1):20-32.
230. Hing K, Gibson I, Revell P, Best S, Bonfield W. Influence of Phase Purity on the in Vivo Response to Hydroxyapatite. Key Engineering Materials 2000;13:373-376.
231. Hellmich C, Ulm F. Micro mechanical Model for Ultrastructural Stiffness of Mineralized Tissues. Journal of Engineering Mechanic.128(8):898-908.
232. Sun L, Berndt C, Gross K, Kucuk A. Material fundamentals and clinical performance of plasma- sprayed hydroxyapatite coatings: A review. J Biomed Mater Res. 2001;58(5):22.
233. Administration USFaD. Calcium Phosphate (Ca-P) Coating Draft Guidance for Preparation of FDA Submissions for Orthopaedic and Dental Endosseous Implants. In: Administration USFaD, editor. USA2004.

234. Pang Y, Bao X. Influence of Temperature, Ripening Time and Calcination on the Morphology and Crystallinity of Hydroxyapatite Nanoparticles. Journal of the European Ceramic Society. 2003;23(10):1697-1704.
235. Lazic S, Zec S, Milijevic N, Milonjic S. The effect of temperature on the properties of hydroxyapatite precipitated from calcium hydroxide and phosphoric acid. Thermochimica Acta. 2001;374(1):13-22.
236. Kawasaki T. Hydroxyapatite as a liquid chromatographic packing. J Chromatogr. 1991;544:147-184.
237. Ipekoglu M, Altintas S. Silver substituted nanosized calcium deficient hydroxyapatite. Materials technology. 2010;25(5):295-230.
238. Ciobanu C, Iconaru S, Le Coustumer P, Constantin L, Predo D. Antibacterial activity of silver-doped hydroxyapatite nanoparticles against gram-positive and gram negative bacteria. Nanoscale Res Lett. 2012;7(1):324-329.
239. Nirmala R, Navamathavan R, Afeesh R, Park H, Kangand H, Kim Y. Characterisation of bioresourced hydroxyapatite containing silver nanoparticles. Materials Reesearch Innovations. 2012;16(4):249-256.
240. Rameshbabu N, Kumar T, Prabhakar T, Sastry V, Murty K, Rao K. Antibacterial nanosized silver substituted hydroxyapatite: synthesis and characterization. J Biomed Mater Res. 2007;80(3):581-591.
241. Stanić V, Janaćković D, Dimitrijević S, Tanasković SB, Mitrić M, Pavlović MS, et al. Synthesis of antimicrobial monophase silver-doped hydroxyapatite nanopowders for bone tissue engineering. Applied Surface Science. 2011;257(9):4510-4518.
242. Lim P, Teo E, Ho B, Tay B, Thian E. Effect of silver content on the antibacterial and bioactive properties of silver-substituted hydroxyapatite. J Biomed Mater Res A. 2013;101(9):2456-2464.
243. Webster T, Ergun C, Doremus R, Bizios R. Hydroxylapatite with substituted magnesium, zinc, cadmium, and yttrium. II. Mechanisms of osteoblast adhesion. J Biomed Mater Res. 2002;59(2):312-317.
244. LeGeros R, Gatti A, Kijkowska R, Mijares D, LeGeros J. Mg-substituted Tricalcium Phosphates: Formation and Properties. Bioceramics. 2004;16:127-130.
245. Ryu H, Hong K, Lee J, Leb J, Kim D, Lee J, et al. Magnesia-doped HA/B-TCP ceramics and evaluation of their biocompatibility. Biomaterials. 2004;25(3):393-401.
246. RZ. L. Incorporation of magnesium in synthetic and in biological apatites. Fearnhead R, S S, editors. Amsterdam: Elsevier; 1984. 32-36 p.
247. LeGeros R, Daculsi G, Kijkowska R, Kerebel B. The effect of magnesium on the formation of apatites and whitlockites. London1989.
248. Bertoni E, Bigi A, Cojazzi G, Gandolfi M, Panzavolta S, Roveri N. Nanocrystals of magnesium and fluoride substituted hydroxyapatite. . J Inorg Biochem. 1998;72(1-2):29-35.
249. Mayer I, Schlam R, Featherstone J. Magnesium-containing carbonate apatites. J Inorg Biochem. 1997;66(1):1-6.
250. Golden D, Ming D. Nutrient-substituted hydroxyapatites: synthesis and characterization. Soil Sci Soc Am J. 1999;63(3):657-664.
251. Okazaki M TJ, Kimura H. . Comparison of crystal lographic properties of Mg, Fe, Na, CO3, F, and Cl-containing apatites. J Osaka Univ Dent Sch. 1986;26:79-89.

252. Patel P. Magnesium calcium hydroxyapatite solid solutions. Journal of Inorganic and Nuclear Chemistry. 1980;42:1129-1132.
253. Chiranjeevirao S, Hemmerle J, Voegel J, Frank R. A method of preparation and characterization of magnesium apatites. Inorg Chim Acta. 1982;67:183-187.
254. Serre C, Papillard M, Chavassieux P, Voegel J, Boivin G. Influence of magnesium substitution on a collagen-apatite biomater- ial on the production of a calcifying matrix by human osteoblasts. J Biomed Mater Res. 1998;42(4):626-633.
255. Dorozhkin SV. Amorphous calcium (ortho)phosphates. Acta Biomater. 2010 Dec;6(12):4457-4475.
256. Kannan S, Lemos I, Rocha J, Ferreira J. Synthesis and characterization of magnesium substituted biphasic mixtures of controlled hydroxyapatite/B-tricalcium phosphate ratios. J Solid State Chem. 2005;178(10):3190-3196.
257. Gibson I, Bonfield W. Preparation and characterization of magnesium/carbonate co-substituted hydroxyapatites. J Mater Sci Mater Med. 2002;13(7):685-693.
258. Bigi A, Falini, G., Foresti, E. and Ripamonti, A. Rietveld structure refinement of synthetic magnesium substituted B-tricalcium phosphate. Zeitschrif fur Kristallographic. 1996;211:13-16.
259. Kim S, Lee J, Kim Y, Riu D, Jung S, Lee Y, et al. Synthesis of Si, Mg substituted hydroxyapatites and their sintering behaviors. Biomaterials. 2003;24(8):1389-1398.
260. Cacciotti I, Bianco A, Lombardi M, Montanaro L. Mg-substituted hydroxyapatite nanopowders: Synthesis, thermal stability and sintering behavior. J Eur Ceram Soc. 2009;29(14):2969-2978.
261. Aqif Anwar Chaudhry aJG, a Martin Vickers,a Jeremy Karl Cockcroft,a Ihtesham Rehman,b Jonathan Knowlesd and Jawwad Arshad Darr. Synthesis and characterisation of magnesium substituted 1 calcium phosphate bioceramic nanoparticles made via continuous

hydrothermal flow synthesis. Jiurnal of material chemistry. 2008.
262. Posner A, Betts F, Blumenthal N. Formation and structure of synthetic and bone hydroxyapatites. Progress in Crystal Growth and Characterization. 1980;3(1):40-64.
263. Hesaraki S, Farhangdoust S, Ahmadi K, Nemati R, Khorami M. Phase evaluation and lattice parameters of strontium/magnesium incorporated beta-tricalcium phosphate bioceramics. Journal of the Australian Ceramic Society 2012;48(2):166-172.
264. Enderlea R, Gotz-Neunhoeffer F, Gobbels M, Muller F, Greil P. Influence of magnesium doping on the phase transformation temperature of b-TCP ceramics examined by Rietveld refinement. Biomaterials. 2005;26(17):3379-3384.
265. Neuman W, Mulryan B. Synthetic hydroxyapatite crystals. IV. Magnesium incorporation. Calcif Tissue Res. 1971;7(2):133-138.
266. Thian E, Konishi T, Kawanobe Y, Lim P, Choong C, Aizawa M. Zinc-substituted hydroxyapatite: a biomaterial with enhanced bioactivity and antibacterial properties. J Mater Sci Mater Med. 2013;24(2):437-445.
267. LeGeros R, Taheri M, Quirologico G, LeGeros J, editors. 2nd international phosphorus 1989; Boston.
268. Miyaji F, Kono Y, Suyama Y. Formation and structure of zinc-substituted calcium hydroxyapatite. Mater Res Bull. 2005;40(2):209-220.

269. Hayakawa S, Ando K, Tsuru K, Osaka A, Fujii E, Kawabata K, et al. Structural characterization and protein adsorption property of hydroxyapatite particles modified with zinc ions. J Am Ceram Soc. 2007;90(2):565-569.
270. David S, Best S. Production of zinc substituted hydroxyapatite using various precipitation routes. Biomed Mater. 2012;8(2).
271. Neuman F, Neuman M. The chemical dynamis of bone mineral Chicago: University of Chicago; 1958.
272. Pak C, Bartter C. Osteoporosis. The Lancet. 1970;295(7639):180-182.
273. Avnimeleh Y. Organic residues in modern agriculture. Isreal J Chem. 1968;25:1-10.
274. M. Jelinke ea. J of Modern trend in Laser Physics. 2011;21:1265-1269.
275. LeGeros R, Trautz O, Klein E, LeGeros J. Two types of carbonate substitution in the apatite structure. Experientia. 1969;25(1):5-7.
276. Elliott J. Structure and Chemistry of the Apatites and Other Calcium Orthophosphates: Elsevier; 1994. 389 p.
277. Gouadec G, Colomban P. Raman Spectroscopy of nanomaterials: How spectra relate to disorder, particle size and mechanical properties. Progress in Crystal Growth and Characterization of Materials. 2007;53(1):1-56.
278. Sprio S, Pezzotti G, Celotti G, Landi E, Tampieri A. Raman and cathodoluminescence spectroscopies of magnesium-substituted hydroxyapatite powders. Journal of Material Research. 2005;20(4):1009-1016.
279. de Mul F, Hottenhuis M, Bouter P, Greve J, Arends J, ten Bosch J. Micro-Raman line broadening in synthetic carbonated hydroxyapatite. J Den Res. 1986;65(3):437-440.
280. Chaudhry A, Goodall J, Vickers M, Cockcroft J, Rehman I, Knowles J, et al. Synthesis and characterisation of magnesium substituted calcium phosphate bioceramic nanoparticles made via continuous hydrothermal flow synthesis. J Mater Chem. 2008;18(48):5900-5908.
281. Koutsopoulos S. Synthesis and characterization of hydroxyapatite crystals: a review study on the analytical methods. J Biomed Mater Res. 2002;62(4):600-612.
282. Gomes S, Nedelec J, Jallot E, Sheptyakov D, Renaudin G. Unexpected mechanism of Zn2+ insertion in calcium phosphate bioceramics. Chem Mat 2011;23(12):3072-3085.
283. Gomes S, Nedelec J, Renaudin G. On the effect of temperature on the insertion of zinc into hydroxyapatite Acta Biomater. 2012;8(3):1180-1189.
284. LeGeros R, Bonel G, Legros R. Types of "H2O" in human enamel and in precipitated apatites. Calcif Tiss Res. 1978;26(1):111-118.
285. Locardi B, Pazzaglia E, Gabbi C, Profile B. Thermal behaviour of hydroxyapatite intended for medical applications. Biomaterials. 1993;14(6):437-441.
286. Rootare H, Craig R. Vapor Phase Adsorption of Water on Hydroxyapatite. J Dent Res. 1977;56(12):1437-1448.
287. Baravelli S, Bigi A, Ripamonti A, Roveri N, Foresti E. Thermal behavior of bone and synthetic hydroxyapatites submitted to magnesium interaction in aqueous medium. J Inorg Biochem. 1984;20(1):1-12.
288. K.S. Oh SHP, Y.K. Jeong. Antimicrobial Effects of Ag Doped Hydroxyapatite Synthesized from Co-precipitation Route. Key Engineering Materials. 2004;264-268:2111-2114.

289. Kishi S, Yamaguchi M. Inhibitory effect of zinc compounds on osteoclast-like cell formation in mouse marrow cultures. Biochem Pharmocol. 1994;15(48):1225-1230.
290. Sunderman F. Metal carcinogenesis in experimental animals. Food Cosmet Toxicol. 1971;9(1):105-120.
291. Saboori A. RM, Mutarzadeh F., Sheikhi M., Tahriri M., Karimi M. . Synthesis, characterization and in vitro bioactivity of sol-gel-derived SiO2-CaO-P2O5-MgO bioglass. Mater Sci. 2009; 29:335-340.
292. Qu S, Fan H, Chen J, Feng J, Fu R, Wei D, et al. Effect of Crystallinity of calcium phosphate Ceramics on Osteoblast proliferation In Vitro. Materaials Science Letters. 2001;20(4):331-332.
293. Evans EJ. Cell damage In Vitro follwing Direct Contact with Fine Particles of Titanium, Titanium Alloy and Cobalt-Chromemolybdenum Alloy. Biomaterials. 1994;15:713-717.
294. Lang H, JP K, Mertens T. Comparative test of the Soluble Toxicity of Hydroxyapatite Ceramics Using Human and Animal Osteoblast. Deutsch Zahnarztl Z. 1989;44(2):135-137.
295. Homann V, Edwards K, Webb E, Butker A. Siderophores of Marinobacter aquaeolei: petrobactin and its sulfonated derivatives. Biometals. 2009;22(4):565-571.
296. Yamamoto A, Honma R, Sumita M. Cytotoxicity evaluation of 43 metal salts using murine fibroblasts and osteoblastic cells. J Biomed Mater Res A. 1998;39(2):331-340.
297. Sandukas S, Yamamoto A, Rabiei A. Osteoblast adhesion to functionally graded hydroxyapatite coatings doped with silver. J Biomed Mater Res A. 2011;97(4):490-497.
298. Dorozhkin S. V. EM. Biological and medical significance of calcium phosphates. Angew Chem Int Ed. 2002;41:3130-3146.
299. Sader M. S. LRZ, Soares G. A. . Human osteoblasts adhesion and proliferation on magnesium-substituted tricalcium phosphate dense tablets. J Mater Sci Mater Med. 2009;20:521-527.
300. Staiger M, Pietak A, Huadmai J, Dias G. Magnesium and its alloys as orthopedic biomaterials: a review. Biomaterials. 2006;27(9):1728-1734.
301. Tavares D, Castro L, Soares G, Alves G, Granjeiro J. Synthesis and cytotoxicity evaluation of granular magnesium subsituted B-tricalcium phosphate. J Appl Oral Sci. 2013;21(1):37-42.
302. Li X, Senda K, Ito A, Sogo Y, Yamazaki A. Effect of Zn and Mg in tricalcium phosphate and in culture medium on apoptosis and actin ring formation of mature osteoclasts. Biomed Mater. 2008;3(4).
303. Xue W, Dahlquist K, Banerjee A, Bandyopadhyay A, Boss S. Synthesis and characterization of tricalcium phosphate with Zn and Mg based dopants. J Mater Sci Mater Med. 2008;19:2669-2677.
304. Gronowicz G, MacCarthy M. Response of human osteoblasts to implant materials: Integrin-mediated adhesion. J Orthop Res. 1996;14(6):878-887.
305. Ryan L, Cheung H, LeGeros R, Kurup I, Toth J, Westfall P, et al. Cellular Responses to Whitlockite. Calcif Tissue Int. 1999;65(5):374-377.
306. Zreiqat H, Howlett C, Zannettino A, Evans P, Schulze-Tanzil G, Knabe C, et al. Mechanisms of magnesium-stimulated adhesion of osteoblastic cells to commonly used orthopaedic implants. J Biomed Mater Res. 2002;62(2):175-184.

307. Yamasaki Y YY, Okazaki M, Shimazu A, Kubo T, Akagawa Y, et al. . Action of FG-MgCO3 Ap-collagen composite in promoting bone formation. Biomaterials. 2003;24:4913-4920.
308. Yamasaki Y YY, Okazaki M, Shimazu A, Uchida T, Kubo T, et al. Synthesis of functionally graded MgCO3 apatite accelerating osteoblast adhesion. J Biomed Mater Res. 2002;62:99-105.
309. Zaveri T, Dolgova N, Chu B, Lee JC, Wong J, Lele T, et al. Contributions of surface topography and cytotoxicity to the macrophage response to zinc oxide nanorods. Biomaterials. 2010;31(11):2999-3007.
310. Thian E, Konishi T, Kawanobe Y, Lim P, Choong C, Aizawa M. Zinc-substituted hydroxyapatite: a biomaterial with enhanced, bioactivity and antibacterial properties. J Mater Sci Mater Med. 2013;24(2):437-445.
311. Webster T, Massa-Schlueter E, Smith J, Slamovich E. Osteoblast response to hydroxyapatite doped with divalent and trivalent cations. Biomaterials. 2004;25(11):2111-2121.
312. Ito A, Ojima K, Naito H, Ichinose N, Tateishi T. Preparation, solubility, and cytocompatibility of zinc-releasing calcium phosphate ceramics. J Biomed Mater Res. 2000;50(2):178-183.
313. Yamamoto M, Kato, K., and Ikada, Y. Ultrastructure of the interface between cultured osteoblasts and surface modified polymer substrates. J Biomed Mater Res. 1997;37(1):29-36.
314. Ni S, Chang J, Chou L. In vitro studies of novel CaO-SiO2-MgO system composite bioceramics. J Mater Sci Mater Med. 2008;19(1):359-367.
315. Benoit D, Schwartz M, Durney A, Anseth K. Small functional groups for controlled differentiation of hydrogel-encapsulated human mesenchymal stem cells. Nat Mater. 2008;7:816-823.
316. Xynos I, Edgar A, Buttery L, Hench L, Polak J. Gene expression profiling of human osteoblasts following treatment with the ionic products of Bioglass 45S5 dissolution. J Biomed Mater Res. 2001;55(2):152-157.
317. Liu X HW, Fang Z, Kienzle A, Feng Q. Influence of silver nanoparticles on osteogenic differentiation of human mesenchymal stem cells. Jornal of Biomed Nanotechnol. 2014;10(7).
318. Mahmood M, Li Z, Casciano D, Khodakovskaya M, Chen T, Karmakar A, et al. Nanostructural materials increase mineralization in bone cellsand affect gene expression through miRNA regulation. J Cell Mol Med. 2011;15(11):2297-2306.
319. Albers C, Hofstetter W, Siebenrock K, Landmann R, Klenke F. Cytotoxic effects of ions silver and silver nano-particles on osteoblasts and osteoclasts in vitro. J Bone Joint Surg Br. 2012;94:163.
320. Revell P, Damien E, Zhang X, Evans P, Howlett C. The effect of magnesium ions on bone bonding to hydroxyapatite. Key Eng Mater. 2004;254-256:447-450.
321. Hartwig A. Role of magnesium in genomic stability. Mutat Res/Fund Mol Mech Mutagen. 2001;475:113-121.
322. Leidi M, Dellera F, Mariotti M, Maier J. High magnesium inhibits human osteoblast differentiation in vitro. Magness Res. 2011;24(1):1-6.

323. Cai Y, Zhang J, Zhang S, Venkatraman S, Zeng X, Du H, et al. Osteoblastic cell response on fluoridated hydroxyapatite coatings: the effect of magnesium incorporation. Biomed Mater. 2010;5(5):7-14.
324. Lee D, Lee K, Kim J, Choi M, Chang J. Effects of Magnesium Ion on Proliferation and Differentiation of Human Bone Marrow Stromal Cells. Biology and Biomechanics of Spinal Disorders 2.
325. Li L, Gao Y, Wang Y. Evaluation of cyto-toxicity and corrosion behavior of alkali-heat-treated magnesium in simulated body fluid. Surf Coat Technol. 2004;185:92-98.
326. Kwon Y, Lee D, Hong S. Magnesium vs. machined surfaced titanium - osteoblast and osteoclast differentiation. J Adv Prosthodont. 2014;6(3):157-164.
327. Park K, Lee B, Piao X, Lee K, Park S, Oh H, et al. Effect of magnesium and calcium phosphate coatings on osteoblastic responses to the titanium surface. jornal of advance Prosthodont 2013;5:402-410.
328. Yamaguchi M, Yamguchi R. Action of zinc on bone metabolism in rats/increase in alkaline phosphate activity and DNA content. Biomechanical Pharmacology. 1985;35(5):773-777.
329. Ito A, Otsuka M, Kawamura H, Ikeuchi M, Ohgushi H, Sogo Y, et al. Zinc-containing tricalcium phosphate and related materials for promoting bone formation. Current Applied Physics. 2004;5:402-406.
330. Badr-Mohammadi M, Hesaraki S, Zamanian A. Mechanical properties and in vitro cellular behavior of zinc-containing nano-bioactive glass doped biphasic calcium phosphate bone substitutes. J Mater Sci Mater Med. 2014;25(1):185-197.
331. Seo H, Cho Y, Kim T, Shin H, Kwun I. Zinc may increase bone formation through stimulating cell proliferation, alkaline phosphatase activity and collagen synthesis in osteoblastic MC3T3-E1 cells. Nutr Res Pract. 2010;4(5):356-361.
332. Cerovic A, Miletic I, Sobaijic S, Blagojevic D, Radusinovic M, El-Sohemy A. Effects of zinc on the mineralization of bone nodules from human osteoblast-like cells. Biol Trace Elem Res. 2007;116(1):61-71.
333. Yang F, Dong W, He F, Wang X, Zhao S, Yang G. Osteoblast response to porous titanium surfaces coated with zinc-substituted hydroxyapatite. Oral Surg Oral Med Oral Pathol Oral Radiol. 2012;113(3):313-318.
334. Uysal I, Severcan F, Tezcaner A, Evis Z. Co-doping of hydroxyapatite with zinc and fluoride improves mechanical and biological properties of hydroxyapatite. Progress in Natural Science: Materials International. 2014;24(4):340-349.
335. Jones S, Bowler P, Walker M, Parsons D. Controlling wound bioburden with a novel silver-containing Hydrofiber dressing. Wound Repair Regen. 2004;12(3):288-294.
336. Benn T, Westerhoff P. Nanoparticle silver released into water from commercially available sock fabrics,. Environ Sci Technol. 2008;42(11):4133-4139.
337. Jain P, Pradeep T. Potential of silver nanoparticle-coated polyurethane foam as an antibacterial water filter. Biotechnol Bioeng. 2005;90(1):59-63.
338. Jelínek M, Weiserová M, Kocourek T, Zezulová M, Strnad J. Biomedical properties of laser prepared silver-doped hydroxyapatite. Laser Physics. 2011;21(7):1265-1269.
339. Berger T, Spadaro J, Chapin S, Becker R. Electrically Generated Silver Ions: Quantitative Effects on Bacterial and Mammalian Cells. Antimicrob Agents Chemother. 1976;9(2):357-358.

340. Nover L, Scharf K, Neuman D. Formation of cytoplasmic heat shock protein granules in tomato cell cultures and leaves. Mol Cell Bio. 1983;3(9):1648-1655.
341. Sondi I, Salopek-Sondi B. Silver nanoparticles as antimicrobial agent: a case study on E. coli as a model for Gram-negative bacteria. J Colloid Interface Sci. 2004;275(1):177-182.
342. Kim T, Feng Q, Kim J, Wu J, Chen G, Cui F. Antimicrobial effects of metal ions (Ag+, Cu2+, Zn2+) in hydroxyapatite. J Mater Sci Mater Med. 1998;9(3):129-134.
343. Sun T, Hao H, Hao W, Yi S, Li X, Li J. Preparation and antibacterial properties of titanium-doped ZnO from different zinc salts. Nanoscale Res Lett. 2014 2014/02/27;9(1):1-11.
344. Feng Q, Wu J, Chen G, Cui F, Kim T, Kim J. A mechanistic study of the antibacterial effect of silver ions on Escherichia coli and Staphylococcus aureus. J Biomed Mater Res. 2000;52(4):662-668.
345. Jung W, Koo H, Kim K, Shin S, Kim S, Park Y. Antibacterial activity and mechanism of action of the silver ion in Staphylococcus aureus and Escherichia coli. Appl Environ Microbiol. 2008;74(7):2171-2178.
346. Jun J, Kuk E, Yu K, Kim J, Park S, Lee H, et al. Antimicrobial effects of silver nanoparticles. Nanomed Nanotechnol Biol Med. 2007;3(1):95-101.
347. Hamouda T, Myc A, Donovan B, Shih A, Reuter D, Baker J. A novel surfactant nanoemulsion with a unique non-irritant topical antimicrobial activity against bacteria, enveloped viruses and fungi. Microbiol Res. 2000;156(1):1-7.
348. Dibrov P, Dzioba J, Gosink K, Hase C. Chemiosmotic mechanism of antimicrobial activity of Ag(+) in Vibrio cholerae. Antimicrob Agents Chemother. 2002;46(8):2668-2670.
349. Amro N, Kotra L, Wadu-Mesthrige K, Bulychev A, Mobashery S, Liu G. High-resolution atomic force microscopy studies of the Escherichia coli outer membrane: structural basis for permeability. Langmuir 2000;16(6):2789-2796.
350. Nagarajan P, Rajagopalan V. Enhanced bioactivity of ZnO nanoparticles—an antimicrobialstudy. J Sci Technol Adv Mater. 2008;9(3).
351. Cioffi N, Rai M. Nano-Antimicrobials: Progress and Prospects: Springer; 2012.
352. Chung R, Hsieh M, Huang C, Perng L, Wen H, Chin T. Antimicrobial effects and human gingival biocompatibility of hydroxyapatite sol-gel coatings. J Biomed Mater Res B Appl Biomater. 2006;76(1):169-178.
353. Zakaria Z, Mat Desa A, Ramasamy K, Ahmat N, Mohamad A, Israf D, et al. Lack of antimicrobial activities of Dicranopteris linearisextracts and fractions. Afr J Microbial. 2010;4(2):071-075.
354. Toshiaki O, Osamu Y, Yasuhiro I, Zenbe N. Antibacterial activity of ZnO powder with crystallographic orientation. J Mater Sci Mater Med. 2008;19(3):1407-1413.
355. Matei A, Cernica I, Cadar O, Roman C, Schiopu V. Synthesis and characterization of ZnO – polymer nanocomposites. Int J Mater Form. 2008;1(1):767-770.
356. Rizwan W, Nagendra K, Akhilesh K, Anurag M, Hwang I, You-Bing Y, et al. Fabrication and growth mechanism of ZnO nanostructures and their cytotoxic effect on human brain tumor U87, cervical cancer HeLa, and normal HEK cell. J Biol Inorg Chem. 2010;16(3):431-443.

357. Ohsumi Y, Kitamoto K, Anraku Y. Changes induced in the permeability barrier of the yeast plasma membrane by cupric ion. J Bacteriol. 1988;170(6):2676-2682.
358. Pasquet J, Chevalier Y, Pelletier J, Couval E, Bouvier D, Bolzinger M-A. The contribution of zinc ions to the antimicrobial activity of zinc oxide. Colloids and Surfaces A: Physicochemical and Engineering Aspects. 2014;457(0):263-274.
359. Wang C, Liu L, Zhang A, Xie P, Lu J, Zou X. Antibacterial effects of zinc oxide nanoparticles on Escherichia coli K88. African Journal of Biotechnology 2014;11(44):10248-10254.
360. Soderberg TA, Sunzel B, Holm S, Elmros T, Hallmans G, Sjoberg S. Antibacterial effect of zinc oxide in vitro. Scand J Plast Reconstr Surg Hand Surg. 1990;24(3):193-197.
361. Reddy K, Kevin F, Jason B, Denise G, Cory H, Alex P. Selective toxicity of zinc oxide nanoparticles to prokaryotic and eukaryotic systems. J Appl Phys Lett. 2007;90(21):1-4.
362. Selahattin A, Kadri G, Ramazan C. The effect of zinc on microbial growth. Tr J Med Sci. 1998;28:595-597.
363. Canani R, Ruotolo S. The Dawning of the "Zinc Era" in the Treatment of Pediatric Acute Gastroenteritis Worldwide? J Pediatr Gastroenterol Nutr. 2006;42(3):253-255.
364. Venkatasubbu G, Ramasamy S, Ramakrishnan V, Kumar J. Nanocrystalline hydroxyapatite and zinc doped hydroxyapatite as carrier material for controlled delivery of ciprofloxacin. 3 Biotech. 2011;1(3):173-186.